

Synthesis of novel manganese-based oxide catalysts for combustion of volatile organic compounds

by

Jinggang Zhao

Supervisor: Prof. Dr Guoqing Guan

Graduate School of Science and Technology

Hirosaki University

2023

ABSTRACT

Volatile organic compounds (VOCs) released from various chemical industrial processes, transporting sections, necessities manufacturing and human daily activities are severely harmful to environment, animals and plants due to their contributions to air pollution, e.g., photochemical smog, inhalable particles and tropospheric ozone. Among various VOCs purification technologies that have been developed such as catalytic oxidation, incineration, biodegradation, adsorption, wet scrubbing, plasma process and photocatalysis methods, catalytic combustion of VOCs has attracted wide attention owing to its high efficiency, low cost, non-secondary pollution and easy operation. Supported noble metal and non-noble metal oxides are two common catalysts for the catalytic VOCs combustion. However, the former's high price and unsatisfactory stability properties have long been motivating the search and development of the latter. Among non-noble metal oxide catalysts, Mn-based ones have been widely explored due to their tunable multiple valences and excellent redox capacity. However, traditional catalyst synthesis routes are needed to improve and modify in order to adapt to the advanced concepts of high efficiency, environmental protection and innovation advocated by today's society. Therefore, after reviewing the VOCs catalytic oxidation mechanisms and the construction strategies as well as advantages of microscopic heterogeneous structures that seriously affect catalyst performances, this work developed three novel and highly efficient Mn-based catalysts and applied them to the catalytic toluene combustion.

Firstly, a novel green pectin-driven sol-gel with an auto-combustion route was successfully applied for the synthesis of manganese oxide catalysts, which exhibited superior catalytic performance for low-temperature combustion of toluene compared to those cases using manganese oxide catalysts synthesized by traditional citric acid and glycine-driven sol-gel routes. The characterization results showed that the MnO_x -P catalyst synthesized by the present method exhibited a unique hierarchical mesoporous structure with lower crystallinity and smaller grain size, leading to abundant active

species and defect structures. Comparing with the catalysts synthesized by those traditional sol-gel methods, the $\text{MnO}_x\text{-P}$ catalyst had excellent low-temperature reducible performance and better oxygen mobility, which should be resulted from the specific interaction of chelation and calcination processes. In addition, the $\text{MnO}_x\text{-P}$ catalyst exhibited satisfactory long-term stability and water tolerance during catalytic toluene combustion process.

Secondly, for the first time, a nanosheet-state CoMnx mixed oxide with multifarious active regions was synthesized by oxidation-etching assembly of metal organic framework (MOF) precursor and applied for catalytic combustion of toluene at low temperatures. The obtained optimum catalyst denoted as CoMn6 showed excellent performance, which achieved 90% conversion of 1,000 ppm toluene under a weight hourly space velocity (WHSV) of $60,000 \text{ cm}^3 \cdot \text{g}^{-1} \cdot \text{h}^{-1}$ at 219°C . While, it also exhibited long-term stability with strong water resistance property. The characterizations of physicochemical properties indicated that the oxidation-etching assembly process built an abundant mesoporous structure in the CoMnx catalyst, which greatly increased the specific surface area (SSA). Especially, potassium permanganate as oxidant and manganese source led to uniform dispersion and assembling of cobalt atoms, which caused the generation of low-crystallinity CoMnx mixed oxide with abundant dislocations, vacancies, phase interfaces and amorphous structures, resulting in excellent low-temperature reducibility, outstanding lattice oxygen mobility and abundant active species such as Mn^{3+} , Co^{3+} and adsorbed oxygen species. Density functional theory (DFT) calculations demonstrated that gaseous oxygen with the longer bond length (1.406 \AA) and stronger adsorption energy (-4.443 eV) could be adsorbed and activated well on the $\text{MnCo}_2\text{O}_{4.5}$ (311) plane, which is beneficial for the toluene oxidation. In situ diffuse reflectance infrared spectroscopy (DRIFTS) technique was applied to track the intermediates of toluene combustion under different atmospheres, which further deduced the contributions of different active regions and oxidation mechanism over the CoMnx catalyst. The present facile strategy of oxidation-etching assembly of the MOF precursor for the creating of novel catalyst with high performance could be applied in a wide variety of materials besides VOC combustion catalysts.

Finally, a nanoparticles-stacking MnCo_x oxide with multifarious active phases was successfully synthesized by a starch-paste assisted method, which achieved complete combustion of 1,000 ppm toluene at 226 °C. The characterization results showed that by using this method, it resulted in not only the construction of the porous structure but also successful enrichment of active species such as trivalent manganese, trivalent cobalt and electrophilic oxygen species, thanks to the intensive interaction of Mn and Co species with the assistance of starch-paste. The special metal dispersibility and valence adjustment functions of starch contributed to the production of multifarious active phases with amazing reducibility as well as oxygen mobility at lower temperature. In situ DRIFTS experiments and DFT calculation results showed that the synergistic complementary regions provided vibrant lattice oxygen and the reproducible electrophilic oxygen species for toluene combustion, guaranteeing the continuous and efficient catalytic performance. This study provides a new viewpoint and idea for creating of novel catalysts with multiple active regions.

ACKNOWLEDGEMENTS

First and foremost, I would like to express my sincerest gratitude to my learned, rigorous, and respectable supervisor, Professor Dr. Guoqing Guan for giving me this valuable opportunity to study for PhD degree in his group, as well as the encouragements, supports and professional academical guidance during my PhD program.

I am extremely grateful to Professor Dr. Abuliti Abudula, Graduate School of Science and Technology, Hirosaki University, for his generous help on my life and research. I also thank Associate Professor Dr. Akihiro Yoshida for his useful advice on my instrument repair.

I would like to extend my thanks to Dr. Peifen Wang, senior sister apprentice, for her patience and detailed guidance on my experiments and instrument operation.

Deepest appreciation is also given to Prof. Dr. Guangwen Xu, Lei Shi and Xuejun Zhang, Shenyang University of Chemical Technology, who introduced and recommended me to this research group.

I would like to give my thanks to all members in our group for their warm helps. I would like to thank all professors and staffs at Institute of Regional Innovation (IRI) and Graduated School of Science and Technology, Hirosaki University, for their thoughtful help and supports.

I would like to express my deepest appreciation to my parents and little sister, for their continued understanding, encouragement and support in my life and study.

Finally, I would like to give my deep thanks to ZiQoo Chemical Co. Ltd., Japan, and Shared Facility Center for Science and Technology (SFCST), Hirosaki University, Japan, for their kind support to my research.

Thank you all very much.

Jinggang Zhao

TABLE OF CONTENTS

ABSTRACT	I
ACKNOWLEDGEMENTS	IV
TABLE OF CONTENTS	V
LIST OF TABLES	VIII
LIST OF FIGURES	IX
LIST OF SCHEMES	XV
CHAPTER 1 Introduction	1
1.1 General introduction	1
1.2 Reaction mechanism for catalytic VOCs oxidation.....	3
1.3 Types and construction strategies of heterostructures.....	5
1.3.1 Dislocation structure	7
1.3.2 Vacancy heterogeneity	10
1.3.3 Interface structure	14
1.3.4 Interbedded structure	17
1.3.5 Heteroatomic doping.....	19
1.4 Function and superiority of heterogeneous structure in VOCs combustion ..	20
1.4.1 Reducibility and oxygen mobility enhancement.....	20
1.4.2 Adsorption and activation sites	22
1.4.3 Transfer sites	26
1.4.4 Acidity sites.....	28
1.4.5 Other special functions	30
1.5 Objective of this study	30
1.6 Scope of this dissertation	31
References	33
CHAPTER 2 Synthesis of MnO_x from pectin-driven sol-gel route for catalytic oxidation of toluene	48
2.1 Introduction.....	48
2.2 Experimental and measurements	50
2.2.1 Catalyst preparation	50
2.2.2 Catalytic performance test	51
2.2.3 Catalyst characterization	52

2.3 Result and discussion.....	53
2.3.1 Morphologies of prepared MnO _x catalysts	53
2.3.2 N ₂ adsorption-desorption studies	54
2.3.3 Crystalline phase structure of prepared catalysts.....	55
2.3.4 TEM and HRTEM results of the prepared MnO _x catalysts.....	58
2.3.5 Reducibility analysis	59
2.3.6 Oxygen mobility analysis	61
2.3.7 Surface composition and oxidation state	61
2.3.8 Catalytic performances and dynamics results.....	63
2.3.9 Pectin usage effect, catalytic stability and water vapor effect	64
2.4 Conclusions.....	65
References	67
CHAPTER 3 Nanosheet-state cobalt-manganese oxide with multifarious active regions derived from oxidation-etching of metal organic framework precursor for catalytic combustion of toluene.....	73
3.1 Introduction.....	73
3.2 Experimental and measurements	75
3.2.1 Catalyst preparation	75
3.2.2 Catalytic performance test	77
3.2.3 Catalyst characterization.....	78
3.3 Result and discussion.....	79
3.3.1 SEM and N ₂ adsorption-desorption characterizations	79
3.3.2 XRD and Raman analyses	82
3.3.3 XPS analysis	85
3.3.4 HRTEM and EDX analysis results	88
3.3.5 H ₂ -TPR and O ₂ -TPD analyses	90
3.3.6 EPR spectrum.....	93
3.3.7 Catalytic performances and kinetic studies.....	94
3.3.8 WHSV effect, durability and water vapor resistance evaluations.....	97
3.3.9 In situ DRIFTS, DFT calculations and mechanism analysis	99
3.4 Conclusions.....	106
References	108

CHAPTER 4 Biostarch-assisted synthesis of microscopic heterogeneous manganese-cobalt oxides for efficient catalytic combustion of toluene	115
4.1 Introduction.....	115
4.2 Experimental and measurements	117
4.2.1 Catalyst preparation	117
4.2.2 Catalytic performance test	119
4.2.3 Catalyst characterization	120
4.3 Result and discussion.....	121
4.3.1 Morphology and porous structure of prepared catalysts.....	121
4.3.2 Crystalline phase structure of prepared catalysts.....	124
4.3.3 Surface chemical properties of prepared catalysts.....	126
4.3.4 Unpaired electron analysis for catalysts	129
4.3.5 HR-TEM image and EDX mapping results	130
4.3.6 Reducibility and oxygen species mobility	132
4.3.7 Catalytic performances and dynamics	135
4.3.8 In situ DRIFTS, DFT calculations and oxidation mechanism	140
4.3.9 Discussion on the function of starch paste in catalyst synthesis.....	147
4.4 Conclusions.....	149
References	151
CHAPTER 5 Conclusions and prospects	158
5.1 Conclusions.....	158
5.2 Prospects	160
List of publications and presentations	162
List of patents	164
List of awards	165
Curriculum vitae	166

LIST OF TABLES

Table 1.1 Catalytic VOCs combustion performances over various developed catalysts with different heterostructures.	6
Table 2.1 N ₂ adsorption-desorption, XRD and TEM analysis results for all prepared MnO _x catalysts.	55
Table 2.2 The results of H ₂ -TPR, O ₂ -TPD, normalized reaction rate, and apparent activation energy for prepared MnO _x catalysts.	62
Table 3.1 Textural properties and XRF analysis results of all prepared catalysts.	81
Table 3.2 Analysis results of H ₂ -TPR profiles, O ₂ -TPD profiles, XPS element compositions, specific reaction rates, and activation energy for all prepared samples.	87
Table 3.3 Summary and comparison of the catalytic performance for toluene over supported and nanosized Mn-Co mixed oxide catalysts reported in literature and this work.	96
Table 3.4 Assignments of main IR bands appearing in the <i>in situ</i> experiments of toluene combustion over the CoMn6 catalyst.	106
Table 4.1 N ₂ adsorption-desorption, XRF and XRD analysis results of the prepared catalysts.	125
Table 4.2 Summary of XPS, H ₂ -TPR, O ₂ -TPD analysis results, apparent activation energy and reaction rates for total toluene combustion over the prepared catalysts.	135
Table 4.3 Summary and comparison of toluene combustion performance over nanosized Mn-Co-based catalysts presented in other reports and all catalysts in this work.	139
Table 4.4 Vibratory assignments of main <i>in situ</i> DRIFTS bands in toluene oxidation process over the CoMn6.6 catalyst.	146

LIST OF FIGURES

Fig. 1.1. Schematic diagrams of various VOCs treatment processes: (a) adsorption, (b) absorption, (c) condensation, (d) membrane separation, (e) plasma, (f) thermal incineration, (g) photocatalysis, (h) biodegradation and (i) catalytic oxidation technologies.	3
Fig. 1.2. Schematic diagrams of degradation mechanisms for VOCs oxidation: (a) MVK, (b) L-H and (c) E-R mechanisms.	5
Fig. 1.3. SEM images of samples of 14Co1Mn (a1), 5Co1Mn (a2), 2Co1Mn (a3) catalysts; Catalytic activities of the prepared samples for toluene combustion (b); HRTEM images of 14Co1Mn (c1, c2), 5Co1Mn (c3, c4), 2Co1Mn (c5, c6) catalysts [57].	8
Fig. 1.4. HRTEM (a1, amplified a1-1 to a1-4 and dislocation diagram a1-5) and TEM (a2) image of Mn ₂ Co catalyst; Catalytic activity of prepared MnCo samples for toluene combustion (a3) [60]. TEM image (b1) and amplified TEM images (b1-1 to b1-4) of Fe1Mn5 sample; Catalytic activity of prepared FeMn samples for toluene combustion (b2) [92].	10
Fig. 1.5. Schematic process of synthesis procedure (a) and SEM image (b) for D-NiCo ₂ O ₄ ; EPR spectra for D-NiCo ₂ O ₄ and NiCo ₂ O ₄ (c); Catalytic performances for propane combustion over NiCo ₂ O ₄ and D-NiCo ₂ O ₄ catalysts (d) [87].	13
Fig. 1.6. Schematic illustration of the preparation process for MnOx-NA catalyst (a); EPR profiles (b) and evaluation of catalytic acetone oxidation (c) over MnOx-NA, MnOx-A and MnOx-B catalysts [96].	13
Fig. 1.7. Schematic process for the synthesis of heterogeneous MnO ₂ @Co ₃ O ₄ catalyst (a1) and its SEM (a2), TEM (a3) and HRTEM (a4) images [100]; SEM (b1), TEM (b2) and HRTEM (b2) images of CeO ₂ @Co ₃ O ₄ [101]; SEM (c1) and HRTEM (c2) images of α @ β -MnO ₂ , and the toluene oxidation scheme on the α @ β -MnO ₂ catalyst (c3) [102].	15

- Fig. 1.8.** Schematic illustration of the conjectural evolution mechanism for mesocrystalline CeO_2 (a), and its TEM (b) and HRTEM (c, d) images [103]. 16
- Fig. 1.9.** Schematic illustration of the phase change of fresh $\text{Cu}_1\text{Co}_2\text{Fe}_1\text{-CO}_3$ LDH (a), $\text{Cu}_1\text{Co}_2\text{Fe}_1\text{O}_x$ catalysts obtained by calcining $\text{Cu}_1\text{Co}_2\text{Fe}_1\text{-CO}_3$ at 400 °C (b), 500 °C (c) and 600 °C (d); HRTEM images of $\text{Cu}_1\text{Co}_2\text{Fe}_1\text{O}_x$ calcined at 500 °C (e-g) and its FFT image (h) [46]. 17
- Fig. 1.10.** (a) Synthetic schemes for the preparation of $\text{K}_2\text{Mn}_4\text{O}_8$ and K-OMS-2 catalysts, and their catalytic evaluation to soot [130]; (b) Synthetic scheme of $\text{CuO-}\delta\text{-MnO}_2$ hybrid composites by a self-propagated flaming strategy [104]; (c) Scheme of surface in situ modification for Mn_2O_3 with (right) or without (left) Cu insertion [105]; (d) Schematic of the fabricated process for ultrathin $\delta\text{-MnO}_2$ nanosheets [106]. 18
- Fig. 1.11.** Schematic of the synthesis process of $\text{MnO}_x/\text{Co}_3\text{O}_4$ sample (a) [58]; Proposed formation process of amorphous ZrMn mixed oxide (b) [107]; Schematic illustration of the synthesis route for $\text{Cu}_{0.4}\text{Ce}_{0.6}\text{-C}$ and $\text{Cu}_{0.4}\text{Ce}_{0.6}\text{-DR}$ samples [108]. 20
- Fig. 1.12.** H_2 -TPR profiles (a1), O_2 -TPD profiles (a2) and the toluene conversion vs reaction temperature (a3) over Co_3O_4 (black line), $\text{Mn}_{0.2}\text{Co}_{0.8}\text{O}_x$ (red line), $\text{Mn}_{0.3}\text{Co}_{0.7}\text{O}_x$ (blue line), $\text{Mn}_{0.4}\text{Co}_{0.6}\text{O}_x$ (green line), $\text{Mn}_{0.5}\text{Co}_{0.5}\text{O}_x$ (purple line) [134]; H_2 -TPR profiles (b1), O_2 -TPD profiles (b2) and the toluene conversion vs reaction temperature (b3) [60]; H_2 -TPR profiles (c1), O_2 -TPD profiles (c2) and the acetone conversion vs reaction temperature (c3) [96]. 22
- Fig. 1.13.** Diagram of the microstructure for I- MnO_2 and L- MnO_2 catalysts, and the adsorption energies of water and oxygen molecules on them (a1); Arrhenius plots of MnO_2 samples (a2) [14]. Wavelet transform data analysis of Ce L₃-edge EXAFS spectra for $\text{CeO}_2\text{-MC}$ (b1) and $\text{CeO}_2\text{-PC}$ (b2); Time-resolved in situ DRIFTS profiles of toluene in the pre-adsorption stage on $\text{CeO}_2\text{-MC}$ (b3) and $\text{CeO}_2\text{-PC}$ (b4) catalysts [103]. 24
- Fig. 1.14.** Adsorption energies of oxygen molecule on oxygen vacancy from

Mn ₃ O ₄ (a1), Ce-Mn ₃ O ₄ (a2 and a3), Mn ₃ O ₄ -V _{Mn} (b1) and Ce-Mn ₃ O ₄ -V _{Mn} (b2 and b3) catalysts. Ce: yellow; Mn: purple; O: red; adsorbed O ₂ molecule: cyan [97]; The adsorption energies of oxygen over the 311 facet of the prepared CoFe ₂ O ₄ , CuFe ₂ O ₄ and CuCoFe ₂ O ₄ catalysts (c). (legend: red O, purple Co, green Cu and gold iron) [46].	26
Fig. 1.15. Oxygen species replenishment mechanism of spinel catalysts in catalytic combustion of toluene (a1); Arrhenius plots of toluene oxidation over Co ₃ O ₄ , MnO _x , Co ₃ O ₄ /MnO _x and spinel CoMn ₂ O ₄ catalysts (a2) [138]. Slab and density of states for Mn ₃ O ₄ (b1) and Mn ₃ O ₄ -V _{Mn} (b2) catalysts [97].	28
Fig. 1.16. Profiles of NH ₃ -TPD (a), spectra obtained from (b) pyridine adsorbed FTIR and (c) CH ₃ OH-FTIR experiments over the prepared catalysts; (d) by-products distribution during 1,2-DCE combustion and (e) 1,2-DCE conversion vs reaction temperature [107].	30
Fig. 2.1. SEM images of MnO _x -C (a, d), MnO _x -G (b, e) and MnO _x -P (c, f) catalysts.	53
Fig. 2.2. N ₂ adsorption-desorption isotherms (a) and the pore-size distribution curves (b) of the prepared MnO _x catalysts.	54
Fig. 2.3. (a) XRD patterns and (b) Raman spectra of prepared MnO _x samples.	55
Fig. 2.4. TEM and HRTEM images of MnO _x -C (a, b), MnO _x -G (c, d) and MnO _x -P (e, f) catalysts (inset: grain size distributions).	58
Fig. 2.5. (a) H ₂ -TPR profiles and (b) initial H ₂ consumption rates of the prepared MnO _x catalysts.	59
Fig. 2.6. O ₂ -TPD profiles of prepared MnO _x samples.	61
Fig. 2.7. XPS spectra of Mn 2p (a) and O 1s (b) for the prepared catalysts.	61
Fig. 2.8. Catalytic activity for toluene combustion (a), CO ₂ selectivity and (b) Arrhenius plots (c) over the prepared MnO _x catalysts.	63
Fig. 2.9. Effect of pectin dosage (a), durability experiments at 237 °C for 50 h (b), and the influence of 5 vol.% water vapor at 234 °C (c) on the catalytic performance over MnO _x catalyst synthesized by pectin-driven sol-gel route.	

.....	64
Fig. 3.1. SEM images of the CoO _x (a), MnO _x (b), CoMn1 (c), CoMn6 (d) and CoMn11 (e) samples; (f) N ₂ adsorption-desorption isotherms and pore size distributions (inset) of all samples.	79
Fig. 3.2. XRD patterns (a) and Raman spectra (b) of CoO _x , MnO _x and CoMn _x samples; (c) XRD patterns of synthetic and simulated ZIF-67.....	82
Fig. 3.3. XPS spectra of (a) Mn 2p, (b) Co2p and (c) O 1s for the prepared catalysts; (d) Comparison histogram of molar ratio for active components in each catalyst.	85
Fig. 3.4. HRTEM images of the CoO _x (a), MnO _x (b) and CoMn6 (c) catalysts (insets: FFT of characteristic crystal planes); Magnification views of edge dislocations from Fig. 3.4c (C1-C4) and schematic illustration of edge dislocation (C5); EDX mapping of CoMn6 sample (d).....	88
Fig. 3.5. (a) H ₂ -TPR profiles, (b) initial H ₂ consumption rate and (c) O ₂ -TPD profiles of prepared samples.	90
Fig. 3.6. EPR spectra for CoO _x , MnO _x and CoMn _x samples.	93
Fig. 3.7. (a) Toluene conversions vs reaction temperature, (b) CO ₂ selectivity, (c) Arrhenius plots for toluene combustion and (d) relationship between T ₉₀ and E _a values for the prepared catalysts.	95
Fig. 3.8. (a) Effect of WHSV on the toluene conversion, (b) durability and (c) water vapor resistance evaluation over the CoMn6 catalyst.....	97
Fig. 3.9. In situ DRIFTS spectra of toluene combustion over the CoMn6 catalyst exposed at (a) toluene of 1,000 ppm in air atmosphere, (b) toluene of 1,000 ppm in N ₂ atmosphere, (c) toluene of 1,000 ppm in air/5 vol.% water atmosphere; MnO _x sample exposed at (d) toluene of 1,000 ppm in air atmosphere, (e) toluene of 1,000 ppm in N ₂ atmosphere. The schematic illustration of toluene combustion mechanism over CoMn6 catalyst (f).....	99
Fig. 3.10. Diagram of DFT calculation results for adsorption energies and bond lengths of O ₂ (a) and toluene (b) molecules adsorbed on MnCo ₂ O _{4.5} and Co ₃ O ₄ phases.....	104

Fig. 4.1. SEM images of the prepared (a) MnO_x , (b) CoO_x , (c) $\text{MnCo}_{3.3}$, (d) $\text{MnCo}_{6.6}$ and (e) $\text{MnCo}_{9.9}$ samples; (f) N_2 adsorption-desorption isotherms and pore diameter distribution curves (inset) of all catalysts.	122
Fig. 4.2. XRD patterns (a) and Raman spectra (b) of as-synthesized pure MnO_x , CoO_x and MnCo_x composite oxides.....	124
Fig. 4.3. XPS spectra for the prepared catalysts: (a) Mn 2p, (b) Co 2p and (c) O 1s; (d) Bar comparison chart of the proportions for active species in all catalysts.....	126
Fig. 4.4. EPR spectra of MnCo_x , MnO_x and CoO_x samples.....	129
Fig. 4.5. HR-TEM image of (a) CoO_x , (b) MnO_x and (c) $\text{MnCo}_{6.6}$ samples with the FFT result (inset); Magnification images of selected area for edge dislocation (c1-c4) and schematic representation of multifarious regions (c5) from Fig. 4.5c; EDX mapping for $\text{MnCo}_{6.6}$ sample (d).	130
Fig. 4.6. H_2 -TPR curves (a), initial H_2 consumption rate (b) and O_2 -TPD profiles (c) of the as-prepared catalysts.	132
Fig. 4.7. (a) Toluene conversion and (b) corresponding CO_2 formation ratio as a function of the reaction temperature over the prepared catalysts; (c) Arrhenius plots for toluene combustion and (d) combinatorial comparison diagram of E_a and T_{90} values; Effects of (e) WHSV and (f) duration with water vapor on toluene catalytic performance over $\text{MnCo}_{6.6}$ catalyst.	135
Fig. 4.8. Time-dependent in situ DRIFTS spectra of toluene oxidation over $\text{MnCo}_{6.6}$ catalyst with (a) toluene/air atmosphere, (b) toluene/ N_2 atmosphere, and pure MnO_x catalyst with (c) toluene/air atmosphere, (d) toluene/ N_2 atmosphere; Temperature-dependent in situ DRIFTS spectra of toluene oxidation over $\text{MnCo}_{6.6}$ (e) and MnO_x (f) catalysts with the increasing of temperatures in toluene/air atmosphere.	140
Fig. 4.9. Diagrams of DFT calculations for the adsorption properties of (a) oxygen and toluene (b) molecules on the spinel structure, and (c) combustion mechanism of toluene over $\text{MnCo}_{6.6}$ catalyst in air atmosphere.....	144
Fig. 4.10. FT-IR spectra of potato starch (a), starch paste with cobalt dispersed (b),	

catalyst precursor obtained after oxidative shear process (c) and MnCo_{6.6}
catalyst (d), Corresponding references: a, b, c [58]; e, f, g [59]; h, i, j [60]; d,
k [61]..... 148

LIST OF SCHEMES

Scheme 3.1. Diagram of synthetic route and morphological evolution for CoMnx mixed oxide catalyst.	77
Scheme 4.1. Schematic illustration of synthetic strategy and morphological evolution for the preparation of MnCoO _x catalyst.	119
Scheme 4.2. Schematic illustration of the starch functions in the synthesis process of MnCox catalysts.	147

CHAPTER 1 Introduction

1.1 General introduction

Volatile organic compounds (VOCs) generally represent a class of organic compounds with boiling point lower than 250 °C at room temperature under atmospheric pressure (101.325 kPa), including aromatics, aliphatic hydrocarbons, halogenated hydrocarbons, O/N/S containing compounds [1, 2]. The main emission sources of VOCs include but are not limited to petrochemical industry, construction/decoration materials, printing industry, transportation, solvents, electronic component plants and textile manufacturers [3, 4]. In recent years, as the precursors of forming photochemical smog, inhalable particulate matter and tropospheric ozone, VOCs in the environment have become nonnegligible air pollutants and seriously endangered the ecological environment, buildings, and the health of animals and plants owing to their corrosivity, toxic and carcinogenicity [5, 6]. Hence, various VOCs treatment technologies (Fig. 1.1) have been developed to control the emitted VOCs concentration, which include adsorption (Fig. 1.1a), absorption (Fig. 1.1b), condensation (Fig. 1.1c), membrane separation (Fig. 1.1d), plasma (Fig. 1.1e), thermal incineration (Fig. 1.1f), photocatalysis (Fig. 1.1g), biodegradation (Fig. 1.1h) and catalytic oxidation (Fig. 1.1i) technologies [2, 7-9]. Among them, the catalytic oxidation method is favored due to its simple operation, low cost, high efficiency and no secondary pollution, in which the catalytic VOC efficiency is directly affected by the type and properties of the catalyst.

Currently, the catalysts for VOCs oxidation are mainly divided into supported noble metal-based catalysts (e.g., Pt- [10], Pd- [11], Ag- [12] and Au- [13] based ones), non-noble metal-based catalysts represented by Mn- [14, 15], Co- [16, 17], Ce- [18, 19] and their mixture based oxides. Although the former ones always have high VOCs catalytic activity, their high price, easy poisoning, easy sintering nature not only restrict their wide industrial applications, but also inspire researchers to develop and modify the latter ones [20, 21]. Over the years, a large number of transition metal and rare earth

metal-based catalysts for the VOCs combustion have been developed via different synthesis processes, e.g., impregnation method [22, 23], coprecipitation approach [24, 25], selective dissolution method [26], sol-gel method [27, 28], soft/hard template method [29-31], hydrothermal method [32], in-situ crystallization [33], sacrificial metal-organic frameworks (MOFs) [34, 35], redox reaction route [36, 37] and vapor deposition method [7]. Moreover, researchers have adopted various strategies to optimize the comprehensive VOCs catalytic performances of non-noble metal-based catalysts, such as morphological control [38-40], crystal plane/phase regulation [41, 42], support selection [43-45], defect structure creation [37, 46, 47], surface modification [48-50], porous structure construction [48, 51], microheterogeneity fabrication [52, 53] and so on. Especially, based on the analysis of recent literatures, it is found that the microscopic heterostructures constructed intentionally or unintentionally in catalysts are always accompanied by electron redistribution and the change of coordination environment, which would induce different physicochemical properties in the catalyst and affect the VOCs catalytic performance [54-57]. For instances, Han et al. [58] synthesized a $\text{MnO}_x/\text{Co}_3\text{O}_4$ catalyst with local lattice distortion by incorporating Mn species into the surface octahedral sites of Co_3O_4 , in which the enhanced disordered structure on the surface rather than the bulk phase led to the generation of more active Co^{3+} species, achieving a better catalytic activity for toluene oxidation. Zhou et al. [59] investigated the effect of crystalline integrity on the catalytic VOCs combustion performance over three kinds of MnO_x catalysts, i.e., pure amorphous, partial crystallization and intact crystal MnO_x oxides, and confirmed that the abundant unsaturated coordination bonds and defect structures in amorphous phase can optimize the adsorption ability of catalyst while the crystalline phase could facilitate the adsorption and activation of oxygen species. As a result, the catalyst with partial crystallization achieved optimum catalytic activity for toluene oxidation due to the synergistic effect of crystalline and amorphous phases. In addition, Wang et al. [60] also found that the catalysts with micro-heterostructures such as partial crystallization, defects, interfaces, etc., exhibited much higher reducibility and oxygen mobility than those with high crystallinity, thereby exhibiting excellent catalytic performance for

toluene oxidation. In short, the construction of an appropriate proportion of microscopic heterostructures in catalysts is an effective strategy to optimize catalytic activity for low-temperature VOCs combustion.

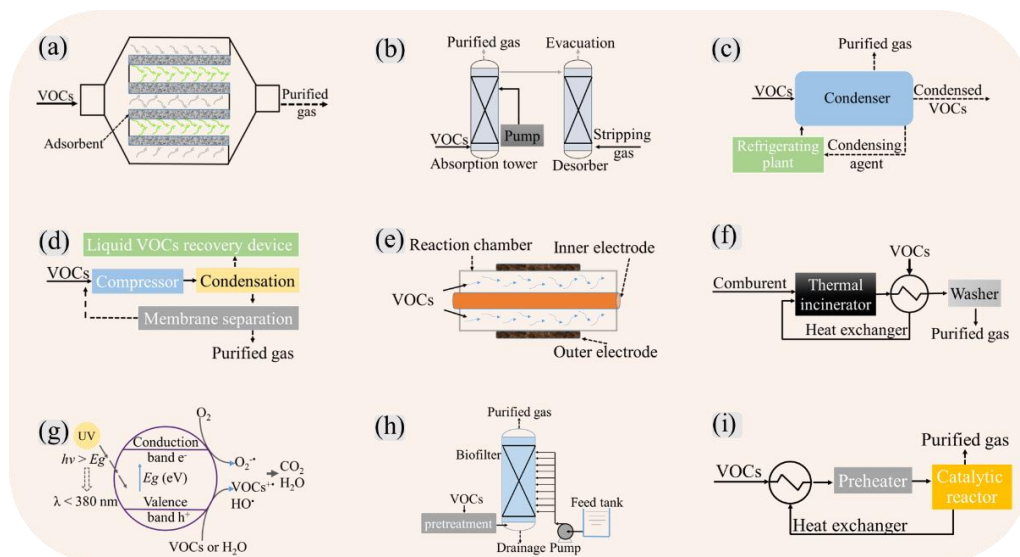


Fig. 1.1. Schematic diagrams of various VOCs treatment processes: (a) adsorption, (b) absorption, (c) condensation, (d) membrane separation, (e) plasma, (f) thermal incineration, (g) photocatalysis, (h) biodegradation and (i) catalytic oxidation technologies.

1.2 Reaction mechanism for catalytic VOCs oxidation

In the exploration of the catalytic VOCs oxidation mechanisms, Mars-van Krevelen (MVK), Langmuir-Hinshelwood (L-H) and Eley-Rideal (E-R) dynamics models have been proposed mainly. Currently, the most widely applicable model for VOCs oxidation is the MVK model verified by Mars and van Krevelen in 1954, which reveals that the oxidation reaction should occur between organic molecules and lattice oxygen species on the catalyst surface, such as those on the Mn-based [61-63], Co-based [16, 64, 65], Ce-based [66, 67] and other metal-based catalysts [46, 68, 69]. As illustrated in Fig. 1.2a, the MVK mechanism states that VOCs molecules are first adsorbed on the surface of the catalyst and then react with lattice oxygen species, and at the same time oxygen vacancies are formed in the catalyst. Subsequently, the reduced sites are rapidly re-oxidized by gaseous oxygen in the feed or bulk oxygen from the catalyst to realize the catalytic oxidation performance recovery. The oxidation and reduction rates in the

catalytic oxidation process should be equal in the steady state, which is also known as the redox mechanism. In addition, the VOC reaction rate ($-R_{voc}$) under the MVK mechanism can be expressed according to the kinetic equation (Eq. (1)): $-R_{voc} = \frac{k_{O_2}k_{voc}P_{voc}P_{O_2}}{\gamma k_{voc}P_{voc} + k_{O_2}P_{O_2}}$, where, P_{O_2} and P_{voc} are partial pressures of oxygen and VOC, respectively; k_{O_2} and k_{voc} are the rate constants of re-oxidation of catalyst and VOC oxidation, respectively; γ is the stoichiometry coefficient of O_2 in the deep VOC oxidation [1, 70]. Another commonly used model for the catalytic VOC oxidation mechanism is the L-H model, which is suitable for most supported noble metal catalysts [41, 71] and many non-noble metal based ones [72-74]. L-H model considers that the oxidation reaction occurs between the adsorbed VOC molecules and oxygen species (Fig. 1.2b). Hence, the adsorption and activation efficiency of the reactant molecules by the adsorption and active sites determine the oxidation rate. Moreover, according to whether the adsorption sites of VOC and oxygen molecules are similar or not, the L-H model can be divided into single-site L-H model and dual-site L-H model [8, 75], and the reaction rates ($-R_{voc}$) of single-site and dual-site models can be calculated from the Eq. (2): $-R_{voc} = \frac{kK_{voc}K_{O_2}P_{voc}P_{O_2}}{(1+K_{voc}P_{voc}+K_{O_2}P_{O_2})^2}$ and Eq. (3): $-R_{voc} = \frac{kK_{voc}K_{O_2}P_{voc}P_{O_2}}{(1+K_{voc}P_{voc})+(1+K_{O_2}P_{O_2})}$, respectively [3]. Besides, the E-R mechanism is also often used to analyze the catalytic combustion of VOCs on noble- [76-78] or non-noble metal-based catalysts [23, 79], in which the catalytic process occurs between the adsorbed oxygen species and gaseous VOC rather than the adsorbed VOC molecules (Fig. 1.2c) [8, 80, 81]. The reaction rate ($-R_{voc}$) of VOCs oxidation over E-R mechanism can be represent by Eq. (4): $-R_{voc} = \frac{kK_{voc}P_{voc}P_{O_2}}{1+K_{voc}P_{voc}}$ [82]. Actually, the catalytic VOCs combustion efficiencies based on these three mechanisms are also closely related to the chemical properties of VOCs. The VOCs oxidation processes represented by nonpolar aromatic compounds with electron-rich environment tend to undergo electrostatic attraction, π -complexation, π - π interactions, etc. By contrast, polar VOCs molecules with heteroatoms contained (e.g., halogen-, O-, S- or N-) are more likely to participate in the formation of hydrogen bonds and the generation of electron donor-acceptor,

polar-polar, acid-base interactions due to their lone pair of electrons, thereby exhibiting better adsorption than nonpolar molecules [75, 83]. It is worth noting that no matter which mechanism is adopted, the generation rate of active oxygen species on catalyst surface and cyclic mobility of lattice oxygen species are important factors affecting the catalytic efficiency, which has been shown to be positively related to the microscopic heterostructure in the catalyst [56, 57, 84-88].



Fig. 1.2. Schematic diagrams of degradation mechanisms for VOCs oxidation: (a) MVK, (b) L-H and (c) E-R mechanisms.

1.3 Types and construction strategies of heterostructures

Generally, micro-heterostructures in the catalysts could be mainly classified into structural defects and specific structures. Table 1.1 summarizes the typical microscopic heterogeneous catalysts used in the catalytic combustion of VOCs. The structural defects can mainly be divided into vacancies, dislocations species, etc., and the specific structures generally includes interfaces, special crystal structures, heteroatom heterostructures, acceptors/carrier structures, etc. The existence of micro-heterostructures in catalyst materials is usually accompanied by the generation of crystal micro-strain, strong interaction of different phases, and low-coordinating oxygen atoms, which always result in abundant adsorption sites as well as active centers, and more reactive oxygen species in the catalyst, leading to synergistic and complementary catalytic effects for VOCs oxidation [89-91]. In situ generation and post-reconstruction are two prevalent strategies for heterostructure creation in catalysts, e.g., doping strategy, surface modification, etching strategy, and thermal treatment reduction strategy.

Table 1.1 Catalytic VOCs combustion performances over various developed catalysts with different heterostructures.

Heterostructure	Catalyst	VOC	Condition	T ₉₀ (°C)	E _a (kJ/mol)	Ref.
Dislocation	5Co1Mn	Toluene	1000 ppm, 60,000 mL/(g·h)	247	112	[57]
Dislocation	Mn2Co1	Toluene	1000 ppm, 60,000 mL/(g·h)	236	-	[60]
Dislocation	Fe1Mn5	Toluene	1000 ppm, 30,000 mL/(g·h)	209	66.4	[92]
Dislocation	1% Sm/CeO ₂	Toluene	1000 ppm, 60,000 mL/(g·h)	211	-	[93]
Anion vacancy	LaFeO ₃	Toluene	1000 ppm, 20,000 mL/(g·h)	312.1	101.1	[94]
Anion vacancy	OMS-70	Benzene	2000 m·g ⁻³ , 48,000 mL/(g·h)	237	-	[95]
Anion vacancy	D-NiCo ₂ O ₄	Propane	0.5 vol.%, 60,000 mL/(g·h)	194	77.5	[87]
Anion vacancy	MnO _x -NA	Acetone	600 ppm, 18,600 mL/(g·h)	167	67.5	[96]
Anion vacancy	MnO _x -CeO ₂ -s	Ethyl Acetate	500 ppm, 60,000 mL/(g·h)	205	-	[74]
Cation Vacancy	Mn ₃ O ₄ -2V _{Mn}	Formaldehyde	80 ppm, 30,000 mL/(g·h)	65	32.8	[97]
Cation Vacancy	CoMnNiO _x	Propane	0.2%, 18,000 mL/(g·h)	200	44.1	[98]
Cation Vacancy	MnO ₂	Formaldehyde	150 ppm, 120,000 mL/(g·h)	96	34.3	[37]
Cation Vacancy	La _{1-x} Ce _x MnO ₃	Methane	1000 ppm, 90,000 mL/(g·h)	459	-	[99]
Core-shell interface	MnO ₂ @Co ₃ O ₄	Benzene	1000 ppm, 120,000 mL/(g·h)	247	-	[100]
Core-shell interface	CeO ₂ @Co ₃ O ₄	Toluene	2000 ppm, 20,000 mL/(g·h)	225	82	[101]
Core-shell interface	α@β-MnO ₂	Toluene	500 ppm, 30,000 h ⁻¹	192	62.4	[102]

Intergranular interface	CeO ₂	Toluene	1000 ppm, 60,000 mL/(g·h)	237	74	[103]
Intergranular interface	CoMn oxide	Toluene	1000 ppm, 60,000 mL/(g·h)	219	28.8	[35]
Intergranular interface	Cu _y Co ₃₋ Fe ₁ O _x	Toluene	800 ppm, 60,000 mL/(g·h)	238	36.6	[46]
Interbedded structure	Mn ₁₀ Cu ₁ -S	Toluene	1000 ppm, 30,000 mL/(g·h)	258	-	[104]
Interbedded structure	Mn ₂ O ₃ /MnO ₂	Toluene	1000 ppm, 60,000 mL/(g·h)	233	88.9	[105]
Interbedded structure	Mn ₂ O ₃ /MnO ₂	Propene	1000 ppm, 60,000 mL/(g·h)	181	56.5	[105]
Interbedded structure	δ-MnO ₂	Hydrothion	5000 ppm, 15,000 mL/(g·h)	~178	-	[106]
Heteroatomic doping	MnO _x /Co ₃ O ₄	Toluene	1000 ppm, 120,000 mL/(g·h)	242	163	[58]
Heteroatomic doping	ZrMn oxide	1,2-DCE	1000 ppm, 30,000 mL/(g·h)	287	31	[107]
Heteroatomic doping	CuO-CeO ₂	Toluene	500 ppm, 50,000 h ⁻¹	~246	-	[108]

1.3.1 Dislocation structure

The concept of "dislocation" was first proposed by Italian mathematician and physicist Vito Volterra in 1905. Dislocation can be regarded as the dividing line between the slipped part and the non-slipped part in the crystal, and its existence has a great impact on the physical properties of the material. It was reported that heteroatoms and oxygen vacancies usually segregate near dislocation cores of crystalline materials to form enrichment and depletion regions with ca. 1-2 nm radius according to the principle of elastic energy minimization. During this process, the elastic interaction promotes the attraction of the dopant ions by the dislocation strain field, and at the same time, the attracted metal ions could attract the oxygen vacancies through the electrostatic interaction, resulting in the segregation distribution phenomenon, which will inevitably regulate the electron transfer and oxygen diffusion behavior of the material [\[109\]](#). Therefore, it can be considered that the existence of dislocation structures in catalysts

can adjust the electronic structure and chemical properties of materials, thus optimizing the catalytic VOCs oxidation performance [87, 110, 111].

Liu et al. [57] synthesized a series of mesoporous hollow microsphere MnCo oxides using two-step hydrothermal method (Fig. 1.3a), in which the Co^{2+} (radius: 0.58 Å) in tetrahedral sites and Co^{3+} (radius: 0.61 Å) in octahedral sites are partially substituted by Mn^{2+} (0.66 Å) and Mn^{3+} (0.65 Å), thereby resulting in the partially disordered spinel structure with better activity (Fig. 1.3b). Meanwhile, slips and dislocations founded in MnCo catalyst can be considered as a carrier for low-coordinating cationic species (Fig. 1.3c), which tend to promote the mobility of oxygen species in the oxidation reaction and in turn increase the catalytic activity.

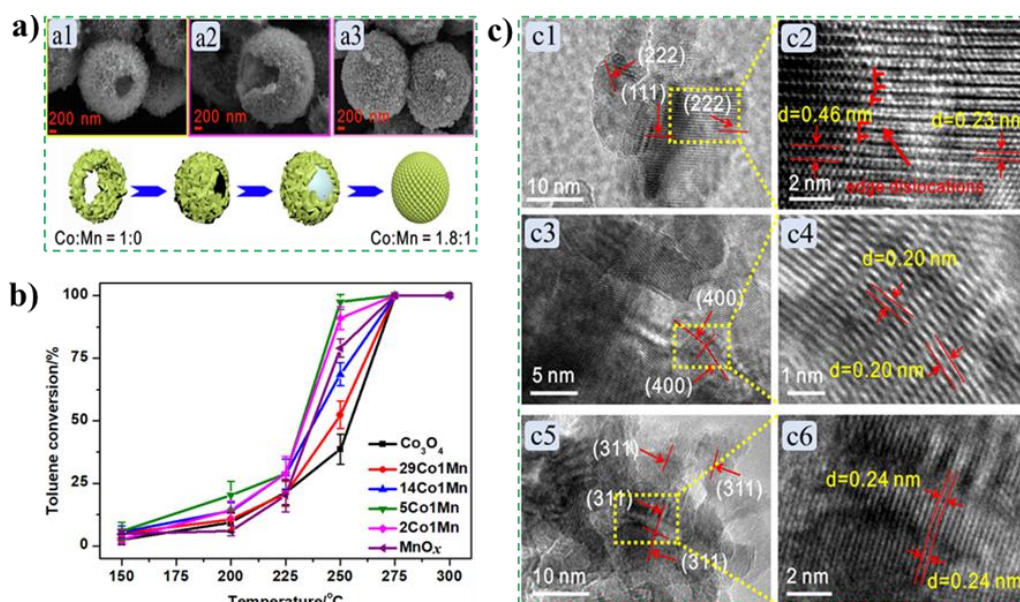


Fig. 1.3. SEM images (a) of samples of 14Co1Mn (a1), 5Co1Mn (a2), 2Co1Mn (a3) catalysts; Catalytic activities of the prepared samples for toluene combustion (b); HRTEM images (c) of 14Co1Mn (c1, c2), 5Co1Mn (c3, c4), 2Co1Mn (c5, c6) catalysts [57]. Copyright 2021 Elsevier.

Wang et al. [60] prepared a kind of Mn-Co mixed oxide with abundant defects using a facile agar-gel method. It is found that the special helical conformational structure and chemical reactions in the agar-gel aging process positively influenced the appearance of dislocation structures in the catalyst (Fig. 1.4a1 and 1.4a2). On the one hand, the metal ions adsorbed in the helical conformation region will undergo crystal twist deformation during the crystallization process to form dislocations and amorphous

structures. On the other hand, the short chain structure produced by the hydrolysis process of agar will also produce defect structures such as dislocations with the assistance of oxidation reaction and thus exposed more catalytic sites. In addition, the Mn₂Co mixed oxide synthesized by the agar gel method exhibited excellent catalytic performance, and the complete conversion of 1,000 ppm toluene was achieved at 238 °C (Fig. 1.4a3). Yang et al. [92] developed a series of homogenous Fe-Mn oxides by an interfacial redox-precipitation method. Characterization analysis demonstrated that the joint effect of iron doping and interfacial synthesis leads to a considerable amount of lattice intersection (yellow "T" marks) in high-resolution transmission electron microscope (HRTEM) image of Fe₁Mn₅ sample (Fig. 1.4b1), which means the existence of a large number of defective crystals, thereby improving the activation probability of molecular oxygen and lattice oxygen mobility. Among them, the catalyst Fe₁Mn₅ exhibited the best catalytic performance for toluene combustion, which achieved 90% conversion of 1,000 ppm toluene at 209 °C (Fig. 1.4b2). Wang et al. [93] prepared a series of samarium doped CeO₂ (x% Sm/CeO₂) catalysts by pyrolysis of metal organic framework precursor, in which the best catalyst 1% Sm/CeO₂ with nanorod morphology showed a T₉₀ of 211 °C. In addition, compared with pure CeO₂, 1% Sm/CeO₂ catalyst exhibited rich dislocations, which contributed to the production of reactive oxygen species in the latter's crystal structure and thereby optimizing the toluene catalytic performance.

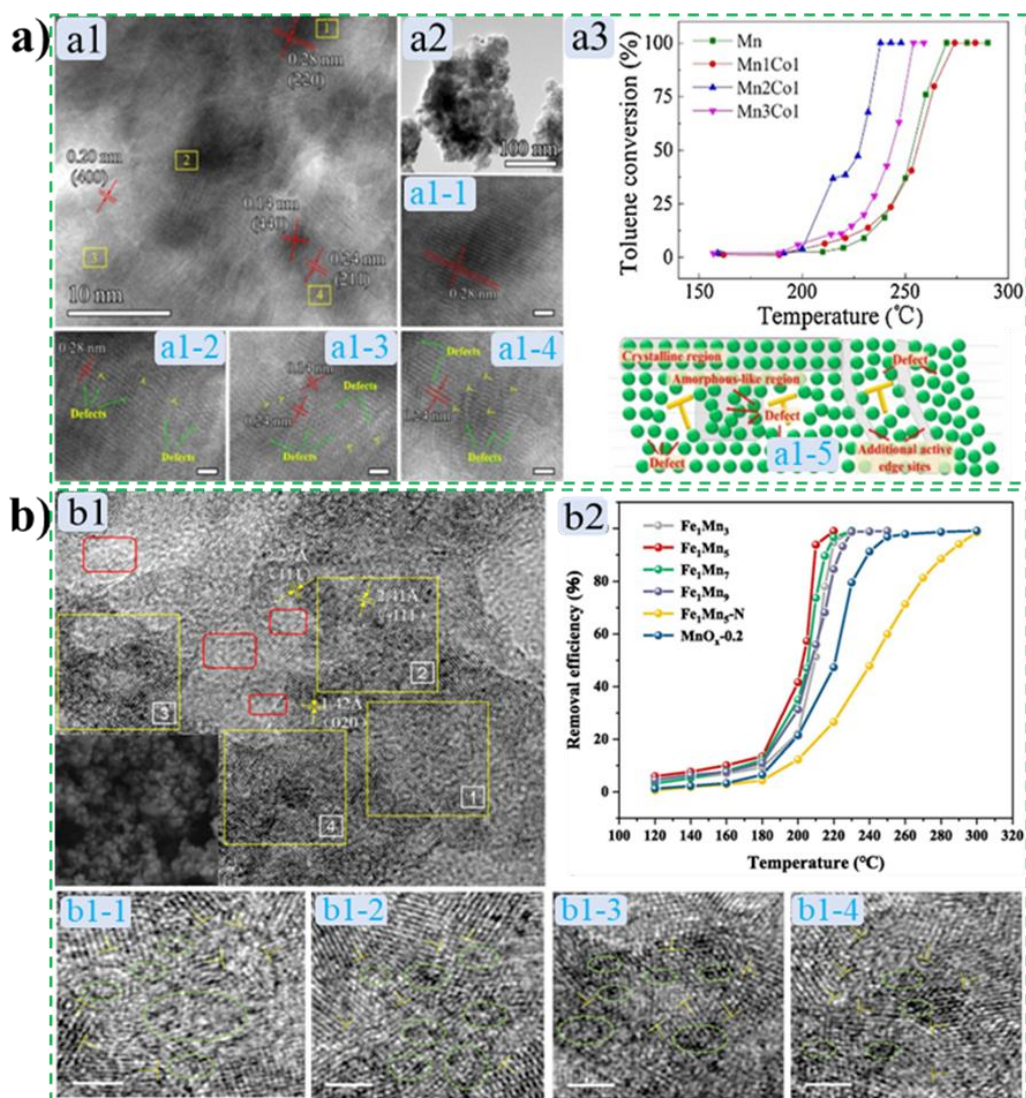


Fig. 1.4. HRTEM (a1, amplified a1-1 to a1-4 and dislocation diagram a1-5) and TEM (a2) images of Mn₂Co₁ catalyst; Catalytic activity of prepared MnCo samples for toluene combustion (a3) [60]. Copyright 2020 Elsevier. TEM image (b1) and amplified TEM images (b1-1 to b1-4) of Fe₁Mn₅ sample; Catalytic activity of prepared FeMn samples for toluene combustion (b2) [92]. Copyright 2022 Elsevier.

1.3.2 Vacancy heterogeneity

Vacancy defects in catalyst have been demonstrated to be important in the degradation of gaseous VOCs pollutants due to their special functions, e.g., promotion of electron transport, enhancement of oxygen mobility, activation of oxygen molecules and regulation of the surface chemical properties of catalysts [92, 112, 113]. Among them, vacancy defects can be divided into cation vacancies [37, 99, 114] and anion vacancies [94, 115] based on the initial ion species occupied in the vacancy sites, which

also are the two most common types of vacancy heterogeneity in catalysts.

(I) *Anion vacancy*

In the 1960s, Tompkins proposed the concept of oxygen vacancies firstly [116]. With the development of catalytic materials for VOCs combustion, the positive roles of the most common anion vacancies (i.e., oxygen vacancies) formed in catalysts have been confirmed by numerous studies [18, 95, 117]. In fact, the three most commonly used non-noble metal-based catalysts for the catalytic combustion of VOCs are Ce-based, Co-based and Mn-based ones. For the Ce-based catalysts, the oxygen orbital can hybridize with the complicated Ce 3d_{5/2} and Ce 3d_{3/2} orbitals to form oxygen vacancies as follows, Eq. (5): $4Ce^{4+} + O^{2-} \rightarrow 4Ce^{4+} + 2e^{-}/Vacancy + 0.5O_2 \rightarrow 2Ce^{4+} + 2Ce^{3+} + Vacancy + 0.5O_2$ [118]. Therefore, the presence of oxygen vacancy plays an important role in the adsorption, transformation and transportation of oxygen species. For the Mn-based catalysts, the loss of oxygen atoms can easily occur during the folded coordination of Mn 3d and O 2p orbitals, which will lead to the generation of oxygen vacancies to maintain electrical neutrality. During the oxidation of VOCs, the emergence (Eq. (6) and (7))/annihilation (Eq. (8)) cycle of oxygen vacancies in the Mn-based catalyst is as follows, Eq. (6): $Mn^{4+} + O^{2-} \rightarrow Mn^{3+}/Mn^{4+} + 1/2 O_2(g) + Vacancy$; Eq. (7): $VOC + Mn^{4+} + O_{ads}/O^{2-} \rightarrow H_2O + CO_2 + Mn^{3+}/Mn^{2+} + Vacancy$; Eq. (8): $Mn^{3+}/Mn^{2+} + Vacancy + O_2(g) \rightarrow Mn^{4+} + O_{2ads}^{2-} \rightarrow Mn^{4+} + O^{2-} + O_{ads}$ [119]. Herein, VOCs can be adsorbed by low-valent Mn ions and react with lattice oxygen or adsorbed oxygen species, accompanied by the electronic adjustment and the oxygen conversion processes. For the Co-based catalysts, the emergence-annihilation cycling of oxygen vacancies can be supported by the hybridization of Co³⁺ species and O 2f or O 3f orbitals, which could be expressed as follows, Eq. (9): $Co^{3+} \leftrightarrow Vacancy \leftrightarrow Co^{2+}$ [120]. One can see that the oxygen vacancies in the catalyst are of great significance in electronic regulation, oxygen/VOCs adsorption, oxygen conversion, oxygen transfer, and oxygen storage [46, 121, 122]. In addition, various synthesis strategies for the generation of oxygen vacancy have been developed to enhance the

intrinsic catalytic performance, e.g., thermal treatment, doping strategy, reduction strategy, and etching strategy [115, 123-125]. Zhang et al. [87] built a multi-defective D-NiCo₂O₄ spinel catalyst by a mechano-chemical strategy (Fig. 1.5a), in which the Na assisted milling/etching process can fracture the bulk (Fig. 1.5b) and accelerate the exposure of surface oxygen vacancies, which have been detected by electron paramagnetic resonance (EPR) spectra (Fig. 1.5c). Thereout, the oxygen mobility and active oxygen species of D-NiCo₂O₄ spinel were optimized so that a better catalytic propane performance than the normal NiCo₂O₄ spinel catalyst was achieved (Fig. 1.5d). Zheng et al. [96] synthesized a kind of ultrafine MnOx nanoparticles (MnOx-NA) by two-step sequential calcination of MOF in different atmospheres (Fig. 1.6a), in which the in-situ carbon-confinement-oxidation strategy led to the exposure of more active oxygen species and oxygen vacancies compared with the MnOx catalysts prepared with air atmosphere (MnOx-A) and the other method (MnOx-B) (Fig. 1.6b). As a result, MnOx-NA catalyst exhibited the best catalytic performance for acetone oxidation among the obtained three catalysts (Fig. 1.6c). Jiang et al. [74] synthesized a CeO₂-supported Mn catalyst by introducing Mn cations to the Ce-BTC support with an impregnation method, by which the enhanced Frankel oxygen vacancy concentration provided crucial active sites for catalytic ethyl acetate oxidation while the stable F-OVs recovery potential of the prepared catalysts guaranteed the high temperature stability of oxidation reaction.

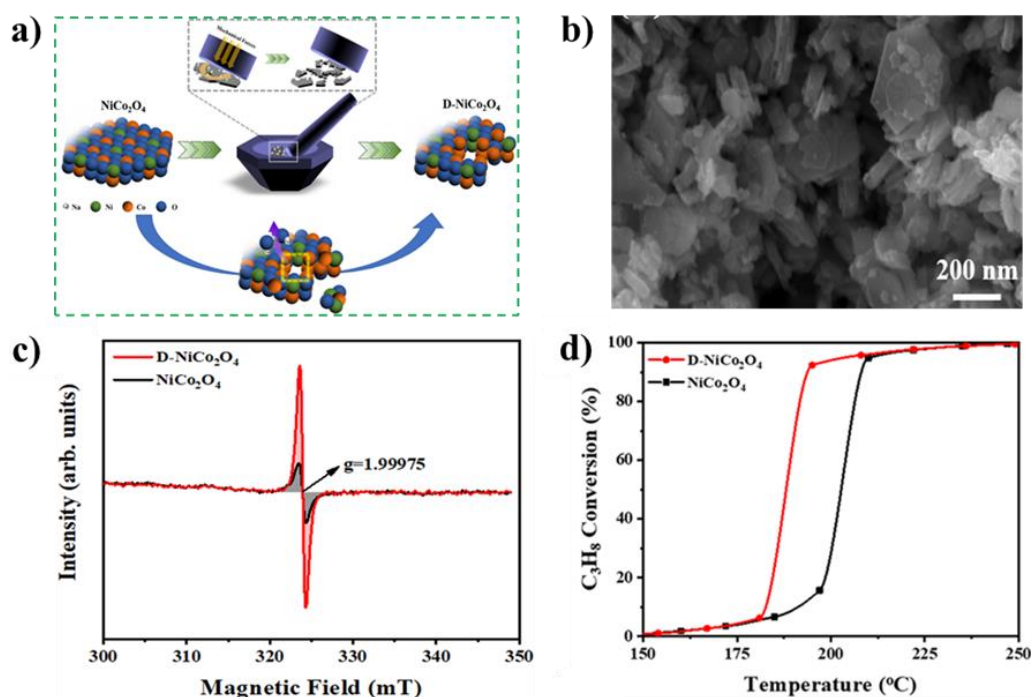


Fig. 1.5. Schematic process of synthesis procedure (a) and SEM image (b) for D-NiCo₂O₄; EPR spectra for D-NiCo₂O₄ and NiCo₂O₄ (c); Catalytic performances for propane combustion over NiCo₂O₄ and D-NiCo₂O₄ catalysts (d) [87]. Copyright 2022 Elsevier.

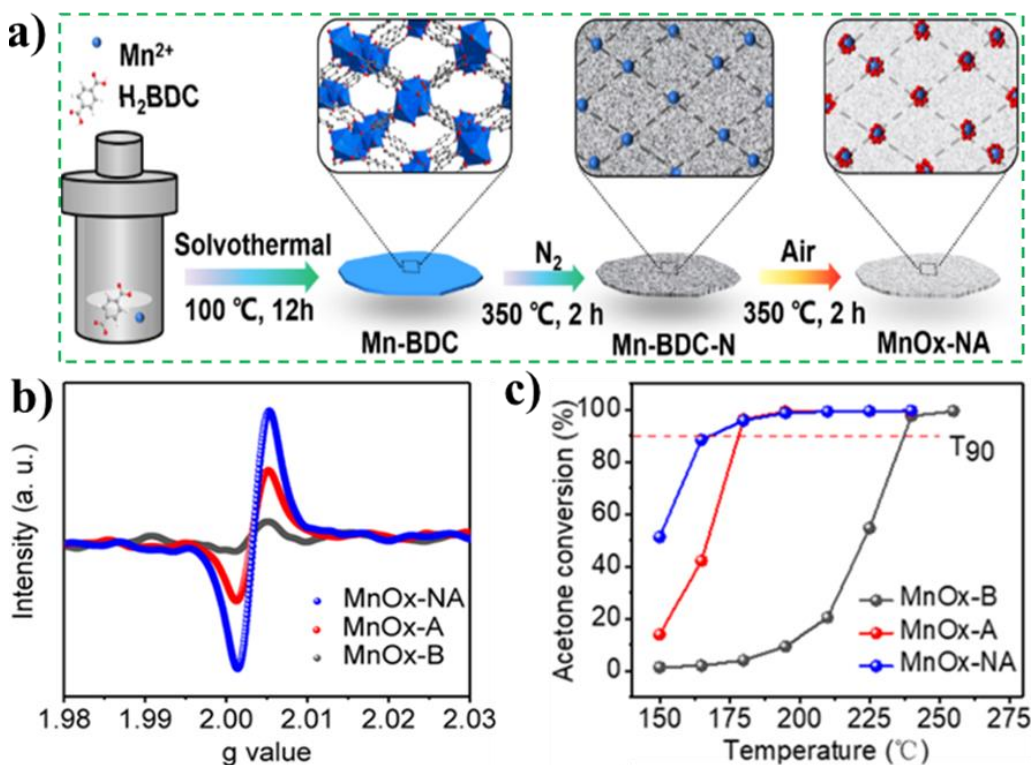


Fig. 1.6. Schematic illustration of the preparation process for MnOx-NA catalyst (a); EPR profiles (b) and evaluation of catalytic acetone oxidation (c) over MnOx-NA, MnOx-A, and MnOx-B.

MnO_x-A and MnO_x-B catalysts [96]. Copyright 2021 American Chemical Society.

(II) Cation Vacancy

Constructing cation-vacancy heterogeneity in catalysts is also an effective strategy to change the orbital distribution, optimize the electronic structure near the vacancy and enrich the active sites, which could improve the adsorption capacity of protons and promote the decomposition of VOCs in the next step [97, 98, 126, 127]. Wang et al. [37] designed a kind of potassium (K⁺) type birnessite MnO₂ by a facile redox reaction under water bath condition, and the different amounts of manganese vacancies were obtained via adjusting the reactant ratio of oxidizing (KMnO₄) and reducing ((NH₄)₂C₂O₄) agents. The results showed that the presences of manganese vacancy and K⁺ in birnessite catalyst induced the formation of unsaturated oxygen species and active oxygen species, respectively, thus resulting in the improved activity for HCHO oxidation. Ding et al. [99] synthesized a La-deficient La_{1-x}Ce_xMnO₃ mixed oxides through a selective acid etching method, in which the incorporation of a small amount of Ce for perovskite led to better reducibility, larger specific surface area with a stabilized structure, resulting in higher activity in the oxidation of methane.

1.3.3 Interface structure

As a typical heterostructure, the interface formed by the interfacial coupling of different or same crystal phases could easily produce interactions between two active components like strong metal-support interactions (SMSI). Besides, the emergence of interface structure is often accompanied by the generation of lattice strain and space charge layer, which can promote the formation of structural defects and electron transfer, and thus optimize catalytic activity. The construction strategies of the interface structure used for VOCs combustion generally include the creation of core-shell structure [39, 101], supported structure [128, 129] and intergranular interface [35, 103].

(I) Core-shell and supported structure interface

Tang et al. [100] synthesized a heterogeneous MnO₂@Co₃O₄ catalyst by decorating Co₃O₄ nanoparticles on one dimensional (1D) MnO₂ nanorod with a sequential reflux-hydrothermal method (Fig. 1.7a). It is found that the strong synergistic effect from the hetero-interface of MnO₂ and Co₃O₄ significantly promoted the low-temperature

reducibility and enriched the active adsorbed oxygen species, and thus resulted in a better activity for benzene combustion on the heterogeneous $\text{MnO}_2@\text{Co}_3\text{O}_4$ catalyst. Fang et al. [101] prepared a kind of $\text{CeO}_2@\text{Co}_3\text{O}_4$ catalyst with a core-shell structure by sacrificing zeolite imidazolate frameworks (ZIFs) based material (Fig. 1.7b). Compared with pure Co_3O_4 and CeO_2 , the synergistic interface effect between the core and the shell in the bimetallic catalyst improved the reducibility and oxygen transfer of the bimetallic material, as well as the activity of $\text{CeO}_2@\text{Co}_3\text{O}_4$ catalyst towards toluene oxidation. Huang et al. [102] constructed a hierarchical $\alpha@\beta\text{-MnO}_2$ catalyst with abundant bi-phase interfaces by adjusting the hydrothermal temperature, in which the larger specific area and strong synergy from the interface effect could be conducive to the adsorption of reactants and accelerate the electron transfer process, and therefore enhanced the catalytic activity for toluene oxidation (Fig. 1.7c).

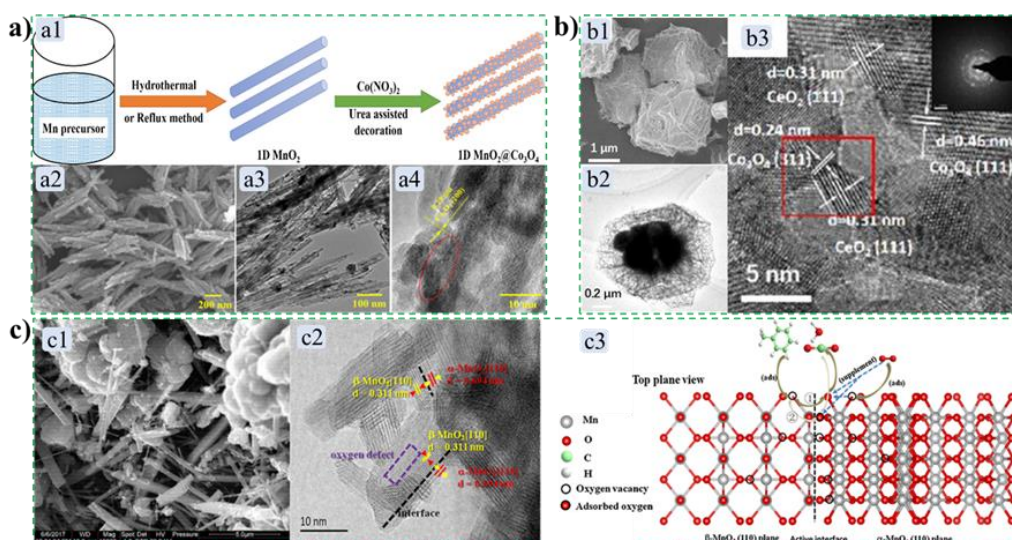


Fig. 1.7. Schematic process for the synthesis of heterogeneous $\text{MnO}_2@\text{Co}_3\text{O}_4$ catalyst (a1) and its SEM (a2), TEM (a3) and HRTEM (a4) images [100]. Copyright 2016 Elsevier. SEM (b1), TEM (b2) and HRTEM (b2) images of $\text{CeO}_2@\text{Co}_3\text{O}_4$ [101]. Copyright 2020 American Chemical Society. SEM (c1) and HRTEM (c2) images of $\alpha@\beta\text{-MnO}_2$, and the toluene oxidation scheme on the interface of $\alpha@\beta\text{-MnO}_2$ catalyst (c3) [102]. Copyright 2018 Elsevier.

(II) Intergranular interface

Su et al. [103] synthesized a homogeneous CeO_2 catalyst with abundant Ce-Ce mesocrystalline interfaces via a self-flaming route, which exhibited boosted catalytic

performance compared to the traditional CeO_2 for toluene combustion (Fig. 1.8a). Characterization results (Fig. 1.8(b-d)) showed that the highly ordered packing of small-sized grains contributed to the abundant Ce-Ce homogeneous interfaces, on which the interfacial oxygen vacancies were considered to promote the activation, regeneration, and migration behaviors of oxygen species, and then naturally optimized the redox property and oxygen storage capacity of the catalyst, contributing the effectively catalytic degradation of toluene to CO_2 . Li et al. [46] synthesized a series of composite metal oxide catalysts with rich phase interfaces by adjusting calcination temperature and used them for the catalytic combustion of toluene. As we can see from Fig. 1.9(a-d), with the increase of calcination temperature, the single-phase oxides of different metals in the catalyst could slowly combine to form a solid solution structure, accompanied by a large number of interface adjustments, which would inevitably change the physical and chemical properties of the catalyst. Additionally, the HRTEM (Fig. 1.9(e-g)) and fast Fourier transformation (FFT) (Fig. 1.9h) images of $\text{Cu}_1\text{Co}_2\text{Fe}_1\text{O}_x$ calcined at 500 °C also confirmed the abundant phase interfaces in the catalyst, which should greatly enrich the active oxygen species in the catalyst and lower the reducible temperature, thus promoting the catalytic toluene combustion performance.

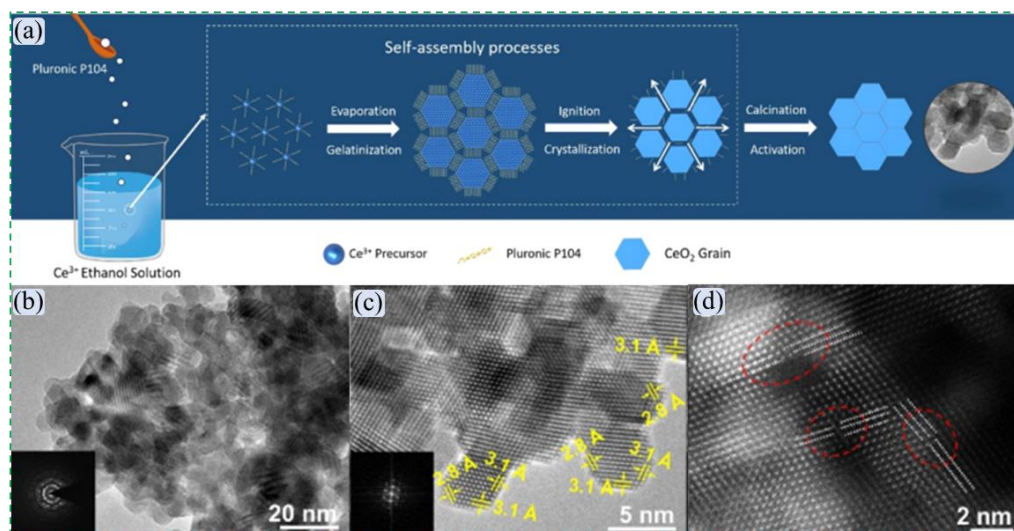


Fig. 1.8. Schematic illustration of the conjectural evolution mechanism for mesocrystalline CeO_2 (a), and its TEM (b) and HRTEM (c, d) images [103]. Copyright 2021 American Chemical Society.

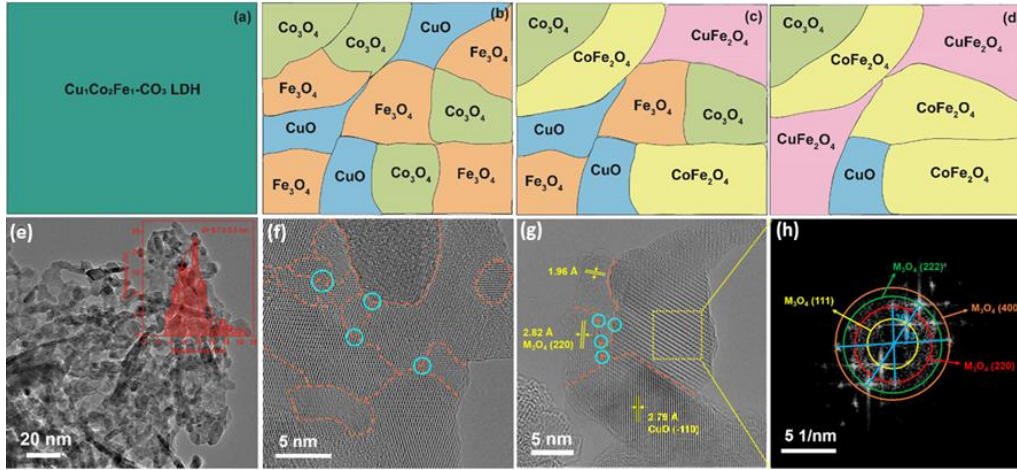


Fig. 1.9. Schematic illustration of the phase change of fresh $\text{Cu}_1\text{Co}_2\text{Fe}_1\text{-CO}_3$ LDH (a), $\text{Cu}_1\text{Co}_2\text{Fe}_1\text{O}_x$ catalysts obtained by calcining $\text{Cu}_1\text{Co}_2\text{Fe}_1\text{-CO}_3$ at 400 °C (b), 500 °C (c) and 600 °C (d); HRTEM images of $\text{Cu}_1\text{Co}_2\text{Fe}_1\text{O}_x$ calcined at 500 °C (e-g) and its FFT image (h) [46]. Copyright 2020 Elsevier.

1.3.4 Interbedded structure

Among various catalytic materials for VOCs combustion, some catalysts with special crystal structures (e.g., birnessite and cryptomelane) often exhibit unique catalytic performance since their idiographic spatial structures [104-106, 130]. Yu et al. [130] synthesized the birnessite-type $\text{K}_2\text{Mn}_4\text{O}_8$ and cryptomelane-type $\text{K}_{2-x}\text{Mn}_8\text{O}_{16}$ catalysts successfully through a facile redox reaction route with glucose and potassium permanganate in different experimental conditions and applied in catalytic soot combustion (Fig. 1.10a). It was found that the water and potassium ions in the layered structure of the $\text{K}_2\text{Mn}_4\text{O}_8$ catalyst could promote the sulfur and water resistances of the catalyst. Sulfur dioxide in the soot contacts with water molecules to form sulfuric acid, which could increase the accessibility of the catalyst to the soot. Meanwhile, the presence of interlayer potassium ions reduced the formation energy of oxygen vacancies and then improved the active oxygen content. Li et al. [104] synthesized a kind of layered $\text{CuO-}\delta\text{-MnO}_2$ hybrid composite by a technique with self-propagated flaming between KMnO_4 and copper (II) acetate monohydrate, and used it for the oxidation of toluene (Fig. 1.10b). The crystal structure and reducibility of layered $\text{CuO-}\delta\text{-MnO}_2$ catalyst could be optimized by the adjustment of molar ratio of $\text{KMnO}_4/\text{C}_4\text{H}_6\text{CuO}_4\cdot\text{H}_2\text{O}$, and thus improve the catalytic activity for toluene combustion.

Yang et al. [105] designed a nanosphere $\text{Mn}_2\text{O}_3@\text{MnO}_2$ catalyst by in situ surface modification of Mn_2O_3 with $\text{Cu}^{2+}\text{-H}^+/\text{KMnO}_4$ treatment, in which the K^+ in the mezzanine of the $[\text{MnO}_6]^\delta$ layers could be substituted by isolated $\text{Cu}^{\delta+}$ species (Fig. 1.10c). As such, the outermost $\text{Mn}^{(4-\varepsilon)+}$ would receive slight electrons from $\text{Cu}^{\delta+}$ species along with a decrease in the interlayer distance and crystallinity, which was thought to promote the generation of oxygen vacancies and the enhancement of oxygen mobility, and thus boosted the activity of $\text{Mn}_2\text{O}_3@\text{MnO}_2$ catalyst for toluene and propene combustions. Zheng et al. [106] (Fig. 1.10d) synthesized a kind of cross-linked (nanosheet and nanobelt) birnessite-type MnO_2 by a facile CTAB-intercalation exfoliation route. The obtained ultrathin structure could expose more surface atoms and oxygen vacancies. Especially, the exposed (100) plane of the crosslinked ultrathin nanosheets with more deficient oxygen species and strong reducibility exhibited superior H_2S catalytic performance comparing with its (001) plane as well as the (002) plane.

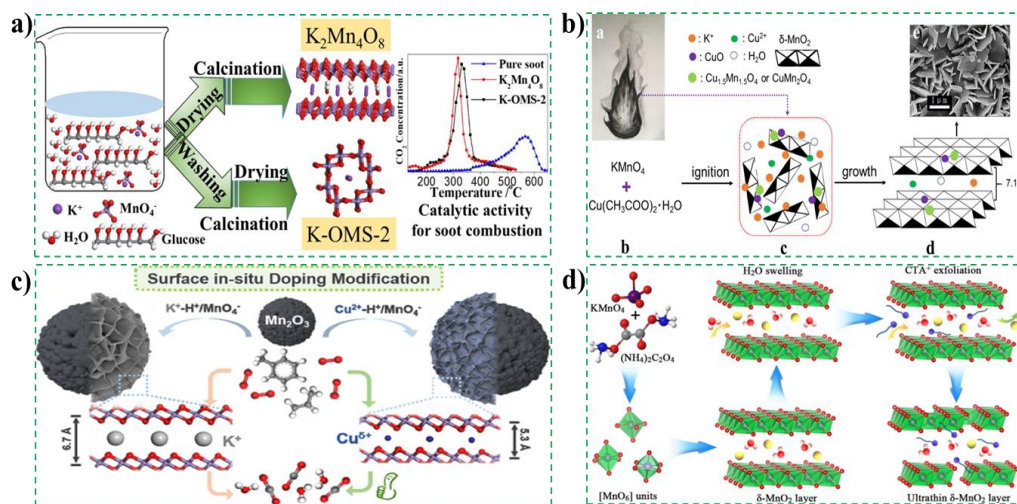


Fig. 1.10. (a) Synthetic schemes for the preparation of $\text{K}_2\text{Mn}_4\text{O}_8$ and K-OMS-2 catalysts, and their catalytic evaluation to soot [130]. Copyright 2020 Elsevier. (b) Synthetic scheme of $\text{CuO}-\delta\text{-MnO}_2$ hybrid composites by a self-propagated flaming strategy [104]. Copyright 2017 American Chemical Society. (c) Scheme of surface in situ modification for Mn_2O_3 with (right) or without (left) Cu insertion [105]. Copyright 2021 American Chemical Society. (d) Schematic of the fabricated process for ultrathin $\delta\text{-MnO}_2$ nanosheets [106]. Copyright 2021 Elsevier.

1.3.5 Heteroatomic doping

In recent years, heteroatom doping has been widely studied and confirmed to improve the physicochemical properties of catalysts, and thus enhanced their catalytic performances for VOCs oxidation [107, 108, 131]. Han et al. [58] fabricated a $\text{MnO}_x/\text{Co}_3\text{O}_4$ sample by introducing Mn species into the surface of spinel Co_3O_4 derived from ZIF-67 (Fig. 1.11a). The results showed that the obtained $\text{MnO}_x/\text{Co}_3\text{O}_4$ catalyst exposed more local lattice distortions rather than bulk defect and more Co^{3+} species on the catalyst surface due to the occupation behavior of octahedral Co sites by Mn species as well as the electron transfer from Co to Mn species, which significantly enhanced the low-temperature reducibility and oxygen mobility of the catalysts, thereby leading to a substantial boost in catalytic performance. Chen et al. [107] prepared an amorphous ZrMn mixed oxide catalyst using a novel reflux assisted redox method and used for catalytic oxidation of 1, 2-dichloroethane (1,2-DCE) (Fig. 1.11b). Compared with the pristine MnO_x and ZrO_2 , the uniform dispersion of Zr in Mn species induced more surface oxygen species, lattice distortion, acid amount, and excellent reducibility in the catalyst, and thus exhibited a better catalytic activity and less chlorine-containing by-products in the oxidation of 1,2-DCE. Zeng et al. [108] developed a highly active $\text{Cu}_x\text{-Ce}_{1-x}\text{-DR}$ oxide for the catalytic combustion of toluene through a novel double redox method of hydrothermal treatment followed by a calcination process (Fig. 1.11c). Due to a higher Cu^{2+} ion concentration incorporated in CeO_2 lattice, the strong Cu-Ce interaction was excited, which facilitated the electron transfer between the CuO and CeO_2 . As a result, the formed abundant oxygen vacancies and surface-adsorbed oxygen species enhanced the redox property and oxygen mobility of the catalyst.

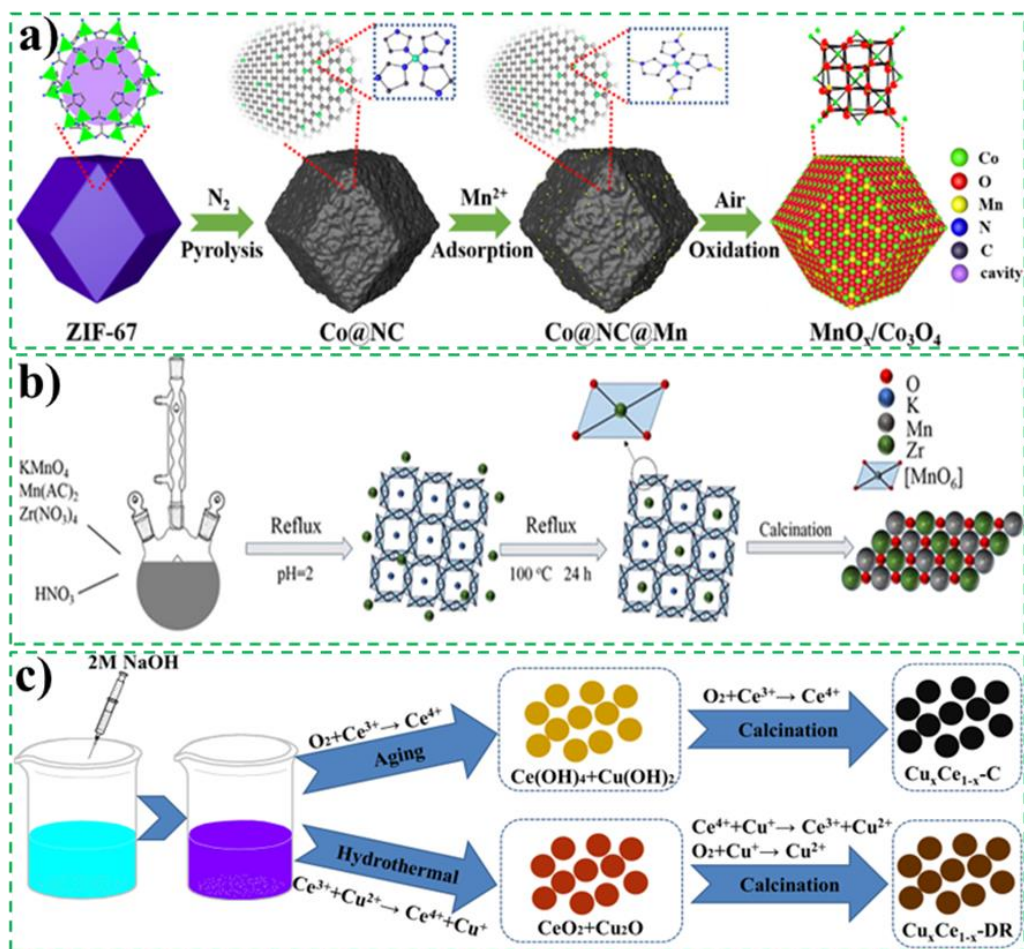


Fig. 1.11. Schematic of the synthesis process of $\text{MnO}_x/\text{Co}_3\text{O}_4$ sample (a) [58]. Copyright 2021 Elsevier. Proposed formation process of amorphous ZrMn mixed oxide (b) [107]. Copyright 2021 Elsevier. Schematic illustration of the synthesis route for $\text{Cu}_{0.4}\text{Ce}_{0.6}\text{-C}$ and $\text{Cu}_{0.4}\text{Ce}_{0.6}\text{-DR}$ samples [108]. Copyright 2020 Elsevier.

1.4 Function and superiority of heterogeneous structure in VOCs combustion

According to the above analysis, the construction of suitable heterostructures in the catalyst has a positive impact on the catalytic VOCs combustion performance, attributing to the optimization of the surface/overall physicochemical properties and/or the provision of the specific action sites by the heterostructure.

1.4.1 Reducibility and oxygen mobility enhancement

It is well known that the reducibility and oxygen mobility of catalysts used for catalytic VOCs combustion are the key factors determining the catalytic performance, which can often be optimized by constructing microscopic heterogeneous structures in the catalysts [132, 133]. For examples, Zhang et al. [134] synthesized a series of Mn

doped Co_3O_4 spinel catalysts ($\text{Mn}_a\text{Co}_{1-a}\text{O}_x$) with the microscopic heterogeneous structure by a solvothermal method and successfully applied for the catalytic combustion of toluene. The H_2 temperature programmed reduction analysis (H_2 -TPR) results (Fig. 1.12a1) showed that, with the increase of manganese content doped, the low-temperature reduction peak of the $\text{Mn}_a\text{Co}_{1-a}\text{O}_x$ catalysts gradually shifted to the low-temperature direction. In addition, the $\text{Mn}_{0.4}\text{Co}_{0.6}\text{O}_x$ catalyst exhibited the largest low-temperature ($< 400\text{ }^\circ\text{C}$) H_2 consumption among various prepared $\text{Mn}_a\text{Co}_{1-a}\text{O}_x$ catalysts. These all indicated that the reducibility of the heterogeneously doped catalyst was improved greatly. For the oxygen mobility, Fig. 1.12a2 reveals that the $\text{Mn}_a\text{Co}_{1-a}\text{O}_x$ catalysts exhibited a decreased desorption temperature of oxygen species and an increased desorption amount with the increase in doping amount of manganese, which indicated that manganese doping realized the improvement of oxygen mobility. The optimization of the comprehensive oxidation ability of the $\text{Mn}_a\text{Co}_{1-a}\text{O}_x$ catalyst led to a significant improvement in its catalytic performance for the toluene combustion, and the $\text{Mn}_{0.4}\text{Co}_{0.6}\text{O}_x$ showed the best catalyst performance (Fig. 1.12a3). Wang et al. [60] utilized agar hydrolysis and oxidation effects to assist in the synthesis of a series of manganese-cobalt composite metal oxides and used them for the catalytic combustion of toluene. The H_2 -TPR results in Fig. 1.12b1 show that MnCo mixed oxides had lower reduction temperatures and larger reduction peak areas, especially for the Mn_2Co_1 catalysts, which indicated that the hydrolysis and oxidation actions between agar and metal ions successfully optimized the reducibility MnCo of catalysts. In addition, as shown in Fig. 1.12b2, the MnCo mixed oxides also exhibited lower oxygen desorption temperatures and larger oxygen desorption amounts, which indicated the improved oxygen mobility. In fact, the excellent reducibility and oxygen mobility of MnCo catalysts are closely related to the abundant phase interfaces and dislocation defects in the catalysts with low crystallinity caused by the special agar structure, and thus contributed the excellent catalytic toluene combustion performance (Fig. 1.12b3). Zheng et al. [96] synthesized an ultrafine manganese oxide nanoparticle ($\text{MnO}_x\text{-NA}$) with abundant oxygen vacancies and crystallite interfaces by an in-situ carbon-confinement-oxidation method, which exhibited better low-temperature reducibility

(Fig. 1.12c1) and more surface oxygen desorption capacity (Fig. 1.12c2) than the bulk manganese oxide (MnOx-B) and manganese oxide (MnOx-A) obtained by direct calcination of MOF, and thus exhibited lower activation energy in the catalytic acetone combustion (Fig. 1.12c3).

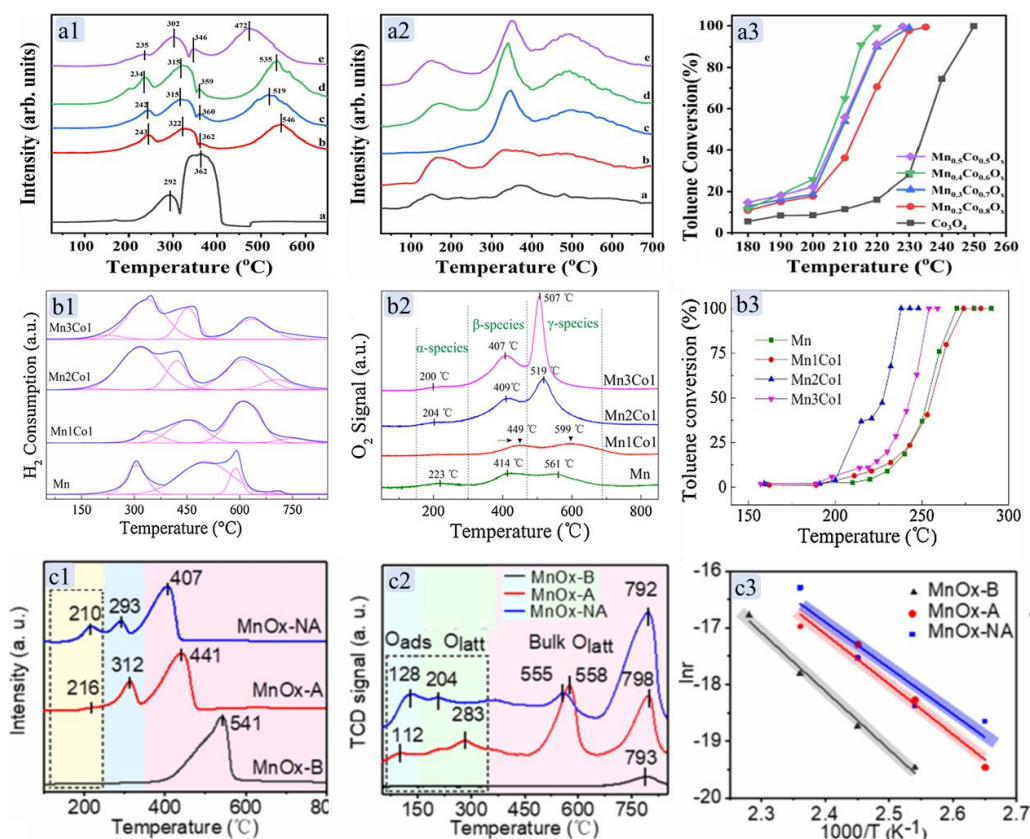


Fig. 1.12. H₂-TPR profiles (a1), O₂-TPD profiles (a2) and the toluene conversion vs reaction temperature (a3) over Co₃O₄ (black line), Mn_{0.2}Co_{0.8}O_x (red line), Mn_{0.3}Co_{0.7}O_x (blue line), Mn_{0.4}Co_{0.6}O_x (green line), Mn_{0.5}Co_{0.5}O_x (purple line) [134]. Copyright 2022 Elsevier. H₂-TPR profiles (b1), O₂-TPD profiles (b2) and the toluene conversion vs reaction temperature (b3) [60]. Copyright 2020 Elsevier. H₂-TPR profiles (c1), O₂-TPD profiles (c2) and the acetone conversion vs reaction temperature (c3) [96]. Copyright 2021 American Chemical Society.

1.4.2 Adsorption and activation sites

As mentioned above in the catalytic VOCs oxidation mechanisms, no matter which mechanism is used to carry out the oxidation reaction, sufficient surface adsorption and activation sites are required for the first adsorption of VOCs or/and O₂ molecules. Generally, the microscopic heterostructure represented by oxygen vacancies in catalysts

is always accompanied by the existence of an unbalanced charge environment or unsaturated low-valence metal species, which usually promotes the adsorption and activation of reactive species [97, 105, 135].

Among the two manganese dioxides synthesized by Wang et al. [14], i.e., MnO_2 with isolated K^+ (I- MnO_2) and localized K^+ (L- MnO_2), the K^+ ions in different microenvironments affected the electronic structure of the catalyst surface and at the same time realized the adjustment of the adsorption and activation capabilities for the reactant molecules. The calculation results showed that O_2 and H_2O molecules exhibit smaller adsorption energies on I- MnO_2 catalyst, and are thus more easily adsorbed (Fig. 1.13a1). For this reason, the active oxygen species and surface hydroxyl would be generated from the reaction between protons and chemisorbed oxygen, and the decomposition of water molecules on the saturation site. As for L- MnO_2 , the localized potassium atoms on Mn vacancy site could maximize the interaction between K^+ and MnO_2 support and thus showed lower electron density, resulting in a weakened ability to conduct electrons from potassium ions. Because of such properties, the adsorption capacity of oxygen and the desorption capacity of water as one of the products are improved, thereby reducing the apparent activation energy for the catalytic oxidation of formaldehyde (Fig. 1.13a2). As shown in the contour plot of wavelet transform (Fig. 1.13b1, 1.13b2), compared with the Ce L_3 -edge extended X-ray absorption fine structure (EXAFS) spectra of conventional CeO_2 -PC, the interface-rich CeO_2 -MC synthesized by Su et al. [103] via a self-combustion method exhibited weaker vibrational strengths of Ce-O and Ce-Ce bonds, which should be attributed to the suppression of photoelectron multiple scattering by homogeneous interface-induced lattice disorder. As we can see, time-resolved in situ diffuse reflectance infrared spectroscopy (DRIFTS) profiles of toluene in the pre-adsorption stage on different catalysts (Fig. 1.13b) show that the spectrum on CeO_2 -MC (Fig. 1.13b3, 1.13b4) has more characteristic product absorption peaks, which indicates that the abundant interface in CeO_2 -MC catalyst could more likely adsorb and activate the surface oxygen, and then participate in the initial toluene oxidation.

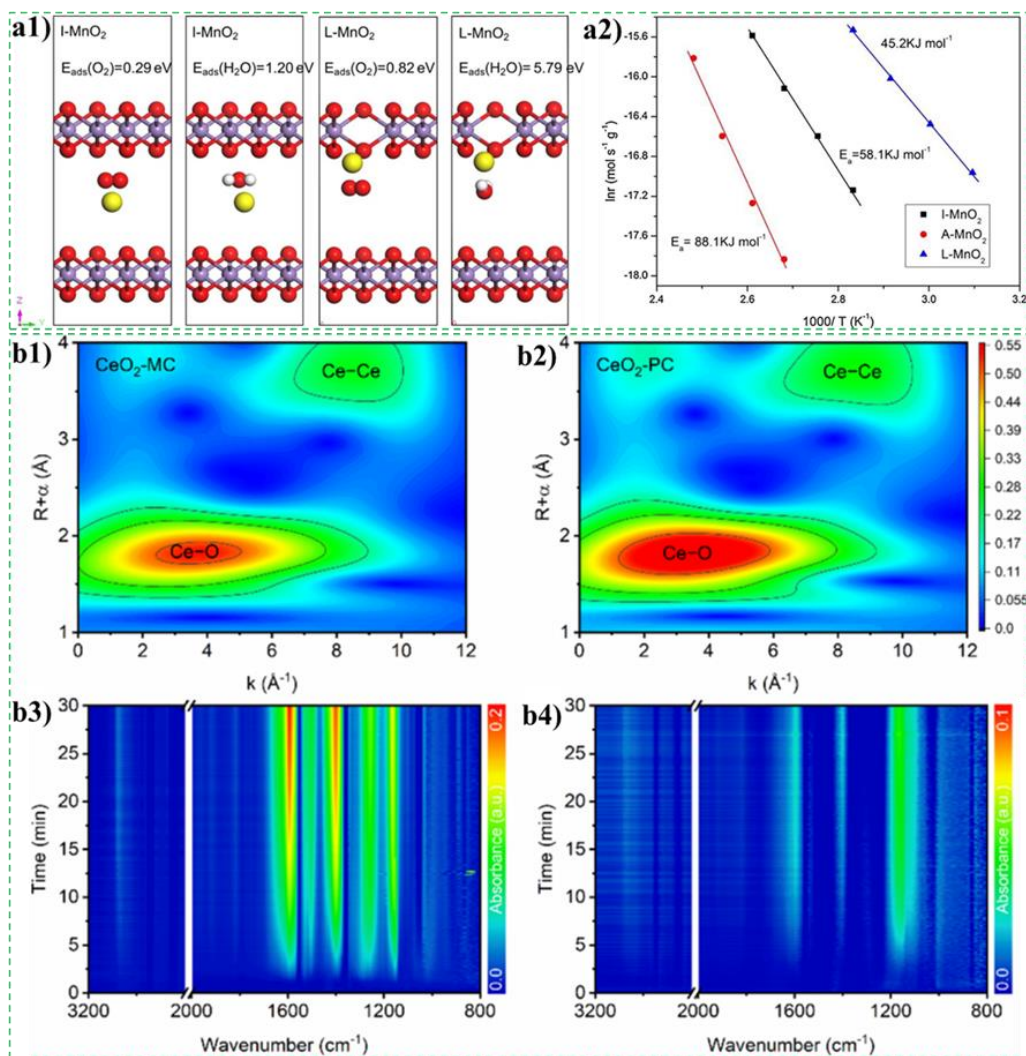


Fig. 1.13. Diagram of the microstructure for I-MnO₂ and L-MnO₂ catalysts, and the adsorption energies of water and oxygen molecules on them (a1); Arrhenius plots of MnO₂ samples (a2) [14]. Copyright 2017 Elsevier. Wavelet transform data analysis of Ce L₃-edge EXAFS spectra for CeO₂-MC (b1) and CeO₂-PC (b2); Time-resolved in situ DRIFTS profiles of toluene in the pre-adsorption stage on CeO₂-MC (b3) and CeO₂-PC (b4) catalysts [103]. Copyright 2021 American Chemical Society.

He et al. [97] fabricated a Mn defect-rich Mn₃O₄ catalyst by pyrolyzing Ce-doped MnCO₃ under N₂ atmosphere, and the content of Mn defects in Mn₃O₄ was optimized by changing the Ce content to improve the catalytic performance of formaldehyde oxidation. Furthermore, the formed Mn defects further promoted the generation of oxygen vacancies and activation of neighboring O atoms. In addition, as shown in Fig. 1.14a, the adsorption energies of oxygen molecules on the Ce1-Mn₃O₄ (-5.35 and -6.33

eV) and Ce₂-Mn₃O₄ (-5.88 and -6.54 eV) modes are much lower than those on the Mn₃O₄ (-1.78 and -2.05 eV), which means the easier O₂ absorbed and activated performance on oxygen vacancies of Ce doped Mn₃O₄. As can be seen from Fig. 1.14b, with the Ce substitution to Mn sites of defected Mn₃O₄, the adsorption energies of O₂ on oxygen vacancies decreased from -1.66 eV to -1.86 and -1.94 eV, which indicates an enhanced O₂ activation ability of oxygen vacancy from Ce doped Mn₃O₄-V_{Mn} catalyst. Thus, both Mn defect and Ce atom doping could effectively optimize the adsorption and activation performance of oxygen molecules by oxygen vacancies in the catalyst resulting from the local electronic structure and coordination environment, and thus significantly improved the catalytic activity of HCHO oxidation. Li et al. [46] used the co-precipitation method to synthesize a series of spinel structure catalysts with abundant and different phase interfaces by adjusting the metal species, atomic ratio and calcination temperature. As shown in Fig. 1.14c, the CuCoFe₂O₄ catalyst with more phase interfaces showed a higher adsorption energy of oxygen (-0.84 eV) than those of the two kinds of bimetallic spinel CoFe₂O₄ (-0.59 eV) and CuFe₂O₄ (-0.64 eV) catalysts. In addition, oxygen molecules have a longer bond length (1.29 Å) on trimetallic CuCoFe₂O₄ catalyst. Therefore, it can be concluded that catalysts with more phase interfaces are more likely to adsorb and activate oxygen molecules, and then participate in the oxidation process of VOCs. Zhang et al. [136] proved that oxygen vacancies can provide HOH active sites by adsorbing H₂O through a combined experimental and theoretical investigation, thereby promoting the transformation of adsorbed oxygen to surface lattice oxygen.

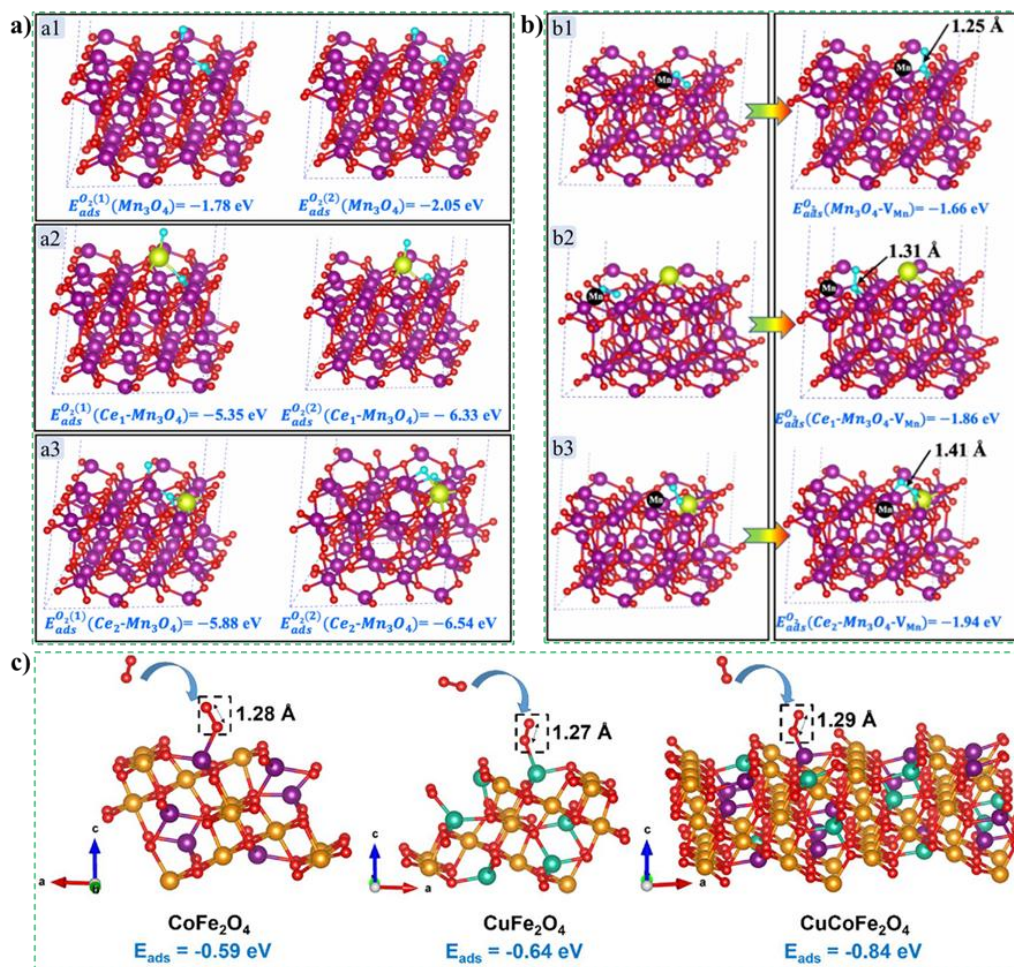


Fig. 1.14. Adsorption energies of oxygen molecule on oxygen vacancy from Mn_3O_4 (a1), $Ce-Mn_3O_4$ (a2 and a3), $Mn_3O_4-V_{Mn}$ (b1) and $Ce-Mn_3O_4-V_{Mn}$ (b2 and b3) catalysts. Ce: yellow; Mn: purple; O: red; adsorbed O_2 molecule: cyan [97]. Copyright 2021 American Chemical Society. The adsorption energies of oxygen over the 311 facet of the prepared $CoFe_2O_4$, $CuFe_2O_4$ and $CuCoFe_2O_4$ catalysts (c). (legend: red O, purple Co, green Cu and gold iron) [46]. Copyright 2020 Elsevier.

1.4.3 Transfer sites

In the above-mentioned MVK, E-R and L-H mechanisms, abundant and continuous lattice oxygen and adsorbed oxygen species in catalyst ensure the continuous and efficient oxidation of VOCs, which emphasizes the significance of oxygen or electron transfer centers in the regeneration of reactive oxygen species [74, 133, 137]. Dong et al. [138] investigated the specific role of different oxygen species in the $CoMn_2O_4$ catalyzed combustion of toluene through in situ designed temperature-programmed experiments. The experimental results showed that the surface lattice oxygen firstly

reacted with toluene molecules and was consumed. Afterwards, the abundant bulk lattice oxygen rapidly moved to the catalyst surface under the induction of oxygen vacancies to recover the consumed surface lattice oxygen. Simultaneously, the gas phase oxygen was also adsorbed and transformed into bulk lattice, thereby realizing the continuous supply of oxygen species (Fig. 1.15a1). As such, the intrinsic catalytic performance of the spinel CoMn_2O_4 catalyst was enhanced and thus exhibited a lower apparent activation energy in the oxidation of toluene (Fig. 1.15a2). He et al. [97] deeply investigated the effect of defects on the electronic structure of catalysts by calculating the density of states (DOSs) of Mn_3O_4 and defective Mn_3O_4 (Fig. 1.15b1 and 1.15b2). As shown in Fig. 1.15b1, pristine Mn_3O_4 shows the spin-polarized DOS at the Fermi level (E_f), and the O p/Mn d orbits mainly contributed the effect on the valence and conduction bands. The spin-down and spin-up states indicate the half-metallic feature of pristine Mn_3O_4 , leading to a half-metallic gap of 0.49 eV. When a defect concentration of about 2.27% was introduced into pristine Mn_3O_4 , the defect manganese is still spin-polarized at the E_f and exhibits a small half-metallic gap of 0.22 eV (Fig. 1.15b2). Normally, the narrower half-metallic gap always means the enhanced electrical conductivity and electron mobility. Therefore, the Mn defect can facilitate the transfer of electrons from the active center to the adsorbed oxygen species while narrow the energy bandgap and ultimately improve the oxidative performance for the formaldehyde combustion.

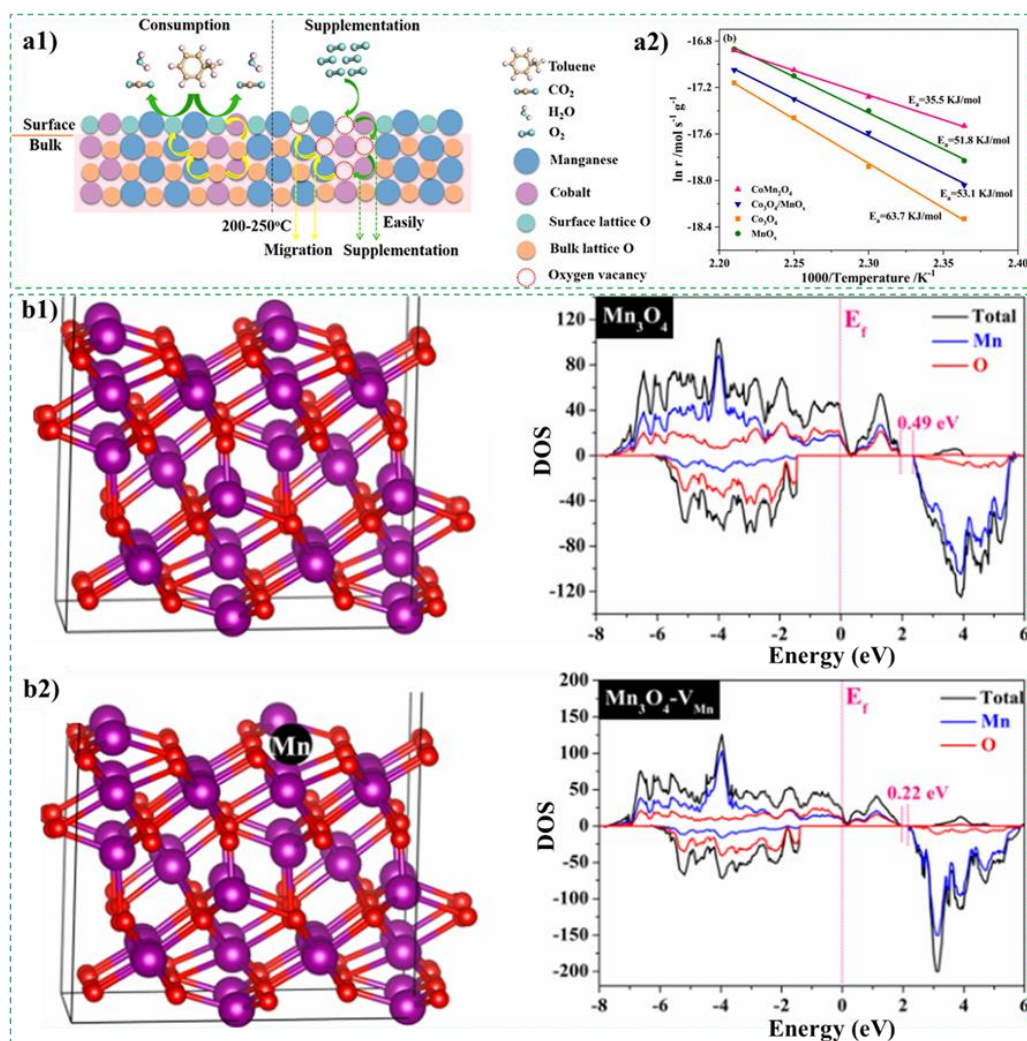


Fig. 1.15. Oxygen species replenishment mechanism of spinel catalysts in catalytic combustion of toluene (a1); Arrhenius plots of toluene oxidation over Co₃O₄, MnO_x, Co₃O₄/MnO_x and spinel CoMn₂O₄ catalysts (a2) [138]. Copyright 2019 American Chemical Society. Slab and density of states for Mn₃O₄ (b1) and Mn₃O₄-V_{Mn} (b2) catalysts [97]. Copyright 2021 American Chemical Society.

1.4.4 Acidity sites

In recent years, the catalytic removal of halogenated VOCs has gradually attracted widespread attention. It was found that the acidity and acid site of the catalyst are important for the decomposition of halide species in halogenated VOCs. On the one hand, some heteroatom doping can provide a moderate amount of acidity to the catalyst; on the other hand, the oxygen vacancies on the catalyst surface are also considered as Lewis acidic sites [125, 128, 139, 140]. Among the pristine MnO_x, ZrO_x and Zr-doped MnO₂ heterostructure catalysts synthesized through the reflux-assisted redox method

or typical co-precipitation method from Chen group [107], R-ZrMn catalyst from the reflux route exhibited the most total acidity amount and acid sites (Fig. 1.16a), which are benefited from the abundant homogeneous Mn-O-Zr bonds in the catalyst. Moreover, in addition to the Lewis acid sites shown in the Fig. 1.16b, characteristic spectra of Brønsted acid sites (Fig. 1.16b) and redox sites (Fig. 1.16c) appeared on the R-ZrMn catalyst, which resulted in fewer chlorinated intermediates (Fig. 1.16d) and excellent overall catalytic activity in the catalytic 1,2-dichloroethane combustion (Fig. 1.16e). Ding et al. [125] investigated the role of oxygen vacancies for the adsorption characteristics and dissociation processes of methylene chloride oxidation on defective La-Mn perovskite catalyst over density functional theoretical (DFT) calculations. In the dechlorination of methylene chloride, the unoccupied orbitals in the oxygen vacancy (Lewis acid) can combine with the binding orbitals of the Cl atoms, causing the chlorine abstraction and reacting with the proton to generate HCl with a lower activation energy (144.31 kJ/mol). The consumed protons can be also replenished by surface hydroxyl groups originating from the dissociation of water molecules, thus realize the continuous dechlorination of methylene chloride.

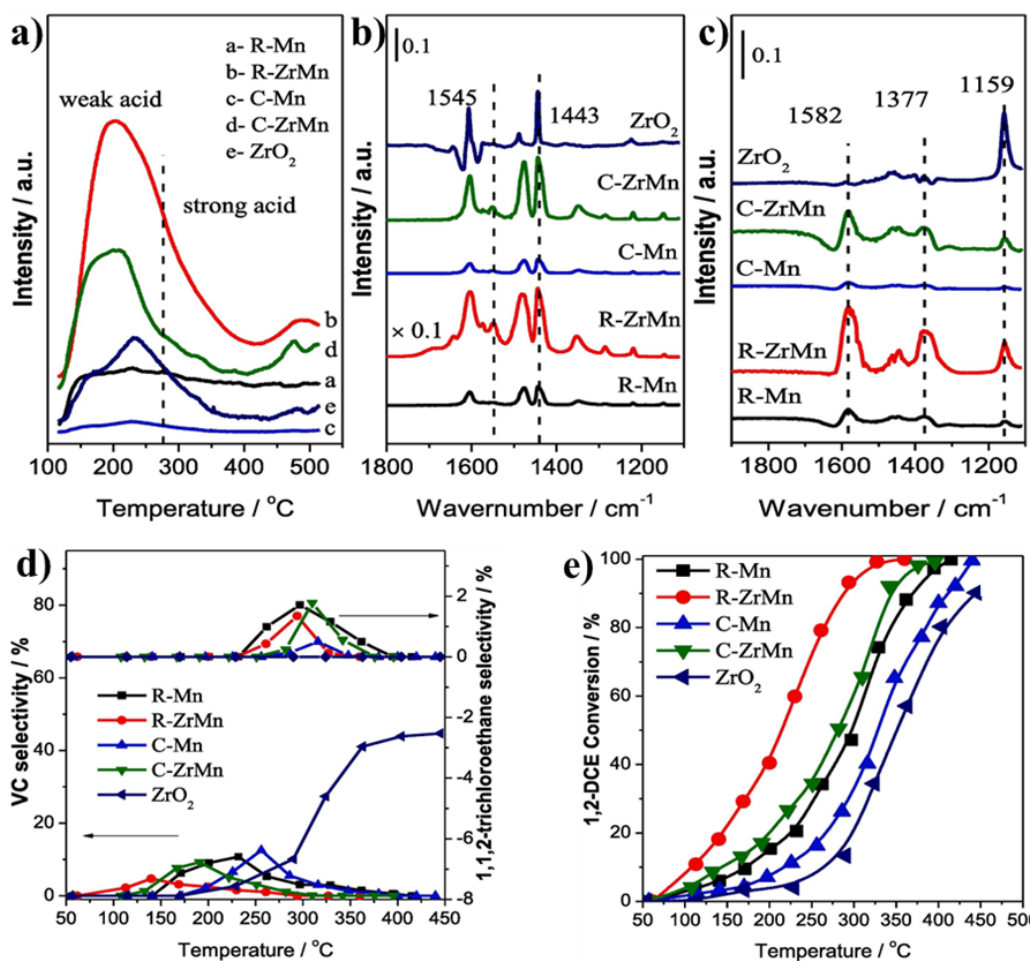


Fig. 1.16. Profiles of NH₃-TPD (a), spectra obtained from (b) pyridine adsorbed FTIR and (c) CH₃OH-FTIR experiments over the prepared catalysts; (d) by-products distribution during 1,2-DCE combustion and (e) 1,2-DCE conversion vs reaction temperature [107]. Copyright 2021 Elsevier.

1.4.5 Other special functions

In addition to the several main functions described above, the construction of heterostructures in catalysts usually exhibits some special functions. For example, Yu et al. [130] stated that the interlayer water of his synthesized birnessite-type K₂Mn₄O₈ catalyst can also play an anti-sulfur effect in the catalytic combustion of soot, in which the water molecules can react with sulfur dioxide to form sulfuric acid species and react with the catalyst owing to the close contact.

1.5 Objective of this study

Catalytic oxidation method for VOCs combustion has attracted wide attention owing to its high efficiency, low cost, non-secondary pollution and easy operation. The high

price and unsatisfactory stability properties of supported noble metal catalysts have long been motivating the search and development of non-noble metal oxides. For the non-noble metal catalysts, Mn-based ones have multiple valences and excellent redox capacity. As reviewed above, the construction of micro-heterostructures can optimize various physical and chemical properties of catalysts, such as improving low-temperature reducibility, optimizing oxygen mobility, providing adsorption and reaction sites, thereby playing an important role in improving the performance of catalytic oxidation of VOCs. Therefore, in order to solve the singleness of traditional catalyst synthesis routes and the mediocrity of catalytic performance, this work developed three novel catalyst synthesis strategies based on the concept of green, efficient and innovative, and successfully synthesized three highly efficient catalysts for catalytic VOCs combustion with microscopic heterogeneous structures. Through conventional characterizations, in situ technology, and theoretical calculations, the synergistic complementarity of the heterostructure in the catalyst was explored, and the catalytic oxidation mechanism of toluene was speculated reasonably. In addition, the durability and water resistance of the catalyst were evaluated.

1.6 Scope of this dissertation

Chapter 1 reviews the construction strategies of micro-heterostructures in VOCs catalytic oxidation catalysts, and analyzes the effect and superiority of catalysts with micro-heterostructures in the catalytic combustion process of VOCs in combination with commonly used catalytic oxidation mechanisms.

Chapter 2 describes a novel green pectin-driven sol-gel with an auto-combustion route to synthesize a manganese oxide. The characterization results showed that the manganese oxide synthesized by the present method exhibited a unique hierarchical mesoporous structure with lower crystallinity and smaller grain size, leading to abundant active species and defect structures. Furthermore, this catalyst had excellent low-temperature reducible performance and better oxygen mobility, which was considered to be resulted from the specific interaction of chelation and calcination processes. It is precisely because this, manganese oxide synthesized by pectin-driven sol-gel method exhibited superior catalytic performance for low-temperature

combustion of toluene compared to those cases using manganese oxide catalysts synthesized by traditional citric acid and glycine-driven sol-gel routes. In addition, this manganese oxide catalyst exhibited satisfactory long-term stability and water tolerance during catalytic toluene combustion process.

Chapter 3 presents a nanosheet-state CoMnx mixed oxide with multifarious active regions synthesized by oxidation-etching assembly of MOF precursor. Characterizations by SEM, N₂ adsorption-desorption, XRF, XRD, Raman, H₂-TPR, O₂-TPD and XPS technologies revealed that CoMnx mixed oxide with low-crystallinity showed abundant dislocations, vacancies, phase interfaces and amorphous structures, resulting in excellent low-temperature reducibility, outstanding lattice oxygen mobility and abundant active species such as Mn³⁺, Co³⁺ and adsorbed oxygen species. With the aid of in situ DRIFTS technique and DFT calculations, the specific roles of the active regions in the process of toluene oxidation and the combustion mechanism of the toluene were analyzed.

Chapter 4 introduces a nanoparticles-stacking MnCox oxide with multifarious active phases synthesized by a starch-paste assisted method. The characterization results show that MnCox oxide exhibits more porous structure and active species such as trivalent manganese, trivalent cobalt and electrophilic oxygen species. The multifunctionality of starch paste in catalyst synthesis was discussed in detail. That is, the special metal dispersibility and valence adjustment functions of starch contributed to the production of multifarious active phases with amazing reducibility as well as oxygen mobility at lower temperature. DFT calculation results and in situ DRIFTS experiments were used to investigate the importance of vibrant lattice oxygen and the reproducible electrophilic oxygen species, as well as the synergy and complementarity of different active phases.

Chapter 5 summarizes the important innovative results in this research and prospects the challenges in future work.

References

- [1] C. He, J. Cheng, X. Zhang, M. Douthwaite, S. Patisson, Z. Hao, Recent Advances in the Catalytic Oxidation of Volatile Organic Compounds: A Review Based on Pollutant Sorts and Sources, *Chem. Rev.*, 119 (2019) 4471-4568.
- [2] Y. Zheng, K. Fu, Z. Yu, Y. Su, R. Han, Q. Liu, Oxygen vacancies in a catalyst for VOCs oxidation: synthesis, characterization, and catalytic effects, *J. Mater. Chem. A*, 10 (2022) 14171-14186.
- [3] M.S. Kamal, S.A. Razzak, M.M. Hossain, Catalytic oxidation of volatile organic compounds (VOCs)-A review, *Atmos. Environ.*, 140 (2016) 117-134.
- [4] A. Mirzaei, S.G. Leonardi, G. Neri, Detection of hazardous volatile organic compounds (VOCs) by metal oxide nanostructures-based gas sensors: A review, *Ceram. Int.*, 42 (2016) 15119-15141.
- [5] J.-J. Li, E.-Q. Yu, S.-C. Cai, X. Chen, J. Chen, H.-P. Jia, Y.-J. Xu, Noble metal free, CeO₂/LaMnO₃ hybrid achieving efficient photo-thermal catalytic decomposition of volatile organic compounds under IR light, *Appl. Catal. B: Environ.*, 240 (2019) 141-152.
- [6] Z. Zhang, Z. Jiang, W. Shangguan, Low-temperature catalysis for VOCs removal in technology and application: A state-of-the-art review, *Catal. Today*, 264 (2016) 270-278.
- [7] Y. Zhang, H. Zhang, Y. Yan, Metal-organic chemical vapor deposition of Cu(acac)₂ for the synthesis of Cu/ZSM-5 catalysts for the oxidation of toluene, *Micropor. Mesopor. Mat.*, 261 (2018) 244-251.
- [8] Y. Guo, M. Wen, G. Li, T. An, Recent advances in VOC elimination by catalytic oxidation technology onto various nanoparticles catalysts: a critical review, *Appl. Catal. B: Environ.*, 281 (2021) 119447.
- [9] C. Norsic, J.-M. Tatibouët, C. Batiot-Dupeyrat, E. Fourré, Non thermal plasma assisted catalysis of methanol oxidation on Mn, Ce and Cu oxides supported on γ -Al₂O₃, *Chem. Eng. J.*, 304 (2016) 563-572.
- [10] W. Pei, Y. Liu, J. Deng, K. Zhang, Z. Hou, X. Zhao, H. Dai, Partially embedding Pt nanoparticles in the skeleton of 3DOM Mn₂O₃: An effective strategy for enhancing catalytic stability in toluene combustion, *Appl. Catal. B: Environ.*, 256 (2019) 117814.

- [11] J. He, F. Zheng, Y. Zhou, X. Li, Y. Wang, J. Xiao, Y. Li, D. Chen, J. Lu, Catalytic oxidation of VOCs over 3D@2D Pd/CoMn₂O₄ nanosheets supported on hollow Al₂O₃ microspheres, *J. Colloid Interf. Sci.*, 613 (2022) 155-167.
- [12] L. Yu, R. Peng, L. Chen, M. Fu, J. Wu, D. Ye, Ag supported on CeO₂ with different morphologies for the catalytic oxidation of HCHO, *Chem. Eng. J.*, 334 (2018) 2480-2487.
- [13] Y. Jiang, S. Xie, H. Yang, J. Deng, Y. Liu, H. Dai, Mn₃O₄-Au/3DOM La_{0.6}Sr_{0.4}CoO₃: High-performance catalysts for toluene oxidation, *Catal. Today*, 281 (2017) 437-446.
- [14] J. Wang, J. Li, P. Zhang, G. Zhang, Understanding the “seesaw effect” of interlayered K⁺ with different structure in manganese oxides for the enhanced formaldehyde oxidation, *Appl. Catal. B: Environ.*, 224 (2018) 863-870.
- [15] S. Wu, H. Liu, Z. Huang, H. Xu, W. Shen, O-vacancy-rich porous MnO₂ nanosheets as highly efficient catalysts for propane catalytic oxidation, *Appl. Catal. B: Environ.*, 312 (2022) 121387.
- [16] H. Yi, Z. Yang, X. Tang, S. Zhao, F. Gao, J. Wang, Y. Huang, Y. Ma, C. Chu, Q. Li, J. Xu, Promotion of low temperature oxidation of toluene vapor derived from the combination of microwave radiation and nano-size Co₃O₄, *Chem. Eng. J.*, 333 (2018) 554-563.
- [17] W. Zhang, K. Lassen, C. Descorme, J.L. Valverde, A. Giroir-Fendler, Effect of the precipitation pH on the characteristics and performance of Co₃O₄ catalysts in the total oxidation of toluene and propane, *Appl. Catal. B: Environ.*, 282 (2021) 119566.
- [18] J.M. López, A.L. Gilbank, T. García, B. Solsona, S. Agouram, L. Torrente-Murciano, The prevalence of surface oxygen vacancies over the mobility of bulk oxygen in nanostructured ceria for the total toluene oxidation, *Appl. Catal. B: Environ.*, 174-175 (2015) 403-412.
- [19] B. Song, C. Li, X. Du, S. Li, Y. Zhang, Y. Lyu, Q. Zhou, Superior performance of Cu-Ce binary oxides for toluene catalytic oxidation: Cu-Ce synergistic effect and reaction pathways, *Fuel*, 306 (2021) 121654.
- [20] X. Zhang, H. Zhao, Z. Song, W. Liu, J. Zhao, Z.a. Ma, M. Zhao, Y. Xing, Insight

into the effect of oxygen species and Mn chemical valence over MnO_x on the catalytic oxidation of toluene, *Appl. Surf. Sci.*, 493 (2019) 9-17.

[21] X. Yang, X. Yu, M. Lin, X. Ma, M. Ge, Enhancement effect of acid treatment on Mn_2O_3 catalyst for toluene oxidation, *Catal. Today*, 327 (2019) 254-261.

[22] C. Zhang, C. Wang, H. Huang, K. Zeng, Z. Wang, H.P. Jia, X. Li, Insights into the size and structural effects of zeolitic supports on gaseous toluene oxidation over $\text{MnO}_x/\text{HZSM-5}$ catalysts, *Appl. Surf. Sci.*, 486 (2019) 108-120.

[23] M.R. Morales, M.P. Yeste, H. Vidal, J.M. Gatica, L.E. Cadus, Insights on the combustion mechanism of ethanol and n-hexane in honeycomb monolithic type catalysts: Influence of the amount and nature of Mn-Cu mixed oxide, *Fuel*, 208 (2017) 637-646.

[24] F. Hu, J. Chen, S. Zhao, K. Li, W. Si, H. Song, J. Li, Toluene catalytic combustion over copper modified $\text{Mn}_{0.5}\text{Ce}_{0.5}\text{O}_x$ solid solution sponge-like structures, *Appl. Catal. A: Gen.*, 540 (2017) 57-67.

[25] P. Yang, S. Yang, Z. Shi, Z. Meng, R. Zhou, Deep oxidation of chlorinated VOCs over CeO_2 -based transition metal mixed oxide catalysts, *Appl. Catal. B: Environ.*, 162 (2015) 227-235.

[26] Y. Wei, L. Ni, M. Li, J. Zhao, A template-free method for preparation of MnO_2 catalysts with high surface areas, *Catal. Today*, 297 (2017) 188-192.

[27] A. Giroir-Fendler, M. Alves-Fortunato, M. Richard, C. Wang, J.A. Díaz, S. Gil, C. Zhang, F. Can, N. Bion, Y. Guo, Synthesis of oxide supported LaMnO_3 perovskites to enhance yields in toluene combustion, *Appl. Catal. B: Environ.*, 180 (2016) 29-37.

[28] P. Yang, S. Fan, Z. Chen, G. Bao, S. Zuo, C. Qi, Synthesis of Nb_2O_5 based solid superacid materials for catalytic combustion of chlorinated VOCs, *Appl. Catal. B: Environ.*, 239 (2018) 114-124.

[29] J. González-Prior, R. López-Fonseca, J.I. Gutiérrez-Ortiz, B. de Rivas, Catalytic removal of chlorinated compounds over ordered mesoporous cobalt oxides synthesised by hard-templating, *Appl. Catal. B: Environ.*, 222 (2018) 9-17.

[30] Z. Han, Y. Liu, J. Deng, S. Xie, X. Zhao, J. Yang, K. Zhang, H. Dai, Preparation and high catalytic performance of $\text{Co}_3\text{O}_4\text{-MnO}_2$ for the combustion of o-xylene, *Catal.*

Today, 327 (2019) 246-253.

[31] C. He, B.-T. Xu, J.-W. Shi, N.-L. Qiao, Z.-P. Hao, J.-L. Zhao, Catalytic destruction of chlorobenzene over mesoporous ACeO_x ($A = \text{Co}, \text{Cu}, \text{Fe}, \text{Mn}, \text{or Zr}$) composites prepared by inorganic metal precursor spontaneous precipitation, *Fuel Process. Technol.*, 130 (2015) 179-187.

[32] H. Yi, X. Xie, L. Song, S. Zhao, C. Du, L. Miao, X. Tang, Promotion of rapid microwave-assisted synthesized porous manganese-cobalt catalyst on low-temperature toluene oxidation, *J. Environ. Chem. Eng.*, 10 (2022) 107086.

[33] P. Yang, J. Li, S. Zuo, Promoting oxidative activity and stability of CeO_2 addition on the MnO_x modified kaolin-based catalysts for catalytic combustion of benzene, *Chem. Eng. Sci.*, 162 (2017) 218-226.

[34] B. Chen, X. Yang, X. Zeng, Z. Huang, J. Xiao, J. Wang, G. Zhan, Multicomponent metal oxides derived from Mn-BTC anchoring with metal acetylacetonate complexes as excellent catalysts for VOCs and CO oxidation, *Chem. Eng. J.*, 397 (2020) 125424.

[35] J. Zhao, P. Wang, C. Liu, Q. Zhao, J. Wang, L. Shi, G. Xu, A. Abudula, G. Guan, Nanosheet-state cobalt-manganese oxide with multifarious active regions derived from oxidation-etching of metal organic framework precursor for catalytic combustion of toluene, *J. Colloid Interf. Sci.*, 629 (2022) 706-722.

[36] J. Chen, X. Chen, W. Xu, Z. Xu, J. Chen, H. Jia, J. Chen, Hydrolysis driving redox reaction to synthesize Mn-Fe binary oxides as highly active catalysts for the removal of toluene, *Chem. Eng. J.*, 330 (2017) 281-293.

[37] J. Wang, J. Li, C. Jiang, P. Zhou, P. Zhang, J. Yu, The effect of manganese vacancy in birnessite-type MnO_2 on room-temperature oxidation of formaldehyde in air, *Appl. Catal. B: Environ.*, 204 (2017) 147-155.

[38] J. Wang, G. Zhang, P. Zhang, Layered birnessite-type MnO_2 with surface pits for enhanced catalytic formaldehyde oxidation activity, *J. Mater. Chem.*, A 5 (2017) 5719-5725.

[39] W. Zhao, Y. Zhang, X. Wu, Y. Zhan, X. Wang, C.-T. Au, L. Jiang, Synthesis of Co-Mn oxides with double-shelled nanocages for low-temperature toluene combustion, *Catal. Sci. Technol.*, 8 (2018) 4494-4502.

- [40] T. Chang, Z. Wang, H. An, F. Li, W. Xue, Y. Wang, Morphology effects of CeO₂ for catalytic oxidation of formaldehyde, *J. Environ. Chem. Eng.*, 10 (2022) 108053.
- [41] G. Spezzati, A.D. Benavidez, A.T. DeLaRiva, Y. Su, J.P. Hofmann, S. Asahina, E.J. Olivier, J.H. Neethling, J.T. Miller, A.K. Datye, E.J.M. Hensen, CO oxidation by Pd supported on CeO₂(100) and CeO₂(111) facets, *Appl. Catal. B: Environ.*, 243 (2019) 36-46.
- [42] J. Zhang, Y. Li, L. Wang, C. Zhang, H. He, Catalytic Oxidation of Formaldehyde over Manganese Oxides with Different Crystal Structure, *Catal. Sci. Technol.*, 5 (2015) 2305-2313.
- [43] H. Zhao, H. Wang, Z. Qu, Synergistic effects in Mn-Co mixed oxide supported on cordierite honeycomb for catalytic deep oxidation of VOCs, *J. Environ. Sci.*, (China) 112 (2022) 231-243.
- [44] Y. Guan, Y. Zhou, S. Wang, R. Zou, J. Zhang, X. Fan, Y. Jiao, Structured cobalt-manganese oxides on SiC nano-whisker modified SiC foams for catalytic combustion of toluene, *Chem. Eng. Res. Des.*, 177 (2022) 659-669.
- [45] X. Jiang, W. Xu, S. Lai, X. Chen, Integral structured Co-Mn composite oxides grown on interconnected Ni foam for catalytic toluene oxidation, *RSC Adv.*, 9 (2019) 6533-6541.
- [46] Z. Li, Q. Yan, Q. Jiang, Y. Gao, T. Xue, R. Li, Y. Liu, Q. Wang, Oxygen vacancy mediated Cu_yCo_{3-y}Fe₁O_x mixed oxide as highly active and stable toluene oxidation catalyst by multiple phase interfaces formation and metal doping effect, *Appl. Catal. B: Environ.*, 269 (2020) 118827.
- [47] Q. Ren, S. Mo, J. Fan, Z. Feng, M. Zhang, P. Chen, J. Gao, M. Fu, L. Chen, J. Wu, D. Ye, Enhancing catalytic toluene oxidation over MnO₂@Co₃O₄ by constructing a coupled interface, *Chinese J. Catal.*, 41 (2020) 1873-1883.
- [48] C. Fan, X. Wu, M. Li, X. Wang, Y. Zhu, G. Fu, T. Ma, Y. Tang, Surface chemical reconstruction of hierarchical hollow inverse-spinel manganese cobalt oxide boosting oxygen evolution reaction, *Chem. Eng. J.*, 431 (2022) 133829.
- [49] H. Chen, J. Li, W. Cui, Z. Fei, Q. Tian, Q. Liu, X. Chen, M. Cui, Z. Zhang, J. Tang, X. Qiao, Precise fabrication of surface-reconstructed LaMnO₃ perovskite with

- enhanced catalytic performance in CH₄ oxidation, *Appl. Surf. Sci.*, 505 (2020) 144112.
- [50] X. Dai, X. Wang, Y. Long, S. Pattison, Y. Lu, D.J. Morgan, S.H. Taylor, J.H. Carter, G.J. Hutchings, Z. Wu, X. Weng, Efficient Elimination of Chlorinated Organics on a Phosphoric Acid Modified CeO₂ Catalyst: A Hydrolytic Destruction Route, *Environ. Sci. Technol.*, 53 (2019) 12697-12705.
- [51] Y. Xu, J. Dhainaut, G. Rochard, J.-P. Dacquin, A.-S. Mamede, J.-M. Giraudon, J.-F. Lamonier, H. Zhang, S. Royer, Hierarchical porous ϵ -MnO₂ from perovskite precursor: Application to the formaldehyde total oxidation, *Chem. Eng. J.*, 388 (2020) 124146.
- [52] S. Mo, Q. Zhang, Y. Sun, M. Zhang, J. Li, Q. Ren, M. Fu, J. Wu, L. Chen, D. Ye, Gaseous CO and toluene co-oxidation over monolithic core-shell Co₃O₄-based hetero-structured catalysts, *J. Mater. Chem. A*, 7 (2019) 16197-16210.
- [53] H. Wu, G. Pantaleo, G. Di Carlo, S. Guo, G. Marci, P. Concepción, A.M. Venezia, L.F. Liotta, Co₃O₄ particles grown over nanocrystalline CeO₂: influence of precipitation agents and calcination temperature on the catalytic activity for methane oxidation, *Catal. Sci. Technol.*, 5 (2015) 1888-1901.
- [54] W. Si, Y. Wang, S. Zhao, F. Hu, J. Li, A Facile Method for in Situ Preparation of the MnO₂/LaMnO₃ Catalyst for the Removal of Toluene, *Environ. Sci. Technol.*, 50 (2016) 4572-4578.
- [55] S. Wang, Q. Liu, Z. Zhao, C. Fan, X. Chen, G. Xu, M. Wu, J. Chen, J. Li, Enhanced Low-Temperature Activity of Toluene Oxidation over the Rod-like MnO₂/LaMnO₃ Perovskites with Alkaline Hydrothermal and Acid-Etching Treatment, *Ind. Eng. Chem. Res.*, 59 (2020) 6556-6564.
- [56] J. Yang, L. Li, X. Yang, S. Song, J. Li, F. Jing, W. Chu, Enhanced catalytic performances of in situ-assembled LaMnO₃/ δ -MnO₂ hetero-structures for toluene combustion, *Catal. Today*, 327 (2019) 19-27.
- [57] P. Liu, Y. Liao, J. Li, L. Chen, M. Fu, P. Wu, R. Zhu, X. Liang, T. Wu, D. Ye, Insight into the effect of manganese substitution on mesoporous hollow spinel cobalt oxides for catalytic oxidation of toluene, *J. Colloid Interf. Sci.*, 594 (2021) 713-726.
- [58] D. Han, X. Ma, X. Yang, M. Xiao, H. Sun, L. Ma, X. Yu, M. Ge, Metal organic

framework-templated fabrication of exposed surface defect-enriched Co_3O_4 catalysts for efficient toluene oxidation, *J. Colloid Interf. Sci.*, 603 (2021) 695-705.

[59] L. Zhou, B. Zhang, Z. Li, X. Zhang, R. Liu, J. Yun, Amorphous-microcrystal combined manganese oxides for efficiently catalytic combustion of VOCs, *Mol. Catal.*, 489 (2020) 110920.

[60] P. Wang, J. Wang, X. An, J. Shi, W. Shangguan, X. Hao, G. Xu, B. Tang, A. Abudula, G. Guan, Generation of abundant defects in Mn-Co mixed oxides by a facile agar-gel method for highly efficient catalysis of total toluene oxidation, *Appl. Catal. B: Environ.*, 282 (2021) 119560.

[61] T. Pan, H. Deng, S. Kang, H. He, A simple strategy to tune $\alpha\text{-MnO}_2$ and enhance VOC oxidation via precipitation rate control, *Appl. Surf. Sci.*, 576 (2022) 151823.

[62] M. Piumetti, D. Fino, N. Russo, Mesoporous manganese oxides prepared by solution combustion synthesis as catalysts for the total oxidation of VOCs, *Appl. Catal. B: Environ.*, 163 (2015) 277-287.

[63] P. Wang, J. Wang, J. Zhao, X. Ma, X. Du, S. Peng, X. Hao, B. Tang, A. Abudula, G. Guan, Trace holmium assisting delaminated OMS-2 catalysts for total toluene oxidation at low temperature, *J. Colloid Interf. Sci.*, 608 (2021) 1662-1675.

[64] Z. Huang, M. Zhao, J. Luo, X. Zhang, W. Liu, Y. Wei, J. Zhao, Z. Song, Interaction in $\text{LaO}_x\text{-Co}_3\text{O}_4$ for highly efficient purification of toluene: Insight into LaO_x content and synergistic effect contribution, *Sep. Purif. Technol.*, 251 (2020) 117369.

[65] X. Zhang, M. Zhao, Z. Song, H. Zhao, W. Liu, J. Zhao, Z.a. Ma, Y. Xing, The effect of different metal oxides on the catalytic activity of a Co_3O_4 catalyst for toluene combustion: importance of the structure-property relationship and surface active species, *New J. Chem.*, 43 (2019) 10868-10877.

[66] F. Hu, J. Chen, Y. Peng, H. Song, K. Li, J. Li, Novel nanowire self-assembled hierarchical CeO_2 microspheres for low temperature toluene catalytic combustion, *Chem. Eng. J.*, 331 (2018) 425-434.

[67] M. Piumetti, S. Bensaid, D. Fino, N. Russo, Nanostructured ceria-zirconia catalysts for CO oxidation: Study on surface properties and reactivity, *Appl. Catal. B: Environ.*, 197 (2016) 35-46.

- [68] V.V. Kaichev, D. Teschner, A.A. Saraev, S.S. Kosolobov, A.Y. Gladky, I.P. Prosvirin, N.A. Rudina, A.B. Ayupov, R. Blume, M. Hävecker, A. Knop-Gericke, R. Schlögl, A.V. Latyshev, V.I. Bukhtiyarov, Evolution of self-sustained kinetic oscillations in the catalytic oxidation of propane over a nickel foil, *J. Catal.*, 334 (2016) 23-33.
- [69] D. Baojuan, L. Shumin, L. Deliang, Z. Ruozhu, L. Jingge, H. Qinglan, B. Feng, Catalytic oxidation of ethyl acetate and toluene over Cu-Ce-Zr supported ZSM-5/TiO₂ catalysts, *RSC Adv.*, 6 (2016) 53852-53859.
- [70] S. Ordóñez, L. Bello, H. Sastre, R. Rosal, F. V. Díez, Kinetics of the deep oxidation of benzene, toluene, *n*-hexane and their binary mixtures over a platinum on γ -alumina catalyst, *Appl. Catal. B: Environ.*, 38 (2002) 139-149.
- [71] E.V. Kovalyov, E.M. Sadovskaya, B.S. Bal'zhinimaev, Kinetic features of the deep oxidation of propane over a Pt/fiberglass catalyst, *Chem. Eng. J.*, 349 (2018) 547-553.
- [72] M. Hu, Z. Yao, K.N. Hui, K.S. Hui, Novel mechanistic view of catalytic ozonation of gaseous toluene by dual-site kinetic modelling, *Chem. Eng. J.*, 308 (2017) 710-718.
- [73] Y. Luo, Y. Zheng, X. Feng, D. Lin, Q. Qian, X. Wang, Y. Zhang, Q. Chen, X. zhang, Controllable P-Doping of LaCoO₃ Catalyst for Efficient Propane Oxidation: Optimized Surface Co Distribution and Enhanced Oxygen Vacancies, *ACS Appl. Mater. Interfaces*, 12 (2020) 23789-23799.
- [74] Y. Jiang, J. Gao, Q. Zhang, Z. Liu, M. Fu, J. Wu, Y. Hu, D. Ye, Enhanced oxygen vacancies to improve ethyl acetate oxidation over MnO_x-CeO₂ catalyst derived from MOF template, *Chem. Eng. J.*, 371 (2019) 78-87.
- [75] C. Yang, G. Miao, Y. Pi, Q. Xia, J. Wu, Z. Li, J. Xiao, Abatement of various types of VOCs by adsorption/catalytic oxidation: A review, *Chem. Eng. J.*, 370 (2019) 1128-1153.
- [76] I. Banu, C.M. Manta, G. Bercaru, G. Bozga, Combustion kinetics of cyclooctane and its binary mixture with o-xylene over a Pt/ γ -alumina catalyst, *Chem. Eng. Res. Des.*, 102 (2015) 399-406.
- [77] M.-H. Yuan, C.-C. Chang, C.-Y. Chang, W.-C. Liao, W.-K. Tu, J.-Y. Tseng, D.-R. Ji, J.-L. Shie, Y.-H. Chen, Ozone-catalytic oxidation for gaseous 1,2-dichloroethane in

- air over Pt/Al₂O₃ catalyst, J. Taiwan Inst. Chem. E., 53 (2015) 52-57.
- [78] Y. Chen, Z. Huang, M. Zhou, Z. Ma, J. Chen, X. Tang, Single Silver Adatoms on Nanostructured Manganese Oxide Surfaces: Boosting Oxygen Activation for Benzene Abatement, Environ. Sci. Technol., 51 (2017) 2304-2311.
- [79] M.B. S, H. Idriss, The reaction of propylene to propylene-oxide on CeO₂: An FTIR spectroscopy and temperature programmed desorption study, J. Chem. Phys., 152 (2020) 044712.
- [80] X. Wu, R. Han, Q. Liu, Y. Su, S. Lu, L. Yang, C. Song, N. Ji, D. Ma, X. Lu, A review of confined-structure catalysts in the catalytic oxidation of VOCs: synthesis, characterization, and applications, Catal. Sci. Technol., 11 (2021) 5374-5387.
- [81] H. Huang, Y. Xu, Q. Feng, D.Y.C. Leung, Low temperature catalytic oxidation of volatile organic compounds: a review, Catal. Sci. Technol., 5 (2015) 2649-2669.
- [82] V. R. Choudhary, G. M. Deshmukh, D. P. Mishra, Kinetics of the Complete Combustion of Dilute Propane and Toluene over Iron-Doped ZrO₂ Catalyst, Energ. Fuel., 19 (2005) 54-63.
- [83] Z. Zhang, F. Lin, L. Xiang, H. Yu, Z. Wang, B. Yan, G. Chen, Synergistic effect for simultaneously catalytic ozonation of chlorobenzene and NO over MnCoO_x catalysts: Byproducts formation under practical conditions, Chem. Eng. J., 427 (2022) 130929.
- [84] L. Chen, Y. Liu, X. Fang, Y. Cheng, Simple strategy for the construction of oxygen vacancies on α -MnO₂ catalyst to improve toluene catalytic oxidation, J. Hazard. Mater., 409 (2021) 125020.
- [85] Y. Wang, D. Yang, S. Li, L. Zhang, G. Zheng, L. Guo, Layered copper manganese oxide for the efficient catalytic CO and VOCs oxidation, Chem. Eng. J., 357 (2019) 258-268.
- [86] B. Feng, M. Shi, J. Liu, X. Han, Z. Lan, H. Gu, X. Wang, H. Sun, Q. Zhang, H. Li, Y. Wang, H. Li, An efficient defect engineering strategy to enhance catalytic performances of Co₃O₄ nanorods for CO oxidation, J. Hazard. Mater., 394 (2020) 122540.
- [87] M. Zhang, X. Sui, X. Zhang, M. Niu, C. Li, H. Wan, Z.-A. Qiao, H. Xie, X. Li,

Multi-defects engineering of NiCo_2O_4 for catalytic propane oxidation, *Appl. Surf. Sci.*, 600 (2022) 154040.

[88] L. Bao, S. Zhu, Y. Chen, Y. Wang, W. Meng, S. Xu, Z. Lin, X. Li, M. Sun, L. Guo, Anionic defects engineering of Co_3O_4 catalyst for toluene oxidation, *Fuel*, 314 (2022) 122774.

[89] M. Wu, J. Sun, W. Xiang, S. Chen, Defect engineering in heterogeneous catalytic oxidation catalysts for air pollution elimination: A review of recent progress and strategies, *J. Environ. Chem. Eng.*, 10 (2022) 108734.

[90] L. Wang, Y. Wang, Y. Zhang, Y. Yu, H. He, X. Qin, B. Wang, Shape dependence of nanoceria on complete catalytic oxidation of o-xylene, *Catal. Sci. Technol.*, 6 (2016) 4840-4848.

[91] R. Mi, D. Li, Z. Hu, R.T. Yang, Morphology Effects of CeO_2 Nanomaterials on the Catalytic Combustion of Toluene: A Combined Kinetics and Diffuse Reflectance Infrared Fourier Transform Spectroscopy Study, *ACS Catal.*, 11 (2021) 7876-7889.

[92] S. Yang, Z. Qi, Y. Wen, X. Wang, S. Zhang, W. Li, S. Li, Generation of abundant oxygen vacancies in Fe doped $\delta\text{-MnO}_2$ by a facile interfacial synthesis strategy for highly efficient catalysis of VOCs oxidation, *Chem. Eng. J.*, 452 (2023) 139657.

[93] P. Wang, J. Wang, J. Shi, X. Du, X. Hao, B. Tang, A. Abudula, G. Guan, Low content of samarium doped CeO_2 oxide catalysts derived from metal organic framework precursor for toluene oxidation, *Mol. Catal.*, 492 (2020) 111027.

[94] M. Wu, S. Chen, W. Xiang, Oxygen vacancy induced performance enhancement of toluene catalytic oxidation using LaFeO_3 perovskite oxides, *Chem. Eng. J.*, 387 (2020) 124101.

[95] J. Hou, Y. Li, L. Liu, L. Ren, X. Zhao, Effect of giant oxygen vacancy defects on the catalytic oxidation of OMS-2 nanorods, *J. Mater. Chem. A*, 1 (2013) 6736.

[96] Y. Zheng, Q. Liu, C. Shan, Y. Su, K. Fu, S. Lu, R. Han, C. Song, N. Ji, D. Ma, Defective Ultrafine MnO_x Nanoparticles Confined within a Carbon Matrix for Low-Temperature Oxidation of Volatile Organic Compounds, *Environ. Sci. Technol.*, 55 (2021) 5403-5411.

[97] T. He, Y. Zhou, D. Ding, S. Rong, Engineering Manganese Defects in Mn_3O_4 for

Catalytic Oxidation of Carcinogenic Formaldehyde, *ACS Appl. Mater. Interfaces*, 13 (2021) 29664-29675.

[98] G. Li, K. He, F. Zhang, G. Jiang, Z. Zhao, Z. Zhang, J. Cheng, Z. Hao, Defect enhanced CoMnNiO_x catalysts derived from spent ternary lithium-ion batteries for low-temperature propane oxidation, *Appl. Catal. B: Environ.*, 309 (2022) 121231.

[99] J. Ding, R. Ran, J. Jia, D. Weng, Z. Yang, Highly effective La-deficient La_{1-x}Ce_xMnO₃ mixed oxides for the complete oxidation of methane, *Prog. Nat. Sci.*, 31 (2021) 373-378.

[100] W. Tang, M. Yao, Y. Deng, X. Li, N. Han, X. Wu, Y. Chen, Decoration of one-dimensional MnO₂ with Co₃O₄ nanoparticles: A heterogeneous interface for remarkably promoting catalytic oxidation activity, *Chem. Eng. J.*, 306 (2016) 709-718.

[101] W. Fang, J. Chen, X. Zhou, J. Chen, Z. Ye, J. Li, Zeolitic Imidazolate Framework-67-Derived CeO₂@Co₃O₄ Core-Shell Microspheres with Enhanced Catalytic Activity toward Toluene Oxidation, *Ind. Eng. Chem. Res.*, 59 (2020) 10328-10337.

[102] N. Huang, Z. Qu, C. Dong, Y. Qin, X. Duan, Superior performance of α@β-MnO₂ for the toluene oxidation: Active interface and oxygen vacancy, *Appl. Catal. A: Gen.*, 560 (2018) 195-205.

[103] Z. Su, W. Si, H. Liu, S. Xiong, X. Chu, W. Yang, Y. Peng, J. Chen, X. Cao, J. Li, Boosting the Catalytic Performance of CeO₂ in Toluene Combustion via the Ce-Ce Homogeneous Interface, *Environ. Sci. Technol.*, 55 (2021) 12630-12639.

[104] L. Li, J. Luo, Y. Liu, F. Jing, D. Su, W. Chu, Self-propagated flaming synthesis of highly active layered CuO-δ-MnO₂ hybrid composites for catalytic total oxidation of toluene pollutant, *ACS Appl. Mater. Interfaces*, 9 (2017) 21798-21808.

[105] W. Yang, Y. Wang, W. Yang, H. Liu, Z. Li, Y. Peng, J. Li, Surface In Situ Doping Modification over Mn₂O₃ for Toluene and Propene Catalytic Oxidation: The Effect of Isolated Cu^{δ+} Insertion into the Mezzanine of Surface MnO₂ Cladding, *ACS Appl. Mater. Interfaces*, 13 (2021) 2753-2764.

[106] X. Zheng, J. Cai, Y. Cao, L. Shen, Y. Zheng, F. Liu, S. Liang, Y. Xiao, L. Jiang, Construction of cross-linked δ-MnO₂ with ultrathin structure for the oxidation of H₂S: Structure-activity relationship and kinetics study, *Appl. Catal. B: Environ.*, 297 (2021)

120402.

[107] G. Chen, D. Hong, H. Xia, W. Sun, S. Shao, B. Gong, S. Wang, J. Wu, X. Wang, Q. Dai, Amorphous and homogeneously Zr-doped MnO_x with enhanced acid and redox properties for catalytic oxidation of 1,2-Dichloroethane, *Chem. Eng. J.*, 428 (2022) 131067.

[108] Y. Zeng, K.G. Haw, Z. Wang, Y. Wang, S. Zhang, P. Hongmanorom, Q. Zhong, S. Kawi, Double redox process to synthesize CuO-CeO_2 catalysts with strong Cu-Ce interaction for efficient toluene oxidation, *J. Hazard. Mater.*, 404 (2021) 124088.

[109] L. Sun, D. Marrocchelli, B. Yildiz, Edge dislocation slows down oxide ion diffusion in doped CeO_2 by segregation of charged defects, *Nat. Commun.*, 6 (2015) 6294.

[110] J. Zhang, D. Tan, Q. Meng, X. Weng, Z. Wu, Structural modification of LaCoO_3 perovskite for oxidation reactions: The synergistic effect of Ca^{2+} and Mg^{2+} co-substitution on phase formation and catalytic performance, *Appl. Catal. B: Environ.*, 172-173 (2015) 18-26.

[111] Z. Hou, J. Feng, T. Lin, H. Zhang, X. Zhou, Y. Chen, The performance of manganese-based catalysts with $\text{Ce}_{0.65}\text{Zr}_{0.35}\text{O}_2$ as support for catalytic oxidation of toluene, *Appl. Surf. Sci.*, 434 (2018) 82-90.

[112] P. Wang, J. Zhao, Q. Zhao, X. Ma, X. Du, X. Hao, B. Tang, A. Abudula, G. Guan, Microwave-assisted synthesis of manganese oxide catalysts for total toluene oxidation, *J. Colloid Interf. Sci.*, 607 (2021) 100-110.

[113] S. Zhao, Y. Yang, F. Bi, Y. Chen, M. Wu, X. Zhang, G. Wang, Oxygen vacancies in the catalyst: Efficient degradation of gaseous pollutants, *Chem. Eng. J.*, 454 (2023) 140376.

[114] Q. Qi, W. Zhang, Y. Zhang, G. Bai, S. Wang, P. Liang, Formaldehyde oxidation at room temperature over layered MnO_2 , *Catal. Commun.*, 153 (2021) 106293.

[115] X. Wei, K. Li, X. Zhang, Q. Tong, J. Ji, Y. Cai, B. Gao, W. Zou, L. Dong, CeO_2 nanosheets with anion-induced oxygen vacancies for promoting photocatalytic toluene mineralization: Toluene adsorption and reactive oxygen species, *Appl. Catal. B: Environ.*, 317 (2022) 121694.

- [116] F. C. Tompkins, Superficial chemistry and solid imperfections, *Nature*, 186 (1960) 3-6.
- [117] H. He, X. Lin, S. Li, Z. Wu, J. Gao, J. Wu, W. Wen, D. Ye, M. Fu, The key surface species and oxygen vacancies in $\text{MnO}_x(0.4)\text{-CeO}_2$ toward repeated soot oxidation, *Appl. Catal. B: Environ.*, 223 (2018) 134-142.
- [118] X. Liu, K. Zhou, L. Wang, B. Wang, Y. Li, Oxygen Vacancy Clusters Promoting Reducibility and Activity of Ceria Nanorods, *J. Ind. Eng. Chem.*, 131 (2009) 3140-3141.
- [119] W. Yang, Z.a. Su, Z. Xu, W. Yang, Y. Peng, J. Li, Comparative study of α -, β -, γ - and δ - MnO_2 on toluene oxidation: Oxygen vacancies and reaction intermediates, *Appl. Catal. B: Environ.*, 260 (2020) 118150.
- [120] Y. Li, W. Han, R. Wang, L.-T. Weng, A. Serrano-Lotina, M.A. Bañares, Q. Wang, K.L. Yeung, Performance of an aliovalent-substituted CoCeO_x catalyst from bimetallic MOF for VOC oxidation in air, *Appl. Catal. B: Environ.*, 275 (2020) 119121.
- [121] Y. Huang, Y. Liu, W. Wang, M. Chen, H. Li, S.-c. Lee, W. Ho, T. Huang, J. Cao, Oxygen vacancy-engineered δ - MnO_x /activated carbon for room-temperature catalytic oxidation of formaldehyde, *Appl. Catal. B: Environ.*, 278 (2020) 119294.
- [122] K. Zha, W. Sun, Z. Huang, H. Xu, W. Shen, Insights into High-Performance Monolith Catalysts of Co_3O_4 Nanowires Grown on Nickel Foam with Abundant Oxygen Vacancies for Formaldehyde Oxidation, *ACS Catal.*, 10 (2020) 12127-12138.
- [123] P. Wang, X. Ma, X. Hao, B. Tang, A. Abudula, G. Guan, Oxygen vacancy defect engineering to promote catalytic activity toward the oxidation of VOCs: a critical review, *Catal. Rev.*, (2022) DOI: 10.1080/01614940.2022.2078555.
- [124] Y. Wang, J. Wu, G. Wang, D. Yang, T. Ishihara, L. Guo, Oxygen vacancy engineering in Fe doped akhtenskite-type MnO_2 for low-temperature toluene oxidation, *Appl. Catal. B: Environ.*, 285 (2021) 119873.
- [125] J. Ding, Y. Yang, J. Liu, L. Zhao, Y. Yu, Mechanistic study on the role of oxygen vacancy for methylene chloride oxidation over La-Mn perovskite, *Appl. Surf. Sci.*, 559 (2021) 149979.
- [126] H. Deng, S. Kang, J. Ma, C. Zhang, H. He, Silver incorporated into cryptomelane-type Manganese oxide boosts the catalytic oxidation of benzene, *Appl. Catal. B:*

Environ., 239 (2018) 214-222.

[127] Y. Luo, D. Lin, Y. Zheng, X. Feng, Q. Chen, K. Zhang, X. Wang, L. Jiang, MnO₂ nanoparticles encapsulated in spheres of Ce-Mn solid solution: Efficient catalyst and good water tolerance for low-temperature toluene oxidation, Appl. Surf. Sci., 504 (2020) 144481.

[128] J. Chen, X. Chen, D. Yan, M. Jiang, W. Xu, H. Yu, H. Jia, A facile strategy of enhancing interaction between cerium and manganese oxides for catalytic removal of gaseous organic contaminants, Appl. Catal. B: Environ., 250 (2019) 396-407.

[129] C. Zhang, C. Wang, S. Gil, A. Boreave, L. Retailleau, Y. Guo, J.L. Valverde, A. Giroir-Fendler, Catalytic oxidation of 1,2-dichloropropane over supported LaMnO_x oxides catalysts, Appl. Catal. B: Environ., 201 (2017) 552-560.

[130] D. Yu, Y. Ren, X. Yu, X. Fan, L. Wang, R. Wang, Z. Zhao, K. Cheng, Y. Chen, Z. Sojka, A. Kotarba, Y. Wei, J. Liu, Facile synthesis of birnessite-type K₂Mn₄O₈ and cryptomelane-type K_{2-x}Mn₈O₁₆ catalysts and their excellent catalytic performance for soot combustion with high resistance to H₂O and SO₂, Appl. Catal. B: Environ., 285 (2021) 119779.

[131] C. Dong, Z. Qu, X. Jiang, Y. Ren, Tuning oxygen vacancy concentration of MnO₂ through metal doping for improved toluene oxidation, J. Hazard. Mater., 391 (2020) 122181.

[132] S. Mo, Q. Zhang, J. Li, Y. Sun, Q. Ren, S. Zou, Q. Zhang, J. Lu, M. Fu, D. Mo, J. Wu, H. Huang, D. Ye, Highly efficient mesoporous MnO₂ catalysts for the total toluene oxidation: Oxygen-Vacancy defect engineering and involved intermediates using in situ DRIFTS, Appl. Catal. B: Environ., 264 (2020) 118464.

[133] Z. Su, W. Yang, C. Wang, S. Xiong, X. Cao, Y. Peng, W. Si, Y. Weng, M. Xue, J. Li, Roles of Oxygen Vacancies in the Bulk and Surface of CeO₂ for Toluene Catalytic Combustion, Environ. Sci. Technol., 54 (2020) 12684-12692.

[134] W. Zhang, M. Li, X. Wang, X. Zhang, X. Niu, Y. Zhu, Boosting catalytic toluene combustion over Mn doped Co₃O₄ spinel catalysts: Improved mobility of surface oxygen due to formation of Mn-O-Co bonds, Appl. Surf. Sci., 590 (2022) 153140.

[135] Q. Dai, L.-L. Yin, S. Bai, W. Wang, X. Wang, X.-Q. Gong, G. Lu, Catalytic total

oxidation of 1,2-dichloroethane over VO_x/CeO_2 catalysts: Further insights via isotopic tracer techniques, *Appl. Catal. B: Environ.*, 182 (2016) 598-610.

[136] X. Zhang, F. Bi, Z. Zhu, Y. Yang, S. Zhao, J. Chen, X. Lv, Y. Wang, J. Xu, N. Liu, The promoting effect of H_2O on rod-like MnCeO_x derived from MOFs for toluene oxidation: A combined experimental and theoretical investigation, *Appl. Catal. B: Environ.*, 297 (2021) 120393.

[137] H. Pan, Y. Jian, C. Chen, C. He, Z. Hao, Z. Shen, H. Liu, Sphere-shaped Mn_3O_4 catalyst with remarkable low-temperature activity for methyl-ethyl-ketone combustion, *Environ. Sci. Technol.*, 51 (2017) 6288-6297.

[138] C. Dong, Z. Qu, Y. Qin, Q. Fu, H. Sun, X. Duan, Revealing the Highly Catalytic Performance of Spinel CoMn_2O_4 for Toluene Oxidation: Involvement and Replenishment of Oxygen Species Using In Situ Designed-TP Techniques, *ACS Catal.*, 9 (2019) 6698-6710.

[139] Y. Sun, S. Xu, B. Bai, L. Li, Y. Kang, X. Hu, Z. Liao, C. He, Biotemplate Fabrication of Hollow Tubular $\text{Ce}_x\text{Sr}_{1-x}\text{TiO}_3$ with Regulable Surface Acidity and Oxygen Mobility for Efficient Destruction of Chlorobenzene: Intrinsic Synergy Effect and Reaction Mechanism, *Environ. Sci. Technol.*, 56 (2022) 5796-5807.

[140] Y. Gu, T. Cai, X. Gao, H. Xia, W. Sun, J. Zhao, Q. Dai, X. Wang, Catalytic combustion of chlorinated aromatics over WO_x/CeO_2 catalysts at low temperature, *Appl. Catal. B: Environ.*, 248 (2019) 264-276.

CHAPTER 2 Synthesis of MnO_x from pectin-driven sol-gel route for catalytic oxidation of toluene

2.1 Introduction

Emission of volatile organic compounds (VOCs) from various industrial, transporting sections and human daily activities is severely harmful to environment, building and human health due to their contributions to air pollution, e.g., photochemical smog, inhalable particles and tropospheric ozone [1-3]. Among the VOCs purification technologies (e.g., photo-catalytic oxidation, sorption filtration, thermal combustion, wet scrubbing and catalytic combustion), the catalytic combustion has higher expectation due to its low operating temperature, high efficiency and no secondary pollution [4-6]. Generally, supported noble-metal catalysts (e.g., Pt, Au and Pd) show good catalytic performance in the short-term VOCs combustion, but their high price, easily poisoning and sintering prevent their wide applications [7-9]. Compared to noble-metal based catalysts, a variety of transition metal-based ones (e.g., CoO_x [3, 10, 11], FeO_x [12], NiO_x [13], MnO_x [14-16] and CeO_x [17-19]) have been widely investigated in the catalytic VOCs combustion, which always exhibit excellent stability, high toxicity resistance and low price. Among them, Mn-based ones have been widely explored due to their tunable multiple valences and excellent oxygen mobility. For instance, Zhang et al. [20] synthesized different Mn_2O_3 based catalysts by calcining Mn-MOFs precursors and found that the Mn_2O_3 catalyst prepared by calcinating Mn-MIL-100 in argon and oxygen atmospheres showed better catalytic toluene combustion performance since it had more active species as well as surface adsorbed oxygen species. Yang et al. [21] developed a manganese oxide catalyst by using hydrothermal, calcining, pickling and drying processes in turn, in which the acid treatment with appropriate acid concentration enriched the surface defects and improved oxygen mobility, resulting in optimum catalytic activity. Gu et al. [22] fabricated a flower-like MnO_2 catalyst with a hollow structure by oxidizing/etching pre-synthesized MnCO_3 microspheres, and found that it had excellent catalytic toluene combustion performance owing to abundant acidic

sites, Mn^{4+} and oxygen vacancies existed on it.

Although various manganese-based catalysts have been successfully synthesized by many routes, the cumbersome synthesis processes always prompt people to make efforts to explore simple and efficient synthesis method, which is of great significance for the industrial synthesis of catalysts. The sol-gel method is considered to be a simple way for the synthesis of catalysts with a porous structure and excellent performances. Yang et al. [23] compared catalytic activities of various Mn-based perovskite-type catalysts for toluene combustion, and found that those catalysts synthesized by the citric acid sol-gel way exhibited poor performance owing to their worse low-temperature reducibility and less active manganese species. Castaño et al. [24] fabricated various Mn-based catalysts by a glycine auto-combustion method and utilized for catalytic toluene combustion, and found that the appropriate glycine/nitrate ratio led to more adsorption sites and active centers in the obtained MnO_x catalyst, thereby facilitating the occurrence of redox cycles. As a result, T_{90}/T_{50} values of 258/236 °C under an activity evaluation of 600 ppm toluene were achieved. However, the conventional chelating pore-making agents are always accompanied by the generation of irritating odors during the sol-gel process. Notably, the catalytic activity of catalysts synthesized by these traditional chelating agents is still limited due to the poor reducibility and less active species.

Inspired by the above studies, herein, an eco-friendly pectin-driven sol-gel route was applied for the preparation of porous manganese oxide catalyst successfully. As a comparison, typical chelating agents (citric acid and glycine) were chosen to synthesize reference catalysts. Among them, citric acid chelates metal ions by carboxyl oxygen and hydroxyl oxygen, and glycine chelates metal ions by carboxyl oxygen and amino nitrogen. In addition to the chelating effect of pectin, its unique spatial dispersion and steric hindrance effects of macromolecules to metal atom have also been studied. The catalytic toluene combustion performance over the synthesized catalysts was evaluated by a fixed bed reactor containing the simulated toluene feed gas. The water resistance and long-term stability of the optimal catalyst were determined on the same reaction bed by fixing the reaction temperature and introducing water vapor into the reaction

gas, respectively.

2.2 Experimental and measurements

2.2.1 Catalyst preparation

(I) MnO_x-C catalyst synthesized by citric acid-driven sol-gel method

This is a traditional method. Briefly, 30 mmol of citric acid (A.R., HOOCCH₂C(OH)(COOH)CH₂COOH) was firstly dissolved in 50 mL of distilled water, then 15 mmol of Manganese(II) nitrate hexahydrate (A.R., Mn(NO₃)₂·6H₂O) was added and stirred at ambient temperature for 30 min. After that, the beaker containing the above mixed solution was moved into a water bath and stirred continuously at 80 °C for ca. 2.5 h until a sol state was formed. Finally, the above sol was dried at 140 °C overnight and then calcined at 350 °C for 3 h (heating rate: 2 °C/min) to obtain a black solid product, which is denoted as MnO_x-C.

(II) MnO_x-G catalyst synthesized by glycine-driven sol-gel method

First, 30 mmol of glycine (A.R., H₂NCH₂COOH) and 15 mmol of Manganese(II) nitrate hexahydrate were dissolved in a beaker containing 150 mL of distilled water. Then, the beaker was heated with stirring in an 80 °C water bath for about 3 h. Finally, the obtained sol was transferred into an oven for drying at 140 °C overnight, and then calcined at 350 °C for 3 h (heating rate: 2 °C/min). The obtained black product is denoted as MnO_x-G.

(III) MnO_x-P catalyst synthesized by pectin-driven sol-gel method

The synthesis process of the MnO_x-P catalyst from the pectin-driven sol-gel was as follows: First, 15 mmol of Manganese(II) nitrate hexahydrate was dissolved in 60 mL of distilled water, and then 2 g of pectin powder (C.P., CH₃O- 3.5-8.5%, C₆H₁₀O₇ 50-80%, from Citrus) was slowly introduced to the stirring solution above, and the stirring was continued for 30 min to obtain a transparent dilute sol. After that, the beaker containing the above sol was moved to a water bath (80 °C) and continued to stir for ca. 2 h to obtain a thick sol. Finally, the obtained sol was treated in an oven by drying at 140 °C overnight to form a porous fluffy shaped solid, and then the obtained gel was put in a muffle furnace for calcination (350 °C for 3 h) to obtain the target catalyst, which is denoted as MnO_x-P. In addition, two pectin dosages, i.e., 1 and 3 g, in the

catalyst synthesis process were also used, and the prepared catalysts are denoted as MnO_x-P1 and MnO_x-P3, respectively.

2.2.2 Catalytic performance test

Catalytic degradation of toluene was performed in a tubular quartz micro-reactor (i.d. = 8 mm) under steady atmospheric pressure, in which a uniform mixture of 50 mg catalyst (40-60 mesh) and 500 mg silica sand (40-60 mesh) was loaded. Before each test, N₂ flow (35 mL·min⁻¹) was used to purge the reactor for about half hour in advance to remove air and other impurities in the gas path, and then the simulated VOC containing feed gas (50 mL·min⁻¹) with a weight hourly space velocity (WHSV) of 60,000 cm³·g⁻¹·h⁻¹ consisting of toluene (1,000 ppm) and O₂ (20 vol.%) with balance gas (N₂), was fed into the reactor and kept at 100 °C for a period until the reaction system became stable. After that, the quartz reactor was programmed to heat up to 300 °C, during which the temperature was held constant for 40 min at each target value to analyze the gas composition adequately. The toluene and products in raw gas before and after the reactor were measured by a FT-IR analyzer (FG-120, Horiba) on-line and a gas chromatography machine (GC-2014, Shimadzu). The long-time durability and water tolerance of the optimal catalyst were investigated by holding the reaction temperature at a fixed value for 50 h and mixing steam generated on-line (5 vol.%) into the feed gas, respectively. Toluene conversion (C_t) was calculated by Eq. (1): $C_t = \frac{[\text{toluene}]_{in} - [\text{toluene}]_{out}}{[\text{toluene}]_{in}} \times 100\%$ according to the concentrations at the inlet ($[\text{toluene}]_{in}$) and outlet ($[\text{toluene}]_{out}$). The CO₂ selectivity (C_{CO_2}) was calculated by Eq. (2): $C_{CO_2} = \frac{[CO_2]_{out}}{7 \times [\text{toluene}]_{in}} \times 100\%$ based on the outlet CO₂ ($[CO_2]_{out}$) and toluene $[\text{toluene}]_{in}$ concentrations. In addition, Eq. (3): $r = (C_t \cdot V)/m_{cat}$ and Eq. (4): $r = -kc = [-A \exp(-E_a/RT)]c$ were used to determine apparent activation energy (E_a , kJ·mol⁻¹). Eq. (5): $r^* = r/SSA$ was used to calculate normalized reaction rate (r^* , mol·m⁻²·s⁻¹). Where, m_{cat} represents catalyst mass amount; V is toluene gas flow rate; c is the toluene concentration in the feed; A represents pre-exponential factor; k is rate constant; T is reaction temperature; R is proportional constant; and SSA represents specific surface area of catalyst.

2.2.3 Catalyst characterization

Physicochemical properties of prepared catalysts were analyzed by various characterization techniques. N₂ adsorption-desorption measurements were conducted under liquid nitrogen atmosphere on a Nova 4200 instrument (Quantachrome Inc., USA). Pore structure information and SSA values of MnO_x were acquired by using Barrett-Joyner-Halenda (BJH) method and Brunauer-Emmett-Teller (BET) model, respectively. Raman spectra were collected on an NRS-5100 spectrometer (JASCO) under an He-Ne excitation source (532 nm). Wide-angle X-ray diffraction (XRD) patterns were acquired on a Smartlab XRD diffractometer (Rigaku, Japan) with a Cu-K α radiation ($\lambda = 1.5418 \text{ \AA}$). Surface morphology was observed on a scanning electron microscope (SEM) device (Hitachi SU8010, Japan) with an applied voltage of 10 kV. Transmission electron microscopy (TEM) and high-resolution transmission electron microscope (HRTEM) images were conducted by using a JEM-2100F microscope at 200 kV. XPS instrument (VG Scientific ESCALab250i-XL) was used to test the XPS spectra. H₂ temperature-programmed reduction (H₂-TPR) experiments were tested on a BELCAT device equipped with a TCD detector (Microtrac, Japan). In brief, 50 mg of catalyst in a U-shape quartz reactor was first treated at first in a He atmosphere (50 cm³·min⁻¹) at 300 °C for 30 min. After the sample was cooled to room temperature, it was heated to 900 °C (heating rate: 10 °C /min) in a H₂ (5 vol.%)/Ar atmosphere (50 cm³·min⁻¹), during which H₂ consumption signal was captured by TCD. O₂ temperature-programmed desorption experiments (O₂-TPD) were monitored on the same device to evaluate the oxygen species mobility in all catalysts. First, the pretreatment process of catalyst was performed as that for TPR test. After that, the catalyst was flushed with a stream of oxygen (30 cm³·min⁻¹) at 50 °C for 1 h and then purged by He gas at the same temperature for 1 h. Then, the catalyst was heated to 900 °C with a rate of 10 °C/min in a He atmosphere (30 cm³·min⁻¹), and oxygen desorption signal during this period was recorded with the TCD detector and converted into an image.

2.3 Result and discussion

2.3.1 Morphologies of prepared MnO_x catalysts

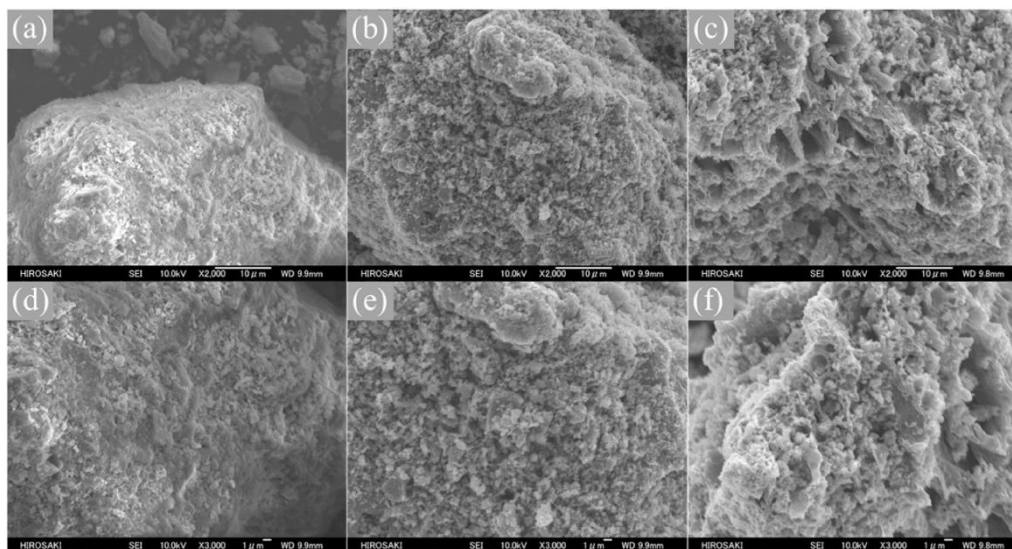


Fig. 2.1. SEM images of $\text{MnO}_x\text{-C}$ (a, d), $\text{MnO}_x\text{-G}$ (b, e) and $\text{MnO}_x\text{-P}$ (c, f) catalysts.

As displayed in Fig. 2.1, apparently, the MnO_x catalysts synthesized by different chelating pore-making agents show different surface structures. The $\text{MnO}_x\text{-C}$ catalyst prepared with citric acid-driven sol-gel method (Fig. 2.1a, d) exhibits an irregular compact block-like packing structure with a small amount of pore structure, which should be the reason of its SSA value as discussed in Section 2.3.2. Contrastively, loose irregular nanoparticle exterior is found on the $\text{MnO}_x\text{-G}$ catalyst (Fig. 2.1b, e), which could be resulted from the ordinary pore-forming ability of the special chelating structure of glycine. For $\text{MnO}_x\text{-P}$ catalyst synthesized with pectin-driven sol-gel method, a large proportion of honeycomb structures with hierarchical pore sizes are constructed (Fig. 2.1c, f), which can be attributed to the superior pore-forming ability of special gelatinous polysaccharide structure of pectin. As we know, abundant pore structures in catalyst can not only facilitate the adsorption capacity of raw gas molecules, but also reduce the mass transfer resistance for the reactant molecules and optimize the distribution of active sites with high stability, and thus the $\text{MnO}_x\text{-P}$ catalyst should have excellent toluene adsorption and transfer performance during toluene oxidation [25-27].

2.3.2 N₂ adsorption-desorption studies

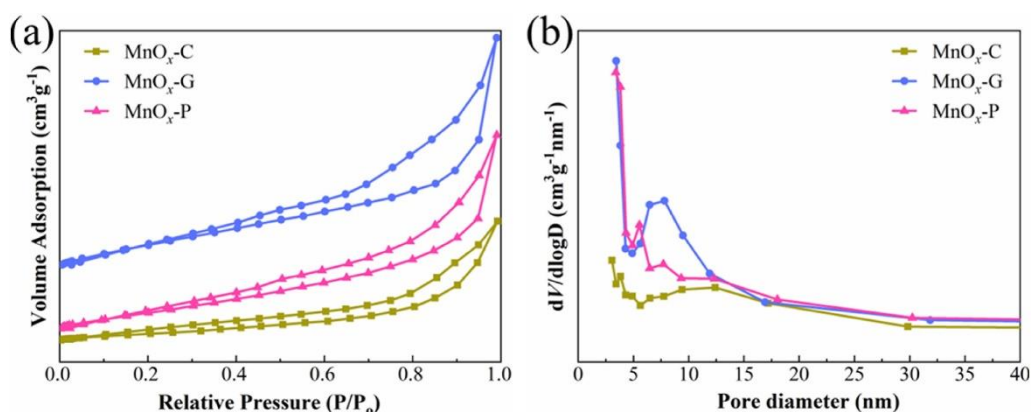


Fig. 2.2. N₂ adsorption-desorption isotherms (a) and the pore-size distribution curves (b) of the prepared MnO_x catalysts.

The porous structures of the MnO_x catalysts were explored by N₂ adsorption-desorption experiments. As displayed in Fig. 2.2a, based on IUPAC classification, all catalysts have similar type IV adsorption-desorption isotherms and H3-shaped hysteresis loops, which are the characteristics of the existence of mesoporous structure in catalysts [28, 29]. It is worth noting that the hysteresis effects in three catalysts caused by different chelating pore formers are observed at different relative pressures with different absorption volumes, which are attributed to the different microstructures of mesopores in the catalysts resulting from the different pore-forming properties of chelating agents. The pore-size distribution curves shown in Fig. 2.2b visually compare the pore difference in different MnO_x catalysts. One can see that two weak peaks centered at ca. 3.7 and 12 nm are observed in the MnO_x-C sample, which indicates a small amount of mesopores with these two ranges of pore sizes in this sample. Furthermore, a strong pore-size distribution peak at ca. 7.5 nm is found in the MnO_x-G catalyst, which implies a large number of relatively uniform pore structure in the catalyst. For the MnO_x-P catalyst, various pore-size distribution peaks located at ca. 5.5, 7.7 and 12.3 nm demonstrate a hierarchical pore structure as mentioned above. It can thus be seen that the pore sizes in all catalysts are larger than 5 times the kinetic diameter of toluene molecules, which is beneficial to overcome the resistance in the mass transfer process of the feedstock [30, 31]. In addition, as summarized in Table 2.1, in which the pore volumes (V_p) and average pore diameters (P_d) of prepared catalysts are calculated

by BJH method, and the SSAs are measured by BET model. The V_p , P_d and SSA values of the catalysts follow the same order of $\text{MnO}_x\text{-G}$ ($0.223 \text{ cm}^3\cdot\text{g}^{-1}$, 3.442 nm and $107.7 \text{ m}^2\cdot\text{g}^{-1}$) $>$ $\text{MnO}_x\text{-P}$ ($0.203 \text{ cm}^3\cdot\text{g}^{-1}$, 3.405 nm and $79.4 \text{ m}^2\cdot\text{g}^{-1}$) $>$ $\text{MnO}_x\text{-C}$ ($0.119 \text{ cm}^3\cdot\text{g}^{-1}$, 3.065 nm and $29.3 \text{ m}^2\cdot\text{g}^{-1}$). It is well known that larger pore volume as well as SSA are important for the improvement of catalytic performance since they can promote the using of active centers and the adsorption performance of reactant molecules on catalysts [32, 33]. Therefore, the pectin and glycine as chelating pore formers show superiority in optimizing the pore structure of the MnO_x catalysts.

Table 2.1 N_2 adsorption-desorption, XRD and TEM analysis results for all prepared MnO_x catalysts.

Catalyst	V_p ($\text{cm}^3\cdot\text{g}^{-1}$)	P_d (nm)	SSA ($\text{m}^2\cdot\text{g}^{-1}$)	Crystallinity ^a (%)	Average grain size ^b (nm)
$\text{MnO}_x\text{-C}$	0.119	3.065	29.3	53.3	18.1
$\text{MnO}_x\text{-G}$	0.223	3.442	107.7	45.4	6.3
$\text{MnO}_x\text{-P}$	0.203	3.405	79.4	28.5	8.8

^a Estimated through the (211) crystal face in XRD patterns. ^b Derived from the TEM images.

2.3.3 Crystalline phase structure of prepared catalysts

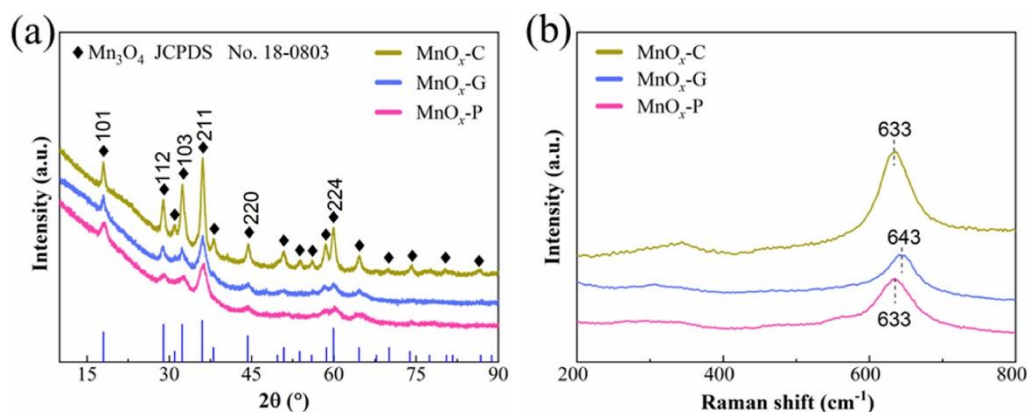


Fig. 2.3. (a) XRD patterns and (b) Raman spectra of prepared MnO_x samples.

In order to explore the effect of organic chelating agent type on the crystallization of

catalysts, XRD patterns were tested (Fig. 2.3a). Obviously, all catalysts show the characteristic crystal phase of Mn_3O_4 (JCPDS No. 18-0803) [34, 35], however, there are different intensities of diffraction peaks among different samples. Moreover, no broad peaks for amorphous carbon are found at around 20° (2θ), indicating that the calcination temperature of 350°C is sufficient to remove the organic template [36, 37]. It can be seen that the diffraction peak intensities of the catalyst synthesized by the citric acid-driven sol-gel method are higher than those of the MnO_x catalysts synthesized by the other two sol-gel methods. Moreover, the crystallinities of the MnO_x catalysts calculated based on the XRD analysis results are listed in Table 2.1, which present the following order: $\text{MnO}_x\text{-C}$ (53.3%) > $\text{MnO}_x\text{-G}$ (45.4%) > $\text{MnO}_x\text{-P}$ (28.5%). It can be considered that the special chelate structure has a great influence on the crystalline state of the obtained MnO_x catalysts, and would inevitably affect the interaction and composition of the active species in the catalysts. For glycine chelates, only two molecules of glycine can form chelate complexes with metal ion through the coordination of Mn ion with carboxyl oxygen and amino nitrogen in glycine. Afterwards, the heating process leads to the breaking of C-N and M-N bonds to form xerogels accompanied by the generation of polluting NH_3 gas, and then the residual organic matter is removed as the temperature rises, thereby forming metal oxides. For citric acid chelates, the coordination between the metal ions and the carboxyl oxygen and hydroxyl oxygen in two molecules of citric acid can also form a chelate complex, and then the organic ligand is removed by heating and calcining to form a metal oxide, accompanied by the escape of other by-product acid gases, such as aconitic acid and itaconic acid. In comparison, for pectin-driven sol-gel method, many carboxyl oxygens in pectin can also coordinate with metal ions to form chelates. Notably, on the one hand, the polysaccharide polymer characteristics of pectin undergo the hydrolysis during the chelation process and realizes the valence adjustment of metal ions. On the other hand, the macromolecular steric hindrance of pectin polymer can limit the formation of long-range order of metal oxides during the crystallization process, and result in the reducing of their crystallinity accompanied by the generation of a large number of active species such as structural defects. Thus, it can be considered that the special chelate structure

of pectin as well as the special thermal interaction during calcination can inhibit the continuous crystallization of the catalysts to a certain extent, thereby resulting in the weaker diffraction peaks in $\text{MnO}_x\text{-P}$ catalyst, which is also consistent with the lower crystallinity. In addition, the transition metal oxides with low crystallinity or amorphous structure are always accompanied by excellent oxygen mobility and reducibility, thus exhibiting excellent catalytic VOCs combustion performance [37, 38]. Fig. 2.3b shows the Raman spectra of the prepared MnO_x . Obviously, a strong stretching vibration peak at 633 or 643 cm^{-1} is found in the spectrum of each sample, which is the characteristic stretching vibration peak of Mn-O-Mn in Mn_3O_4 [39, 40]. Moreover, weaker vibrational features found on the $\text{MnO}_x\text{-G}$ and $\text{MnO}_x\text{-C}$ catalysts can be attributed to the disturbed scattering signal in the low crystallinity material. Furthermore, the metastable stretching vibration of the Mn-O bond in the manganese oxides is more favorable for the movement of oxygen species to take part in oxidation process of toluene.

2.3.4 TEM and HRTEM results of the prepared MnO_x catalysts

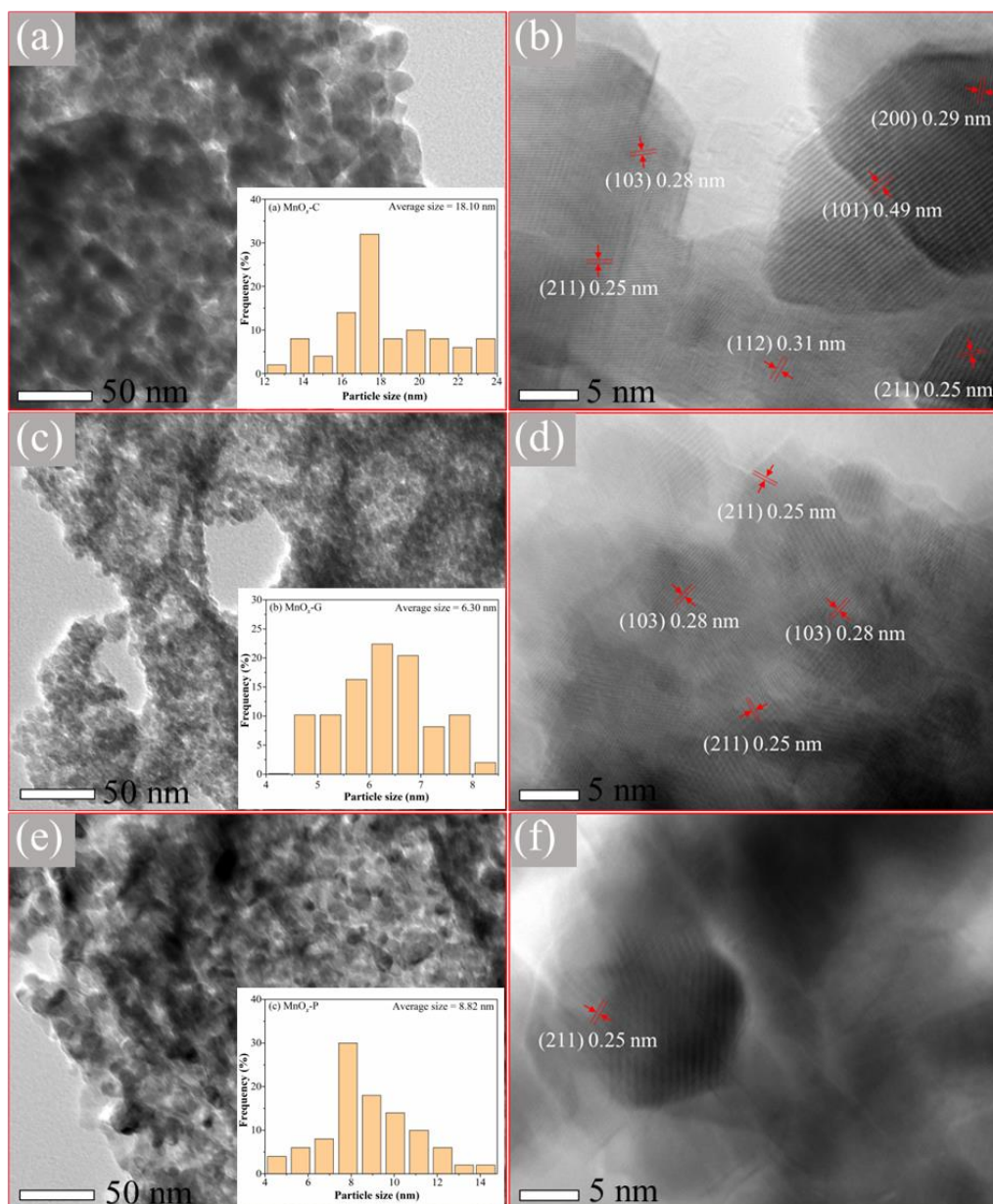


Fig. 2.4. TEM and HRTEM images of $\text{MnO}_x\text{-C}$ (a, b), $\text{MnO}_x\text{-G}$ (c, d) and $\text{MnO}_x\text{-P}$ (e, f) catalysts (inset: grain size distributions).

The TEM and HRTEM results observed in Fig. 2.4 present the microscopic lattice structure of prepared catalysts deeply. As shown in Fig. 2.4a, $\text{MnO}_x\text{-C}$ sample exhibits an irregular polygonal stacking structure with an average grain size of ca. 18.1 nm. Furthermore, several well-defined lattice fringes can be also observed in the HRTEM image of $\text{MnO}_x\text{-C}$ (Fig. 2.4b), which are consistent with the (200), (103), (101), (211), (112) and (211) crystal planes of Mn_3O_4 phase detected in XRD pattern, indicating the good crystalline of $\text{MnO}_x\text{-C}$ structure derived from the citric acid-driven sol-gel method

[41]. The TEM image of $\text{MnO}_x\text{-G}$ shown in Fig. 2.4c also displays the granular accumulation but a smaller grain size than that of $\text{MnO}_x\text{-C}$ sample, and only two characteristic (211) and (103) crystal planes of Mn_3O_4 phase are found on its HRTEM image (Fig. 2.4d), which echoes the weaker XRD characteristic diffraction peaks discussed in Section 2.3.3. As expected, a crystal structure of packing of smaller grains is also shown in the TEM results (Fig. 2.4e) of $\text{MnO}_x\text{-P}$ sample. In addition, a unique (211) crystal plane of Mn_3O_4 phase is found on HRTEM image (Fig. 2.4f). It can be considered that the hydrolysis in chelation process of pectin has a great effect on the electron cloud around metal atom, and the combustion process accompanied by organic steric hindrance can regulate the interatomic interactions, thereby hindering the formation of long-range ordered crystals and resulting the generation of a large number of amorphous structures. In the field of catalytic oxidation of VOCs, low crystallinity or amorphous manganese oxide is usually accompanied by sufficient defect species and Mn^{3+} species (as discussed in Section 2.3.7), which play an important role in the adsorption and activation of gas-phase oxygen to participate in the oxidation of VOCs.

2.3.5 Reducibility analysis

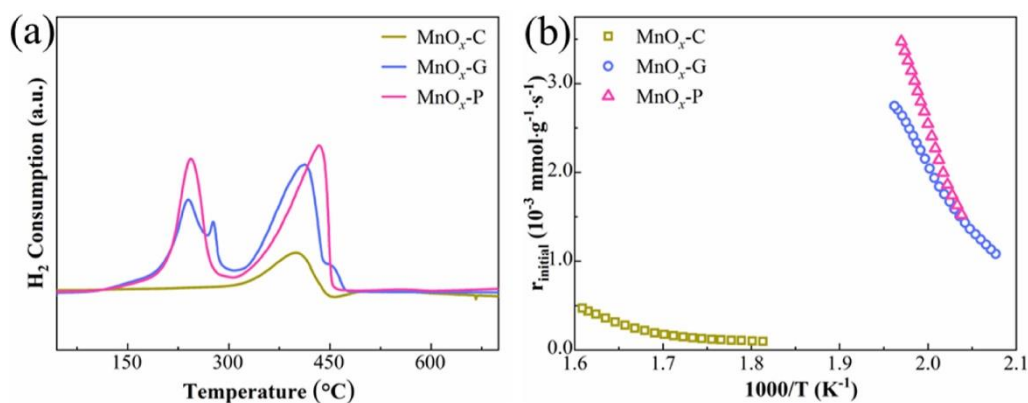


Fig. 2.5. (a) H_2 -TPR profiles and (b) initial H_2 consumption rates of the prepared MnO_x catalysts.

The reducibility of the prepared MnO_x catalysts was evaluated by H_2 -TPR analysis and the related H_2 consumption (H_C) results are displayed in Fig. 2.5a and Table 2.2. As displayed in Fig. 2.5a, different reduction peaks are observed on different catalysts, which correspond to the different reducibility of catalysts synthesized by different sol-gel methods. Notably, only a high-temperature reduction peak at ca. 400 $^{\circ}\text{C}$ is found for

the MnO_x-C catalyst on account of its high crystallinity, which is attributed to the reduction of Mn₃O₄ to MnO species [41, 42]. Whereas, the MnO_x-G catalyst exhibits three main reduction processes centered at ca. 240, 277 and 434 °C, corresponding to the three-step reduction processes of Mn⁴⁺ → Mn³⁺ → Mn^{8/3+} → Mn²⁺ [43, 44]. For the MnO_x-P catalyst, two distinct reduction peaks at 242 and 434 °C can be assigned to the reduction processes of MnO₂/Mn₂O₃ → Mn₃O₄ → MnO [45, 46]. Apparently, the low temperature reduction peaks (< 300 °C) found on the MnO_x-G and MnO_x-C catalysts are the characteristics of their excellent reducibility. Notably, compared with MnO_x-G catalyst, the low-temperature reduction peak of MnO_x-C catalyst exhibits a one-step reduction process, indicating a more homogeneous catalyst structure synthesized by the pectin-driven sol-gel route. It can be considered that the homogeneous MnO_x-C catalyst came from the uniform dispersion of macromolecular chain polymers, which cannot be realized in small molecule glycine. Furthermore, the initial H₂ consumption rates (*r*_{initial}) of the prepared MnO_x catalysts shown in Fig. 2.5b also confirm the excellent low temperature H₂ consumption capacity of MnO_x-P catalyst. In addition, the low-temperature H₂ consumption (*H*_L), high-temperature H₂ consumption (*H*_H) and total H₂ consumption (*H*_T) of the catalysts determined from the peak areas are summarized in Table 2.2, and the three indicators follow the same decreasing order, i.e., MnO_x-P > MnO_x-G > MnO_x-C. Therefore, the MnO_x-P catalyst synthesized by the pectin-driven sol-gel method exhibits the best low-temperature as well as high-temperature reducibility, which should be attributed to the special physical and chemical regulations to the catalyst from the chelation and the combustion processes of pectin.

2.3.6 Oxygen mobility analysis

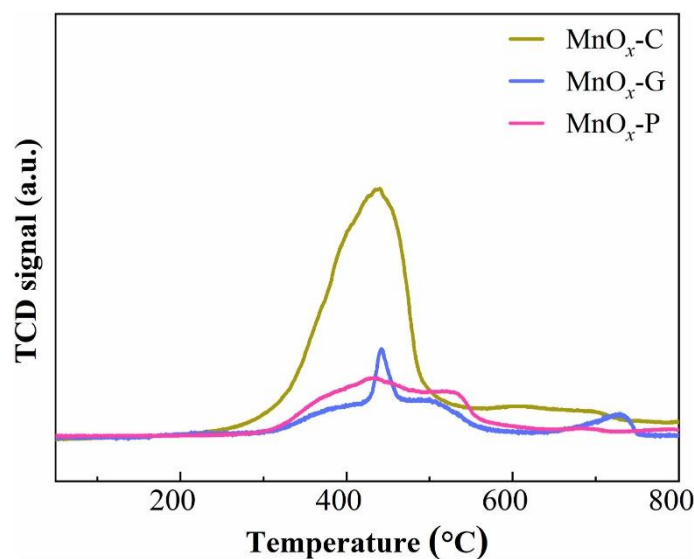


Fig. 2.6. O₂-TPD profiles of prepared MnO_x samples.

From the O₂-TPD curves shown in Fig. 2.6 and desorption amounts of oxygen species summarized in Table 2.2, the oxygen mobility of prepared MnO_x catalysts could be assessed. It is evident that the MnO_x-C catalyst exhibits the lowest initial desorption temperature and the largest desorption amounts of oxygen (0.78 mmol·g⁻¹). While, MnO_x-P catalyst exhibits a lower desorption temperature and a larger amount of oxygen desorption (0.25 mmol·g⁻¹) than that of MnO_x-G catalyst (0.22 mmol·g⁻¹). Therefore, MnO_x catalysts with different oxygen mobility can be constructed by different sol-gel methods, and the MnO_x-C and MnO_x-P catalysts derived from citric acid and pectin chelating agent have stronger oxygen mobilities, which would be more conducive to the oxygen delivery and replenishment in toluene oxidation process [47-49].

2.3.7 Surface composition and oxidation state

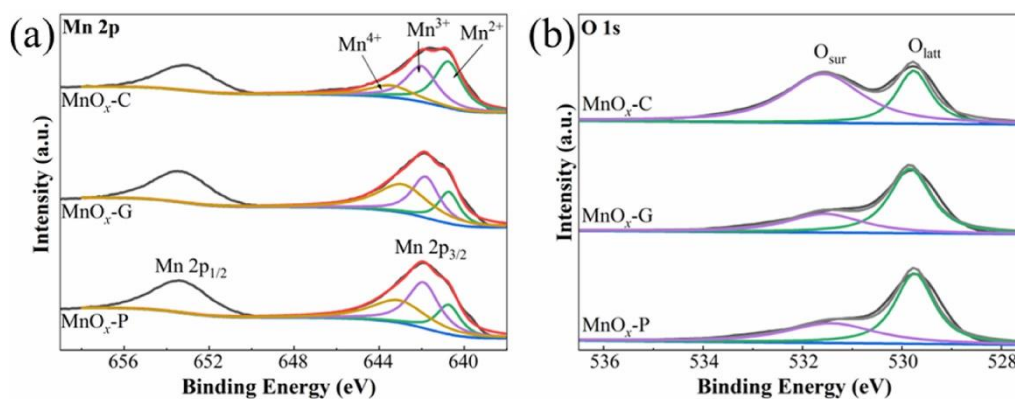


Fig. 2.7. XPS spectra of Mn 2p (a) and O 1s (b) for the prepared catalysts.

Fig. 2.7 shows the Mn 2p, O 1s XPS spectra of three catalysts and the corresponding species proportions are listed in Table 2.2. As shown in Fig. 2.7a, all Mn 2p spectra consist of Mn 2p_{1/2} (653.2 ± 0.2 eV) and Mn 2p_{3/2} (641.6 ± 0.2 eV) signals, and the latter can be fitted into three components including Mn⁴⁺ (643.3 ± 0.2 eV), Mn³⁺ (642.0 ± 0.1 eV) and Mn²⁺ (640.7 ± 0.1 eV) species [50, 51]. It is well known that the valence state of manganese has a great influence on the catalytic performance of VOCs. Therefore, the proportions of different manganese species were calculated by integrating the deconvoluted peak areas and presented in Table 2.2. It can be seen that MnO_x-P catalyst exhibits the highest Mn³⁺ content (42.8%) compared to the other two catalysts. In addition, the contents of Mn⁴⁺ in MnO_x-G (44.7%) and MnO_x-P (36.5%) catalysts are much higher than that in MnO_x-C (18.2%) sample. During the oxidation of VOC over manganese-based catalysts, the presence of Mn³⁺ species is always accompanied by the generation of oxygen vacancies, which is of great significance for the adsorption and activation of oxygen molecules [52]. Furthermore, the Mn⁴⁺ species in catalyst can enhance the low temperature reducibility and accelerate the deep oxidation of VOCs. Thus, MnO_x-P from pectin-driven sol-gel route should exhibit excellent catalytic toluene performance by virtue of its abundant Mn³⁺ and Mn⁴⁺ species. As shown in Fig. 2.7b, the O 1s spectra of all catalysts can be deconvoluted into two components at 529.7 ± 0.1 eV and 531.5 ± 0.1 eV, attributing to lattice oxygen (O_{latt}) and surface adsorbed oxygen (O_{sur}) [49]. Generally, electrophilic surface-adsorbed oxygen always plays an important role in the catalytic oxidation of VOCs [48]. However, from the calculation results shown in Table 2.2, it is found that the order of surface oxygen content is not completely consistent with the order of activities (Section 2.3.8), which can be attributed to the disadvantages of MnO_x-C in other aspects, such as small specific surface area and poor low-temperature reducibility.

Table 2.2 The results of H₂-TPR, O₂-TPD, normalized reaction rate, and apparent activation energy for prepared MnO_x catalysts.

Sample	H _c (mmol·g ⁻¹) ^a			O _D (mmol·g ⁻¹) ^a	Surface species ratio ^b			r*×10 ⁷ ^c (mol·m ⁻² ·s ⁻¹)	E _a ^d (kJ·mol ⁻¹)
	H _L	H _H	H _T		Mn ³⁺ /ΣMn ⁿ⁺	Mn ⁴⁺ /ΣMn ⁿ⁺	O _{sur} /(O _{sur} +O _{latt})		
MnO _x -C	/	0.63	0.63	0.78	37.5	18.2	67.7	3.8	173.7

MnO _x -G	0.93	1.43	2.36	0.21	34.9	44.7	34.6	2.6	75.3
MnO _x -P	0.98	1.45	2.43	0.25	42.8	36.5	39.3	4.7	57.2

^a Calculated based on the characteristic peak area. ^b Obtained from peak area of deconvolution and $\sum \text{Mn}^{n+}$ means the sum of surface Mn^{4+} , Mn^{3+} and Mn^{2+} species. ^c Normalized reaction rate at 240 °C. ^d Obtained from Arrhenius plot slopes.

2.3.8 Catalytic performances and dynamics results

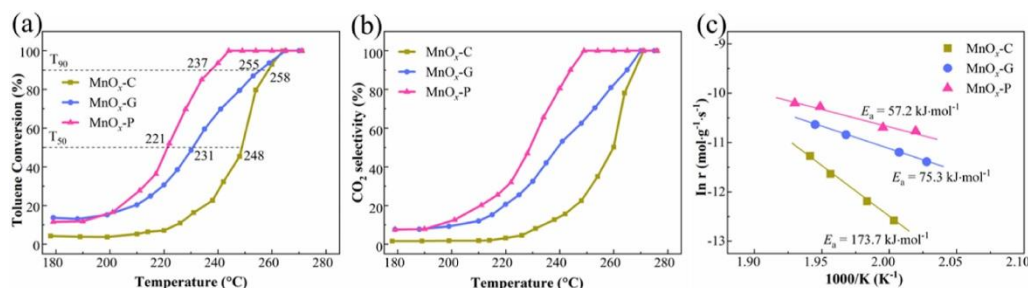


Fig. 2.8. Catalytic activity for toluene combustion (a), CO₂ selectivity and (b) Arrhenius plots (c) over the prepared MnO_x catalysts.

The catalytic performances of the prepared MnO_x catalysts for toluene combustion and the corresponding CO₂ selectivity are shown in Fig. 2.8a and b, respectively. One can see from Fig. 2.7a that the activity profiles over all the prepared catalysts increase with the reaction temperature increase, indicating the improved catalytic activity with the increased temperature. Obviously, the MnO_x-P catalyst exhibits the best catalytic toluene combustion performance due to its lowest T₅₀ (221 °C, temperature with 50% toluene conversion) and T₉₀ (237 °C, temperature with 90% toluene conversion) values. The MnO_x-G catalyst exhibits moderate T₅₀ (231 °C) and T₉₀ (255 °C) values, indicating its ordinary catalytic performance. The MnO_x-C catalyst with the worst catalytic performance exhibits the highest T₅₀ (248 °C) and T₉₀ (258 °C) values. The CO₂ selectivity trend with the increase of temperature (Fig. 2.8b) is consistent with the toluene conversion, but some temperature delays are observed due to the preferential formation of intermediates during toluene oxidation [53, 54]. Furthermore, as can be seen from the Arrhenius plots illustrated in Fig. 2.8c, E_a of toluene oxidation on the catalysts follows the same decreased order as T₉₀ and T₅₀, i.e, MnO_x-C (173.7 kJ·mol⁻¹) > MnO_x-G (75.3 kJ·mol⁻¹) > MnO_x-P (57.2 kJ·mol⁻¹), which indicates the different activation abilities of toluene on different MnO_x catalysts, and the activation on MnO_x-

P catalyst occurs more easily due to the lowest energy required [55]. Moreover, the largest normalized reaction rate ($4.7 \times 10^{-7} \text{ mol} \cdot \text{m}^{-2} \cdot \text{s}^{-1}$) shown in Table 2.2 also indicates the higher intrinsic reaction efficiency of the $\text{MnO}_x\text{-P}$ catalyst. On the one hand, it can be considered that the special hierarchical mesoporous structure constructed by the pectin-driven sol-gel method can optimize the adsorption and mass transfer process of toluene molecules. While, the special thermal regulation of pectin from the calcination process can lead to better low temperature reducibility, more active species and more satisfactory oxygen mobility in the $\text{MnO}_x\text{-P}$ catalyst, thereby improving intrinsic catalytic performance for toluene combustion.

2.3.9 Pectin usage effect, catalytic stability and water vapor effect

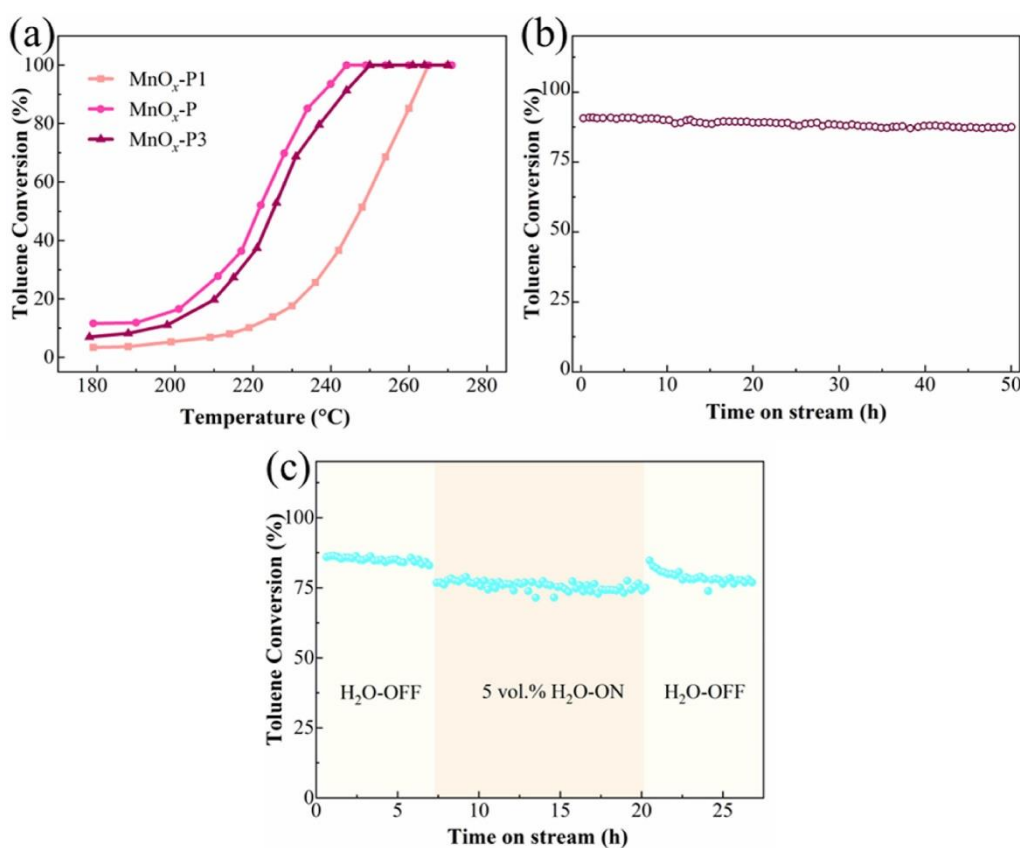


Fig. 2.9. Effect of pectin dosage (a), durability experiments at 237 °C for 50 h (b), and the influence of 5 vol.% water vapor at 234 °C (c) on the catalytic performance over MnO_x catalyst synthesized by pectin-driven sol-gel route.

The effect of different amounts of pectin used in the catalyst synthesis on the catalytic performance was evaluated (Fig. 2.9a). Obviously, either increasing ($\text{MnO}_x\text{-P3}$) or decreasing ($\text{MnO}_x\text{-P1}$) the pectin usage would result in a lower catalytic performance

than that of the $\text{MnO}_x\text{-P}$ catalyst. Therefore, in this study, the usage amount of 2 g pectin is the optimal usage amount that can balance the catalytic performance and resource saving factor. To evaluate the durability of the catalyst, the catalytic combustion reaction of 1,000 ppm toluene on $\text{MnO}_x\text{-P}$ catalyst was held constant at 237 °C for 50 h and the evaluation results are shown in Fig. 2.9b. It is found that the conversion of toluene gradually reduces with the prolongation of the reaction time, and the conversion after 50 h reaction only decreases by about 4%, indicating a better long-time stability. In practice, VOCs emissions are always accompanied by some water vapor, and thus the water resistance of catalysts is of great significance in practical applications. Therefore, by introducing 5 vol.% water vapor into 1,000 ppm toluene feed gas, the water resistance of the optimal $\text{MnO}_x\text{-P}$ catalyst was tested (Fig. 2.9c). Firstly, the toluene conversion is stabilized at around 85% by a continued catalytic reaction at 234 °C for 7 h. After that, the toluene conversion decreases by about 10% after the introduction of 5 vol.% water vapor into the reaction gas. However, when the water vapor is removed after the reaction is continued for ca. 20 h, the toluene conversion is recovered largely, which indicates a better water resistance of $\text{MnO}_x\text{-P}$ catalyst.

2.4 Conclusions

In summary, $\text{MnO}_x\text{-C}$, $\text{MnO}_x\text{-G}$ and $\text{MnO}_x\text{-P}$ catalysts were successfully synthesized by sol-gel process using citric acid, glycine and pectin chelating pore formers, respectively. SEM and N_2 adsorption-desorption results showed that different chelating agents resulted in different pore volumes and pore distributions in the catalysts, among which a hierarchical mesoporous structure with various pore distributions was formed in the $\text{MnO}_x\text{-P}$. HRTEM and XRD results indicated that different chelating agents caused differences in the crystallinity and grain size of MnO_x catalysts, and the $\text{MnO}_x\text{-P}$ catalyst exhibited the lowest crystallinity (28.5%) as well as smaller grain size (8.8 nm), which are attributed to the inhibition effect to long-range ordered crystals from the pectin chelation and combustion processes. In addition, this low crystallinity and small grain size are always accompanied by better oxygen mobility and abundant defect structures, which are very beneficial to the improvement of catalytic performance. According to the $\text{H}_2\text{-TPR}$ and initial H_2 consumption rate

results, the $\text{MnO}_x\text{-P}$ catalyst exhibited excellent low- temperature reducibility as well as the largest hydrogen consumption rate and initial hydrogen consumption rate, which are closely related to its abundant reducible active species. $\text{O}_2\text{-TPD}$ analysis confirmed the satisfactory oxygen mobility of $\text{MnO}_x\text{-P}$ catalyst, which is important for oxygen species to take part in the toluene combustion process. In addition, the $\text{MnO}_x\text{-P}$ catalyst exhibited excellent long-time stability and water tolerance. Therefore, the synthesis of metal oxide catalyst materials by the pectin-driven sol-gel method is a facile, novel, green and potential material synthesis route.

References

- [1] C. He, J. Cheng, X. Zhang, M. Douthwaite, S. Patisson, Z. Hao, Recent Advances in the Catalytic Oxidation of Volatile Organic Compounds: A Review Based on Pollutant Sorts and Sources, *Chem. Rev.*, 119 (2019) 4471-4568.
- [2] Y. Guo, M. Wen, G. Li, T. An, Recent advances in VOC elimination by catalytic oxidation technology onto various nanoparticles catalysts: a critical review, *Appl. Catal. B: Environ.*, 281 (2021) 119447.
- [3] J. González-Prior, R. López-Fonseca, J.I. Gutiérrez-Ortiz, B. de Rivas, Catalytic removal of chlorinated compounds over ordered mesoporous cobalt oxides synthesised by hard-templating, *Appl. Catal. B: Environ.*, 222 (2018) 9-17.
- [4] S. Xie, Y. Liu, J. Deng, X. Zhao, J. Yang, K. Zhang, Z. Han, H. Arandian, H. Dai, Effect of transition metal doping on the catalytic performance of Au-Pd/3DOM Mn_2O_3 for the oxidation of methane and o-xylene, *Appl. Catal. B: Environ.*, 206 (2017) 221-232.
- [5] L. Zhao, Z. Zhang, Y. Li, X. Leng, T. Zhang, F. Yuan, X. Niu, Y. Zhu, Synthesis of Ce_aMnO_x hollow microsphere with hierarchical structure and its excellent catalytic performance for toluene combustion, *Appl. Catal. B: Environ.*, 245 (2019) 502-512.
- [6] P. Yang, S. Yang, Z. Shi, Z. Meng, R. Zhou, Deep oxidation of chlorinated VOCs over CeO_2 -based transition metal mixed oxide catalysts, *Appl. Catal. B: Environ.*, 162 (2015) 227-235.
- [7] P. Liu, H. He, G. Wei, X. Liang, F. Qi, F. Tan, W. Tan, J. Zhu, R. Zhu, Effect of Mn substitution on the promoted formaldehyde oxidation over spinel ferrite: Catalyst characterization, performance and reaction mechanism, *Appl. Catal. B: Environ.*, 182 (2016) 476-484.
- [8] Z. Ye, J.M. Giraudon, N. Nuns, P. Simon, N. De Geyter, R. Morent, J.F. Lamonier, Influence of the preparation method on the activity of copper-manganese oxides for toluene total oxidation, *Appl. Catal. B: Environ.*, 223 (2018) 154-166.
- [9] L. Yu, R. Peng, L. Chen, M. Fu, J. Wu, D. Ye, Ag supported on CeO_2 with different morphologies for the catalytic oxidation of HCHO, *Chem. Eng. J.*, 334 (2018) 2480-2487.

- [10] G. Li, C. Zhang, Z. Wang, H. Huang, H. Peng, X. Li, Fabrication of mesoporous Co_3O_4 oxides by acid treatment and their catalytic performances for toluene oxidation, *Appl. Catal. A: Gen.*, 550 (2018) 67-76.
- [11] H. Yi, Z. Yang, X. Tang, S. Zhao, F. Gao, J. Wang, Y. Huang, Y. Ma, C. Chu, Q. Li, J. Xu, Promotion of low temperature oxidation of toluene vapor derived from the combination of microwave radiation and nano-size Co_3O_4 , *Chem. Eng. J.*, 333 (2018) 554-563.
- [12] B. Solsona, T. García, R. Sanchis, M.D. Soriano, M. Moreno, E. Rodríguez-Castellón, S. Agouram, A. Dejoz, J.M. López Nieto, Total oxidation of VOCs on mesoporous iron oxide catalysts: Soft chemistry route versus hard template method, *Chem. Eng. J.*, 290 (2016) 273-281.
- [13] H. Wang, W. Guo, Z. Jiang, R. Yang, Z. Jiang, Y. Pan, W. Shangguan, New insight into the enhanced activity of ordered mesoporous nickel oxide in formaldehyde catalytic oxidation reactions, *J. Catal.*, 361 (2018) 370-383.
- [14] X. Zheng, J. Cai, Y. Cao, L. Shen, Y. Zheng, F. Liu, S. Liang, Y. Xiao, L. Jiang, Construction of cross-linked $\delta\text{-MnO}_2$ with ultrathin structure for the oxidation of H_2S : Structure-activity relationship and kinetics study, *Appl. Catal. B: Environ.*, 297 (2021) 120402.
- [15] Y. Wei, L. Ni, M. Li, J. Zhao, A template-free method for preparation of MnO_2 catalysts with high surface areas, *Catal. Today*, 297 (2017) 188-192.
- [16] D. Li, X. Wu, Y. Chen, Synthesis of Hierarchical Hollow MnO_2 Microspheres and Potential Application in Abatement of VOCs, *J. Phys. Chem. C*, 117 (2013) 11040-11046.
- [17] F. Hu, J. Chen, Y. Peng, H. Song, K. Li, J. Li, Novel nanowire self-assembled hierarchical CeO_2 microspheres for low temperature toluene catalytic combustion, *Chem. Eng. J.*, 331 (2018) 425-434.
- [18] T. Chang, Z. Wang, H. An, F. Li, W. Xue, Y. Wang, Morphology effects of CeO_2 for catalytic oxidation of formaldehyde, *J. Environ. Chem. Eng.*, 10 (2022) 108053.
- [19] L. Wang, Y. Wang, Y. Zhang, Y. Yu, H. He, X. Qin, B. Wang, Shape dependence of nanocerium on complete catalytic oxidation of o-xylene, *Catal. Sci. Technol.*, 6 (2016)

4840-4848.

[20] X. Zhang, X. Lv, F. Bi, G. Lu, Y. Wang, Highly efficient Mn_2O_3 catalysts derived from Mn-MOFs for toluene oxidation: The influence of MOFs precursors, *Mol. Catal.*, 482 (2020) 110701.

[21] X. Yang, X. Yu, M. Lin, X. Ma, M. Ge, Enhancement effect of acid treatment on Mn_2O_3 catalyst for toluene oxidation, *Catal. Today*, 327 (2019) 254-261.

[22] W. Gu, C. Li, J. Qiu, J. Yao, Facile fabrication of flower-like MnO_2 hollow microspheres as high-performance catalysts for toluene oxidation, *J. Hazard. Mater.*, 408 (2021) 124458.

[23] J. Yang, L. Li, X. Yang, S. Song, J. Li, F. Jing, W. Chu, Enhanced catalytic performances of in situ-assembled $\text{LaMnO}_3/\delta\text{-MnO}_2$ hetero-structures for toluene combustion, *Catal. Today*, 327 (2019) 19-27.

[24] M.H. Castaño, R. Molina, S. Moreno, Effect of Mg and Al on manganese oxides as catalysts for VOC oxidation, *Mol. Catal.*, 443 (2017) 117-124.

[25] Y. Zheng, Q. Liu, C. Shan, Y. Su, K. Fu, S. Lu, R. Han, C. Song, N. Ji, D. Ma, Defective Ultrafine MnO_x Nanoparticles Confined within a Carbon Matrix for Low-Temperature Oxidation of Volatile Organic Compounds, *Environ. Sci. Technol.*, 55 (2021) 5403-5411.

[26] T. Pan, H. Deng, S. Kang, H. He, A simple strategy to tune $\alpha\text{-MnO}_2$ and enhance VOC oxidation via precipitation rate control, *Appl. Surf. Sci.*, 576 (2022) 151823.

[27] Z. Huang, J. Zhao, Z. Song, W. Liu, X. Zhang, Y. Mao, H. Zhao, M. Zhao, S. Liu, Z. Wang, Controllable construction of Ce-Mn- O_x with tunable oxygen vacancies and active species for toluene catalytic combustion, *Appl. Organomet. Chem.*, 34 (2020) e5958.

[28] S. Mo, Q. Zhang, J. Li, Y. Sun, Q. Ren, S. Zou, Q. Zhang, J. Lu, M. Fu, D. Mo, J. Wu, H. Huang, D. Ye, Highly efficient mesoporous MnO_2 catalysts for the total toluene oxidation: Oxygen-Vacancy defect engineering and involved intermediates using in situ DRIFTS, *Appl. Catal. B: Environ.*, 264 (2020) 118464.

[29] H. Chen, J. Li, W. Cui, Z. Fei, Q. Tian, Q. Liu, X. Chen, M. Cui, Z. Zhang, J. Tang, X. Qiao, Precise fabrication of surface-reconstructed LaMnO_3 perovskite with

- enhanced catalytic performance in CH₄ oxidation, *Appl. Surf. Sci.*, 505 (2020) 144112.
- [30] P. Yang, S. Fan, Z. Chen, G. Bao, S. Zuo, C. Qi, Synthesis of Nb₂O₅ based solid superacid materials for catalytic combustion of chlorinated VOCs, *Appl. Catal. B: Environ.*, 239 (2018) 114-124.
- [31] Z. Cheng, Z. Chen, J. Li, S. Zuo, P. Yang, Mesoporous silica-pillared clays supported nanosized Co₃O₄-CeO₂ for catalytic combustion of toluene, *Appl. Surf. Sci.*, 459 (2018) 32-39.
- [32] M.T. Nguyen Dinh, C.C. Nguyen, T.L. Truong Vu, V.T. Ho, Q.D. Truong, Tailoring porous structure, reducibility and Mn⁴⁺ fraction of ε-MnO₂ microcubes for the complete oxidation of toluene, *Appl. Catal. A: Gen.*, 595 (2020) 117473.
- [33] X. Zhang, H. Zhao, Z. Song, W. Liu, J. Zhao, Z.a. Ma, M. Zhao, Y. Xing, Insight into the effect of oxygen species and Mn chemical valence over MnO_x on the catalytic oxidation of toluene, *Appl. Surf. Sci.*, 493 (2019) 9-17.
- [34] X. Lin, S. Li, H. He, Z. Wu, J. Wu, L. Chen, D. Ye, M. Fu, Evolution of oxygen vacancies in MnO_x-CeO₂ mixed oxides for soot oxidation, *Appl. Catal. B: Environ.*, 223 (2018) 91-102.
- [35] Y. Wang, D. Yang, S. Li, L. Zhang, G. Zheng, L. Guo, Layered copper manganese oxide for the efficient catalytic CO and VOCs oxidation, *Chem. Eng. J.*, 357 (2019) 258-268.
- [36] Y. Luo, Y. Zheng, J. Zuo, X. Feng, X. Wang, T. Zhang, K. Zhang, L. Jiang, Insights into the high performance of Mn-Co oxides derived from metal-organic frameworks for total toluene oxidation, *J. Hazard. Mater.*, 349 (2018) 119-127.
- [37] P. Wang, J. Wang, X. An, J. Shi, W. Shangguan, X. Hao, G. Xu, B. Tang, A. Abudula, G. Guan, Generation of abundant defects in Mn-Co mixed oxides by a facile agar-gel method for highly efficient catalysis of total toluene oxidation, *Appl. Catal. B: Environ.*, 282 (2021) 119560.
- [38] C.-W. Ahn, Y.-W. You, I. Heo, J.S. Hong, J.-K. Jeon, Y.-D. Ko, Y. Kim, H. Park, J.-K. Suh, Catalytic combustion of volatile organic compound over spherical-shaped copper-manganese oxide, *J. Ind. Eng. Chem.*, 47 (2017) 439-445.
- [39] B. Wang, C. Chi, M. Xu, C. Wang, D. Meng, Plasma-catalytic removal of toluene

over CeO₂-MnO_x catalysts in an atmosphere dielectric barrier discharge, Chem. Eng. J., 322 (2017) 679-692.

[40] H. He, X. Lin, S. Li, Z. Wu, J. Gao, J. Wu, W. Wen, D. Ye, M. Fu, The key surface species and oxygen vacancies in MnO_x(0.4)-CeO₂ toward repeated soot oxidation, Appl. Catal. B: Environ., 223 (2018) 134-142.

[41] H. Pan, Y. Jian, C. Chen, C. He, Z. Hao, Z. Shen, H. Liu, Sphere-Shaped Mn₃O₄ Catalyst with Remarkable Low-Temperature Activity for Methyl-Ethyl-Ketone Combustion, Environ. Sci. Technol., 51 (2017) 6288-6297.

[42] P. Wang, J. Wang, J. Zhao, X. Ma, X. Du, S. Peng, X. Hao, B. Tang, A. Abudula, G. Guan, Trace holmium assisting delaminated OMS-2 catalysts for total toluene oxidation at low temperature, J. Colloid Interf. Sci., 15 (2022) 1662-1675.

[43] X. Li, J. Zheng, S. Liu, T. Zhu, A novel wormhole-like mesoporous hybrid MnCoO_x catalyst for improved ethanol catalytic oxidation, J. Colloid Interf. Sci., 555 (2019) 667-675.

[44] X. Xu, P. Wang, W. Xu, J. Wu, L. Chen, M. Fu, D. Ye, Plasma-catalysis of metal loaded SBA-15 for toluene removal: Comparison of continuously introduced and adsorption-discharge plasma system, Chem. Eng. J., 283 (2016) 276-284.

[45] J. Zhao, P. Wang, C. Liu, Q. Zhao, J. Wang, L. Shi, G. Xu, A. Abudula, G. Guan, Nanosheet-state cobalt-manganese oxide with multifarious active regions derived from oxidation-etching of metal organic framework precursor for catalytic combustion of toluene, J. Colloid Interf. Sci., 629 (2022) 706-722.

[46] Z. Hou, J. Feng, T. Lin, H. Zhang, X. Zhou, Y. Chen, The performance of manganese-based catalysts with Ce_{0.65}Zr_{0.35}O₂ as support for catalytic oxidation of toluene, Appl. Surf. Sci., 434 (2018) 82-90.

[47] C. Dong, Z. Qu, Y. Qin, Q. Fu, H. Sun, X. Duan, Revealing the Highly Catalytic Performance of Spinel CoMn₂O₄ for Toluene Oxidation: Involvement and Replenishment of Oxygen Species Using In Situ Designed-TP Techniques, ACS Catal., 9 (2019) 6698-6710.

[48] W. Pei, Y. Liu, J. Deng, K. Zhang, Z. Hou, X. Zhao, H. Dai, Partially embedding Pt nanoparticles in the skeleton of 3DOM Mn₂O₃: An effective strategy for enhancing

- catalytic stability in toluene combustion, *Appl. Catal. B: Environ.*, 256 (2019) 117814.
- [49] P. Wang, J. Zhao, Q. Zhao, X. Ma, X. Du, X. Hao, B. Tang, A. Abudula, G. Guan, Microwave-assisted synthesis of manganese oxide catalysts for total toluene oxidation, *J. Colloid Interf. Sci.*, 607 (2021) 100-110.
- [50] M. Piumetti, D. Fino, N. Russo, Mesoporous manganese oxides prepared by solution combustion synthesis as catalysts for the total oxidation of VOCs, *Appl. Catal. B: Environ.*, 163 (2015) 277-287.
- [51] W. Tang, X. Wu, D. Li, Z. Wang, G. Liu, H. Liu, Y. Chen, Oxalate route for promoting activity of manganese oxide catalysts in total VOCs' oxidation: effect of calcination temperature and preparation method, *J. Mater. Chem. A*, 2 (2014) 2544-2554.
- [52] C. Dong, Z. Qu, X. Jiang, Y. Ren, Tuning oxygen vacancy concentration of MnO₂ through metal doping for improved toluene oxidation, *J. Hazard. Mater.*, 391 (2020) 122181.
- [53] X. Yang, X. Ma, X. Yu, M. Ge, Exploration of strong metal-support interaction in zirconia supported catalysts for toluene oxidation, *Appl. Catal. B: Environ.*, 263 (2020) 118355.
- [54] L. Zhang, S. Zhu, R. Li, W. Deng, C. Hong, D. Liu, L. Guo, Ag-Doped δ -MnO₂ Nanosheets as Robust Catalysts for Toluene Combustion, *ACS Appl. Nano Mater.*, 3 (2020) 11869-11880.
- [55] R. Peng, X. Sun, S. Li, L. Chen, M. Fu, J. Wu, D. Ye, Shape effect of Pt/CeO₂ catalysts on the catalytic oxidation of toluene, *Chem. Eng. J.*, 306 (2016) 1234-1246.

CHAPTER 3 Nanosheet-state cobalt-manganese oxide with multifarious active regions derived from oxidation- etching of metal organic framework precursor for catalytic combustion of toluene

3.1 Introduction

As a type of typical gaseous pollutants, volatile organic compounds (VOCs) have a wide range of outdoor and indoor emission sources, such as chemical industrial process, automobile transportation, necessities manufacturing and other human daily activities [1, 2]. Their substandard emissions could lead to the formations of inhalable particles, tropospheric ozone and photochemical smog, which seriously threaten the environmental quality and public health due to their highly toxic, mutagenic effects and carcinogenic properties [3, 4]. Many physical and chemical VOCs treatment technologies including incineration, biodegradation, adsorption, membrane separation, wet scrubbing, plasma process, photocatalysis and catalytic oxidation have been developed [5, 6]. Among them, catalytic combustion of VOCs has attracted wide attention because of its high efficiency, low cost, non-secondary pollution and low operating temperature [7, 8]. However, the development of high-efficiency catalysts is the key for the catalytic combustion.

Supported noble metal catalysts such as Pt, Au and Pd based catalysts [9, 10], transition metal (e.g., Mn, Co, Fe and Cu) and rare-earth metal based catalysts (e.g., Ce and La) [11-14], have been proven to be effective for VOCs combustion. Although the noble based ones always exhibit better catalytic performance, its practical application is always limited by its high cost, low reserve and low thermal stability [7]. In recent years, it is found that the doped transition and rare-earth metal catalysts such as MnFe [15], MnNi [16], NbTi [17], CeCo [18], CoCu [19], and CoNi [20] generally exhibit better catalytic performance than single metal based ones. Among them, Mn-based catalysts always exhibit excellent performance due to their polymorphism and

polyvalence. Tang et al. [16] synthesized hierarchical porous Mn-Ni based composite materials successfully using an oxalic acid route, which showed larger specific surface area (SSA) and more surface-adsorbed oxygen species than those synthesized by the traditional coprecipitation method, thereby exhibiting high low-temperature catalytic performance for the combustion of benzene. Ahn et al. [21] prepared MnCu mixed oxide materials by a wet granulation way. It was found that the amorphous structure formed by the low-temperature calcination resulted in excellent low temperature reducibility with high catalytic performance. Dong et al. [22] synthesized nanoflower-type spinel structure CoMn_2O_4 using a sol-gel method with oxalic acid, which possessed lower activation energy in toluene combustion. In addition, it had more oxygen vacancies, larger SSA, and higher oxygen mobility so that it had excellent catalytic ability for toluene combustion. Wang et al. [23] synthesized a CoMn_xO_y catalyst using a redox coprecipitation driving method. The results showed that the gaseous oxygen could be effectively adsorbed by the phase interface and activated to generate electrophilic species ($\text{O}^\cdot/\text{O}_2^\cdot$), which was very important for the catalytic combustion of toluene. Thus, on the one hand, a larger SSA is critical to the catalytic performance since it is directly related to the exposure of more active sites with higher adsorption efficiency of VOCs on the catalysts. On the other hand, the homogeneous amorphous structure fabricated by various transition metal elements and the existence of phase interfaces or oxygen vacancies in the materials also tend to improve the catalytic performance. However, besides the large SSA, catalytic materials simultaneously possessing a large number of the above-described multiple active structures/species were rarely reported.

Recently, metal organic framework (MOF) materials with a special three-dimensional (3D) structure have been used as the precursors of VOC combustion catalysts. Zhao et al. [24] applied a MOF template strategy to prepare a kind of Mn-Co mixed oxide catalyst with a dual-shell nanocage structure, which had higher lattice oxygen mobility with more active Co^{3+} sites, thereby benefitting for the catalytic combustion of toluene. Luo et al. [25] also synthesized a kind of Mn-Co mixed oxide catalyst by calcining of the MOF precursor, which achieved a uniform dispersion of Mn

and Co species, however, exhibited a mediocre toluene catalytic performance with poor water resistance since it had fewer active species. Hence, it is important to enhance the interaction between mixed elements to build abundant active regions or species to improve catalytic performance for the MOF-derived catalysts.

Inspired by the homogeneous active species/structures in the catalysts prepared by the sacrificial MOF template method, in this study, a strategy by oxidation-etching assembly of MOF precursor (shown in Scheme 3.1), a kind of nanosheet-state CoMnx mixed oxide catalyst with multifarious active regions and abundant active species was successfully synthesized. Due to the synergistic effects of different active regions, continuous and efficient catalytic combustion of toluene at a low temperature was realized. The synthesized samples were analyzed by X-ray fluorescence (XRF), scanning electron microscope (SEM), high resolution transmission electron microscope (HRTEM) equipped with an X-ray energy dispersive detector (EDX), nitrogen adsorption-desorption, X-ray diffraction (XRD), Raman spectrum, an electron paramagnetic resonance (EPR) spectrum, hydrogen temperature-programmed reduction (H_2 -TPR), oxygen temperature-programmed desorption (O_2 -TPD) and X-ray photoelectron spectroscopy (XPS). While, assisting with density functional theory (DFT) calculations and in situ diffuse reflectance infrared spectroscopy (DRIFTS) measurements, the oxidation mechanism of toluene on the catalyst was investigated. It is expected to provide a facile strategy to create novel catalysts with high performance for the VOCs combustion at low temperatures.

3.2 Experimental and measurements

3.2.1 Catalyst preparation

(I) Synthesis of ZIF-67

First, ZIF-67 was synthesized by modifying previous reported method [26]. Typically, 20 mL of aqueous solution containing 1.8 g of cobalt(II) nitrate hexahydrate ($\text{Co}(\text{NO}_3)_2 \cdot 6\text{H}_2\text{O}$, Wako, Japan) and 20 mg of cetyl trimethyl ammonium bromide (CTAB, Wako, Japan) was quickly poured into another aqueous solution (175 mL) containing 11.2 g of 2-methylimidazole (Wako, Japan), and stirred at 25 °C overnight. Then, the obtained precipitate was washed with deionized water (DIW), ethanol, and then collected by

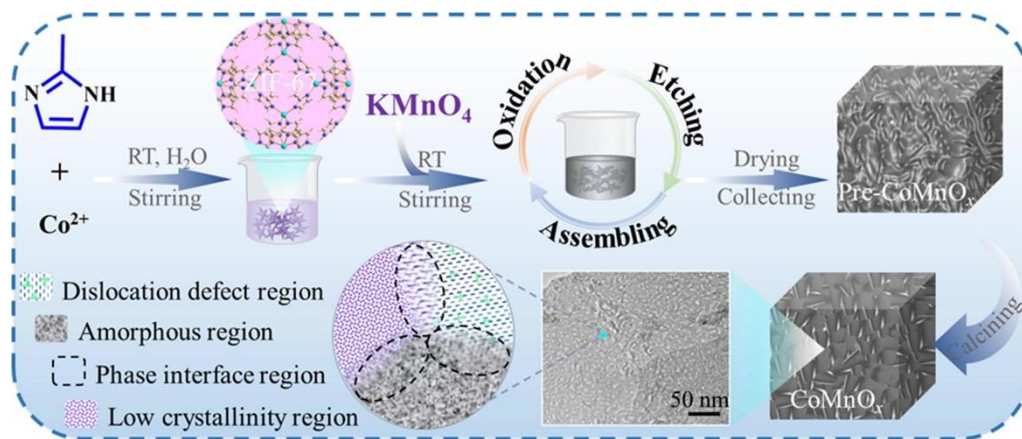
centrifugation. Thereafter, the resulting purple solid product was vacuum dried at 60 °C overnight and transferred to 110 °C oven and treated for 12 h. The XRD analyses below confirmed the successful synthesis of ZIF-67 with a star-shape.

(II) Synthesis of CoMnx catalysts

As illustrated in Scheme 3.1, 400 mg of ZIF-67 powders were dispersed in 100 mL of DIW ultrasonically. Then, 100 mL of potassium permanganate (KMnO₄, Wako, Japan) aqueous solution with designed concentrations (1 g·L⁻¹, 6 g·L⁻¹, 11 g·L⁻¹) was poured into the ZIF-67 slurry quickly and stirred magnetically for 1 h, and then kept still for 30 min. Thereafter, the obtained suspension was collected by centrifugation with water-washing and ethanol-washing operations successively. Finally, the assembled black solid was vacuum treated at 60 °C for 12 h and then calcined in an air muffle furnace at 350 °C (heating rate of 2 °C/min) for 3 h. The prepared samples are labelled as CoMn1, CoMn6 and CoMn11 respectively based on the KMnO₄ concentrations added.

(III) Synthesis of CoO_x and MnO_x samples

The synthesized ZIF-67 above was calcined in an air muffle furnace at 350 °C for 3 h with a heating rate of 2 °C/min to obtain a pure CoO_x sample. While, 100 mL of KMnO₄ aqueous solution (6 g·L⁻¹) was poured into another 100 mL of aqueous solution containing 400 mg of 2-methylimidazole and stirred until a large amount of precipitation was produced. After static treatment, centrifugation, washing, drying and calcination at 350 °C, pure MnO_x sample was obtained. All the chemical reagents involved in the experiments are analytical grade.



Scheme 3.1. Diagram of synthetic route and morphological evolution for CoMnx mixed oxide catalyst.

3.2.2 Catalytic performance test

Evaluation of catalytic performance for the toluene combustion over the prepared catalyst was carried out at the atmospheric pressure in a micro fixed bed reactor equipped with a quartz tube (inner diameter = 8.0 mm), in which 50 mg of catalysts (40-60 mesh) was loaded. Firstly, only a nitrogen flow was introduced into the reaction bed at 100 °C for 30 min to remove air and impurities. After that, 50 mL/min of feed gas containing 1,000 ppm of toluene, 20 vol.% O₂ and N₂ as balance gas, corresponding to the 60,000 cm³·g⁻¹·h⁻¹ of weight hourly space velocity (WHSV), was introduced into the reaction system at 100 °C for 30 min to stabilize reaction gas. Subsequently, the reactor was heated from 100 to 300 °C at a heating rate of 10 °C/min. Herein, when the target temperature of reaction system was reached, it was kept for about 40 min for the measurement. The gas compositions of entering/exiting the reaction system were on-line analyzed by a FT-IR analyzer (Horiba, FG-120), a gas chromatography (GC) equipped with a flame ionization detector (FID, GC-2014, Shimadzu) and a thermal conductivity detector (TCD, GC-8A, Shimadzu). In this study, the catalytic performances at different WHSVs (30,000, 60,000 and 120,000 cm³·g⁻¹·h⁻¹) were also tested by adjusting the amounts of catalyst filling amount. In addition, by passing water vapor (5 vol.% and 10 vol.%) into the feed gas, the effect of water on the catalytic performance of target catalyst was also tested. All of the above experiments were repeated for at least 3 times, and the average results are shown in the following sections. The long-term stability of 50 h for the optimal catalyst was evaluated without changing the reaction temperature. The toluene conversion (C_t , Eq. (1)), CO₂ selectivity (C_{CO_2} , Eq. (2)), normalized reaction rate (r , mol·g⁻¹·s⁻¹, Eq. (3)) and the apparent activation energy (E_a , kJ·mol⁻¹, Eq. (4)) were calculated using the following formulas [27, 28]:

$$C_t = \frac{[\text{toluene}]_{in} - [\text{toluene}]_{out}}{[\text{toluene}]_{in}} \times 100\% \quad (1)$$

$$C_{CO_2} = \frac{[CO_2]_{out}}{7 \times [\text{toluene}]_{in}} \times 100\% \quad (2)$$

$$r = (C_t \cdot V) / m_{cat} \quad (3)$$

$$r = -kc = [-A \exp (-E_a/RT)]c \quad (4)$$

where $[\text{toluene}]_{in}$ (ppm) and $[\text{toluene}]_{out}$ (ppm) are toluene concentrations of the inlet and outlet of reactor, respectively. $[\text{CO}_2]_{out}$ (ppm) is the outlet CO_2 concentration. V represents toluene gas flow rate. m_{cat} is catalyst mass amount. k represents the rate constant. A is pre-exponential factor. c represents concentration of toluene in feed stream. R represents proportional constant. T is reaction temperature.

3.2.3 Catalyst characterization

Material morphology was observed on SEM instrument (Hitachi SU8010, Japan) at an applied voltage of 15 kV. Nitrogen adsorption-desorption experiments were tested at 77 K on Nova 4200 equipment (Quantachrome Inc., USA) after vacuum degassing operation at 300 °C for 12 h. The SSA and pore structure information of the catalysts were obtained using the Brunauer-Emmett-Teller (BET) and the Barrett-Joyner-Halenda (BJH) models, respectively. The composition of metallic elements in the mixed oxide samples were determined by X-ray Fluorescence (XRF) analysis (EDX-800HS, Shimadzu). The crystal phase information of prepared materials was tested on an XRD machine (Rigaku Smartlab, Japan) with the $\text{Cu-K}\alpha$ radiation ($\lambda = 1.5418 \text{ \AA}$) at a diffraction angle range of 10-80° with the scanning rate of 10 °/min. HRTEM images were measured on a JEM-2100F equipment at 200 kV, on which EDX mapping (Horiba EMAX) was equipped for the elemental analysis. XPS spectra were collected on an XPS instrument (VG Scientific ESCALab250i-XL) using an $\text{Al-K}\alpha$ radiation as the excitation source. The binding energy (BE) of C1 s (284.6 eV) was used for calibration, and the XPSPEAK software was used to fit all XPS peaks. Raman spectra were acquired on a Raman spectrometer (JASCO NRS5100) with an exciting source of 532 nm. EPR spectrum was recorded at room temperature on a Bruker A300 instrument (Bruker, Germany) to investigate the defect information in the materials. The H_2 -TPR experiments were performed on a BELCAT instrument (Microtrac, Japan). In brief, a measured amount of sample (40 mg) filled in a U-shaped quartz tube was pretreated at 300 °C in a helium gas flow (50 mL/min) for 30 min and then cooled down to 30 °C. The sample was heated at a rate of 10 °C/min from 30 to 900 °C in 5 vol.% H_2/Ar mixed gas flow (50 mL/min) and the H_2 consumption signal was captured by TCD. The O_2 -

TPD experiments were also tested on this instrument and the same operation as TPR was used to pre-process the sample (40 mg). After that, the sample was treated in an oxygen gas flow (30 mL/min) at 50 °C for 60 min and then purged with a helium gas flow (30 mL/min) for 60 min. Then, the material was heated from 50 to 900 °C at a rate of 10 °C/min under a helium gas flow (30 mL/min), and the signal of desorbed oxygen was collected by TCD. DFT was used to simulate the adsorption energy of O₂ molecules on the spinel structure. In situ DRIFTS studies were recorded on a Frontier FTIR spectrometer (PerkinElmer) equipped with a DRIFTS cell and a liquid nitrogen-cooled mercury cadmium telluride (MCT) detector. All spectra of samples were collected in the range of 4000-650 cm⁻¹ with 32 scans. Prior to each experiment, the catalyst was heated to 300 °C in a nitrogen atmosphere (100 mL/min) and treated for 30 min to remove impurities from the sample. After the sample was cooled to 50 °C, the background in the nitrogen atmosphere was collected. After that, toluene (1,000 ppm) contained gases with different environments (toluene-N₂, toluene-air and toluene-air-5 vol.% H₂O) were introduced into the in-situ reaction cell. Subsequently, the spectral information after the catalytic reaction reached equilibrium under different reaction time at 218 °C was recorded.

3.3 Result and discussion

3.3.1 SEM and N₂ adsorption-desorption characterizations

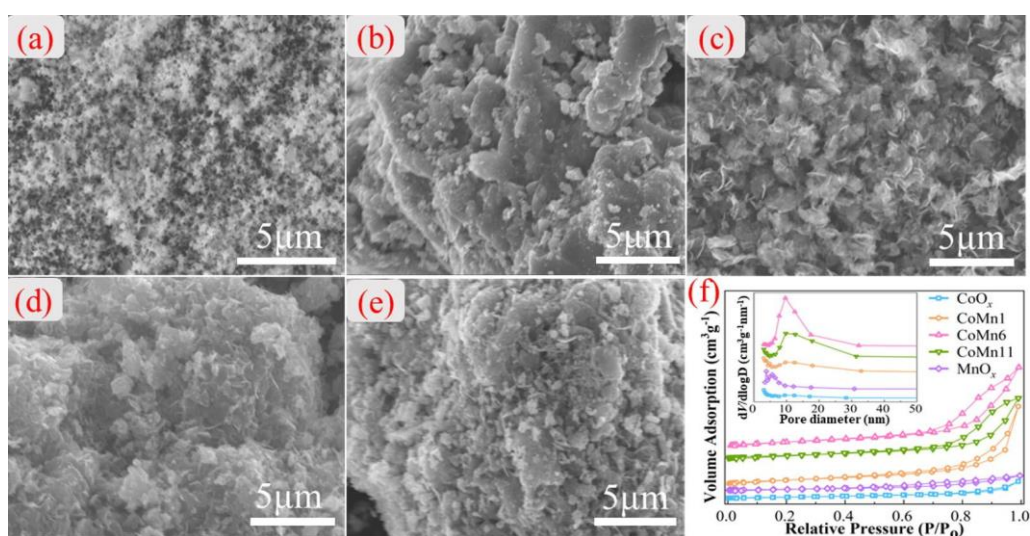


Fig. 3.1. SEM images of the CoO_x (a), MnO_x (b), CoMn1 (c), CoMn6 (d) and CoMn11 (e) samples; (f) N₂ adsorption-desorption isotherms and pore size distributions (inset)

of all samples.

Fig. 3.1(a-e) depict the SEM micrographs of all the prepared samples. The CoO_x sample obtained by calcining ZIF-67 showed regular and scattered 3D star-like morphology with a diameter of ca. 500 nm (Fig. 3.1a). The MnO_x sample presented a smooth and dense structure (Fig. 3.1b). This kind of structure caused its lower SSA and porosity, which is always one of the reasons with the low catalytic performance. For the assembled CoMn_x catalysts (Fig. 3.1c-e), it is obvious that the CoMn1 catalyst exhibited lots of curled nanosheets and irregular blocks (Fig. 3.1c), which indicated that the oxidation-etching assembly of ZIF-67 precursor by potassium permanganate resulted in reassembling of nanostructure to generate a new structure. Comparing with CoMn1 sample, the CoMn6 catalyst exhibited more curled nanosheets with an assembled sheet-like structure, indicating that with the addition of more potassium permanganate, the sufficient etching and self-assembly of the material were achieved (Fig. 3.1d). Generally, the generation of sheet-like assembling structure would be conducive to the transfer of toluene molecules in the porous material to contact more active sites in the catalyst. However, as the content of potassium permanganate was continuously increased (e.g., CoMn11 catalyst), the sheet-like stacked structure was transitioned to a dense block structure (Fig. 3.1e), which might lead to the blockage of some pores with the decrease of SSA, thereby affecting the adsorption and decomposition performance of toluene molecules in the material. Based on these results, it can be concluded that a new material with a sheet-like stacked structure can be synthesized by the assembly strategy with the oxidation-etching of MOF precursor, and the morphology and structure of CoMn_x sample can be adjusted by changing the content of KMnO_4 .

The SSAs and pore size distributions of catalysts were of great significance to the utilization of active components and adsorption/transfer of VOCs molecules. N_2 adsorption-desorption isotherms (Fig. 3.1f) show that all prepared samples possessed type IV isotherms and H3-shaped hysteresis loops according to the IUPAC classification, which are the typical characteristics of mesoporous material [29, 30]. Moreover, compared with the pure CoO_x and MnO_x samples, the CoMn_x samples

exhibited more obvious hysteresis phenomenon, which also indicated that the rich pore structures were formed during the assembling process whereas the manganese content added had a certain influence on the pore distribution. The pore structure information was also proved by the pore size distributions as shown in the inset of Fig. 3.1f. Obviously, only weak pore size distribution peaks centered at ca. 3.8 and ca. 5.5 nm, and peaks centered at ca. 6.5 and ca. 10 nm were found in MnO_x and CoO_x samples, respectively. Whereas, the CoMnx catalysts showed stronger peaks in the range of ca. 6-28 nm, especially for the CoMn6 and CoMn11 catalysts, which should be helpful to overcome the mass transfer limit of toluene resulting from their channel diameters being greater than five times the kinetic diameter of toluene ($5 \times \text{ca. } 5.8 \text{ \AA}$) [31, 32]. It is noteworthy that too much manganese content added (e.g., CoMn11) could result in the decrease of pore numbers, which indicated that over-assembly process should be inconducive to the generation of porous structure. This is consistence with the observed flake-shape collapse as shown in the SEM image (Fig. 3.1e). The average pore diameters (P_d), pore volumes (P_v) and SSAs of all catalytic materials were also calculated and summarized in Table 3.1. Obviously, among the synthesized catalysts, CoMn6 sample showed largest SSA (163.0 m²/g) and P_v (0.59 cm³/g) with a suitable P_d (9.6 nm). This could not only facilitate the utilization of active sites in the catalyst and increase the contact probability between the reactant and material, but also improve the transfer efficiency of reactants and products by overcoming mass transfer resistance [31]. In addition, the decreased SSA (94.3 m²/g) and P_v (0.45 cm³/g) of the CoMn11 sample also illustrated the adverse effect by the addition of excessive manganese during the catalyst synthesis. Thus, the oxidation-etching assembly process with a suitable potassium permanganate content could optimize the pore structure of CoMnx catalysts, which would promote the catalyst performance for the toluene combustion.

Table 3.1 Textural properties and XRF analysis results of all prepared catalysts.

Sample	SSA ^a	P_d ^b	P_v ^b	Element content (at. %) ^c			Crystal size ^d
	(m ² /g)	(nm)	(cm ³ /g)	Co	Mn	K	d_{311} (nm)

CoO _x	30.0	3.0	0.12	100	/	/	22.0
MnO _x	38.0	3.8	0.12	/	86.5	13.5	/
CoMn1	130.7	3.1	0.55	75.5	23.1	1.4	9.6
CoMn6	163.0	9.6	0.59	31.0	59.3	9.7	7.1
CoMn11	94.3	9.8	0.45	20.3	67.2	12.5	/

^a Calculated by BET model. ^b Measured from BJH model. ^c Obtained by XRF technique.

^d Determined through Scherrer formulation from the (311) diffraction peak in the XRD patterns.

3.3.2 XRD and Raman analyses

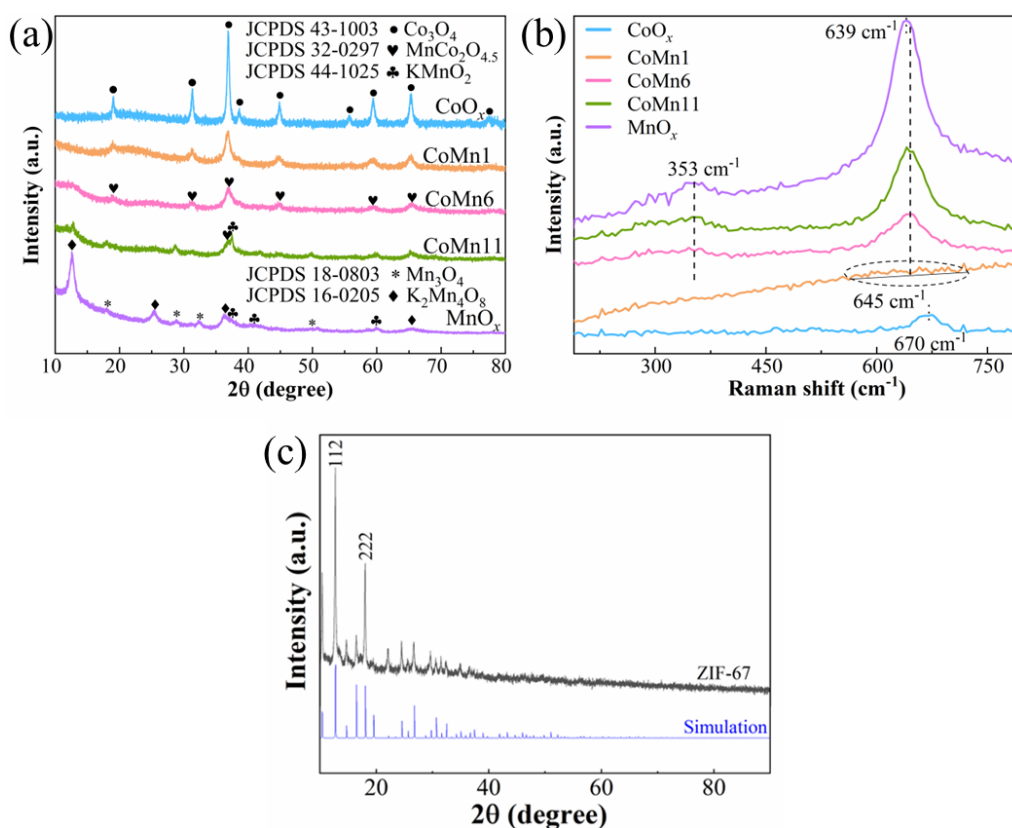


Fig. 3.2. XRD patterns (a) and Raman spectra (b) of CoO_x, MnO_x and CoMnx samples; (c) XRD patterns of synthetic and simulated ZIF-67.

Fig. 3.2a shows the crystal textures of CoO_x, MnO_x and CoMnx catalysts monitored by the wide-angle XRD patterns. Obviously, the pure CoO_x sample showed the characteristic diffraction peaks of typical face-centered cubic spinel Co₃O₄ (JCPDS No. 43-1003) at 19.0, 31.3, 36.8, 38.5, 44.8, 55.7, 59.4, 65.2 and 77.3° (2θ), corresponding

to the (111), (220), (311), (222), (400), (422), (511), (440) and (533) crystalline planes, respectively [33]. While, the pure MnO_x sample exhibited a main $\text{K}_2\text{Mn}_4\text{O}_8$ phase with (001), (002), (220) and (242) faces at 12.7, 25.4, 36.2 and 65.7°, (JCPDS No. 16-0205) [34]. In addition, faint characteristic peaks of Mn_3O_4 (18.0, 28.9, 32.4 and 50.9°, JCPDS No. 18-0803) and KMnO_2 (37.4, 40.5 and 59.9°, JCPDS No. 44-1025) were also found in the XRD pattern of MnO_x . Compared with the pure MnO_x sample, the $\text{K}_2\text{Mn}_4\text{O}_8$ diffraction peaks in CoMn_x oxides nearly disappeared, except for the extremely faint peak in CoMn11 sample. With the addition of low content of manganese to the MOF precursor, the peak intensity of Co_3O_4 in CoMn1 sample decreased sharply. However, with the continuous increase in the manganese content, the peak intensity in the XRD pattern of CoMn6 was only changed a little. Moreover, despite of the high content of manganese in CoMn6 sample, no diffraction peaks of manganese species were found and the weak peaks with higher FWHM (half of the maximum intensity) in CoMn6 catalyst was in good agreement with the spinel $\text{MnCo}_2\text{O}_{4.5}$ phase (JCPDS No. 32-0297) [23]. The smaller grain size (7.1 nm) of CoMn6 calculated by Scherer formula based on $\text{MnCo}_2\text{O}_{4.5}$ (311) plane also confirmed the partial substitution of Co atoms by Mn atom with smaller diameter (Table 3.1). This also showed that the oxidation-etching assembly process realized the doping of manganese into cobalt atom framework, which also resulted in the formation of amorphous phase accompanying with the lower crystallinity $\text{MnCo}_2\text{O}_{4.5}$ phase due to the strong interaction between manganese and cobalt atoms. In general, the formed lower crystallinity phase or/and amorphous phase can serve as the carrier of active oxygen species to achieve excellent catalytic performance for VOCs combustion [35, 36]. Aguilera et al. [37] reported that the doping of cobalt on manganese oxides can result in the formation of the MnCo mixed oxides with low crystallinity, thus optimizing the number of redox sites and improving the catalytic oxidation performance. Wang et al. [5] also prepared a kind of amorphous MnCo mixed oxide with a defect-rich structure by an agar-gel method, which exhibited excellent catalytic performance for the toluene oxidation due to its better reducibility with abundant active species such as Mn^{3+} , Co^{3+} and oxygen vacancies. Therefore, the CoMn6 catalyst with lower crystallinity constructed in this work might also have

satisfactory catalytic ability for the toluene combustion.

Fig. 3.2b depicts Raman spectra of the prepared catalysts. For the pure CoO_x catalyst, one band centered at 670 cm^{-1} was attributed to the A_{1g} vibration mode of spinel structure Co_3O_4 resulting from the occurrence of octahedral sites, which is in accordance with the XRD analysis result [38]. With the addition of manganese, the A_{1g} vibration mode signal of Co_3O_4 in CoMnx samples became extremely faint, which indicated that the existence of strong interaction between manganese and cobalt species interfered the normal vibration of metal-oxygen bond [5, 39]. This also explained the greatly reduced diffraction peaks of Co_3O_4 in the XRD pattern (Fig. 3.2a). Two obvious bands centered at ca. 353 and 639 cm^{-1} were detected in the pure MnO_x catalyst. The former should be attributed to out-of-plane bending modes of Mn_2O_3 [40] and the latter related to the Mn-O-Mn stretching mode of Mn_3O_4 [41]. It is worth noting that with the addition of cobalt, the two characteristic peaks in the CoMnx catalysts were significantly weakened, which indicated the occurrence of long-range disordered accumulation of poor crystalline structure from Mn-O- Co^{3+} bonds. In addition, in CoMnx catalysts, the high-frequency shift of out-of-plane bending modes for Mn-O bond also proved the incorporation of Co^{3+} into MnO_x [39]. As such, the oxygen mobility of the CoMnx catalyst would be improved due to the generation of abundant weak binding capacity species (Mn-O, Co-O, Mn-O-Co bonds and Mn- \circ -Co species; \circ stands for oxygen vacancy), thereby exhibiting excellent catalytic performance [39]. Synthetic and simulated ZIF-67 XRD patterns shown in Fig. 3.2c confirmed the successful synthesis of ZIF-67.

3.3.3 XPS analysis

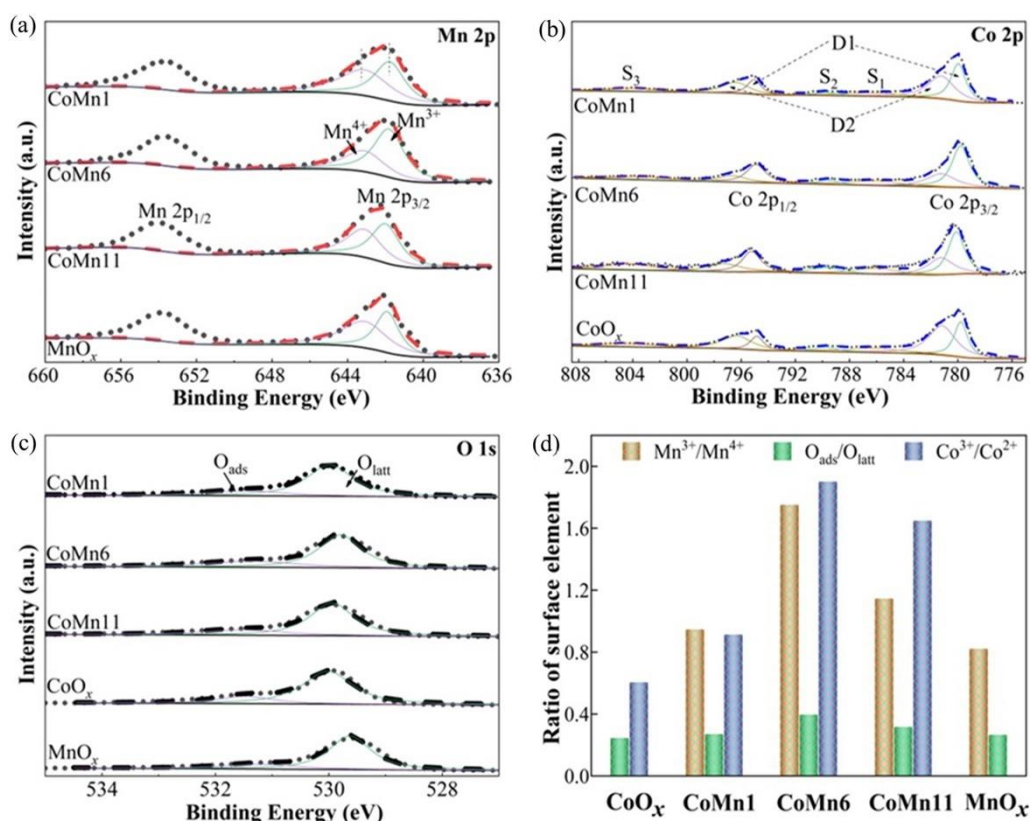


Fig. 3.3. XPS spectra of (a) Mn 2p, (b) Co2p and (c) O 1s for the prepared catalysts; (d) Comparison histogram of molar ratio for active components in each catalyst.

The element valences and compositions on the catalyst surface were determined by XPS analysis (Fig. 3.3) and the relevant results are summarized in Table 3.2. The Mn 2p XPS spectra presented in Fig. 3.3a showed two asymmetric peaks situated at BEs of 642.0 ± 0.2 and 653.8 ± 0.2 eV, corresponding to Mn 2p_{3/2} and Mn 2p_{1/2} signals, respectively [42, 43]. The asymmetrical Mn 2p_{3/2} spectra of all samples were deconvoluted into two components in the BE intervals of 641.8-642.0 eV and 643.2-643.3 eV, being assigned to Mn³⁺ and Mn⁴⁺, respectively, indicating the coexistence of different manganese valences on the catalyst surface [42, 43]. The chemical valences of metallic elements played a key role in catalytic performance, and thus the molar ratios of Mn³⁺ to Mn⁴⁺ were calculated and listed in Table 3.2. The ratios of Mn³⁺/Mn⁴⁺ in the CoMnx catalysts were higher than that of the pure MnO_x sample (0.82), where the CoMn6 sample showed the highest Mn³⁺/Mn⁴⁺ ratio (1.75). Therefore, it could be concluded that the oxidation-etching assembly process stimulated the strong interaction

between Mn and Co oxides, which in turn promoted the production of more Mn^{3+} species. It was reported that the weaker binding capacity in Mn^{3+} -O bond than that in Mn^{4+} -O bond implied the easier escaping of the oxygen species in the former to participate in the oxidation reaction. In addition, based on the principle of electroneutrality, the presence of low-valent manganese species (Mn^{3+}) is always accompanied by the generation of oxygen vacancies to maintain electrostatic balance: $-\text{Mn}^{4+}-\text{O}^{2-}-\text{Mn}^{4+}- \rightarrow -\text{Mn}^{4+}-\text{O}^{\bullet}-\text{Mn}^{3+}- + 1/2\text{O}_2$ (O^{\bullet} represented oxygen vacancy) [44]. As such, the abundant oxygen vacancy defects on the surface of the CoMn6 catalyst could quickly adsorb and activate gaseous oxygen to participate in the toluene oxidation process [45].

While, as shown in Fig. 3.3b, Co 2p XPS spectra of all samples containing cobalt element exhibited two main peaks at ca. 780.1 ± 0.2 and 795.2 ± 0.2 eV, corresponding to the spin-orbital peaks of Co 2p_{3/2} and Co 2p_{1/2}, respectively. The splitting value (ΔE = ca. 15.2 eV) of Co 2p spin-orbit calculated by formula: $\Delta E = E(\text{Co } 2p_{1/2}) - E(\text{Co } 2p_{3/2})$, indicated the coexistence of Co^{3+} and Co^{2+} species on the catalyst surface [18]. As previous reports [23, 24], the entire Co 2p spectrum could be deconvoluted into two main spin-orbit doublets (D1 and D2) accompanied by three satellite peaks (S1, S2 and S3). The D1 peaks at ca. 780 and ca. 794.9 eV were assigned to the octahedral Co^{3+} , and the D2 peaks at ca. 781.3 and ca. 796.9 eV were assigned to the tetrahedral Co^{2+} in the catalyst surface. In addition, the existence of three satellite peaks at 785.8 ± 0.3 (S1), 789.9 ± 0.3 (S2) and 803.5 ± 0.3 (S3) eV reconfirmed the coexistence of mixed cobalt valence states [33]. The surface $\text{Co}^{3+}/\text{Co}^{2+}$ molar ratios listed in Table 3.2 showed the decreased order of CoMn6 (1.90) > CoMn11 (1.62) > CoMn1 (0.91) > CoO_x (0.60), which proved that the oxidation-etching assembly process increased the Co^{3+} contents in CoMnx catalysts. This also echoed the electron transfer process of $\text{Mn}^{4+} + \text{Co}^{2+} \leftrightarrow \text{Mn}^{3+} + \text{Co}^{3+}$, caused by the strong interaction between manganese and cobalt oxides induced by the oxidation etching assembly process. Generally, Co^{3+} species has superior low-temperature reduction ability than Co^{2+} species (as discussed in H₂-TPR section), and a larger $\text{Co}^{3+}/\text{Co}^{2+}$ ratio always provides excellent VOC catalytic oxidation ability. Mei et al. [46] found that more Co^{3+} species in mesoporous cobalt

oxide could not only promote the production of more adsorbed oxygen species in the oxidation reaction, but also improve the adsorb ability to the reactant molecules. Xie et al. [47] reported that Co^{3+} species in the cobalt oxide catalyst was the predominant active site, which can improve the VOCs catalytic oxidation ability and increase the target product selectivity.

The O 1s XPS spectra of all catalysts displayed in Fig. 3.3c were fitted into two distinct sub-bands at 529.8 ± 0.2 and 531.5 ± 0.2 eV, which are attributed to the surface lattice oxygen (O_{latt} , O^{2-}) and labile adsorption oxygen species (O_{ads} , e.g., O^- , O_2^- and/or O_2^{2-}) [39]. It should be noted that the electrophilic O_{ads} species activated by defect sites always shows better catalytic performance in the deep VOCs oxidation. The ratios of $\text{O}_{\text{ads}}/\text{O}_{\text{latt}}$ for all catalysts summarized in Table 3.2 followed the sequence: CoMn6 (0.40) > CoMn11 (0.32) > CoMn1 (0.27) > MnO_x (0.26) > CoO_x (0.24), which implied that the oxidation-etching assembly process could provide sufficient active oxygen species or abundant defective structures. Fig. 3.3d intuitively compares the ratio results of the active components discussed above. One can see that the CoMn6 and CoMn11 samples showed higher ratios of $\text{Mn}^{3+}/\text{Mn}^{4+}$, $\text{Co}^{3+}/\text{Co}^{2+}$ and $\text{O}_{\text{ads}}/\text{O}_{\text{latt}}$ than those of CoMn1, MnO_x , and CoO_x samples, which also indicated that the oxidation-etching assembly process can effectively adjust and optimize the active structure in the CoMnx catalysts, and as a result, the CoMn6 sample could exhibit excellent catalytic potential resulting from its highest proportion of active species, e.g., Mn^{3+} , Co^{3+} and O_{ads} species.

Table 3.2 Analysis results of H_2 -TPR profiles, O_2 -TPD profiles, XPS element compositions, specific reaction rates, and activation energy for all prepared samples.

Sample	H_c (mmol/g) ^a		O_d (mmol/g) ^a			Surface molar ratio ^a			$r \times 10^6$ ^b (mol·g ⁻¹ ·s ⁻¹)	E_a ^c (kJ/mol)
	H_l	H_t	O_{suf}	O_{bulk}	O_t	$\text{Mn}^{3+}/\text{Mn}^{4+}$	$\text{Co}^{3+}/\text{Co}^{2+}$	$\text{O}_{\text{ads}}/\text{O}_{\text{latt}}$		
CoO_x	1.5	6.4	0.053	0.259	0.312	--	0.6	0.24	2.6	66.6
MnO_x	1.1	2.7	0.040	0.087	0.127	0.82	--	0.26	12.8	63.7
CoMn1	1.6	4.8	0.029	0.149	0.178	0.95	0.91	0.27	10.3	43.6
CoMn6	2.8	4.5	0.115	0.138	0.253	1.75	1.90	0.40	24.0	28.8
CoMn11	2.1	2.8	0.101	0.060	0.161	1.15	1.62	0.32	21.3	33.2

^a Calculated based on the characteristic peak areas. ^b Specific reaction rates at 215 °C. ^c

Obtained from Arrhenius plots slopes.

3.3.4 HRTEM and EDX analysis results

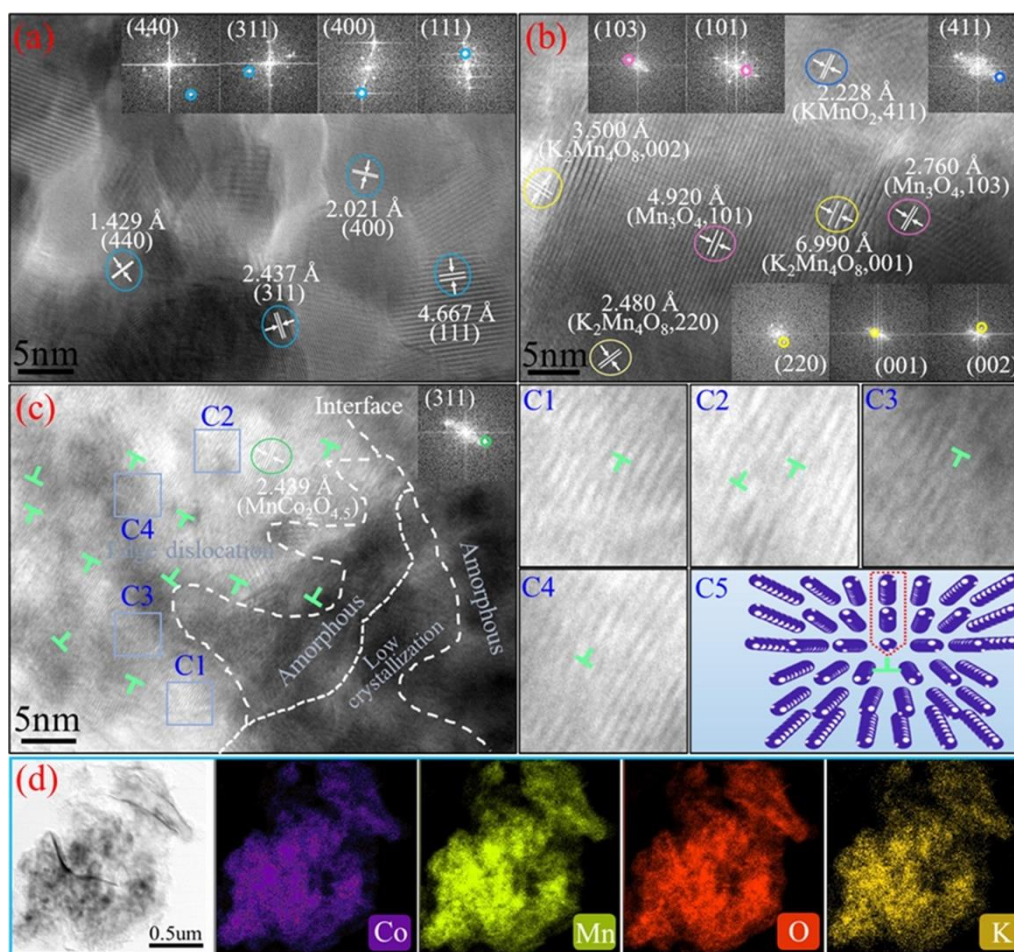


Fig. 3.4. HRTEM images of the CoO_x (a), MnO_x (b) and CoMn6 (c) catalysts (insets: FFT of characteristic crystal planes); Magnification views of edge dislocations from Fig. 3.4c (C1-C4) and schematic illustration of edge dislocation (C5); EDX mapping of CoMn6 sample (d).

Further insights into the influence of oxidation-etching assembly process on the crystal texture of catalysts were also analyzed by HRTEM and the related images are shown in Fig. 3.4(a-c). Obviously, distinct lattice fringes were observed in CoO_x sample (Fig. 3.4a), and the interplanar spacings of 1.429, 2.437, 2.021 and 4.667 Å corresponding to (440), (311), (400) and (111) planes of spinel Co_3O_4 calculated respectively by fast Fourier transform (FFT) are shown in the insets, which indicated that the CoO_x sample obtained by direct calcination of MOF precursor resulted in higher crystallinity. For the pure MnO_x sample (Fig. 3.4b), the relevant planes of different crystal phases were detected and the lattice spacings were also determined from FFT

algorithm. Herein, the lattice spacings of 2.480, 3.500 and 6.990 Å marked as yellow rings corresponded to the (220), (002) and (001) planes of $\text{K}_2\text{Mn}_4\text{O}_8$ phase, respectively. The lattice spacings of 4.920 and 2.760 Å marked by pink rings are the (101) and (103) planes characteristic of Mn_3O_4 phase, respectively. The (411) plane of KMnO_2 phase with a lattice spacing of 2.228 Å was also detected and circled in blue. In conclusion, both the pure CoO_x and MnO_x samples exhibited visible, rich and complete lattice fringes, which are consistent with the results of high crystallinity in the XRD analysis results. Remarkably, compared with the pure CoO_x and MnO_x samples, no clear lattice fringes were found in HRTEM image of CoMn6 sample (Fig. 3.4c) except for the faint (311) plane of $\text{MnCo}_2\text{O}_{4.5}$ phase. This phenomenon indicated that the oxidation-etching assembly process resulted in the formation of amorphous MnCo oxide structure rich in manganese atoms and $\text{MnCo}_2\text{O}_{4.5}$ phase with low crystallinity, also proving the successful assembly of Mn atom into cobalt oxide framework. It is consistent with the weak diffraction peaks in XRD pattern as shown in Fig. 3.2a and the uniform elemental distribution in the EDX mapping (Fig. 3.4d). Furthermore, it is worth noting that sufficient edge dislocations (marked with green "T"), large areas of amorphous structure and abundant phase interfaces were also observed in HRTEM image of CoMn6 catalyst (Fig. 3.4c). Herein, the presence of abundant dislocations led to the generation of intermittent and deformed lattice fringes. For distinguishing edge dislocation defect clearly, four edge defect regions in Fig. 3.4c were partially enlarged and shown in C1-C4, and their possible formation mechanism is briefly illustrated in C5. Actually, low crystallinity and amorphous types of catalytic materials always exhibit excellent catalytic oxidation performance in the catalytic oxidation of VOCs due to their superior oxygen mobility and abundant active sites [48]. The abundant structural defects or interfaces on the catalyst surface could provide sufficient capacity for adsorbing and activating gaseous oxygen, ensuring the abundant supply of reactive oxygen species during the oxidation of VOCs [5]. Moreover, structural defects could provide unbalanced electronic environment for improving the transport of lattice oxygen and the quenching-reproduction cycle of oxygen vacancies in catalyst, which is beneficial to improve oxidation performance of catalyst [49, 50]. In summary, by the

oxidation-etching assembly of MOF precursor, a kind of low-crystallinity CoMnx mixed oxide catalyst with abundant defects, amorphous structure and phase interfaces was obtained, which is expected to improve the catalytic performance for VOCs combustion.

3.3.5 H₂-TPR and O₂-TPD analyses

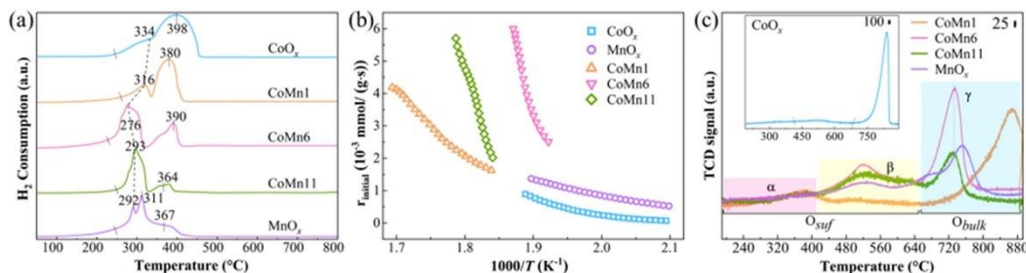


Fig. 3.5. (a) H₂-TPR profiles, (b) initial H₂ consumption rate and (c) O₂-TPD profiles of prepared samples.

Reduction behaviors of all prepared samples were investigated by H₂-TPR experiments and the corresponding results are shown in Fig. 3.5(a-b) and Table 3.2. In H₂-TPR profiles (Fig. 3.5a), two obvious reduction peaks of the pure CoO_x sample at 334 and 398 °C are attributed to the two-step reduction process of Co³⁺ to Co²⁺ and Co²⁺ to Co⁰ [33], respectively. For the pure MnO_x sample, three reduction processes centered at 292, 311 and 367 °C were detected, which corresponded to the reductions of MnO₂ to Mn₂O₃, Mn₂O₃ to Mn₃O₄ and Mn₃O₄ to MnO [39], respectively. For the CoMnx catalysts, two-step reduction processes occurred at different temperatures accompanied with different reduction intensities were found. The first peaks occurred at the low temperatures were assigned to the simultaneous reductions of Co³⁺ to Co²⁺ as well as Mn⁴⁺ to Mn³⁺ and/or Mn^{8/3+}, whereas the second peaks were related to the reductions of Co²⁺ to Co⁰ as well as Mn³⁺ and/or Mn^{8/3+} to Mn²⁺ species [39]. Obviously, with the interaction of cobalt and manganese species, the low-temperature reduction peaks from CoO_x merged with the first two low temperature reduction peaks from MnO_x into the expanded peaks and shifted to lower temperatures. Especially for the CoMn6 sample, the merged reduction peak area was expanded greatly and shifted to a lowest temperature (276 °C), indicating that the MnCo6 catalyst with low degree of crystallinity synthesized by the oxidation-etching assembly process exhibited superior

reduction performance. It is reported that the Schottky defects formed by the spinel structure would shorten the metal-oxygen bond, and the resulting asymmetric distortion of crystal or/and the lengthening of periodic crystal framework could promote the mobility of oxygen species in the spinel structure catalyst, thereby exhibiting better reduction performance [22]. Especially, the inherently unstable metal-oxygen bonds in the amorphous structure could also enhance the reduction performance of catalyst. Considering the XRD and HRTEM analysis results, it could be inferred that the low crystallinity spinel $\text{MnCo}_2\text{O}_{4.5}$, amorphous structure and rich defect structure in the catalyst could be beneficial to improve the reduction performance. In addition, the H_2 consumption (H_c) of all catalysts including total H_2 consumption (H_t) and low temperature H_2 consumption (H_l) were quantitatively calculated and summarized in Table 3.2. The H_t decreased in the order of CoO_x (6.4 mmol/g) > CoMn1 (4.8 mmol/g) > CoMn6 (4.5 mmol/g) > CoMn11 (2.8 mmol/g) > MnO_x (2.7 mmol/g), which however are not matched well with the catalytic performance of the catalyst as discussed in Section 3.3.7. The H_l decreased in the sequence of CoMn6 (2.8 mmol/g) > CoMn11 (2.1 mmol/g) > CoMn1 (1.6 mmol/g) > CoO_x (1.5 mmol/g) > MnO_x (1.1 mmol/g), which was basically in agreement with the order of their catalytic performance as shown in the Section 3.3.7. It could be inferred that the H_l should be not the only factor to evaluate the catalytic performance, and the reduction performance in low temperature stage also played a key role in the catalytic combustion of toluene. Moreover, the initial H_2 consumption rate (r_{initial} , $\text{mmol} \cdot \text{g}^{-1} \cdot \text{s}^{-1}$) of the catalysts (Fig. 3.5b) was calculated based on 20% of the initial H_c to further evaluate the low-temperature reduction performance of each sample [51]. One can see that the r_{initial} followed the sequence of $\text{CoMn6} > \text{CoMn11} > \text{CoMn1} > \text{MnO}_x > \text{CoO}_x$, which is in good agreement with the catalytic activity as shown in the Section 3.3.7. This further confirmed the importance of the low-temperature reduction performance of the catalyst in the catalytic oxidation reaction, and as a result, the MnCo_x composite oxide catalysts prepared by the oxidation-etching assembly process exhibited excellent low temperature reduction performance, especially CoMn6 sample (Section 3.3.7).

While, O_2 -TPD experiments were performed to examine the oxygen species and

mobility in the catalyst material. As shown in Fig. 3.5c, all samples could be divided into three desorption areas (α , β and γ), corresponding to the desorption of three oxygen species. The α oxygen species desorbed at lower temperatures ($< 400\text{ }^{\circ}\text{C}$) could be attributed to the physical and chemical adsorbed oxygen species on the catalyst surface [49]; β oxygen species located in the middle temperature range ($400\text{--}640\text{ }^{\circ}\text{C}$) were assigned to the desorption of surface/subsurface lattice oxygen resulting from the unsaturated and broken Mn-O, Co-O and/or Mn-O-Co bonds [45]; γ oxygen species desorbed at high temperature ($> 650\text{ }^{\circ}\text{C}$) were ascribed to the lattice oxygen in the catalyst bulk [52]. The α peak profiles with the temperatures of all samples were similar, indicating that the samples had similar surface adsorbed oxygen species content in the initial state. However, the intensities of β and γ peaks in all samples showed obvious differences, indicating that the oxidation-etching assembly process made a greater impact on the lattice oxygen mobility of catalysts. Especially, the β peak intensities of CoMn6 and CoMn11 catalysts were significantly higher than those of other samples, indicating their better surface lattice oxygen mobility resulting from the sufficient unstable crystal structures (i.e., dislocation, vacancy and interface defects) in the catalyst. Considering the accepted evolution process of oxygen molecules during the toluene oxidation, i.e., $\text{O}_{2(\text{gas})} \rightarrow \text{O}_{2^{-}(\text{ads})} \rightarrow \text{O}_{2^{2-}(\text{ads})} \rightarrow 2\text{O}^{-}(\text{ads}) \rightarrow 2\text{O}^{2-}(\text{latt})$, more surface metastable crystal structures or defects could efficiently adsorb and activate gaseous oxygen during the continuous process of toluene oxidation, thus promoting the high-speed circulation of active lattice oxygen species. In addition, the desorption temperature of γ oxygen species of CoMn6 and CoMn11 catalysts shifted to lower temperatures, which should be due to the excellent bulk lattice oxygen mobility caused by the weak metal-oxygen bonds of amorphous structure and low crystallinity $\text{MnCo}_2\text{O}_{4.5}$ structure in the catalysts [52]. According to the Mars-van Krevelen (MVK) oxidation cycle mechanism, the bulk lattice oxygen with higher mobility is easier to transfer to surface sites, and the nucleophilic attack ability of lattice oxygen should play a vital role in both adsorption and deep oxidation of toluene, which would also be proved by in situ DRIFTS analysis [7, 42, 53]. In addition, the oxygen storage capacity (OSC) of catalysts was quantitatively estimated by integrating the desorption peak area

(Table 3.2). It is obvious that the desorption amounts of surface oxygen species (O_{surf}) for CoMn6 (0.115 mmol/g) and CoMn11 (0.101 mmol/g) catalysts were more than those for other samples, which also confirmed that the oxidation-etching assembly process enriched the unstable lattice oxygen species with high mobility. Herein, although the pure CoO_x and CoMn1 catalysts showed higher bulk lattice oxygen (O_{bulk}) and total oxygen (O_t) contents, their higher desorption temperatures indicated their poor lattice oxygen mobility. In contrast, the CoMn6 catalyst exhibited satisfactory surface and bulk lattice oxygen mobility due to the generation of plentiful active regions and defect species built up by the oxidation-etching assembly process, which would lead to superior low-temperature toluene oxidation performance as discussed in Section 3.3.7.

3.3.6 EPR spectrum

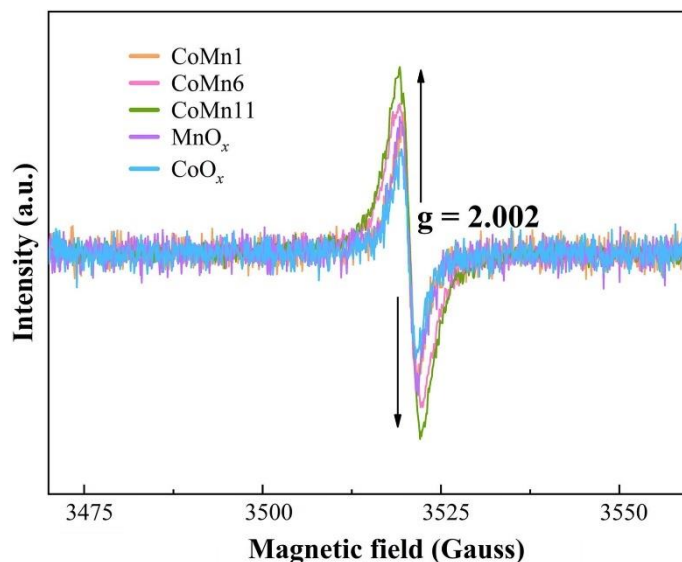


Fig. 3.6. EPR spectra for CoO_x , MnO_x and $CoMnx$ samples.

The EPR analysis shown in Fig. 3.6 was employed to identify the unpaired electron species in entire catalysts. Obviously, all EPR spectra exhibited centrosymmetric lines with a same g factor of 2.002 but different intensities, which meant that there were different contents of unpaired electron species in different catalysts, e.g., superoxide ion (O_2^-) or oxygen vacancies [54]. It is obvious that the $CoMnx$ catalysts, especially CoMn6 and CoMn11 samples, showed higher peak intensities than MnO_x and CoO_x catalysts, indicating the higher defect species contents in CoMn6 and CoMn11 samples. Thus, the assembly strategy derived from the oxidation-etching of MOF precursor

indeed built plentiful unpaired electron structures in the Co-Mn mixed oxides, which is consistent with the HRTEM analysis results (Fig. 3.4). It is worth noting that the CoMn11 sample exhibited stronger peak intensity than that of CoMn6 sample, but the catalytic activity was lower than the latter (as discussed in Section 3.3.7). Herein, on the one hand, the excessive manganese content led to the collapse of porous structure, making some defect species unable to contact the reactant molecules, thereby reducing the utilization of active oxygen. On the other hand, compared to the CoMn6 sample, the CoMn11 sample exhibited mediocre low temperature reduction capacity, ordinary lattice oxygen mobility and insufficient active species. It could thus be considered that more unpaired electrons defects in catalysts should be important for toluene catalytic oxidation, and the overall catalytic performance of catalyst would be determined by multiple factors, i.e., texture properties, defect structures, active oxygen contents, low temperature reducibility and lattice oxygen mobility originated from the synergistic complementary contributions of various active regions and active species in the catalytic material [36].

3.3.7 Catalytic performances and kinetic studies

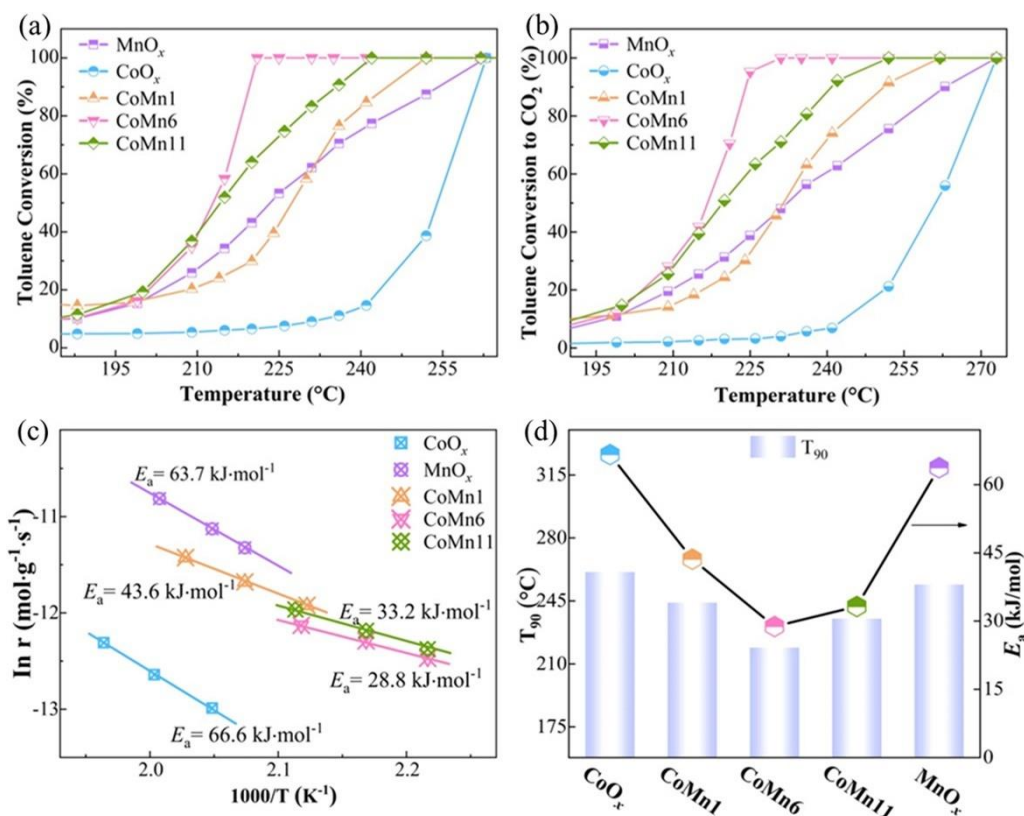


Fig. 3.7. (a) Toluene conversions vs reaction temperature, (b) CO₂ selectivity, (c) Arrhenius plots for toluene combustion and (d) relationship between T₉₀ and E_a values for the prepared catalysts.

The catalytic performances for toluene combustion over the prepared catalysts were evaluated by conducting catalytic oxidation experiments on simulated polluted gas containing 1,000 ppm toluene. The toluene conversion, CO₂ selectivity and T_x (the temperature corresponding to x% of toluene conversion) are shown in Fig. 3.7a, 3.7b and Table 3.3, respectively. As presented in Fig. 3.7a, the toluene conversions over all catalysts increased with the increase in reaction temperature, and all catalysts achieved complete toluene conversion before 262 °C. According to the T₉₀ values, the catalytic performances of the prepared catalysts decreased in the following order: CoMn6 (219 °C) > CoMn11 (236 °C) > CoMn1 (244 °C) > MnO_x (254 °C) > CoO_x (261 °C). The CO₂ selectivity over different catalysts showed the same trend as their toluene conversions (Fig. 3.7b), except for some temperature delay relating to the generation of intermediates in the toluene oxidation process (as discussed in Section 3.3.9). Obviously, the toluene conversion temperatures over CoMnx catalysts were lower than those over the pure MnO_x and CoO_x samples, and the CoMn6 catalyst showed the most excellent catalytic performance among all the catalysts with the lowest T₅₀ (212 °C), T₉₀ (219 °C) and T₁₀₀ (222 °C). As discussed above, CoMn6 catalyst derived from the assembly strategy by oxidation-etching of MOF precursor resulted in the creation of multiple types of active regions with plenty of active species, such as amorphous region, low-crystallinity structure and phase interfaces, which contributed the excellent low temperature reducibility, superior oxygen mobility and sufficient active oxygen species in the final catalyst. Furthermore, due to the better porous structures in CoMn6 catalyst, the defect structures such as dislocations and oxygen vacancies in the catalyst could be effectively utilized to desorb and activate gaseous oxygen species to active oxygen, and then captured by metastable Mn³⁺ and Co³⁺ species and used to restore the depleted oxygen species in the catalyst, resulting in the excellent and recyclable catalytic performance of the catalyst. Additionally, the normalized reaction rate (r) and apparent activation energy (E_a) for toluene combustion over the prepared catalysts verified the

accelerating effects of above active regions and species on the intrinsic activity of the catalysts. The $r \times 10^6$ values shown in Table 3.2 decreased in the following order CoMn6 ($24.0 \text{ mol} \cdot \text{g}^{-1} \cdot \text{s}^{-1}$) > CoMn11 ($21.3 \text{ mol} \cdot \text{g}^{-1} \cdot \text{s}^{-1}$) > MnO_x ($12.8 \text{ mol} \cdot \text{g}^{-1} \cdot \text{s}^{-1}$) > CoMn1 ($10.3 \text{ mol} \cdot \text{g}^{-1} \cdot \text{s}^{-1}$) > CoO_x ($2.6 \text{ mol} \cdot \text{g}^{-1} \cdot \text{s}^{-1}$), which are opposite to the T_{50} values and basically opposite to the T_{90} values in toluene oxidation reaction. Furthermore, E_a values calculated by the Arrhenius plot (Fig. 3.7c) and the related results are listed in Table 3.2. One can see that the CoMnx catalysts exhibited lower Arrhenius plots slopes ($\ln r$ vs T^{-1}) than the pure MnO_x and CoO_x samples, which indicated the lower E_a for toluene combustion over CoMnx catalysts. Herein, the E_a values increased in the following order: CoMn6 (28.8 kJ/mol) < CoMn11 (33.2 kJ/mol) < CoMn1 (43.6 kJ/mol) < MnO_x (63.7 kJ/mol) < CoO_x (66.6 kJ/mol), which is consistent with the order of T_{90} values (Fig. 3.7d). As such, the reactant molecules should be more easily activated on the CoMnx catalysts to participate the oxidation process, resulting in excellent low temperature activity due to the low activation energy barrier [27, 28]. Besides, compared with previous reports, the nanosheet state CoMn6 catalyst reported in this work exhibited more outstanding catalytic activity for toluene combustion under the similar reaction conditions (Table 3.3). Therefore, the oxidation-etching assembly strategy not only optimized the porous structure of the CoMnx catalysts, but also built the multi-active regions and active components, thereby enhancing the intrinsic catalytic performance of the catalysts.

Table 3.3 Summary and comparison of the catalytic performance for toluene over supported and nanosized Mn-Co mixed oxide catalysts reported in literature and this work.

Catalyst	Synthetic method	SSA (m^2/g)	GHSV ($\text{ml} \cdot \text{g}^{-1} \cdot \text{h}^{-1}$ or h^{-1})	Conc. (ppm)	Toluene conversion ($^{\circ}\text{C}$)			Ref.
					T_{50}	T_{90}	T_{100}	
CMO@SNW/SiC	Hydrothermal	12.3	9,000	5,000	254.5	256	257	[55]
$\text{Co}_{1.5}\text{Mn}_{1.5}\text{O}_4/\text{Ni foam}$	Hydrothermal	14.2	30,000	1,000	263	267	270	[44]
$\text{Co}_{0.67}\text{Mn}_{0.33}/\text{cordierite}$	Impregnation	--	45,000	1,000	223	238	250	[56]
$\text{MnO}_x/\text{Co}_3\text{O}_4\text{-10}$	Pyrolysis	112.0	60,000	1,000	230	234	242	[57]
CoMn-1	Precipitation	8.0	15,000	1,000	220	250	260	[58]
MOF-Mn1Co1	Pyrolysis	47.0	96,000	500	226	240	300	[25]
5Co1Mn oxides	Hydrothermal	114.0	60,000	1,000	232	247	275	[59]

Mn ₂ CoI oxides	Pyrolysis	85.4	60,000	1,000	228	236	238	[5]
α -MnO ₂ @Co ₃ O ₄	Pyrolysis	54.9	48,000	1,000	220	229	232	[60]
Co ₁ Mn ₁ BHNCs	Pyrolysis	45.0	60,000	1,000	232	248	300	[24]
CoO _x	Pyrolysis	30.0	60,000	1,000	254	261	262	
CoMnI	Oxidation-Etching	130.0	60,000	1,000	227	244	252	This work
CoMn6	Oxidation-Etching	163.0	60,000	1,000	212	219	222	
CoMn11	Oxidation-Etching	94.3	60,000	1,000	214	236	242	
MnO _x	Redox	38.0	60,000	1,000	223	254	262	

3.3.8 WHSV effect, durability and water vapor resistance evaluations

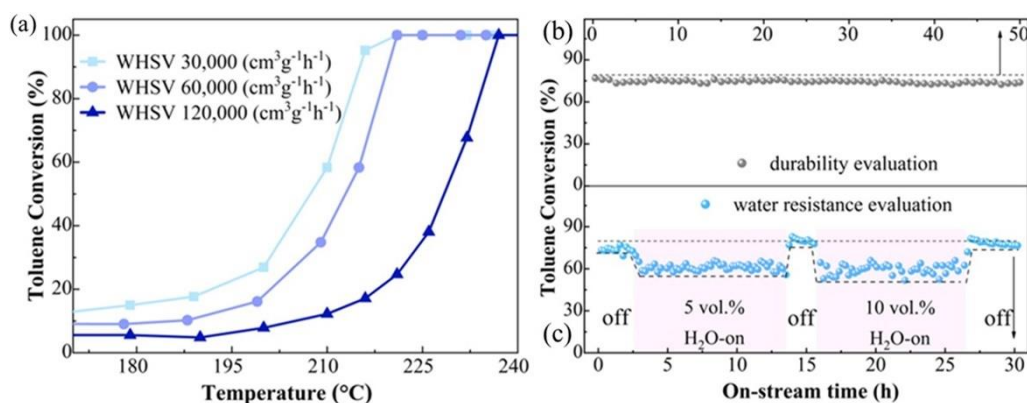


Fig. 3.8. (a) Effect of WHSV on the toluene conversion, (b) durability and (c) water vapor resistance evaluation over the CoMn6 catalyst.

Fig. 3.8a shows the effect of WHSV on the toluene conversion by adjusting the dosage of CoMn6 catalyst. As the WHSV was increased from 60,000 to 120,000 cm³·g⁻¹·h⁻¹, the T₉₀ value increased from 219 to 235 °C. When the WHSV was decreased to 30,000 cm³·g⁻¹·h⁻¹, the T₉₀ value also decreased to 215 °C. Thus, the WHSV had great influence on the catalytic efficiency, which should be mainly attributed to the different contact time between toluene molecules and active sites with different WHSVs. Toluene molecules would be discharged from the reaction system before being activated timely on the active sites under a higher WHSV. While, a lower WHSV always has inherent inefficiency in the practical application. Therefore, a suitable WHSV value should be crucial for a practical catalytic reaction. It is generally known that the durability and water resistance of catalysts are two important indicators for evaluating VOCs oxidation performance. Fig. 3.8b shows the toluene conversion over the CoMn6 catalyst in 50 h in a continuous operation at 217 °C with the WHSV of 60,000 cm³·g⁻¹·h⁻¹. Only a slight activity decrease (ca. 3%) occurred in around 37 h and remained unchanged after that, which indicated a good long-term operational stability of CoMn6

catalyst. Fig. 3.8c displays the water resistance of the CoMn6 catalyst for catalytic combustion of toluene at 217 °C with the WHSV of 60,000 cm³·g⁻¹·h⁻¹. After the reaction was stabilized for about 2.5 h, 5 vol.% water vapor was introduced into the reaction system, and as a result, the toluene conversion rate decreased by about 10%; After that, the water vapor was stopped after performing for about 13 h, and the toluene conversion rate was quickly recovered. While, at about 16 h, when 10 vol.% water vapor was introduced, the toluene conversion rate was decreased by about 15%, and then recovered rapidly with the removal of water vapor. Herein, when water vapor was introduced into the reaction system, water molecules and reactant molecules competed for adsorption on the surface of CoMn6 catalyst, thereby reducing the contact probability between reactants and active sites. On the other hand, the introduction of water vapor could inhibit the formation of some intermediate species such as maleic anhydride (as discussed in Section 3.3.9), an important reaction intermediate in the process of toluene oxidation, thereby affecting the progress of the oxidation reaction. However, when the introduction of water vapor was stopped, the rapid recovery of activity indicated a good water resistance property of CoMn6 catalyst.

3.3.9 In situ DRIFTS, DFT calculations and mechanism analysis

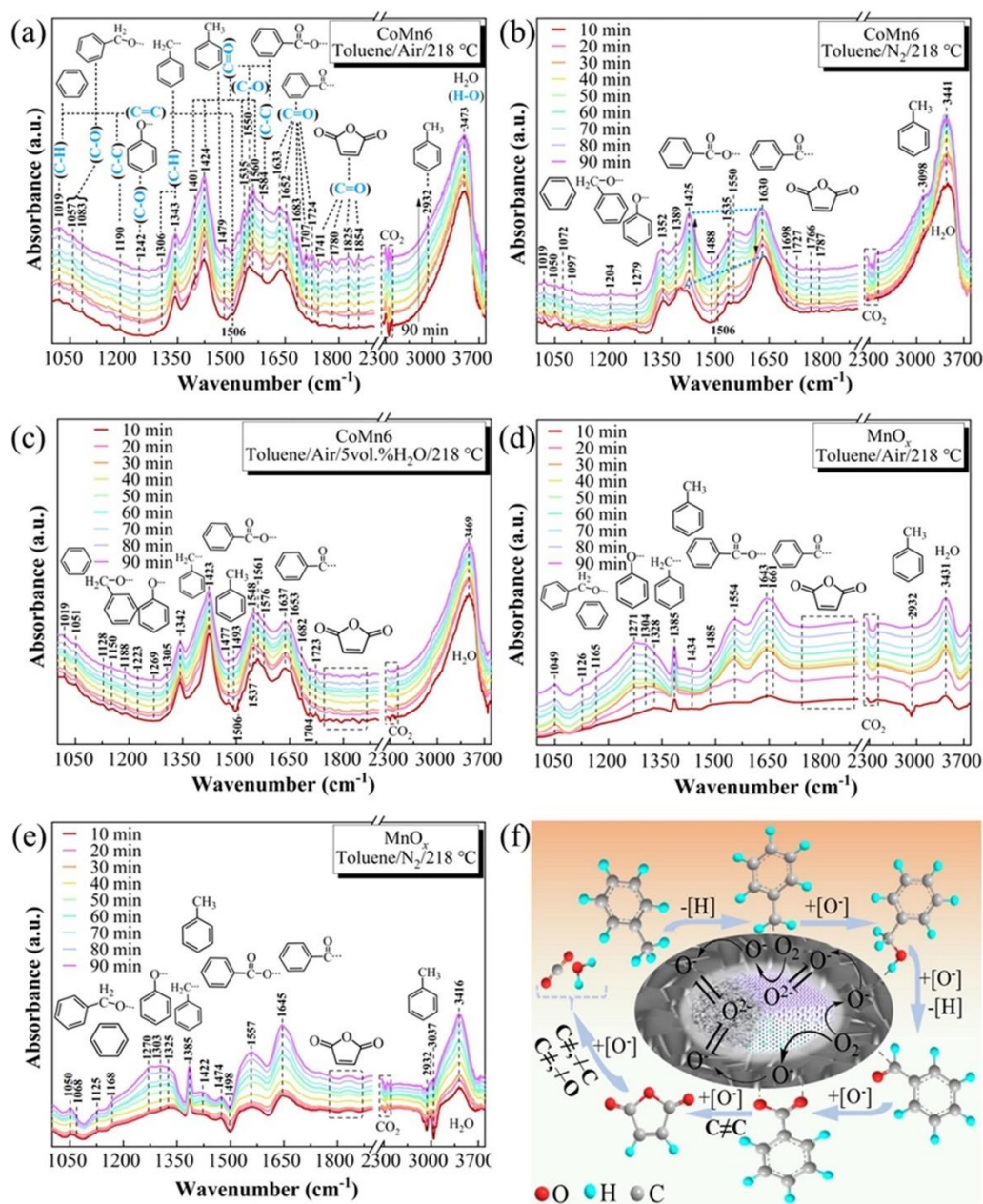


Fig. 3.9. In situ DRIFTS spectra of toluene combustion over the CoMn6 catalyst exposed at (a) toluene of 1,000 ppm in air atmosphere, (b) toluene of 1,000 ppm in N₂ atmosphere, (c) toluene of 1,000 ppm in air/5 vol.% water atmosphere; MnO_x sample exposed at (d) toluene of 1,000 ppm in air atmosphere, (e) toluene of 1,000 ppm in N₂ atmosphere. The schematic illustration of toluene combustion mechanism over CoMn6 catalyst (f).

To further track the toluene combustion pathways over the CoMn6 catalyst, the intermediates in toluene oxidation process were probed by in situ DRIFTS technology

(Fig. 3.9(a-e)), and based on the results, the mechanism of toluene oxidation over the CoMn6 catalyst was deduced (Fig. 3.9f). As shown in Fig. 3.9a, the time-dependent DRIFTS spectra of toluene combustion over CoMn6 catalyst at 218 °C in air atmosphere were recorded, and the assignments are shown in the insets and Table 3.4. The faint bands at 1019, 1479 and 2932 cm^{-1} should be ascribed to the $\nu(\text{C-H})$ in-plane bending vibration of aromatic ring, asymmetric deformation and symmetric stretching vibration of $\nu(\text{C-H})$ in methyl ($-\text{CH}_3$), respectively [45, 61], and the ones at 1190 and 1506 cm^{-1} assigned to antisymmetric $\nu(\text{C-C})$ stretching vibration and typical skeleton vibrations of $\nu(\text{C=C})$ in the toluene ring [45]. The peaks at 1306 and 1343 cm^{-1} were the characteristics of deformation vibration and in-plane bending vibration in methylene, respectively, symbolizing the formation of benzyl (Ph-CH_2-) species cleaved from toluene [45, 59]. The bands appeared at 1057 and 1083 cm^{-1} were related to stretching vibrations of $\nu(\text{C-O})$ in benzyl alcohol ($\text{Ph-CH}_2\text{-O-}$) and a weak peak at 1242 cm^{-1} was recognized as the stretching vibrations of $\nu(\text{C-O})$ in phenolate (Ph-OH) [5]. Several prominent peaks located in the range of 1630-1727 cm^{-1} were attributed to stretching vibration of carbonyl $\nu(\text{C=O})$, implying the existence of benzaldehyde species [30, 62]. The bands appeared at 1584 and 1550 cm^{-1} were related to skeletal C-C stretching vibrations and antisymmetric C-O stretching of benzoate species [61]. Furthermore, the dominant bands at 1401, 1424, 1535 and 1560 cm^{-1} indicated the presence of carboxylate group [63, 64]. The increased intensities of carbonyl and carboxylate peaks with reaction time indicated the aggregation of benzaldehyde and benzoate on the catalyst surface, implying that these two species should be the important intermediates during the oxidation of toluene. Additionally, the $\Delta\nu$ value (159 cm^{-1}) between symmetric (1401 cm^{-1}) and asymmetric (1560 cm^{-1}) stretching vibrations of $\nu(\text{C=O})$ in benzoate species was close to the free ion value, which is a feature of bridging structure between carboxylate and metal ion on the catalyst surface [63, 64]. It is worth noting that several peaks appeared at 1741, 1780, 1825 and 1854 cm^{-1} slowly became obvious with the prolongation of reaction time, which are associated with the asymmetric and symmetric $\nu(\text{C=O})$ stretching vibrations of adsorbed cyclic anhydride species, reflecting the formation of maleic anhydride [5, 36]. This phenomenon

indicated that benzoate had undergone further deep oxidation with the active oxygen of CoMn6 catalyst to form anhydride species. By comparing the accumulation rates of the benzoate and anhydride species on the catalyst surface, it could be concluded that the C=C breakage of the aromatic ring to form dehydrated anhydride was the rate-controlling step in toluene oxidation. The characteristic absorption bands of carbon dioxide and water molecules were also detected at about 2300-2400 and 3410-3480 cm^{-1} , respectively, proving that some toluene molecules had undergone the final oxidation process to form small molecular products [64, 65]. Fig. 3.9b monitored the time-dependent DRIFTS spectra of the toluene catalytic process over CoMn6 catalyst at 218 °C in a nitrogen atmosphere. Some weak infrared absorption peaks related to aromatic ring, benzyl and benzyl alcohol appeared in the low-frequency region (1000-1360 cm^{-1}). The bands related to carbon dioxide and water also appeared at around 2350 and 3440 cm^{-1} , respectively, indicating that a small amount of deep oxidation of toluene could occur in the absence of gaseous oxygen. The main characteristic peak relating to benzaldehyde carbonyl still appeared at ca. 1630 cm^{-1} , and the peaks of carboxyl groups were also detected at 1389, 1425, 1535 and 1550 cm^{-1} , which also proved that toluene could be oxidized to the key intermediates by the active lattice oxygen species in the CoMn6 catalyst in the absence of gaseous oxygen. However, the relative intensity of benzoate peaks in a nitrogen atmosphere was significantly lower than that in the air atmosphere. The reason should be that the limited intrinsic active lattice oxygen and adsorbed oxygen species in the CoMn6 catalyst would not be resurged after participating in the oxidation reaction in the nitrogen atmosphere so that the continuous oxidation process of toluene and intermediates could not be maintained. With the reaction time increasing, the characteristic peak intensity of benzaldehyde was weakened, accompanied with the slightly enhanced of benzoate peaks. In addition, the maleic anhydride peaks increased first and then decreased with the time increasing, which also demonstrated that even in the presence of residual benzoate, insufficient oxidative capacity was hard to promote the rate controlling step, i.e., the conversion of benzoate to maleic anhydride. Fig. 3.9c shows the effect of 5 vol.% water vapor on the generation and conversion of intermediates during the toluene oxidation process over

the CoMn6 catalyst in the air atmosphere. Infrared absorption peaks related to aromatic ring, benzyl alcohol and benzyl were found in the low frequency region, obvious carbonyl peaks related to aldehydes appeared at 1637-1723 cm^{-1} , and the strong carboxyl peaks associated with benzoate existed at 1423, 1548 and 1561 cm^{-1} . However, the peaks of the cyclic anhydride at 1740-1800 cm^{-1} were negligible, which indicated that the presence of water had no obvious effect on the generation of the alcohol, aldehyde, benzoate intermediates. However, the presence of water vapor affected the chemical reaction equilibrium, which should be not conducive to the formation of maleic anhydride by C=C breaking. Another reason should be that water molecules and reactant molecules competed for adsorption on the catalyst surface, which reduced the contact probability between reactants and active sites, thus inhibiting the catalytic performance of the CoMn6 catalyst. Fig. 3.9d and 3.9e show the time-dependent DRIFTS spectra of catalytic oxidation of toluene over the MnO_x catalyst at 218 °C in air (Fig. 3.9d) and nitrogen (Fig. 3.9e) atmospheres, respectively. It is obvious that the distributions of toluene oxidation intermediates over the MnO_x catalyst in two atmospheres were much simpler than those in the CoMn6 catalysis system, which should be attributed to the low degree and incomplete oxidation of toluene, resulting from the lack of abundant and diverse active sites in the pure MnO_x sample. The contents of low-frequency intermediates, such as benzyl alcohol and benzyl produced on MnO_x catalyst surface were obvious, while the characteristic peaks of benzoate and benzaldehyde species were weaker, which indicated that toluene adsorbed on the surface of MnO_x catalyst could be converted into inferior intermediates easily. However, due to the unsatisfactory low-temperature oxidation performance, benzyl and benzyl alcohol could not be oxidized into those intermediates such as benzoate and benzaldehyde continuously. As a result, the rate-controlling step of forming anhydrides was hard to occur, which was demonstrated by the unobserved anhydride, weaker carbon dioxide and water peaks.

By comparing Fig. 3.9a and 3.9b, the deep oxidation process of toluene on the surface of CoMn6 catalyst could occur in both oxygen-presence and oxygen-absence environments. Herein, the difference was that the intensity of benzaldehyde peak in

oxygen-presence environment was lower than that of benzoate, whereas the opposite was true in the oxygen-absence environment. Moreover, the oxygen-presence oxidation process produced more maleic anhydride than the oxygen-absence catalysis process. Therefore, it could be concluded that the surface lattice oxygen of the catalyst can participate in the incompletely deep oxidation of toluene as electron donor and oxygen source. By comparing Fig. 3.9b and 3.9e, the formation of benzoate species due to the participation of lattice oxygen in MnO_x catalyst was much lower than that by using the CoMn6 catalyst. As stated above, since CoMn6 catalyst had abundant active lattice oxygen and superior lattice oxygen mobility, it should be more beneficial for the formation of benzoate species. While, by comparing Fig. 3.9a and 3.9d, it is obvious that the toluene deep oxidation intermediates (benzoate and maleic anhydride) and complete oxidation products (CO_2 and water) produced on the CoMn6 catalyst were far more than those on the pure MnO_x catalyst. This phenomenon should be attributed to the fact that the CoMn6 catalyst assembled by oxidation-etching of MOF precursor provided enough active electrophilic adsorbed oxygen species, which are prone to perform ring-opening attack on the aromatic ring carrying high-density electron regions, and finally resulted in complete oxidation. Moreover, the gaseous O_2 molecules in the reaction feedstock were adsorbed and then activated by the abundant structural defects such as edge dislocations, oxygen vacancies, and phase interfaces in the CoMn6 catalyst, thereby continuously providing highly active electrophilic adsorption oxygen species, which could not only participate in the deep oxidation of toluene, but also replenish and restore the consumed lattice oxygen species in the catalyst so that the catalyst maintained high-performance cyclability [59].

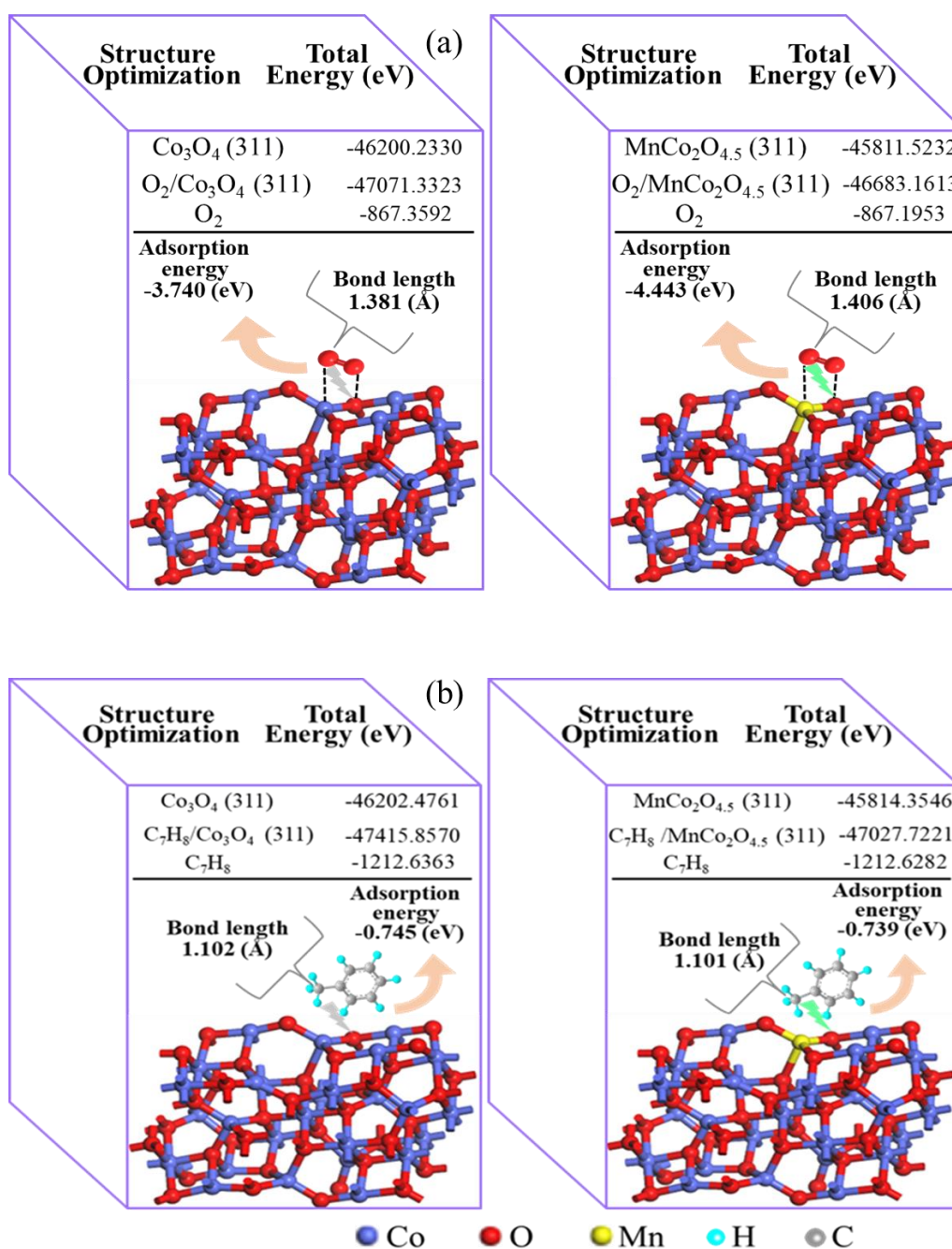


Fig. 3.10. Diagram of DFT calculation results for adsorption energies and bond lengths of O₂ (a) and toluene (b) molecules adsorbed on MnCo₂O_{4.5} and Co₃O₄ phases.

Furthermore, due to the formation of spinel MnCo₂O_{4.5} with low crystallinity in the CoMn6 catalyst, the adsorption energies and bond lengths of O₂ and toluene molecules adsorbed on MnCo₂O_{4.5} (311) and Co₃O₄ (311) planes were simulated by DFT calculations. As seen from Fig. 3.10a, the adsorption energy of O₂ molecules on MnCo₂O_{4.5} (311, -4.443 eV) was stronger than that on the Co₃O₄ plane (311, -3.740 eV), indicating the stronger chemisorption capacity for O₂ molecules on the MnCo₂O_{4.5}

(311) plane. In addition, compared with the isolated O₂ molecules, the bond lengths of adsorbed O₂ molecules on the MnCo₂O_{4.5} (311) and Co₃O₄ (311) planes were stretched from 1.240 to 1.406 and 1.381 Å, respectively, which indicated that O₂ molecules should have different degrees of stretching motion on the catalyst surface, and O₂ molecules could be more easily activated on the MnCo₂O_{4.5} phase in the CoMn6 catalyst due to the weak constraints of oxygen atoms with a longer bond length. It can be seen from Fig. 3.10b that the adsorption energy and bond length (C-H) of toluene molecules on MnCo₂O_{4.5} (311) and Co₃O₄ (311) planes were basically the same, which indicates that the spinel structure could mainly improve the adsorption capacity of oxygen molecules. Therefore, the spinel MnCo₂O_{4.5} region in the CoMn6 catalyst should play an important role in the adsorbing and activating of O₂ molecules, which could mutually assist with the above-mentioned kinds of active regions/species to promote toluene oxidation ability of the CoMn6 catalyst.

According to the above analysis, a reliable catalytic toluene combustion mechanism over the MnCo6 catalyst was proposed and illustrated in Fig. 3.9f. That is, the toluene molecule is physically adsorbed on the catalyst surface at first and then, even weak oxidation capacity could promote the dehydrogenation of toluene to form benzyl group (Ph-CH₂-), which can be adsorbed on the catalyst surface stably by a chemical action. Soon, the adsorbed benzyl species could be converted to benzyl alcohol (Ph-CH₂-O-) quickly, but it requires the participation of electrophilic adsorbed oxygen or active lattice oxygen species on the surface of catalyst. Afterwards, more active lattice oxygen species should be required to supply and participate in the further oxidation of benzyl alcohol (Ph-CH₂-O-) to benzaldehyde (Ph-CHO) and then to benzoate (Ph-COO-), which are the key intermediates in the toluene oxidation with the occurrence of deep oxidation. After that, the generated benzoate can be attacked by electrophilic highly reactive adsorbed oxygen to generate maleic anhydride, which could be oxidized to water and carbon dioxide easily. Since the formation of electrophilic adsorbed oxygen generally requires the catalyst to contain abundant active centers, the conversion of intermediate to maleic anhydride will become the rate-controlling step of toluene oxidation. Therefore, the low crystalline and amorphous structure in the CoMn6

catalyst could provide excellent lattice oxygen mobility whereas the active centers such as dislocations, vacancies, and interfaces could adsorb/activate O₂ molecules, which will play an important role in the toluene oxidation.

Table 3.4 Assignments of main IR bands appearing in the *in situ* experiments of toluene combustion over the CoMn6 catalyst.

Wavenumber/cm ⁻¹	Assignment	Corresponding structure
1019	in-plane bending vibration for C-H	aromatic ring
1479, ~2932	asymmetric deformation and symmetric stretching vibration of ν (C-H)	methyl
1190, 1506	antisymmetric ν (C-C) stretching vibration and skeleton ν (C=C) vibrations	aromatic ring
1306, 1343	deformation vibration and in-plane bending vibration from the methylene	benzyl
1057, 1083	stretching vibrations of C-O in alcohols species	benzyl alcohol
~1242	ν (C-O) stretching vibrations in phenolate	phenol
1630-1727	stretching vibrations of ν (C=O) in carbonyl	benzaldehyde
1550	antisymmetric ν (C-O) stretching of carboxyl	benzoate
1401, 1560	symmetric and asymmetric stretching vibrations of ν (C=O) in carboxylate	benzoate
3410-3480	ν (O-H) stretching vibrations	water
1741, 1780, 1825, 1854	symmetric and asymmetric stretching vibrations of ν (C=O) in anhydride	maleic anhydride
2300-2400	asymmetric stretching vibrations of ν (C=O)	carbon dioxide

3.4 Conclusions

In summary, the nanosheet-state CoMnx mixed oxide catalysts for toluene combustion at low temperatures were successfully synthesized using an assembly strategy of oxidation-etching of MOF precursor. Based on the catalyst characterizations, toluene combustion experiments, in-situ measurements and DFT calculations, the following conclusions were reached:

(I) The suitable oxidation-etching process assembled enough mesoporous structures in the CoMnx catalysts with the increased SSA from 30 m²/g (CoO_x) to 163 m²/g (CoMn6), which not only reduced the mass transfer resistance of toluene molecules in the catalyst, but also increased the exposure of more active sites. Especially, the multifarious abundant active regions, i.e., amorphous structure, low crystallinity phase, dislocation region, phase interface region, were efficiently constructed by the oxidation-etching route in the preparation of CoMn6 catalyst, which greatly improved the low-temperature reducibility and oxygen mobility in the catalyst, providing the continuously sufficient reactive oxygen species for toluene oxidation process.

(II) The optimal CoMn6 catalyst exhibited the most abundant Mn^{3+} , Co^{3+} , and active adsorbed oxygen species with more oxygen vacancies, attributing to the strong interaction between manganese and cobalt species during the oxidation-etching assembly process.

(III) The DFT calculation results showed that the O_2 molecules adsorbed on the $\text{MnCo}_2\text{O}_{4.5}$ (311) plane has a longer bond length (1.406 Å) with stronger adsorption energy (-4.443 eV), indicating that the O_2 molecules could be more easily adsorbed and activated on $\text{MnCo}_2\text{O}_{4.5}$ structure in the CoMn6 catalyst.

(IV) Based on the in situ DRIFTS spectra under different atmospheres for the oxidation of toluene on the CoMn6 catalyst. It is found that the oxidation of toluene required sufficient adsorbed oxygen species and active lattice oxygen. The adsorbed oxygen originated from the activation of gaseous oxygen by the crystal defect regions (i.e., dislocations, oxygen vacancies and phase interfaces) and the active lattice oxygen originated from the abundant amorphous crystal and low crystallinity structure in the CoMn6 catalyst played important roles in the catalysis process. In addition, the consumed lattice oxygen could be restored by the activated electrophilic oxygen species.

(V) As a result, the synergistic complementary effects of different active regions contributed to the continuous and efficient catalytic combustion of toluene over the CoMn6 catalyst with 90% conversion of 1,000 ppm toluene under a WHSV of 60,000 $\text{cm}^3 \cdot \text{g}^{-1} \cdot \text{h}^{-1}$ at 219 °C.

References

- [1] Y. Guo, M. Wen, G. Li, T. An, Recent advances in VOC elimination by catalytic oxidation technology onto various nanoparticles catalysts: a critical review, *Appl. Catal. B: Environ.*, 281 (2021) 119447.
- [2] J. Chen, X. Chen, X. Chen, W. Xu, Z. Xu, H. Jia, J. Chen, Homogeneous introduction of CeO_y into MnO_x -based catalyst for oxidation of aromatic VOCs, *Appl. Catal. B: Environ.*, 224 (2018) 825-835.
- [3] S.I. Suárez-Vázquez, S. Gil, J.M. García-Vargas, A. Cruz-López, A. Giroir-Fendler, Catalytic oxidation of toluene by $\text{SrTi}_{1-x}\text{B}_x\text{O}_3$ ($\text{B} = \text{Cu}$ and Mn) with dendritic morphology synthesized by one pot hydrothermal route, *Appl. Catal. B: Environ.*, 223 (2018) 201-208.
- [4] Y. Shu, J. Ji, Y. Xu, J. Deng, H. Huang, M. He, D.Y.C. Leung, M. Wu, S. Liu, S. Liu, G. Liu, R. Xie, Q. Feng, Y. Zhan, R. Fang, X. Ye, Promotional role of Mn doping on catalytic oxidation of VOCs over mesoporous TiO_2 under vacuum ultraviolet (VUV) irradiation, *Appl. Catal. B: Environ.*, 220 (2018) 78-87.
- [5] P. Wang, J. Wang, X. An, J. Shi, W. Shangguan, X. Hao, G. Xu, B. Tang, A. Abudula, G. Guan, Generation of abundant defects in Mn-Co mixed oxides by a facile agar-gel method for highly efficient catalysis of total toluene oxidation, *Appl. Catal. B: Environ.*, 282 (2021) 119560.
- [6] X. Zhang, X. Lv, F. Bi, G. Lu, Y. Wang, Highly efficient Mn_2O_3 catalysts derived from Mn-MOFs for toluene oxidation: The influence of MOFs precursors, *Mol. Catal.*, 482 (2020) 110701.
- [7] Y. Wei, L. Ni, M. Li, J. Zhao, A template-free method for preparation of MnO_2 catalysts with high surface areas, *Catal. Today*, 297 (2017) 188-192.
- [8] Y. Liao, M. Fu, L. Chen, J. Wu, B. Huang, D. Ye, Catalytic oxidation of toluene over nanorod-structured Mn-Ce mixed oxides, *Catal. Today*, 216 (2013) 220-228.
- [9] Z. Ye, J.M. Giraudon, N. Nuns, P. Simon, N. De Geyter, R. Morent, J.F. Lamonier, Influence of the preparation method on the activity of copper-manganese oxides for toluene total oxidation, *Appl. Catal. B: Environ.*, 223 (2018) 154-166.
- [10] Y. Peng, L. Zhang, L. Chen, D. Yuan, G. Wang, X. Meng, F.-S. Xiao, Catalytic

performance for toluene abatement over Al-rich Beta zeolite supported manganese oxides, *Catal. Today*, 297 (2017) 182-187.

[11] C. Zhang, Y. Guo, Y. Guo, G. Lu, A. Boreave, L. Retaillieu, A. Baylet, A. Giroir-Fendler, LaMnO_3 perovskite oxides prepared by different methods for catalytic oxidation of toluene, *Appl. Catal. B: Environ.*, 148-149 (2014) 490-498.

[12] Y. Wang, L. Zhang, L. Guo, Enhanced toluene combustion over highly homogeneous iron manganese oxide nanocatalysts, *ACS Appl. Nano Mater.*, 1 (2018) 1066-1075.

[13] X. Zhang, F. Hou, Y. Yang, Y. Wang, N. Liu, D. Chen, Y. Yang, A facile synthesis for cauliflower like CeO_2 catalysts from Ce-BTC precursor and their catalytic performance for CO oxidation, *Appl. Surf. Sci.*, 423 (2017) 771-779.

[14] C. Wang, C. Zhang, W. Hua, Y. Guo, G. Lu, S. Gil, A. Giroir-Fendler, Catalytic oxidation of vinyl chloride emissions over Co-Ce composite oxide catalysts, *Chem. Eng. J.*, 315 (2017) 392-402.

[15] J. Chen, X. Chen, W. Xu, Z. Xu, J. Chen, H. Jia, J. Chen, Hydrolysis driving redox reaction to synthesize Mn-Fe binary oxides as highly active catalysts for the removal of toluene, *Chem. Eng. J.*, 330 (2017) 281-293.

[16] W. Tang, Y. Deng, W. Li, J. Li, G. Liu, S. Li, X. Wu, Y. Chen, Importance of porous structure and synergistic effect on the catalytic oxidation activities over hierarchical Mn-Ni composite oxides, *Catal. Sci. Technol.*, 6 (2016) 1710-1718.

[17] P. Yang, S. Fan, Z. Chen, G. Bao, S. Zuo, C. Qi, Synthesis of Nb_2O_5 based solid superacid materials for catalytic combustion of chlorinated VOCs, *Appl. Catal. B: Environ.*, 239 (2018) 114-124.

[18] S. Akram, Z. Wang, L. Chen, Q. Wang, G. Shen, N. Han, Y. Chen, G. Ge, Low-temperature efficient degradation of ethyl acetate catalyzed by lattice-doped CeO_2 - CoO_x nanocomposites, *Catal. Commun.*, 73 (2016) 123-127.

[19] M. Zabihi, F. Khorasheh, J. Shayegan, Supported copper and cobalt oxides on activated carbon for simultaneous oxidation of toluene and cyclohexane in air, *RSC Adv.*, 5 (2015) 5107-5122.

[20] X. Zhang, M. Zhao, Z. Song, H. Zhao, W. Liu, J. Zhao, Z.a. Ma, Y. Xing, The

effect of different metal oxides on the catalytic activity of a Co_3O_4 catalyst for toluene combustion: importance of the structure-property relationship and surface active species, *New J. Chem.*, 43 (2019) 10868-10877.

[21] C.-W. Ahn, Y.-W. You, I. Heo, J.S. Hong, J.-K. Jeon, Y.-D. Ko, Y. Kim, H. Park, J.-K. Suh, Catalytic combustion of volatile organic compound over spherical-shaped copper-manganese oxide, *J. Ind. Eng. Chem.*, 47 (2017) 439-445.

[22] C. Dong, Z. Qu, Y. Qin, Q. Fu, H. Sun, X. Duan, Revealing the highly catalytic performance of spinel CoMn_2O_4 for toluene oxidation: involvement and replenishment of oxygen species using in situ designed-TP techniques, *ACS Catal.*, 9 (2019) 6698-6710.

[23] Y. Wang, L. Guo, M. Chen, C. Shi, CoMn_xO_y nanosheets with molecular-scale homogeneity: an excellent catalyst for toluene combustion, *Catal. Sci. Technol.*, 8 (2018) 459-471.

[24] W. Zhao, Y. Zhang, X. Wu, Y. Zhan, X. Wang, C.-T. Au, L. Jiang, Synthesis of Co-Mn oxides with double-shelled nanocages for low-temperature toluene combustion, *Catal. Sci. Technol.*, 8 (2018) 4494-4502.

[25] Y. Luo, Y. Zheng, J. Zuo, X. Feng, X. Wang, T. Zhang, K. Zhang, L. Jiang, Insights into the high performance of Mn-Co oxides derived from metal-organic frameworks for total toluene oxidation, *J. Hazard. Mater.*, 349 (2018) 119-127.

[26] H. Liu, Z. Chen, L. Zhou, X. Li, K. Pei, J. Zhang, Y. Song, F. Fang, R. Che, D. Sun, Rooting bismuth oxide nanosheets into porous carbon nanoboxes as a sulfur immobilizer for lithium-sulfur batteries, *J. Mater. Chem., A* 7 (2019) 7074-7081.

[27] Y. Zheng, Q. Liu, C. Shan, Y. Su, K. Fu, S. Lu, R. Han, C. Song, N. Ji, D. Ma, Defective Ultrafine MnO_x Nanoparticles Confined within a Carbon Matrix for Low-Temperature Oxidation of Volatile Organic Compounds, *Environ. Sci. Technol.*, 55 (2021) 5403-5411.

[28] Y. Zheng, Y. Liu, H. Zhou, W. Huang, Z. Pu, Complete combustion of methane over Co_3O_4 catalysts: influence of pH values, *J. Alloy. Comp.*, 734 (2018) 112-120.

[29] Z. Qu, K. Gao, Q. Fu, Y. Qin, Low-temperature catalytic oxidation of toluene over nanocrystal-like Mn-Co oxides prepared by two-step hydrothermal method, *Catal.*

Commun., 52 (2014) 31-35.

[30] X. Yang, X. Ma, X. Yu, M. Ge, Exploration of strong metal-support interaction in zirconia supported catalysts for toluene oxidation, *Appl. Catal. B: Environ.*, 263 (2020) 118355.

[31] Z. Cheng, Z. Chen, J. Li, S. Zuo, P. Yang, Mesoporous silica-pillared clays supported nanosized $\text{Co}_3\text{O}_4\text{-CeO}_2$ for catalytic combustion of toluene, *Appl. Sur. Sci.*, 459 (2018) 32-39.

[32] Z. Sihaib, F. Puleo, J.M. Garcia-Vargas, L. Retailleau, C. Descorme, L.F. Liotta, J.L. Valverde, S. Gil, A. Giroir-Fendler, Manganese oxide-based catalysts for toluene oxidation, *Appl. Catal. B: Environ.*, 209 (2017) 689-700.

[33] G. Li, C. Zhang, Z. Wang, H. Huang, H. Peng, X. Li, Fabrication of mesoporous Co_3O_4 oxides by acid treatment and their catalytic performances for toluene oxidation, *Appl. Catal. A: Gen.*, 550 (2018) 67-76.

[34] Y. Zhang, F. Tao, S. Cao, K. Yin, X. Chang, R. Fan, C. Fan, L. Dong, Y. Yin, X. Chen, Hierarchical $\text{K}_2\text{Mn}_4\text{O}_8$ nanoflowers: A novel photothermal conversion material for efficient solar vapor generation, *Sol. Energ. Mat. and Sol. C.*, 200 (2019) 110043.

[35] Q. Zhang, X. Liu, W. Fan, Y. Wang, Manganese-promoted cobalt oxide as efficient and stable non-noble metal catalyst for preferential oxidation of CO in H_2 stream, *Appl. Catal. B: Environ.*, 102 (2011) 207-214.

[36] P. Wang, J. Wang, J. Zhao, X. Ma, X. Du, S. Peng, X. Hao, B. Tang, A. Abudula, G. Guan, Trace holmium assisting delaminated OMS-2 catalysts for total toluene oxidation at low temperature, *J. Colloid Interface Sci.*, 608 (2022) 1662-1675.

[37] D.A. Aguilera, A. Perez, R. Molina, S. Moreno, Cu-Mn and Co-Mn catalysts synthesized from hydrotalcites and their use in the oxidation of VOCs, *Appl. Catal. B: Environ.*, 104 (2011) 144-150.

[38] J. Mei, Z. Qu, S. Zhao, X. Hu, H. Xu, N. Yan, Promoting effect of Mn and Ti on the structure and performance of Co_3O_4 catalysts for oxidation of dibromomethane, *J. Ind. Eng. Chem.*, 57 (2018) 208-215.

[39] L. Zhao, Z. Zhang, Y. Li, X. Leng, T. Zhang, F. Yuan, X. Niu, Y. Zhu, Synthesis of Ce_aMnO_x hollow microsphere with hierarchical structure and its excellent catalytic

- performance for toluene combustion, *Appl. Catal. B: Environ.*, 245 (2019) 502-512.
- [40] P. Venkataswamy, K.N. Rao, D. Jampaiah, B.M. Reddy, Nanostructured manganese doped ceria solid solutions for CO oxidation at lower temperatures, *Appl. Catal. B: Environ.*, 162 (2015) 122-132.
- [41] X. Li, J. Zheng, S. Liu, T. Zhu, A novel wormhole-like mesoporous hybrid MnCoO_x catalyst for improved ethanol catalytic oxidation, *J. Colloid Interface Sci.*, 555 (2019) 667-675.
- [42] L. Li, F. Jing, J. Yan, J. Jing, W. Chu, Highly effective self-propagating synthesis of CeO_2 -doped MnO_2 catalysts for toluene catalytic combustion, *Catal. Today*, 297 (2017) 167-172.
- [43] J. Du, Z. Qu, C. Dong, L. Song, Y. Qin, N. Huang, Low-temperature abatement of toluene over Mn-Ce oxides catalysts synthesized by a modified hydrothermal approach, *Appl. Surf. Sci.*, 433 (2018) 1025-1035.
- [44] X. Jiang, W. Xu, S. Lai, X. Chen, Integral structured Co-Mn composite oxides grown on interconnected Ni foam for catalytic toluene oxidation, *RSC Adv.*, 9 (2019) 6533-6541.
- [45] S. Mo, Q. Zhang, J. Li, Y. Sun, Q. Ren, S. Zou, Q. Zhang, J. Lu, M. Fu, D. Mo, J. Wu, H. Huang, D. Ye, Highly efficient mesoporous MnO_2 catalysts for the total toluene oxidation: Oxygen-Vacancy defect engineering and involved intermediates using in situ DRIFTS, *Appl. Catal. B: Environ.*, 264 (2020) 118464.
- [46] J. Mei, J. Xie, Z. Qu, Y. Ke, X. Hu, N. Yan, Ordered mesoporous spinel Co_3O_4 as a promising catalyst for the catalytic oxidation of dibromomethane, *Mol. Catal.*, 461 (2018) 60-66.
- [47] X. Xie, Y. Li, Z.Q. Liu, M. Haruta, W. Shen, Low-temperature oxidation of CO catalysed by Co_3O_4 nanorods, *Nature*, 458 (2009) 746-749.
- [48] G. Zhou, X. He, S. Liu, H. Xie, M. Fu, Phenyl VOCs catalytic combustion on supported CoMn/AC oxide catalyst, *J. Ind. Eng. Chem.*, 21 (2015) 932-941.
- [49] Z. Han, Y. Liu, J. Deng, S. Xie, X. Zhao, J. Yang, K. Zhang, H. Dai, Preparation and high catalytic performance of Co_3O_4 - MnO_2 for the combustion of o-xylene, *Catal. Today*, 327 (2019) 246-253.

- [50] X. Zhu, S. Liu, Y. Cai, X. Gao, J. Zhou, C. Zheng, X. Tu, Post-plasma catalytic removal of methanol over Mn-Ce catalysts in an atmospheric dielectric barrier discharge, *Appl. Catal. B: Environ.*, 183 (2016) 124-132.
- [51] J.-J. Li, E.-Q. Yu, S.-C. Cai, X. Chen, J. Chen, H.-P. Jia, Y.-J. Xu, Noble metal free, $\text{CeO}_2/\text{LaMnO}_3$ hybrid achieving efficient photo-thermal catalytic decomposition of volatile organic compounds under IR light, *Appl. Catal. B: Environ.*, 240 (2019) 141-152.
- [52] X. Yang, X. Yu, M. Lin, X. Ma, M. Ge, Enhancement effect of acid treatment on Mn_2O_3 catalyst for toluene oxidation, *Catal. Today*, 327 (2019) 254-261.
- [53] S. Mo, Q. Zhang, Y. Sun, M. Zhang, J. Li, Q. Ren, M. Fu, J. Wu, L. Chen, D. Ye, Gaseous CO and toluene co-oxidation over monolithic core-shell Co_3O_4 -based hetero-structured catalysts, *J. Mater. Chem. A*, 7 (2019) 16197-16210.
- [54] S.B.T. Tran, H. Choi, S. Oh, J.Y. Park, Defective Nb_2O_5 -supported Pt catalysts for CO oxidation: Promoting catalytic activity via oxygen vacancy engineering, *J. Catal.*, 375 (2019) 124-134.
- [55] Y. Guan, Y. Zhou, S. Wang, R. Zou, J. Zhang, X. Fan, Y. Jiao, Structured cobalt-manganese oxides on SiC nano-whisker modified SiC foams for catalytic combustion of toluene, *Chem. Eng. Res. Des.*, 177 (2022) 659-669.
- [56] H. Zhao, H. Wang, Z. Qu, Synergistic effects in Mn-Co mixed oxide supported on cordierite honeycomb for catalytic deep oxidation of VOCs, *J. Environ. Sci.*, 112 (2022) 231-243.
- [57] D. Han, X. Ma, X. Yang, M. Xiao, H. Sun, L. Ma, X. Yu, M. Ge, Metal organic framework-templated fabrication of exposed surface defect-enriched Co_3O_4 catalysts for efficient toluene oxidation, *J. Colloid Interface Sci.*, 603 (2021) 695-705.
- [58] W. Gu, C. Li, J. Qiu, J. Yao, Facile preparation of porous hollow $\text{Co}_x\text{Mn}_{3-x}\text{O}_4$ normal-reverse coexisted spinel for toluene oxidation, *J. Alloy. Comp.*, 892 (2022) 162185.
- [59] P. Liu, Y. Liao, J. Li, L. Chen, M. Fu, P. Wu, R. Zhu, X. Liang, T. Wu, D. Ye, Insight into the effect of manganese substitution on mesoporous hollow spinel cobalt oxides for catalytic oxidation of toluene, *J. Colloid Interface Sci.*, 594 (2021) 713-726.

- [60] Q. Ren, S. Mo, J. Fan, Z. Feng, M. Zhang, P. Chen, J. Gao, M. Fu, L. Chen, J. Wu, D. Ye, Enhancing catalytic toluene oxidation over $\text{MnO}_2@\text{Co}_3\text{O}_4$ by constructing a coupled interface, *Chinese J. Catal.*, 41 (2020) 1873-1883.
- [61] C. Zhang, C. Wang, H. Huang, K. Zeng, Z. Wang, H.-p. Jia, X. Li, Insights into the size and structural effects of zeolitic supports on gaseous toluene oxidation over $\text{MnO}_x/\text{HZSM-5}$ catalysts, *Appl. Sur. Sci.*, 486 (2019) 108-120.
- [62] Z. Rui, M. Tang, W. Ji, J. Ding, H. Ji, Insight into the enhanced performance of TiO_2 nanotube supported Pt catalyst for toluene oxidation, *Catal. Today*, 297 (2017) 159-166.
- [63] H. Sun, Z. Liu, S. Chen, X. Quan, The role of lattice oxygen on the activity and selectivity of the OMS-2 catalyst for the total oxidation of toluene, *Chem. Eng. J.*, 270 (2015) 58-65.
- [64] P. Wang, J. Zhao, Q. Zhao, X. Ma, X. Du, X. Hao, B. Tang, A. Abudula, G. Guan, Microwave-assisted synthesis of manganese oxide catalysts for total toluene oxidation, *J. Colloid Interface Sci.*, 607 (2021) 100-110.
- [65] A. Lu, H. Sun, N. Zhang, L. Che, S. Shan, J. Luo, J. Zheng, L. Yang, D.-L. Peng, C.-J. Zhong, B. Chen, Surface partial-charge-tuned enhancement of catalytic activity of platinum nanocatalysts for toluene oxidation, *ACS Catal.*, 9 (2019) 7431-7442.

CHAPTER 4 Biostarch-assisted synthesis of microscopic heterogeneous manganese-cobalt oxides for efficient catalytic combustion of toluene

4.1 Introduction

Volatile organic compounds (VOCs) released from transportation, industrial process and other human daily activities always participate in the formation of air pollution, e.g., photochemical smog, tropospheric ozone and inhalable particulate matters, which has shown strong corrosiveness to the environment and carcinogenicity to animals and plants [1, 2]. Compared with other methods including biodegradation, incineration, adsorption, wet oxidative treatments and photocatalysis, catalytic combustion is considered as a promising VOC elimination route since its ideal efficiency, low operating temperature and non-secondary pollution [3, 4]. Therewith, the development of novel, efficient, durable and inexpensive catalysts is of great application significance.

Although supported noble metal catalysts (e.g., Pd, Pt, Au and Ag) exhibit outstanding catalytic performance for VOCs combustion, their high price and unsatisfactory stability have long motivated the search and development for substitute catalysts [5-7]. Recently, it is found that doping-modified binary transition metal oxide catalysts such as MnCu, CoMn [8], MnZr [9], CoNi [10], CoLa [11], CeCu and CeCr [12] generally exhibit the advantages of low price, high thermal stability and good reducibility. Among them, Mn-based ones synthesized via various approaches usually have potential catalytic performance in VOC combustion owing to their structural flexibility and multivalence. Chen et al. [13] synthesized a series of Mn-Fe mixed catalysts by a hydrolysis driving redox reaction method, which displayed vast specific surface areas (SSAs) and abundant Mn^{3+} species with good toluene oxidation performance. Ye et al. [14] prepared two MnCuO_x mixed oxide catalysts using either co-precipitation and redox-precipitation methods, and the MnCuO_x catalyst synthesized using the latter method showed better toluene oxidation performance than that prepared by the coprecipitation method, resulting from the better dispersion of Cu and Mn

species and more exposed active sites. Delimaris et al. [15] prepared a $\text{MnO}_x\text{-CeO}_2$ catalyst through urea combustion way and showed lower reducible temperature as well as larger SSA, which counterbalanced their ordinary specific activity in VOC combustion. Tang et al. [16] constructed a series of hierarchically porous Mn-Ni mixed catalysts with an oxalate route, which exhibited outstanding reducibility at low temperature and enough surface-adsorbed oxygen species due to the synergetic effect between Mn and Ni species. As a result, the benzene catalytic performance was greatly enhanced. Hence, the introduction of heteroatoms in manganese oxides could optimize the physicochemical properties (e.g., SSA, porous structure, exposure of active sites and low-temperature reducibility), thereby improving the VOC catalytic performance. It is worth mentioning that Co species in those spinel materials also has multiple valence states due to the inherent tetrahedral and octahedral structures, in which part of the Co ions could be easily replaced by Mn to form an amorphous or partially defective spinel structure, and thus contributed the generation of Co-O-Mn bonds with low bond energy within the catalyst network, resulting in the improving of oxygen mobility in VOCs oxidation processes. Ren et al. [17] designed a $\text{MnO}_2@\text{Co}_3\text{O}_4$ core-shell catalyst by calcining ZIF-67 grown on a 1D $\alpha\text{-MnO}_2$ material, which showed affluent surface-adsorbed oxygen species owing to the synergistic effect between MnO_2 and Co_3O_4 species resulting from the coupled interfaces, thereby accelerating the oxygen mobility in toluene oxidation. Li et al. [18] prepared a series of wormhole-like amorphous MnCoO_x catalysts induced by the solid solution effect using a template modified sol-gel method, which showed better catalytic performance since they contained more $\text{Co}^{3+}/\text{Mn}^{4+}$ species, stronger reducibility and more uniform active site distribution. Han et al. [19] constructed a kind of $\text{MnO}_x/\text{Co}_3\text{O}_4$ catalyst via impregnating Mn species into Co_3O_4 framework derived from ZIF-67, and found that the occupation of surface Mn in octahedral Co^{3+} sites would cause local but not bulk lattice disorder, which significantly increased the reducibility at a low temperature as well as the effective mobility of lattice oxygen species in virtue of highly exposed local surface defect structures and predominate surface Co^{3+} sites. Liu et al. [20] prepared a kind of mesoporous hollow Mn-substituted Co_3O_4 catalyst according to a modified

solvothermal alcoholysis route, in which the locally disordered spinel structure and mesoporous hollow microsphere structure formed by the atomic substitution process endowed the more surface chemisorbed oxygen species and larger SSA in 5CoMn sample, thus improving the performance for the catalytic oxidation of toluene. It could be seen that those factors including SSA, crystal structure, surface oxygen species, metal ion valence, and reducibility of catalyst could play key roles in the VOC catalytic oxidation performance. Contrary to the conventional view, the formation of moderate local heterostructures in catalysts should be beneficial to the generation of active defect structures. Moreover, the optimization of phase interface concentration could promote the activation of gas phase oxygen and enhance lattice oxygen mobility. Nevertheless, the synthesis of catalysts with multiple active regions/sites for the combustion of VOCs and the dissecting of the synergistic complementarity between active regions/sites are rarely mentioned.

Herein, a nanoparticles-stacking MnCo_x oxide with multifarious active phases and moderate single-electron defect structures was successfully constructed by the assistance of multifunctional starch paste for the first time. The synergistic and complementary effects between the different active regions with appropriate defect structures in the optimal catalyst resulted in the continuous excellent catalytic combustion performance of toluene at low temperature. The physicochemical properties of the obtained MnCo_x oxides were analyzed by various characterizations. In addition, the catalytic combustion process of toluene was analyzed by combining in situ diffuse reflectance infrared spectroscopy (DRIFTS) analyses and density functional theory (DFT) calculations. This study provided an original, green and cheap catalyst synthesis method, which may be considered as a facile route to obtain promising porous composite catalytic materials with multiple active regions for the efficient low-temperature VOCs combustion.

4.2 Experimental and measurements

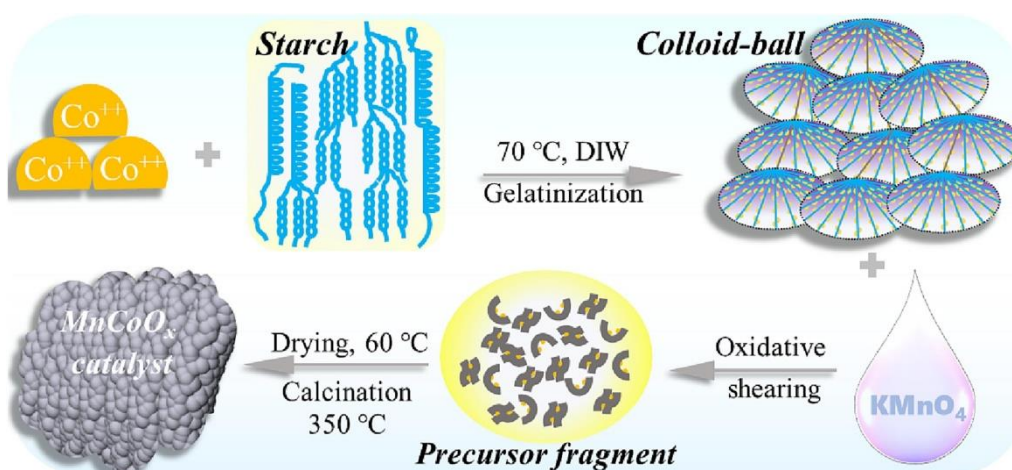
4.2.1 Catalyst preparation

(I) Synthesis of MnCo_x catalysts: The steps of starch-paste assisted synthesis of MnCo_x catalysts are illustrated in Scheme 4.1. The cobalt(II) nitrate hexahydrate

($\text{Co}(\text{NO}_3)_2 \cdot 6\text{H}_2\text{O}$, A.R., Purchased from Wako in Japan) with designed content (3.3, 6.6 or 9.9 mmol) was dissolved in 50 mL of deionized water (DIW). Whereafter, 2 g of potato starch ($((\text{C}_6\text{H}_{10}\text{O}_5)_n$, C.P., Nacalai Tesque Inc., Japan) was added to the above stirring solution slowly and kept stirring for 10 min until a uniform suspension was obtained. Then, the beaker containing the above suspension was moved into a water bath at 70 °C and continued to stir for ca. 90 min until a pink jelly-like paste formed. After aging for 10 min at room temperature (RT), the colloid paste was added into 30 mL of KMnO_4 (A.R., Wako, Japan) solution (0.33 M) and stirred continuously for 3 h to get a black precipitate. Thereafter, the collected precipitate was washed with ethanol and DIW. Finally, the solid precursor product was dried in a 60 °C oven overnight and oxidized in air at 350 °C (heating rate: 2 °C·min⁻¹) for 3 h to obtain the target MnCo_x mixed oxides denoted as $\text{MnCo}_{3.3}$, $\text{MnCo}_{6.6}$ and $\text{MnCo}_{9.9}$ according to the additive amount of $\text{Co}(\text{NO}_3)_2 \cdot 6\text{H}_2\text{O}$. The amount of chemicals added in this process oriented to adjust the catalytic activity.

(II) Synthesis of MnO_x catalyst: The synthesis process and condition for MnO_x catalyst were similar as that of $\text{MnCo}_{6.6}$ catalyst, except that 2 g of starch suspension was gelatinized and aged without $\text{Co}(\text{NO}_3)_2 \cdot 6\text{H}_2\text{O}$. After that, KMnO_4 solution was added to realize the oxidative shearing process, and then the obtained product was washed, collected, dried and finally calcined at 350 °C to obtain the MnO_x catalyst.

(III) Synthesis of CoO_x catalyst: Similar to the above description, the mixed suspension of $\text{Co}(\text{NO}_3)_2 \cdot 6\text{H}_2\text{O}$ (6.6 mmol) and starch (2 g) was gelatinized, aged and dried, and then directly calcined at 350 °C to obtain the CoO_x catalyst.



Scheme 4.1. Schematic illustration of synthetic strategy and morphological evolution for the preparation of MnCoO_x catalyst.

4.2.2 Catalytic performance test

The performance of the obtained catalyst for the combustion of toluene was evaluated on a lab-scale tube reactor (8.0 mm inner diameter) reactor under atmospheric pressure, in which typically 50 mg of the catalyst (40-60 mesh) diluted with 50 mg of inactive quartz sands was loaded in each run. Before each test, the piping system with the purging of N₂ (35 cm³·min⁻¹) was kept at 100 °C for 30 min to remove impurities and air, and then 50 cm³·min⁻¹ of simulated VOC feeding gas consisting of 20 vol.% O₂, 1,000 ppm toluene and N₂ balance gas corresponding to a weight hourly space velocity (WHSV) of 60,000 cm³·g⁻¹·h⁻¹ was fed into the reaction bed and maintained at 100 °C for 30 min for stabilizing the system. After that, the fixed-bed reactor was heated from 100 to 300 °C at a heating rate of 10 °C·min⁻¹. During this process, the temperature was kept constant for 40 min at intervals of 5 or 10 °C until the oxidation products were analyzed. The toluene concentrations of entering/exiting reactor and combustion products were online detected by a chromatography (GC-2014, Shimadzu) and FT-IR analyzer (FG-120, Horiba), respectively. The catalytic toluene combustion performances over the optimal catalyst at different WHSVs (i.e., 120,000, 60,000 and 30,000 cm³·g⁻¹·h⁻¹) were compared by changing the catalyst loading amount. The stability was evaluated by fixing the reaction bed temperature for about 50 h. The water resistance of the catalyst was also explored by introducing different contents of water vapor into the feedstock. The toluene conversion (C_t) was calculated as Eq. (1): $C_t = \frac{[\text{toluene}]_{in} - [\text{toluene}]_{out}}{[\text{toluene}]_{in}} \times 100\%$ and the CO₂ selectivity (C_{CO_2}) was calculated as Eq. (2): $C_{CO_2} = \frac{[CO_2]_{out}}{7 \times [\text{toluene}]_{in}} \times 100\%$, where, $[\text{toluene}]_{in}$ and $[\text{toluene}]_{out}$ represent the toluene concentrations in the feedstock and tail gas, respectively. $[CO_2]_{out}$ is the CO₂ concentration in tail gas. The normalized reaction rate (r , mol·g⁻¹·s⁻¹) was calculated as Eq. (3): $r = (C_t \cdot V)/m_{cat}$ and the apparent activation energy (E_a , kJ·mol⁻¹) was calculated as Eq. (4): $r = -kc = [-A \exp(-E_a/RT)]c$, where, V and m_{cat} represent molar velocity of toluene and catalyst mass amount, respectively. A , c and k are pre-

exponential factor, toluene concentration in feed stream and the rate constant, respectively. T and R represent reaction temperature and proportional constant.

4.2.3 Catalyst characterization

The morphologies of catalysts were characterized by a scanning electron microscope (SEM) apparatus (Hitachi SU8010, Japan) under an accelerating voltage of 15 kV. Wide-angle X-ray diffraction (XRD) patterns were determined on a Rigaku Smartlab (Japan) diffractometer using a Cu K α radiation ($\lambda = 1.5418 \text{ \AA}$) with a step gap of 0.02° and a scanning rate of 1.5 s per step. The nitrogen adsorption-desorption isotherms of the catalysts were obtained on a Nova 4200 instrument (Quantachrome Inc., USA) at -196°C . Prior to the measurements, the catalyst was degassed overnight at 300°C under vacuum. The SSAs of catalysts were calculated according to the standard Brunauer-Emmett-Teller (BET) procedure. The average pore diameter (P_d) and pore volume (V_p) were obtained from the desorption branches of isotherms using the Barrett-Joyner-Halenda (BJH) method. The bulk atomic composition of the catalyst was determined by X-ray fluorescence (XRF) analysis (EDX-800HS, Shimadzu). High-resolution transmission electron microscope (HR-TEM) analyses were performed on a JEM-2100F instrument at 200 kV, where an equipped X-ray energy dispersive (EDX) mapping (Horiba EMAX) was used for the elemental dispersion analysis. X-ray photoelectron spectroscopy (XPS) analysis of the catalyst was recorded on a VG Scientific ESCALab250i-XL instrument with a monochromatized Al-K α radiation. The binding energy (BE) of C1 s was fixed at 284.6 eV to adjust all other spectra, and the spectral peaks were fitted by XPSPEAK software. Raman spectra were obtained on a JASCO NRS-5100 spectrometer, which was excited with a 532 nm laser. The defect information in the materials was detected by electron paramagnetic resonance (EPR) technique and the spectrum was recorded on a Bruker A300 instrument (Germany) at RT. H $_2$ temperature-programmed reduction (H $_2$ -TPR) analysis was performed on a BELCAT automated chemisorption analyzer (Microtrac, Japan) equipped with a thermal conductivity detector (TCD). In brief, 40 mg of the sample was purged in a U-shaped quartz tube and heated at 300°C for 30 min under He gas atmosphere ($50 \text{ cm}^3 \cdot \text{min}^{-1}$). After cooling down to RT, the quartz reactor was continuously injected with

a 5 vol.% H₂/Ar gas flow (50 cm³·min⁻¹) and heated from RT to 900 °C (heating rate of 10 °C·min⁻¹). The H₂ consumption signal during the test was captured by the TCD through the thermal signal and displayed as an electrical signal. The O₂ temperature programmed desorption (O₂-TPD) measurements were also carried out on this analyzer, and the catalyst (40 mg) was pretreated with the same procedure as TPR. After that, the catalyst was exposed to a stream of O₂ gas flow (30 cm³·min⁻¹) at 50 °C for 60 min. Then, the catalyst was heated from 50 to 900 °C (heating rate: 10 °C·min⁻¹) in a stream of He gas flow (30 cm³·min⁻¹), where the signal of desorbed oxygen was captured and transformed by TCD. The DFT calculations provided by Materials Studio 8.0 package were used to explore the adsorption energy (E_{ad}) and bond length changes of raw material molecules on the catalyst surface. In situ DRIFTS spectra recorded within 4000-650 cm⁻¹ (32 scans) were carried out on a Frontier FT-IR spectrometer (PerkinElmer) with a liquid N₂-cooled mercury cadmium telluride (MCT) detector and DRIFTS cell equipped. Typically, the catalyst was pretreated at 300 °C for the sample purification and then cooled down to 50 °C for background collecting. After that, different simulated atmospheres (toluene/air, toluene/N₂) were introduced into the reaction system, and then the toluene oxidation intermediates corresponding to time/temperature-dependent spectra were collected under the programmed heating process.

4.3 Result and discussion

4.3.1 Morphology and porous structure of prepared catalysts

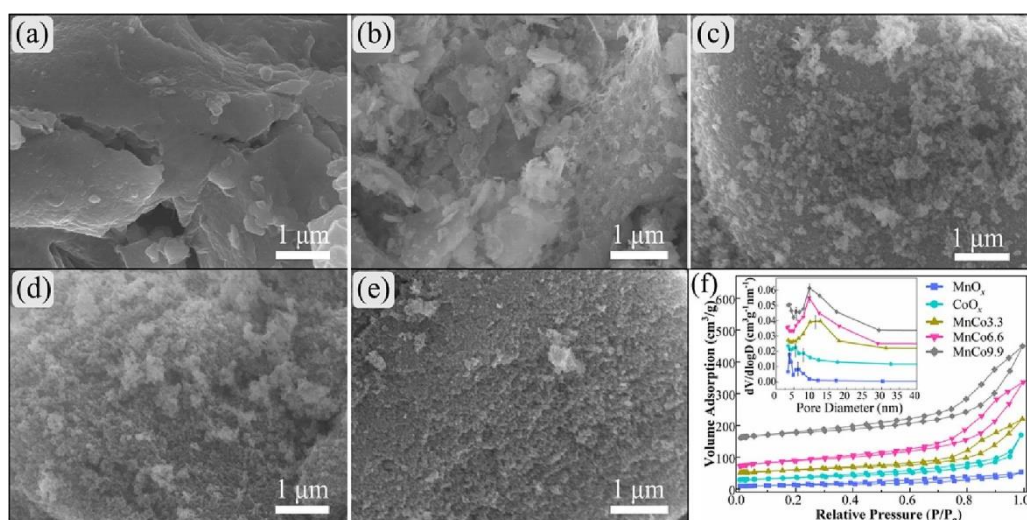


Fig. 4.1. SEM images of the prepared (a) MnO_x , (b) CoO_x , (c) $\text{MnCo}_{3.3}$, (d) $\text{MnCo}_{6.6}$ and (e) $\text{MnCo}_{9.9}$ samples; (f) N_2 adsorption-desorption isotherms and pore diameter distribution curves (inset) of all catalysts.

SEM technique was used to study the morphologies of all the as-prepared catalysts and the results are displayed in Fig. 4.1(a-e). As shown in Fig. 4.1a, the pure MnO_x catalyst exhibits a smooth-surfaced bulk structure in the absence of Mn-Co interaction, which should be responsible for its poor porous structure and lower SSA (Table 4.1). The morphology of pure CoO_x sample (Fig. 4.1b) shows a breadcrumb-like structure deriving from the one-step calcination of starch gel-ball with Co ions adsorbed/dispersed. As shown in Fig. 4.1(c-e), all MnCo_x samples show irregular nanoparticle stacking morphology, which should be attributed to the combined actions of permanganate oxidative shearing effect for starch gel-ball and calcined oxidation processes. Hence, it was believed that the interaction effect between Co ions adsorbed/dispersed in the starch paste and Mn ions should prevent the re-agglomeration of the precursor fragments to form nanoparticle-like structures. Herein, the bound nanoparticle stacking structure should have a great impact on the pore structure and SSAs of the catalysts (discussed below), which also has relationship with the exposure rate of active site as well as the mass transfer of VOC molecules on the catalyst [21, 22]. However, local nongranular agglomerated structures still exist in the $\text{MnCo}_{3.3}$ catalyst (Fig. 4.1c), which is attributed to the insufficient shearing of organic macromolecule with a small amount of oxidant. The excess KMnO_4 added made the nanoparticles formed in $\text{MnCo}_{9.9}$ catalyst (Fig. 4.1e) more compact than those in the $\text{MnCo}_{6.6}$ catalyst (Fig. 4.1d). Therefore, controlling the oxidant ratio should be beneficial for the optimization of the catalyst structure.

Fig. 4.1f and the corresponding data listed in Table 4.1 show the porous structure information of prepared catalysts probed by N_2 adsorption/desorption technique. As displayed in Fig. 4.1f, according to the IUPAC classification, the typical type IV isotherm with a characteristic H3 type hysteresis loop appears at all the catalysts, which is the evidence of mesoporous formation [23]. While, the more obvious hysteresis phenomenon in the MnCo_x catalysts indicates the existence of more mesoporous

structures, which should be benefited from the pore-forming process of the precursor assembly after the oxidative shearing process. The pore diameter distribution curves shown in the inset also nicely illustrate the evolution of the pore structures of the catalysts. The pore-size distribution peaks in the MnO_x catalyst are mainly located at ca. 3.8 and 6 nm, indicating that these two types of mesopores dominate. The CoO_x sample exhibits two weaker peaks at about 5.5 and 7.7 nm, indicating a small amount of mesopores with these two pore sizes. It is worth noting that in addition to the narrow peak at ca. 3.5 nm, the strong and broad peaks in the region of 5-30 nm in the MnCo_x catalysts are the feature of abundant hierarchical mesopores, which can be seen that the oxidative shearing process of the starch paste with cobalt ions dispersed results in the generation of sufficient hierarchical mesopores in the MnCo_x catalyst. Furthermore, these mesopore diameters are greater than five times the kinetic diameter ($5 \times 5.8 \text{ \AA}$) of toluene molecule, which would be beneficial to overcome the mass transfer resistance during VOC combustion process [24, 25]. The P_d , V_p and SSAs of the catalysts calculated from the N_2 adsorption and desorption results are listed in Table 4.1. The P_d and V_p values of prepared catalysts decrease in the orders of MnCo3.3 (12.6 nm) > MnCo9.9 (9.4 nm) > MnCo6.6 (9.3 nm) > MnO_x (3.8 nm) > CoO_x (3.4 nm) and MnCo9.9 ($0.47 \text{ cm}^3 \cdot \text{g}^{-1}$) > MnCo6.6 ($0.44 \text{ cm}^3 \cdot \text{g}^{-1}$) > MnCo3.3 ($0.28 \text{ cm}^3 \cdot \text{g}^{-1}$) > CoO_x ($0.22 \text{ cm}^3 \cdot \text{g}^{-1}$) > MnO_x ($0.07 \text{ cm}^3 \cdot \text{g}^{-1}$), which are consistent with the above pore-size distribution and isotherm results, respectively. In addition, the larger SSAs in MnCo6.6 ($136.2 \text{ m}^2 \cdot \text{g}^{-1}$) and MnCo9.9 ($129.3 \text{ m}^2 \cdot \text{g}^{-1}$) catalysts, as well as the larger V_p would improve their adsorption capacity to the reactant molecules and the utilization of active sites.

4.3.2 Crystalline phase structure of prepared catalysts

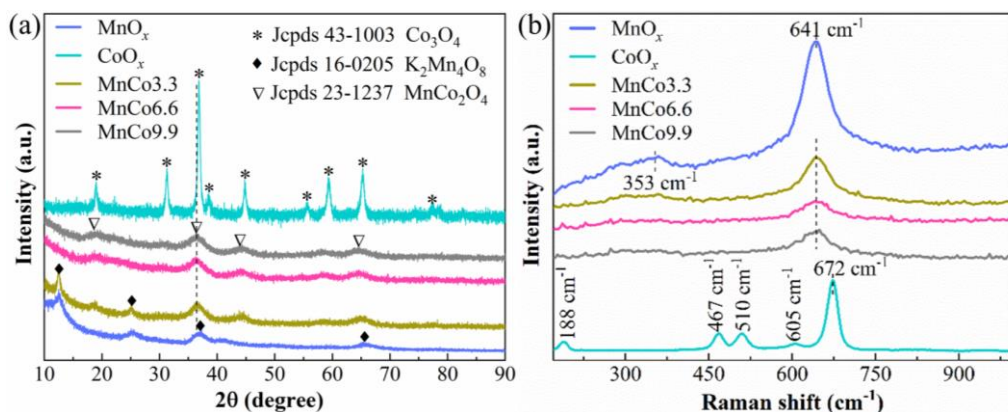


Fig. 4.2. XRD patterns (a) and Raman spectra (b) of as-synthesized pure MnO_x , CoO_x and MnCo_x composite oxides.

The crystalline structures of all synthesized catalysts detected by XRD analysis are depicted in Fig. 4.2a. For CoO_x sample, all the diffraction peaks located at 19.0° , 31.3° , 36.8° , 38.5° , 44.8° , 55.7° , 59.4° , 65.2° and 77.3° (2θ) are in accordance with the (111), (220), (311), (222), (400), (422), (511), (440) and (533) crystal planes of spinel Co_3O_4 phase (JCPDS No. 43-1003), respectively, where no other cobalt oxide phase is found [26]. While, four characteristic peaks at 12.7° , 25.4° , 37.3° and 65.7° found in the pure MnO_x sample are attributed to $\text{K}_2\text{Mn}_4\text{O}_8$ phase (JCPDS No. 16-0205), which is consistent with the reported result [27]. For MnCo_x samples, the diffraction peaks emerged at 18.5° , 36.0° , 43.8° and 63.6° match well with the (111), (311), (400) and (440) planes of cubic spinel MnCo_2O_4 phase (JCPDS No. 23-1237) [28]. One can see that with the introduction of Mn species into CoO_x , the strong peaks of spinel Co_3O_4 disappear rapidly accompanying with the generation of weak characteristic peaks for MnCo_2O_4 phase in MnCo_x samples, which should be resulted from some partial atomic substitution cases of spinel Co sites by Mn atoms. Moreover, the diffraction peaks in $\text{MnCo}_{6.6}$ sample are changed a little with the change of Mn/Co ratio, while two $\text{K}_2\text{Mn}_4\text{O}_8$ characteristic peaks appear in $\text{MnCo}_{9.9}$ catalyst. Therefore, it can be deduced that the oxidative shearing process with an appropriate Mn/Co ratio can lead to the formation of a large amount of MnCoO_x amorphous structures accompanied by the spinel MnCo_2O_4 with smaller grain sizes (Table 4.1). Zhou et al. [29] prepared a supported CoMn/active carbon (AC) composite oxide catalyst using an impregnation

method, in which the formed MnCo spinel structure also provided enough active centers for the combustion of phenyl VOC. Li et al. [30] prepared an amorphous Co-Mn binary oxide, which showed highly defective structure and enhanced reducibility, resulting in excellent catalytic activity in propane combustion. Therefore, the low-crystallinity MnCo_x catalyst synthesized in this work is also expected to possess outstanding catalytic activity in toluene oxidation process.

The metal-oxygen bond vibration and amorphous phase in the prepared samples were detected through Raman analysis. As shown in Fig. 4.2b, for CoO_x catalyst, the three bands of Raman-active F_{2g} symmetry mode were detected at 188, 510 and 605 cm⁻¹ [31]. Two bands at 467 and 672 cm⁻¹ are assigned to E_g and A_{1g} modes, respectively, and the latter is from octahedral sites (CoO₆) of spinel Co₃O₄ phase [31, 32]. The distinct bands observed at about 641 and 353 cm⁻¹ in MnO_x catalyst are recognized as stretching vibration and bending vibration of Mn-O bond in the octahedral [MnO₆], respectively [30]. In the case of MnCo_x mixed oxides, all samples exhibit only the characteristic Mn-O stretching vibration peaks located at about 641 cm⁻¹, which also show a gradually decreasing intensity with the increasing of cobalt ratio. It can be considered that the normal vibration modes in the MnCo_x catalysts were weakened owing to the existence of special interaction between Mn and Co species, which was expected to adjust the concentrations of lattice defects as well as the reactive oxygen species in MnCo_x catalysts. Generally, the appropriate rather than excess or insufficient defect structures in the catalyst can not only activate the gas phase oxygen in time, but also guarantee the cyclic capacity of the lattice oxygen in the toluene combustion process [33].

Table 4.1 N₂ adsorption-desorption, XRF and XRD analysis results of the prepared catalysts.

Catalyst	V _p ^a (cm ³ ·g ⁻¹)	P _d ^a (nm)	SSA ^b (m ² ·g ⁻¹)	Element content (at.%) ^c			Crystal size ^d <i>d</i> ₃₁₁ (nm)
				Mn	Co	K	
MnO _x	0.07	3.8	24.9	81.0	/	19.0	/

CoO _x	0.22	3.4	51.6	/	100	/	18.7
MnCo3.3	0.28	12.6	80.3	64.8	24.3	10.9	3.4
MnCo6.6	0.44	9.3	136.2	61.9	31.6	6.5	2.9
MnCo9.9	0.47	9.4	129.3	59.5	34.3	6.2	2.8

^a Calculated from BJH method. ^b Measured by BET method. ^c Tested by XRF technique.

^d Estimated through Scherrer equation based on the (311) peak feature of XRD patterns.

4.3.3 Surface chemical properties of prepared catalysts

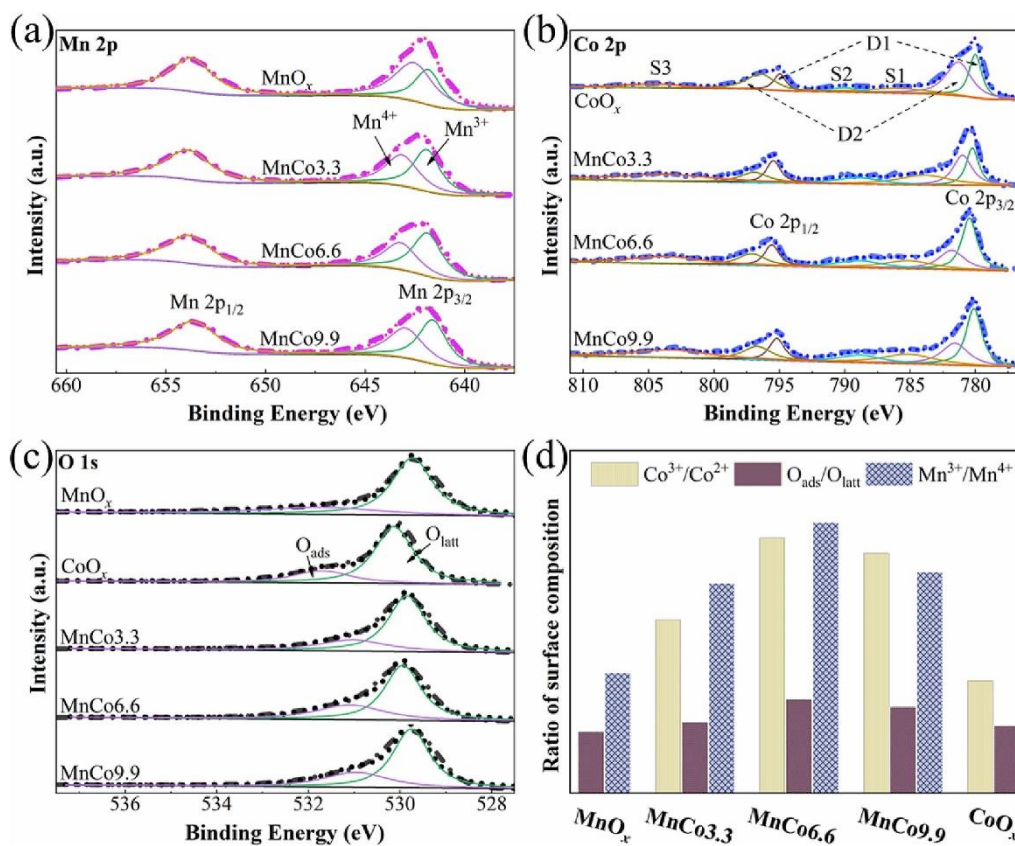


Fig. 4.3. XPS spectra for the prepared catalysts: (a) Mn 2p, (b) Co 2p and (c) O 1s; (d) Bar comparison chart of the proportions for active species in all catalysts.

Fig. 4.3 and the corresponding data in Table 4.2 revealed the oxidation states of metal ions and oxygen species on the surface of catalyst through XPS technique. The Mn 2p spectra of Mn-containing samples illustrated in Fig. 4.3a show two main peaks at binding energies (BEs) around 653.7 ± 0.2 and 642.1 ± 0.2 eV, which are ascribed to Mn 2p_{1/2} and Mn 2p_{3/2} spectra, respectively [9]. Furthermore, each of the asymmetric

Mn 2p_{3/2} spectra can be decomposed into two components centered at about 641.8 ± 0.2 and 643.0 ± 0.3 eV, which are the characteristics of Mn³⁺ and Mn⁴⁺ species, respectively [34, 35]. Generally, due to the presence of Mn³⁺ species, the charge balance in the catalyst requires the presence of oxygen vacancies to remain, and the relational expression is as below: -Mn⁴⁺-O²⁻-Mn⁴⁺- → -Mn⁴⁺-○-Mn³⁺- + 1/2O₂ (○ represents oxygen vacancy) [36]. As a typical lattice defect, the existence of oxygen vacancies can enhance the adsorption and activation of oxygen gas to generate active electrophilic oxygen species, which has been considered as the key active species for the oxidation of VOCs [35]. In addition, the lower binding capacity of the Mn³⁺-O bond makes its oxygen atom more likely to migrate and participate in the toluene oxidation process [37]. Therefore, the ratio of Mn³⁺/Mn⁴⁺ as an indicator for evaluating surface active manganese species can be estimated by the deconvolved peak areas and listed in Table 4.2. When the amount of cobalt added in the experiment is increased from 3.3 to 6.6 mmol, the Mn³⁺/Mn⁴⁺ atomic ratio in the catalyst is increased from 1.10 to 1.42, however, this ratio is decreased to 1.16 with the further increase of cobalt to 9.9 mmol, indicating the effective ion regulation capacity of starch. Therefore, it can be inferred that the electron transfer process during starch hydrolysis ((C₆H₁₀O₅)_n + nH⁺ + nOH⁻ → nC₆H₁₂O₆) would be disturbed by the presence of metal ions, resulting in the rearrangement of the electron cloud around the metal ions with a strong interaction between Mn and Co ions. Meanwhile, the acidic glucose molecules produced from hydrolysis could react with MnO₄⁻ to generate an acidic environment rich in carboxyl groups, which can play a positive role in the process of promoting the generation of active components such as oxygen vacancies and Mn³⁺ species.

XPS spectra of Co 2p for all catalysts containing Co species shown in Fig. 4.3b exhibit two sets of main signals centered at about 780.4 ± 0.2 and 795.5 ± 0.2 eV, which are the characteristic spin-orbitals for Co 2p_{3/2} and Co 2p_{1/2}, respectively [32, 38]. The deconvolution result of the entire Co 2p spectrum shows two characteristic peaks of octahedral Co³⁺ species (D1) at the BEs of 780.2 ± 0.2 and 795.3 ± 0.3 eV, two characteristic peaks of tetrahedral Co²⁺ species (D2) centered at about 781.4 ± 0.3 and 796.8 ± 0.3 eV, and three weak satellite peaks located at about 784.8 ± 0.4 (S1), 789.2

± 0.2 (S2) and 803.7 ± 0.4 eV (S3) [32, 38]. Herein, the appearance of three satellite peaks and the Co 2p spin-orbit splitting energy (ΔE) of ca. 15.1 eV measured by $\Delta E = E(\text{Co } 2p_{1/2}) - E(\text{Co } 2p_{3/2})$ also verify the existence of mixed cobalt valence states on the catalyst surface [38, 39]. It is reported that the surface Co^{3+} in the Co-based catalysts is generally the primary active site for VOC combustion, which can not only lead to the generation of more oxygen vacancy defects and surface adsorbed oxygen species, but also improve the reducibility in the metallic oxide catalysts [40, 41]. The $\text{Co}^{3+}/\text{Co}^{2+}$ ionic ratios (Table 4.2) were also calculated and show a trend of first increasing and then decreasing with the increase in the Co/Mn ratio, and the MnCo6.6 sample has a highest $\text{Co}^{3+}/\text{Co}^{2+}$ ratio (1.34). Therefore, as discussed above, the electron transfer process in the starch hydrolysis process can regulate the valence state of metal ions, and the strong oxidation of high-valence manganese ions under acidic conditions can promote the formation of trivalent cobalt and trivalent manganese ions, which should be conducive to improving the catalytic activity of toluene combustion.

As shown in Fig. 4.3c, the deconvolution results of O 1s spectra for all catalysts were fitted to two components centered at about 531.4 ± 0.4 and 529.9 ± 0.3 eV, corresponding to surface adsorption oxygen species (O_{ads} , e.g., O^- , O_2^{2-} and/or O_2^- species) with low coordination and surface lattice oxygen (O_{latt} , i.e., O^{2-}), respectively [42]. It is well known that the electrophilic O_{ads} species tends to attack the electron-rich region of organic molecule, which plays an important role in the deep oxidation of organics [5]. The $\text{O}_{\text{ads}}/\text{O}_{\text{latt}}$ ratios for all samples shown in Table 4.2 follow the sequence of MnCo6.6 (0.49) > MnCo9.9 (0.45) > MnCo3.3 (0.37) > CoO_x (0.35) > MnO_x (0.32), which indicates that the oxidative shearing in catalyst synthesis can enrich the content of reactive oxygen species. The histogram in Fig. 4.3d visually compares the proportions of active species in the catalysts described above. One can see that the larger proportions of active species in the MnCo x catalysts, especially in the MnCo6.6 catalyst, indicate that the hydrolysis and oxidative shear processes of starch paste are beneficial for the adjustment of metal valences and active oxygen species, which should improve the toluene oxidation performance.

4.3.4 Unpaired electron analysis for catalysts

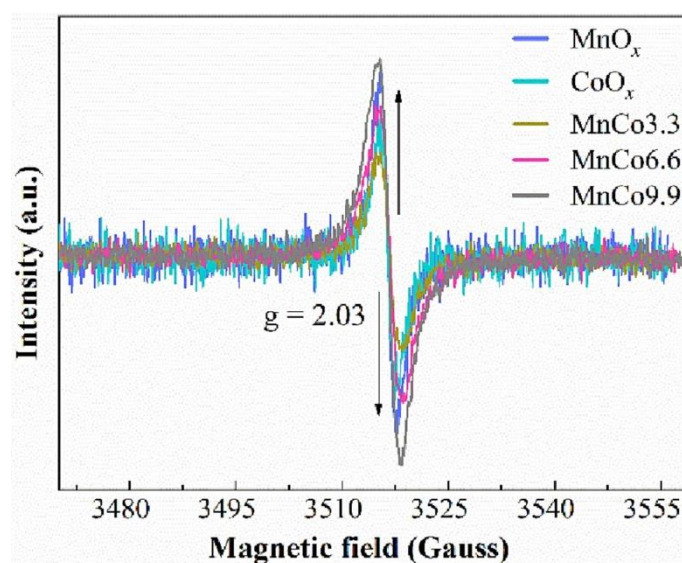


Fig. 4.4. EPR spectra of MnCo_x , MnO_x and CoO_x samples.

The unpaired electron structures such as oxygen vacancy in the synthesized catalysts were analyzed by the EPR technique and shown in Fig. 4.4. Notably, all spectra show centrosymmetric profiles with different intensities at the characteristic g value (2.03) of unpaired electron, indicating different concentrations of unpaired electron species in the catalysts [43]. Obviously, the increased peak intensity with increased Co/Mn ratio tells the different degrees of Mn-Co interactions in the MnCo_x catalysts. Furthermore, the peak intensity in the pure MnO_x sample is stronger than those of $\text{MnCo}_{6.6}$ and $\text{MnCo}_{3.3}$ catalysts but weaker than that of $\text{MnCo}_{9.9}$ sample, which is slightly inconsistent with the order of Mn^{3+} contents, indicating that more defects exist on the $\text{MnCo}_{6.6}$ catalyst surface than those on the bulk phase. Herein, the catalytic oxidation performance of catalysts could be determined by various factors, such as SSA, reducibility, oxygen mobility and active oxygen contents. However, excessive oxygen vacancies in the catalyst bulk are not conducive to the release/storage of reactive oxygen species. Dong et al. [33] used the Cu-doped MnO_2 catalysts with different oxygen vacancy concentrations for the catalytic oxidation of toluene. The results showed that the excessive oxygen vacancies in the catalyst would suppress the reducibility and mobility of lattice oxygen in the prepared catalyst, and then weaken its catalytic activity. Wang et al. [44] prepared an OMS-2 catalyst assisted by holmium for

catalytic oxidation of toluene at low temperature, and found that excessive oxygen vacancies in the catalyst bulk has no positive effect on the production of reactive oxygen species. Similarly, in this study, due to the influence of the starch addition and the ratio of manganese/cobalt on the amorphous structure or low-crystalline structure in the catalyst, the concentration of oxygen vacancies in those structures can also be adjusted by the difference of raw materials in the material synthesis process. Therefore, MnCo6.6 catalyst with adequate surface oxygen vacancies as well as moderate bulk oxygen vacancies should be the important reasons for improving the catalytic performance.

4.3.5 HR-TEM image and EDX mapping results

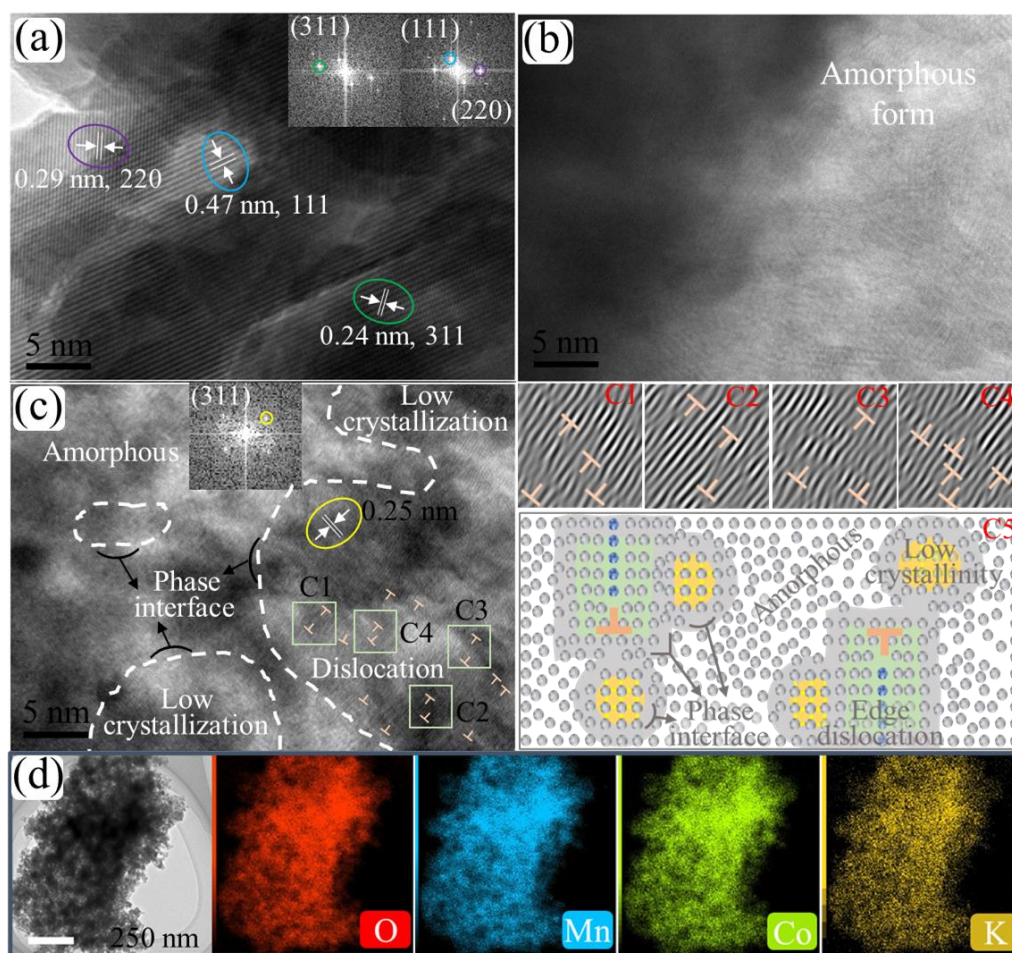


Fig. 4.5. HR-TEM image of (a) CoO_x, (b) MnO_x and (c) MnCo_{6.6} samples with the FFT result (inset); Magnification images of selected area for edge dislocation (c1-c4) and schematic representation of multifarious regions (c5) from Fig. 4.5c; EDX mapping for MnCo_{6.6} sample (d).

The HR-TEM images shown in Fig. 4.5 are used to further investigate the microscopic crystal textures of catalysts. As displayed in Fig. 4.5a, the image of CoO_x sample shows several clear lattice fringes with the interplanar spacings of 0.29, 0.47 and 0.24 nm calculated via Fast Fourier Transform (FFT) algorithm, which correspond to the (220), (111) and (311) planes of spinel Co_3O_4 phase. No obvious fringe is detected in Fig. 4.5b due to its overall amorphous structure in MnO_x bulk, which should be the reason for its excessive unpaired electron structures in catalytic bulk. For the image of $\text{MnCo}_{6.6}$ catalyst (Fig. 4.5c), scattered local lattice fringes with an interplanar spacing of 0.25 nm corresponding to the (311) plane of spinel MnCo_2O_4 phase with low crystallinity are found, which indicate that the process of oxidative shearing and assembly between MnO_4^- and Co species fixed in the starch gel-ball can lead to the well doping with each other. This is consistent with the uniform element dispersion in EDX mapping (Fig. 4.5d). Interestingly, besides local MnCo_2O_4 phase, some other distinct crystalline regions are detected in the image of $\text{MnCo}_{6.6}$ catalyst, i.e., low crystalline region with abundant edge dislocations, amorphous region, and the phase interface between the above regions. Fortunately, it is reported that the MnCo spinel structure always exhibits abundant active species (e.g., Co^{3+} , Mn^{3+} and electrophilic oxygen species) and excellent low temperature reducibility, which always play a key role in VOC catalytic combustion [28, 45, 46]. For amorphous region, the inherent metal-oxygen/defect bonds ($\text{Mn}^{4+}-\text{O}-\text{Mn}^{3+}$ and $\text{Mn}-\text{O}-\text{Co}$) with weak bond strength and strong metal-to-metal interactions always exhibit better lattice oxygen mobility and sufficient unpaired electron species [8, 30]. Moreover, abundant dislocation type lattice defects and interface defects have been reported to be important substances for adsorbing and activating gaseous oxygen, which is of great significance for the cyclic provision of active oxygen species from catalysts for the catalytic combustion of VOCs [17, 20, 38]. In addition, according to other reports, such locally lattice-disordered catalyst can possess more effective defects, surface chemisorbed oxygen species, and superior low-temperature reducibility compared with both the whole lattice disorder and whole lattice ordered catalysts [19, 20]. Therefore, the starch assisted synthesis process proposed in this work successfully realized the construction of microscopic multi-active

regions in locally disordered MnCo6.6 composite oxide, which should have excellent catalytic toluene combustion performance.

4.3.6 Reducibility and oxygen species mobility

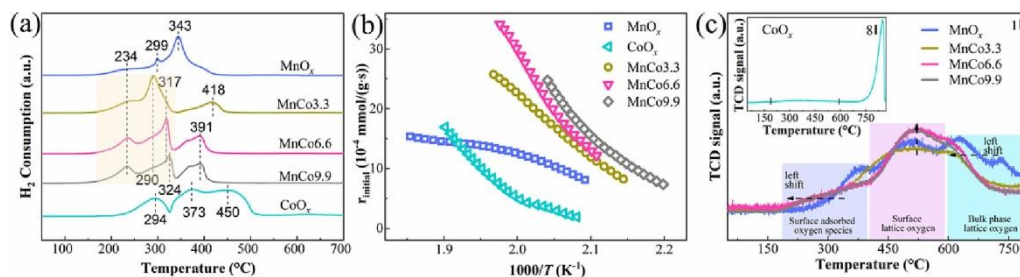


Fig. 4.6. H₂-TPR curves (a), initial H₂ consumption rate (b) and O₂-TPD profiles (c) of the as-prepared catalysts.

Fig. 4.6a and Table 4.2 present the reducibility of all catalysts tested by H₂-TPR technique. As shown in Fig. 4.6a, for the MnO_x catalyst, three reduction stages from low to high temperature are assigned to the following reduction steps: MnO₂ → Mn₂O₃ → Mn₃O₄ → MnO [18]. The typical two-step reduction process of Co₃O₄ phase, i.e., Co³⁺ → Co²⁺ → Co⁰, was also detected in the TPR profile of CoO_x sample, and the broad high-temperature reduction peak (ca. 325-500 °C) indicates a large amount of lattice oxygen in CoO_x catalyst, suggesting its mediocre oxygen mobility capacity [47]. For MnCo_x composite oxides, three similar reduction peaks but different peak intensities and reduction temperatures were detected on each composite catalyst. The low-temperature reduction peak centered at ca. 234 °C is the co-reduction processes of two-step low-temperature reduction of Mn species (Mn⁴⁺ and Mn³⁺) and partial active Co species, which are attributed to the low-temperature merging of reduction peaks caused by the synergistic effect of Mn and Co species, indicating the improved reducibility of the MnCo_x catalysts. Besides, the reduction processes included Mn^{8/3+}, remaining Co³⁺ and part of the Co²⁺ species in the intermediate temperature region (260-340 °C) also shifted to low-temperature side comparing with those for the MnO_x and CoO_x catalysts, which indicate that the bulk reducibility of the MnCo_x catalysts was also enhanced by the formation of low crystalline and amorphous phases. It is worth noting that the high-temperature reduction peaks attributed to the inert Co species in the MnCo_x catalysts also shifted to the low-temperature direction, indicating that the

intrinsic reducibility of the MnCo_x catalysts has been absolutely optimized. Therefore, it can be inferred that the strong interaction between defect species and weakly chemical bonds from the amorphous and low crystalline structures constructed by the oxidative shearing process largely enhanced the reducibility of the MnCo_x catalysts, which is consistent with the speculation results in HR-TEM and should have an irreplaceable function in the oxidation of toluene. The H₂ consumption amount (H_c) for each catalyst presented in Table 4.2 are also used to quantify the reducibility of the catalysts, and the H₂ consumption amount at low temperature (H_l) as well as the sum of H₂ consumption amount (H_{sum}) were calculated separately. Although CoO_x has the largest H_l (1.9 mmol·g⁻¹) and H_{sum} (6.3 mmol·g⁻¹), its higher reduction temperature might be the reason for its poor catalytic performance (discussed in Section 4.3.7). Except for CoO_x sample, the H_l and H_{sum} values of other catalysts follow the orders of MnCo6.6 (1.3 mmol·g⁻¹) > MnCo9.9 (1.1 mmol·g⁻¹) > MnCo3.3 (0.8 mmol·g⁻¹) > MnO_x (0.5 mmol·g⁻¹) and MnCo6.6 (4.0 mmol·g⁻¹) > MnCo9.9 (3.7 mmol·g⁻¹) > MnCo3.3 (3.6 mmol·g⁻¹) > MnO_x (3.4 mmol·g⁻¹), which are consistent with the analytical results of Co³⁺ and Mn³⁺ species with excellent reducibility described in the XPS section, thereby exhibiting difference in catalytic performances (Section 4.3.7). Therefore, the H_c and the reduction temperature are both important indicators to evaluate the reducibility as well as catalytic VOC combustion performance over the catalyst. In addition, H₂ consumption rate (r_{initial}, mmol·g⁻¹·s⁻¹) at the initial stage of the reduction test shown in Fig. 4.6b was computed by the 25% of initial H_c for each catalyst to further investigate the low-temperature reducibility [5]. Obviously, the r_{initial} order consistent with the catalytic activity order again illustrates the significance of the better reducibility at a low temperature derived from the synergetic active regions for toluene oxidation.

O₂-TPD measurements were performed to characterize the properties of oxygen species in all prepared catalysts (Fig. 4.6c). One can see that the TPD profiles of all catalysts consist of three desorption stages. Herein, the low-temperature desorption process (< 400 °C) is attributed to the desorption of initial surface adsorbed oxygen species and the middle temperature desorption peaks (ca. 400-600 °C) can be assigned to the desorption of surface/subsurface lattice oxygen and/or defect lattice oxygen with

metastable metal-oxygen binding capacity [30, 48]. While, the high-temperature desorption peaks ($> 600\text{ }^{\circ}\text{C}$) detected in all profiles belong to the desorption signal of inert bulk lattice oxygen (O_{bulk}) [30, 48]. For CoO_x sample, only faint surface oxygen and sharp O_{bulk} peaks at temperatures ranged below $600\text{ }^{\circ}\text{C}$ and above $750\text{ }^{\circ}\text{C}$ are observed, respectively, indicating the poor oxygen mobility, which should not be favorable for toluene combustion. Compared with the MnO_x sample, the similar and left-shifted surface adsorption oxygen peaks for all MnCo_x catalysts mean the presence of more active adsorbed oxygen species. The stronger surface/subsurface lattice oxygen desorption observed on the MnCo6.6 and MnCo9.9 catalysts suggests that the appropriate Mn/Co ratio during the material synthesis process can result in the generation of more metastable lattice oxygen species and thereby resulting in better lattice oxygen mobility. Meanwhile, the low-temperature shift of bulk lattice oxygen in the MnCo_x catalysts also indicates the improved deep lattice oxygen mobility, which is profited by the unsteady metal-oxygen bonds from amorphous and spinel MnCo_2O_4 structures. In general, the conversion of oxygen species during VOCs oxidation processes is as follows: $\text{O}_{2(\text{free})} \rightarrow \text{O}_{2^{-}(\text{ads})} \rightarrow \text{O}_{2^{2-}(\text{ads})} \rightarrow 2\text{O}^{-}_{(\text{ads})} \leftrightarrow 2\text{O}^{2-}_{(\text{latt})}$ [19]. In the toluene oxidation process, the free oxygen molecules in the raw material are first captured by the surface defective species (e.g., vacancy, dislocation and interface between the phases) and activated to electrophilic adsorbed oxygen species, which can participate in the toluene oxidation process and the replenishment of lattice oxygen. The oxygen storage capacities (OSCs) estimated by calculating the desorption peak areas of all catalysts are listed in Table 4.2. The desorption amount of surface oxygen species (O_{surf}) including surface adsorbed oxygen and surface/subsurface lattice oxygen follows the order of MnCo6.6 ($0.103\text{ mmol}\cdot\text{g}^{-1}$) $>$ MnCo9.9 ($0.101\text{ mmol}\cdot\text{g}^{-1}$) $>$ MnO_x ($0.089\text{ mmol}\cdot\text{g}^{-1}$) $>$ MnCo3.3 ($0.081\text{ mmol}\cdot\text{g}^{-1}$) $>$ CoO_x ($0.028\text{ mmol}\cdot\text{g}^{-1}$), which is consistent with the fact that the metastable $\text{Mn}^{3+}\text{-O}$ structure in the catalyst (described in XPS section) can promote the oxygen mobility. For the CoO_x and MnO_x samples, the high desorption temperatures indicate their worse oxygen mobility. Therefore, it can be considered that the material synthesis method proposed in this work can enrich the active adsorbed oxygen and lattice oxygen in the MnCo_x catalysts, which is of great

significance for the continuous supply of active oxygen required in the toluene oxidation process.

Table 4.2 Summary of XPS, H₂-TPR, O₂-TPD analysis results, apparent activation energy and reaction rates for total toluene combustion over the prepared catalysts.

Catalyst	Proportion of surface species ^a			H _c (mmol/g) ^b		O _d (mmol/g) ^b			E _a ^c (kJ·mol ⁻¹)	r×10 ⁶ ^d (mol·g ⁻¹ ·s ⁻¹)
	Mn ³⁺ /Mn ⁴⁺	Co ³⁺ /Co ²⁺	O _{ads} /O _{latt}	H _l	H _{sum}	O _{surf}	O _{bulk}	O _{sum}		
MnO _x	0.63	-	0.32	0.5	3.4	0.089	0.046	0.135	118.7	7.4
CoO _x	-	0.59	0.35	1.9	6.3	0.028	0.302	0.330	94.8	3.0
MnCo3.3	1.10	0.91	0.37	0.8	3.6	0.081	0.034	0.115	57.2	28.9
MnCo6.6	1.42	1.34	0.49	1.3	4.0	0.103	0.044	0.147	35.7	40.7
MnCo9.9	1.16	1.26	0.45	1.1	3.7	0.101	0.039	0.140	41.5	34.0

^a Obtained from the peak areas of deconvoluted XPS spectra. ^b Calculated based on characteristic consumption or desorption peak areas. ^c Calculated by Arrhenius equation.

^d Specific reaction rates at 226 °C.

4.3.7 Catalytic performances and dynamics

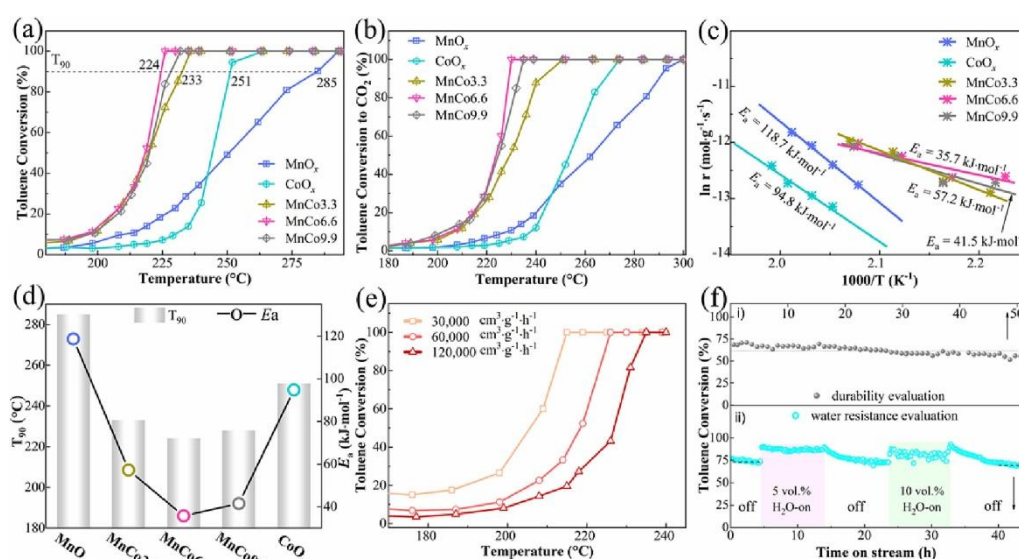


Fig. 4.7. (a) Toluene conversion and (b) corresponding CO₂ formation ratio as a function of the reaction temperature over the prepared catalysts; (c) Arrhenius plots for toluene combustion and (d) combinatorial comparison diagram of E_a and T₉₀ values; Effects of (e) WHSV and (f) duration with water vapor on toluene catalytic performance over MnCo6.6 catalyst.

The catalytic performances of the obtained catalysts for toluene combustion were

measured on a fixed-bed reactor with a continuous toluene stream (1,000 ppm). During the test process, the change of toluene conversion as well as the change of corresponding CO₂ generation ratio with rising reaction temperature are plotted in Fig. 4.7a and 4.7b, respectively. One can see from Fig. 4.7a, the toluene conversions over all catalysts increase with the increasing temperature, and complete conversion of toluene below 293 °C is achieved. It is evident that the steeper conversion curves of the MnCox catalysts at lower temperatures indicate their excellent low-temperature catalytic performance. According to the T₉₀ (temperature value of 90% toluene conversion) listed in Table 4.3, the catalytic activities for toluene combustion over each catalyst have the following order: MnCo6.6 (224 °C) > MnCo9.9 (228 °C) > MnCo3.3 (233 °C) > CoO_x (251 °C) > MnO_x (285 °C). Furthermore, the specific reaction rates ($r \times 10^6$) of toluene at 226 °C for all prepared catalysts were calculated and summarized in Table 4.2, which show that all MnCox catalysts have larger r values than those of pure MnO_x and CoO_x catalysts, and MnCo6.6 catalyst shows a biggest value (40.7). The CO₂ generation ratios shown in Fig. 4.7b are also consistent with the toluene conversions, except that the generated intermediates (discussed in Section 4.3.8) during the toluene combustion resulted in a certain temperature delay in CO₂ generation. It is worth noting that although there are a few reports on the promotion of potassium ions on catalytic performance, considering the seemingly activity inhibition from the K₂Mn₄O₈ phase in MnO_x and MnCo9.9 catalysts and the negative correlation of catalytic activity and potassium content in the manganese containing catalysts, it can be inferred that the role of potassium in the MnCox catalysts should be not obvious. Furthermore, the E_a values listed in Table 4.2 were obtained from the Arrhenius plots shown in Fig. 4.7c. It can be seen that MnCox catalysts show smaller Arrhenius plot slopes ($\ln r$ vs T^{-1}) than those of pure MnO_x and CoO_x catalysts, which are corresponded to the lower E_a values of MnCox catalysts derived from the oxidative shearing process. Notably, the combinatorial diagram (Fig. 4.7d) shows that the E_a values for toluene oxidation catalyzed by prepared samples exhibit the following ascending order: MnCo6.6 (35.7 kJ·mol⁻¹) < MnCo9.9 (41.5 kJ·mol⁻¹) < MnCo3.3 (57.2 kJ·mol⁻¹) < CoO_x (94.8 kJ·mol⁻¹) < MnO_x (118.7 kJ·mol⁻¹). Herein, the diffusion effect during the

test was minimized by the larger WHSV and smaller catalyst particle size. When toluene-lean condition, thin catalyst bed, uniform pore structure and well-proportioned catalyst particle size were used, the heat transfer limitation during the experiment was basically negligible. Therefore, the reactant molecules could be activated more readily on the active sites of the MnCox catalyst to participate in the oxidation reaction due to the lower activation energy barrier, which should be attributed to the enrichment or improvement of the active species (e.g., Mn^{3+} and Co^{3+}), surface oxygen, oxygen vacancies and redox properties in the MnCox catalysts by the hydrolysis and oxidative processes (detailed discussion in Section 4.3.9) in catalyst synthesis process, thereby improving the intrinsic catalytic activity of the catalyst.

Importantly, as shown in Table 4.3, under the similar WHSVs and toluene concentrations, the MnCox catalysts obtained in this work show lower complete conversion temperatures of toluene, and the catalytic performance of MnCox are even better than other reports with lower toluene concentrations as well as lower WHSVs. In addition, although the MnCo3.3 catalyst exhibits a commonplace SSA ($80.3 \text{ m}^2 \cdot \text{g}^{-1}$), its catalytic performance is not particularly worse compared with other reports or the other two MnCox catalysts in this work, which fully demonstrates the superiority of the starch-assisted oxidative shearing method in improving the intrinsic catalytic performance of the catalyst. In combination with the characterizations above, it can be concluded that the starch-paste assisted synthesis of MnCox mixed oxide catalysts can lead to more abundant active Mn^{3+} , Co^{3+} and adsorbed oxygen species thanks to the starch modulation and strong Mn-Co interaction. Besides, the large amount of amorphous MnCoO_x phase and spinel structure with low crystallinity led to an excellent lattice oxygen mobility and reducibility in MnCo6.6 catalyst. Meanwhile, an appropriate amount of oxygen vacancies with plenty of other defect species (e.g., dislocation structures and phase interfaces) ensure sufficient active electrophilic species. Therefore, the complementary and synergistic effects of various active regions with abundant active species contributed an improvement of intrinsic catalytic performance in MnCo6.6 catalyst. In addition, compared with the synthesis process of other MnCo-based catalysts, the starch raw materials involved in this study are cheaper and easier

to obtain. It is obvious that such a catalyst synthesis process is facile and pollutant-free, which should be a very promising catalyst synthesis method.

Fig. 4.7e compares the catalytic activities for the combustion of 1,000 ppm toluene over MnCo6.6 catalyst under different WHSVs. It is obvious that the WHSV has a great influence on the toluene combustion efficiency, and the T_{90} value of toluene oxidation increases to 213, 224 and 232 °C with the increasing of WHSVs. In general, the contact time of reactant molecules with the active sites in the catalyst is inversely related to the WHSV, as such, a lower WHSV always results in a lower toluene complete conversion temperature but a lower VOC treatment efficiency. While, a higher WHSV tends to require a higher VOC conversion temperature, however, the energy consumption should be also considered. Therefore, a suitable WHSV for VOC catalytic combustion is significance to balance energy consumption and catalytic efficiency in a practical process. Fig. 4.7f (i) shows the result of a ca. 50-hour stability evaluation process at 221 °C over the optimal MnCo6.6 catalyst. It is gratified that the long-term stability is also satisfactory compared with those reported performances (Table 4.3). It can be seen that the continuous toluene conversion tends to decrease slowly with time increasing. When the reaction is carried out for 25 h, toluene conversion decreased by about 4% and the toluene conversion decreased to 57% after the residual reaction time, which indicates that although the medium-term stability is appropriate, there is room to improve the longer-term stability. By successively introducing different contents of water vapor into the reaction system, the water resistance of the MnCo6.6 catalyst in toluene oxidation reaction was evaluated at 222 °C and the results are shown in Fig. 4.7f (ii). When the reaction was carried out for 4 h, 5 vol.% of water steam was mixed into the feeding side, which resulted in an increase of ca. 14% in toluene conversion, and the conversion decreased to the initial state slowly after turning off the water vapor. After that, when 10 vol.% of H₂O steam was introduced again for 10 h, an increase of ca. 7% in the toluene conversion was observed, and the toluene conversion decreased again after turning off the water vapor, which is consistent with the results indicated in the previous literature [49, 50]. Herein, the addition of H₂O molecules could activate the hydroperoxyl-like groups on the catalyst surface to participate in the oxidation

reaction. However, excessive water vapor would lead to the competitive adsorption of toluene and water molecules on the active sites, thereby reducing the catalytic performance [37, 50]. Therefore, for the MnCo6.6 catalyst reported in this work, the presence of an appropriate amount of water vapor in the feed is beneficial to the improvement of catalytic performance, and this phenomenon has important practical value.

Table 4.3 Summary and comparison of toluene combustion performance over nanosized Mn-Co-based catalysts presented in other reports and all catalysts in this work.

Catalyst	SSA (m ² ·g ⁻¹)	Conversion temp. ^a (°C)			Conc. (ppm)	GHSV (cm ³ ·g ⁻¹ ·h ⁻¹ or h ⁻¹)		Duration test (h)	Method	Ref.
		T ₁₀₀	T ₉₀	T ₅₀						
MnO _x	24.9	293	285	250	1,000	60,000	/	/	Oxidative shear	This work
CoO _x	51.6	264	251	244	1,000	60,000	/	/	Pyrolysis	
MnCo3.3 oxide	80.3	236	233	219	1,000	60,000	/	/	Oxidative shear	
MnCo6.6 oxide	136.2	226	224	218	1,000	60,000	50	50	Oxidative shear	
MnCo9.9 oxide	129.3	232	228	219	1,000	60,000	/	/	Oxidative shear	
Co ₁ Mn ₁ BHNCs	45.0	300	248	232	1,000	60,000	48	48	Pyrolysis	
MOF-Mn ₁ Co ₁	47.0	300	240	226	500	96,000	/	/	Pyrolysis	
α-MnO ₂ @Co ₃ O ₄	54.9	232	229	220	1,000	48,000	/	/	Pyrolysis	
MnO _x /Co ₃ O ₄ -10	112.0	242	234	230	1,000	60,000	55	55	Pyrolysis	
Mn ₂ Co ₁ oxide	85.4	238	236	228	1,000	60,000	25	25	Pyrolysis	
CMO@SNW/SiC	12.3	257	256	254.5	5,000	9,000	/	/	Hydrothermal	

Co _{0.67} Mn _{0.33} /cordierite	-	250	238	223	1,000	45,000	42	Impregnation	[40]
5Co1Mn oxide	114.0	275	247	232	1,000	60,000	/	Hydrothermal	[20]
Co _{1.5} Mn _{1.5} O ₄ /Ni foam	14.2	270	267	263	1,000	30,000	30	Hydrothermal	[36]
CoMn-1 oxide	8.0	260	250	220	1,000	15,000	100	Precipitation	[28]

^a Temperature error of catalytic performance test in this work is less than 3 °C.

4.3.8 In situ DRIFTS, DFT calculations and oxidation mechanism

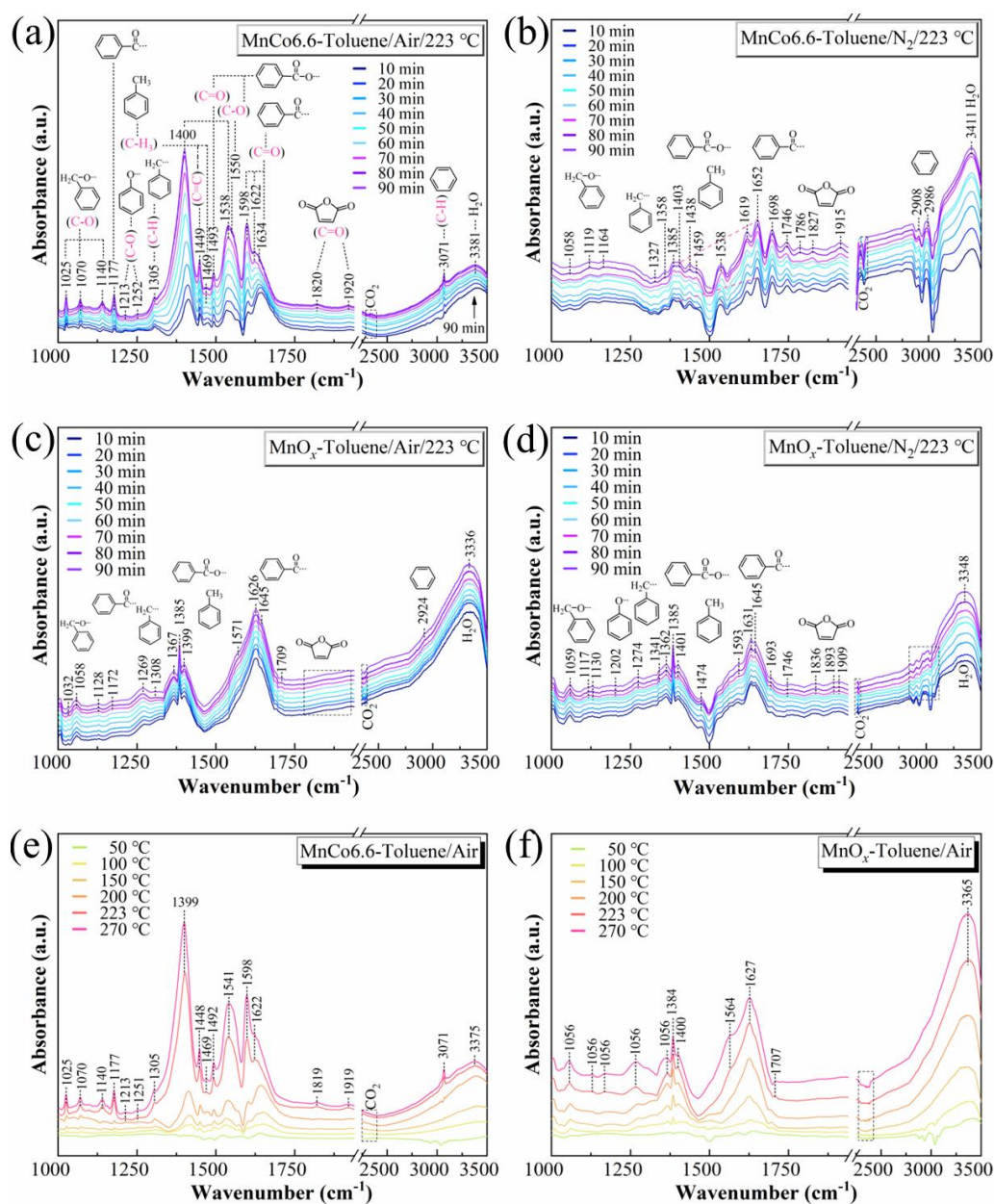


Fig. 4.8. Time-dependent in situ DRIFTS spectra of toluene oxidation over MnCo6.6 catalyst with (a) toluene/air atmosphere, (b) toluene/N₂ atmosphere, and pure MnO_x

catalyst with (c) toluene/air atmosphere, (d) toluene/N₂ atmosphere; Temperature-dependent in situ DRIFTS spectra of toluene oxidation over MnCo_{6.6} (e) and MnO_x (f) catalysts with the increasing of temperatures in toluene/air atmosphere.

As shown in Fig. 4.8, time-dependent and temperature-dependent in situ DRIFTS spectra were recorded to track the formation of intermediates in the combustion of toluene over MnCo_{6.6} and MnO_x catalysts. Fig. 4.8a shows the spectra variation for the combustion of toluene with reaction time accumulation in air atmosphere over MnCo_{6.6} catalyst at 223 °C, and the corresponding vibratory attributions are summarized in the insets of every figure and Table 4.4. The characteristic bands observed at 1469, 3071 and 1449 cm⁻¹ were attributed to the asymmetric deformation vibration signals from $\nu(\text{C-H})$ of methyl group, the stretching vibration of C-H and the skeleton $\nu(\text{C}=\text{C})$ in the aromatic ring, respectively [33, 43]. The peak at around 1305 cm⁻¹ should belong to the deformation vibration of benzyl (Ph-CH₂-), indicating the finished first-step reaction of toluene [50]. The characteristic peaks shown at about 1025, 1058 and 1140 cm⁻¹ can assign to the C-O stretching vibration mode from benzyl alcohol (Ph-CH₂-O-) [19, 53], and two faint bands at 1213 and 1252 cm⁻¹ are identified as the characteristics of stretching signal of $\nu(\text{C-O})$ from phenolate [20, 54]. Notably, several $\nu(\text{C}=\text{O})$ stretching vibration modes related to the carbonyl group in benzaldehyde are found at 1177 cm⁻¹ and the range of 1590-1700 cm⁻¹ [19, 53, 55], which indicate that some of the benzyl alcohol has undergone further oxidation process. Obviously, several prominent peaks appeared at 1400, 1493, 1538 cm⁻¹ and a shoulder peak at 1550 cm⁻¹ are attributed to $\nu(\text{C}=\text{O})$ vibration mode and antisymmetric $\nu(\text{C-O})$ stretching of carboxylate group [19, 43], respectively, implying the generation of a large amount of deeply oxidized intermediate benzoate species. Additionally, the relative positions ($\Delta\nu = 138 \text{ cm}^{-1}$) of asymmetric (1538 cm⁻¹) and symmetric (1400 cm⁻¹) $\nu(\text{C}=\text{O})$ vibrations for benzoate species close to the free ion values demonstrate the benzoate complex with a bridging structure on MnCo_{6.6} catalyst [43]. A series of weak peaks are also observed in the range of about 1700-1950 cm⁻¹, which are attributed to the $\nu(\text{C}=\text{O})$ signals of asymmetric and symmetric stretching changes in maleic anhydride, indicating the completed partial deep oxidation process [44, 56]. Finally, the absorption

peaks for CO₂ and H₂O are detected at the ranges of 2330-2400 cm⁻¹ and 3300-3420 cm⁻¹, respectively, which indicate that part of the toluene has been completely converted [17, 54, 57]. One can see that with the increase of the reaction time, the relative intensity of the benzoate peak surpasses that of benzaldehyde, and the band intensities of maleic anhydride and CO₂ species are also positively correlated with the reaction time, which prove that the contact time between the VOC molecule and active site has an insignificant effect on the catalytic performance as discussed in WHSV effect. The temperature-dependent spectra of toluene combustion in air atmosphere over MnCo_{6.6} catalyst are shown in Fig. 4.8e. One can see that the characteristic bands described above are gradually become more and more obvious with the increasing of reaction temperature. Furthermore, the relative intensities of the characteristic benzoate peaks surpass those of benzaldehyde when the reaction temperature exceeds 200 °C, and the maleic anhydride bands also appear at a further higher temperature, which indicate that the generation of benzoate species from benzaldehyde requires the participation of more reactive oxygen species and thus the generation of maleic anhydride from benzoate species should be the rate-controlling step. The toluene combustion process in N₂ atmosphere were also performed to explore the role of intrinsic oxygen species in MnCo_{6.6} catalyst (Fig. 4.8b). It can be seen that various intermediates can still be detected in the absence of gas-phase oxygen, indicating that the inherent adsorbed and lattice oxygen in the catalyst can contribute the toluene oxidation process. However, with the increase of reaction time, there is no enrichment of other intermediates (e.g., benzoate species) except for a slight increase in the intensity of absorption peak of benzaldehyde, which indicate the limitation of content and activity for the inherent oxygen species in the catalyst. Fig. 4.8c shows the DRIFTS spectra of toluene oxidation test in air atmosphere over pure MnO_x catalyst. Compared with the data shown Fig. 4.8a, the characteristic peak intensities of benzoate and low-frequency intermediates in Fig. 4.8c remain basically unchanged with the increasing of reaction time. Besides, as the reaction temperature increases (Fig. 4.8f), the absorption peak of the benzoate species in the reaction becomes weaker. For the reaction in nitrogen atmosphere (Fig. 4.8d), only the characteristic absorption peak of benzaldehyde is found to increase with

the reaction time. These phenomena indicate that toluene also undergoes oxidation reaction on pure MnO_x catalyst, however, it is difficult for benzaldehyde to undergo further oxidation reaction due to insufficient oxidizing ability.

Therefore, it can be considered from the above description that the oxidation of toluene could occur on the MnCo6.6 and MnO_x catalysts regardless of the presence or absence of gaseous O_2 , that is, either the inherent adsorbed oxygen or the lattice oxygen species of the catalysts should involve in the oxidation reaction. Furthermore, the oxidation of benzaldehyde to benzoate species and then to anhydrides requires an increasing oxidative capacity of the catalyst. For the MnCo6.6 catalyst, the excellent lattice oxygen mobility derived from its mixed amorphous and low-crystallinity spinel characteristic phases associated with abundant active Mn^{3+} and Co^{3+} species should contribute better low-temperature transfer capacity of nucleophilic lattice oxygen in the catalyst, which makes it easier to get involved in the deep oxidation of toluene molecules. Additionally, sufficient dislocations, phase interfaces, and appropriate unpaired electron species in the MnCo6.6 catalyst can adsorb and activate the gaseous O_2 to activate electrophilic oxygen species, which can be considered to be directly participated in the toluene oxidation and replenished lattice oxygen species, thus realizing the sustained and efficient toluene oxidation over the catalyst. On the contrary, the completely amorphous MnO_x catalyst cannot guarantee rich-active oxygen and active lattice oxygen owing to the lack of synergistic and complementary active regions, and thus suspend the deep sustainable oxidation of reaction intermediates, thereby showing a poor catalytic performance.

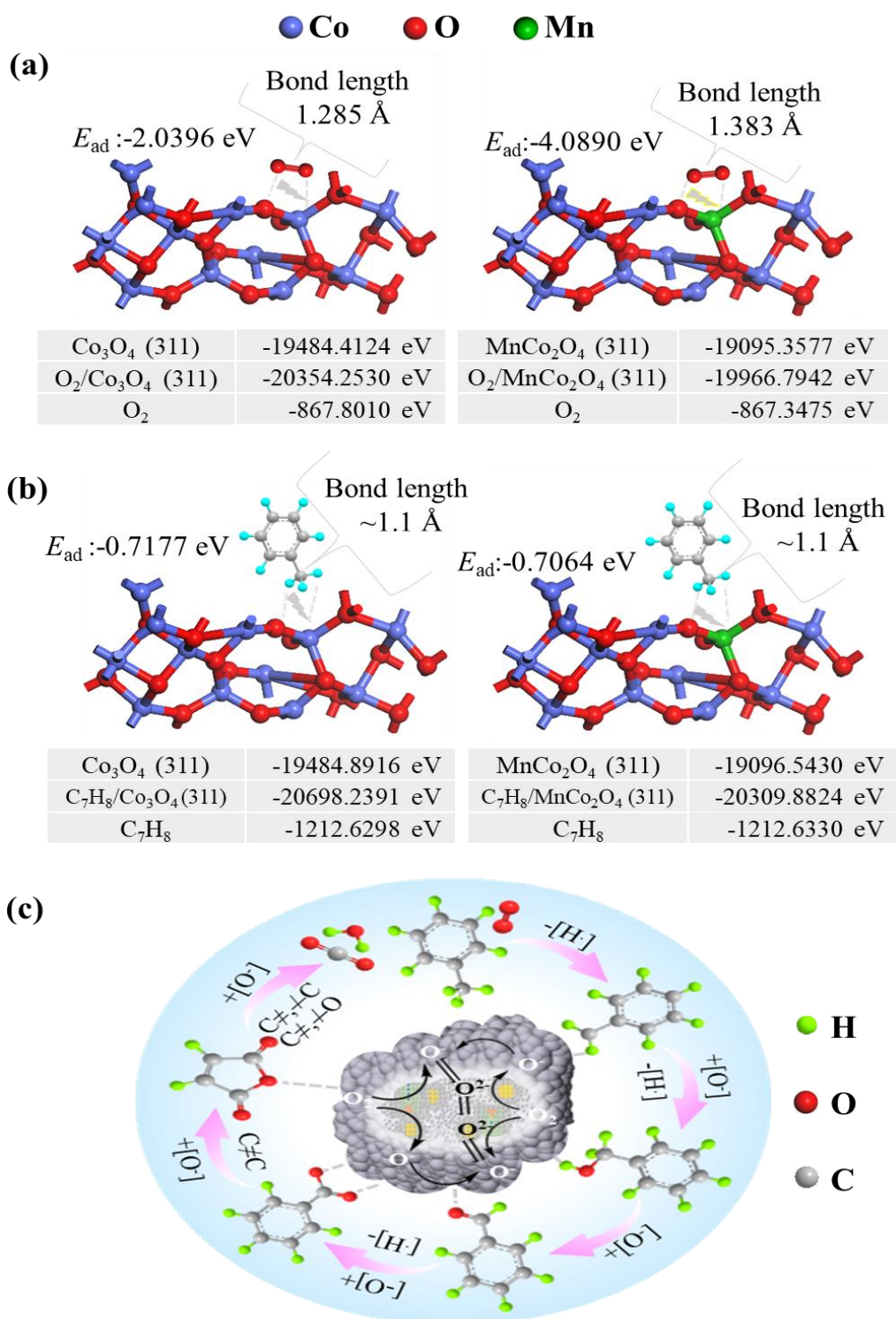


Fig. 4.9. Diagrams of DFT calculations for the adsorption properties of (a) oxygen and toluene (b) molecules on the spinel structure, and (c) combustion mechanism of toluene over MnCo_{6.6} catalyst in air atmosphere.

In addition, DFT theoretical calculations were used to further confirm the promoting effect of spinel phase in the process of toluene oxidation (Fig. 4.9a and 4.9b). As shown in Fig. 4.9a, the E_{ad} of oxygen molecules on Co₃O₄ (311) and MnCo₂O₄ (311) are -

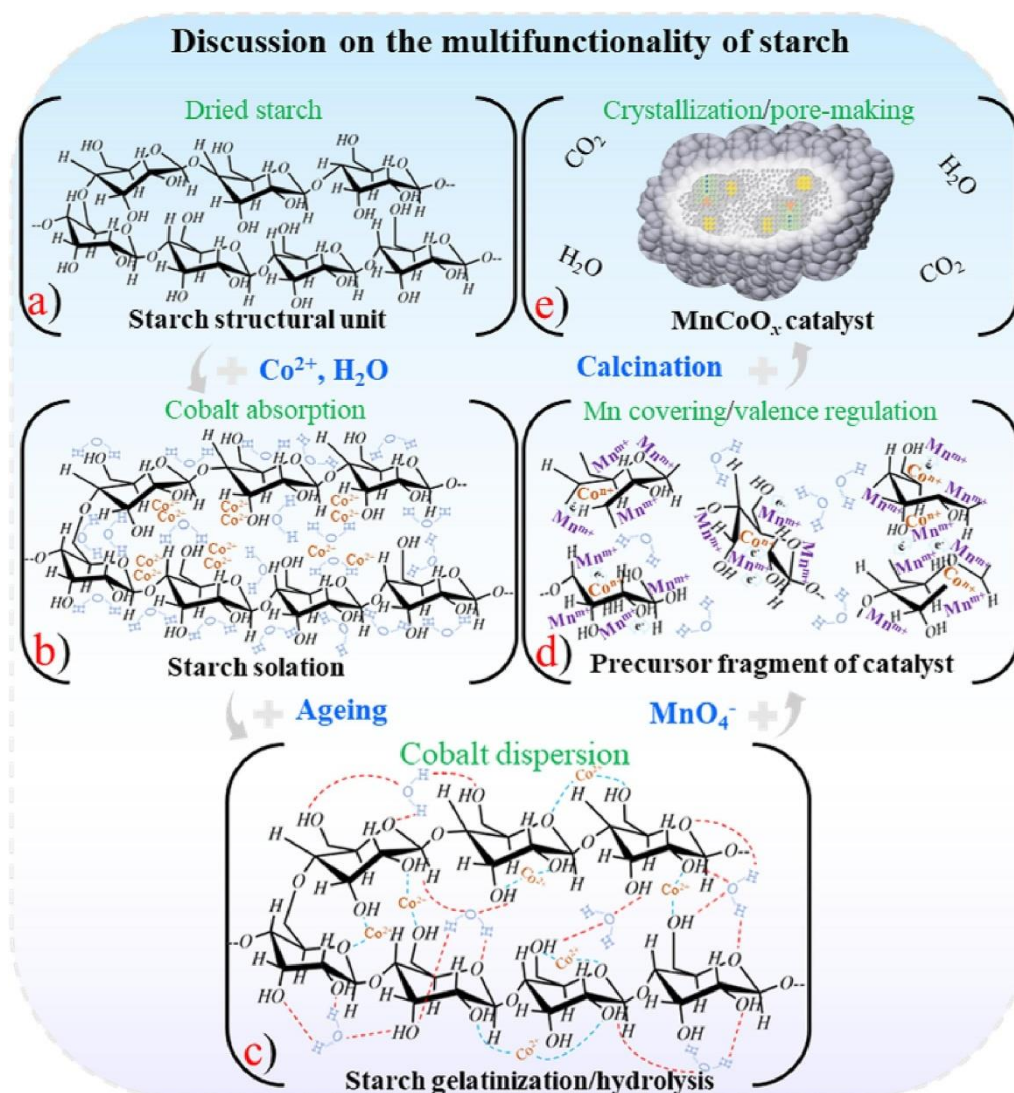
2.0396 and -4.0890 eV, respectively, which indicates a strong O₂ adsorption capacity on the latter. Furthermore, the longer stretch bond length of O adsorbed on the MnCo₂O₄ (311, 1.383 Å) phase indicates that the O atom from O₂ is more likely to break free and be activated than that on Co₃O₄ (311). However, the adsorption properties of Co₃O₄ (311) and MnCo₂O₄ (311) for toluene molecules are similar (Fig. 4.9b). Therefore, it can be considered that MnCo₂O₄ phase in the MnCo_{6.6} catalyst could significantly promote the adsorption and activation capacity of oxygen molecules and has only a little effect on the adsorption performance of toluene. As shown in Fig. 4.9c, a reliable mechanism for toluene combustion over the MnCo_{6.6} catalyst can be deduced based on the above discussion. First, toluene and O₂ molecules would physically diffuse and adsorb on the porous MnCo_{6.6} catalyst. Soon, the physically adsorbed toluene molecules are oxidized through dehydrogenation by the surface adsorbed active oxygen species to generate benzyl (Ph-CH₂-) group. Then, the methylene group in the benzyl group undergoes dehydrogenation reaction with electrophilic oxygen species on the surface/subsurface to generate benzyl alcohol (Ph-CH₂-O-), which would be followed by further hydroxyl oxidation to form benzaldehyde species (Ph-CHO) by electrophilic oxygen species. The above-described oxidation reaction process should occur easily with the participation of surface adsorbed oxygen and some electrophilic oxygen species. Although a large number of electrophilic oxygen species will be consumed in the previous reaction, the abundant defect structures (e.g., dislocations, interfaces and oxygen vacancies) in the MnCo_{6.6} catalyst would activate the surrounding adsorbed gaseous O₂ in time to realize the regeneration of electrophilic oxygen species, which will guarantee the oxidation of benzaldehyde to benzoate (Ph-CH₂-COO-) in the next step. In comparison, such deep oxidations of intermediates to generate large amounts of benzoate species cannot take place on the pure MnO_x catalyst and/or nitrogen atmosphere. Afterwards, the benzoate species are synergistically oxidized by both surface oxygen and subsurface lattice oxygen at a higher temperature to the ring-opening product of maleic anhydride, which is always easily oxidized to carbon dioxide and water. Since this process will occur at a higher temperature, excellent oxygen mobility and abundant active centers are required.

Because of this, it can be considered a rate-controlling step in the catalytic reaction of toluene. Therefore, MnCo6.6 catalyst with the synergistic complementary active regions exhibits better catalytic activity for toluene combustion owing to its sufficient oxidation capacity.

Table 4.4 Vibratory assignments of main in situ DRIFTS bands in toluene oxidation process over the CoMn6.6 catalyst.

Wavenumber/cm ⁻¹	Assignment	Corresponding structure
1469	$\nu(\text{C-H})$ asymmetric deformation vibration	methyl group
3071	$\nu(\text{C-H})$ stretching vibration	aromatic ring
1305	deformation vibration of benzyl	benzyl
1025, 1058, 1140	stretching vibrations of $\nu(\text{C-O})$	benzyl alcohol
1213, 1252	stretching vibrations of $\nu(\text{C-O})$	phenolate
1177, 1598, 1622, 1634	$\nu(\text{C=O})$ stretching vibration of carbonyl group	benzaldehyde
1400	symmetric stretching vibrations of $\nu(\text{C=O})$ in carboxylate group	benzoate species
1538	asymmetric stretching vibrations of $\nu(\text{C=O})$ in carboxylate group	benzoate species
1550	antisymmetric $\nu(\text{C-O})$	benzoate species
~1700-1950	$\nu(\text{C=O})$ symmetric and asymmetric stretching vibrations in anhydride	maleic anhydride
~3300-3420	$\nu(\text{O-H})$ stretching vibrations	absorbed water
~2330-2400	$\nu(\text{C=O})$ asymmetric stretching vibrations	carbon dioxide

4.3.9 Discussion on the function of starch paste in catalyst synthesis



Scheme 4.2. Schematic illustration of the starch functions in the synthesis process of MnCoO_x catalysts.

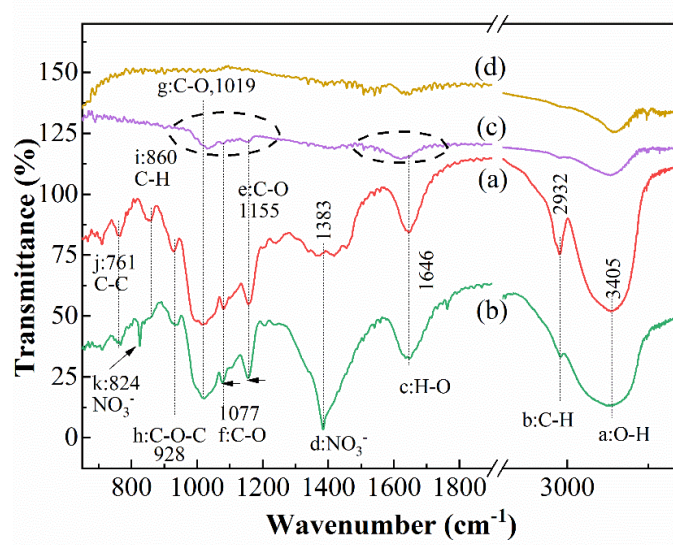


Fig. 4.10. FT-IR spectra of potato starch (a), starch paste with cobalt dispersed (b), catalyst precursor obtained after oxidative shear process (c) and MnCo_{6.6} catalyst (d), Corresponding references: a, b, c [58]; e, f, g [59]; h, i, j [60]; d, k [61].

As described above, the MnCo_{6.6} mixed oxide catalyst synthesized by the starch paste-assisted method exhibited superior catalytic performance due to its abundant mesoporous structure and synergistic active regions. As shown in Scheme 4.2a and Fig. 4.10a, potato starch is a covalent polymer formed by dehydration of α -D-glucopyranose and linked together by glycosidic bonds, which generally exhibits a branched structure with some straight chains [62, 63]. After the Co²⁺ aqueous solution was mixed with the starch and treated in a water bath, the starch would undergo intercrystalline water absorption and swelling, and as such, cobalt ions would be absorbed into the space-confined glucose monomers (Scheme 4.2b) [64]. After that, when the paste obtained above was subjected to room temperature for aging treatment, the cobalt ions would be dispersed and fixed onto the monomer physically and chemically by the formation of a large number of intermolecular hydrogen bonds and coordination bonds [65]. At this time, these metal ions would break the charge balance, resulting in the shift of the vibrational frequency of the C-O covalent bond (Scheme 4.2c, Fig. 4.10b) [66]. In turn, the hydrolysis process of starch also could realize the tuning of valence state due to the influence of the electron cloud structure around the metal ions. Then, a potassium permanganate solution serving as Mn source and oxidant was poured into the paste

obtained above and mixed well. The strong oxidizing potassium permanganate would first oxidatively shear the starch chains with the reducing of Mn valence state, oxidation of the cobalt species and in-situ encapsulation of them in the network. As such, the catalyst precursor composed of a strongly interacting Mn-Co mixture wrapped by fragmented polysaccharide chains would be formed, which was also evidenced by the residual weak C-O vibrational peaks in the FT-IR spectrum (Scheme 4.2d, Fig. 4.10c). Finally, after the above precursor was calcined in a muffle furnace, the target MnCo_x oxide catalyst could be obtained. Herein, due to the differences in the branched and straight chains of starch microstructures, the different dispersion states of metal ions could lead to the formation of various active regions during the calcination and crystallization processes. In addition, the residual organic matter would first form a porous gel, and finally resulted in the formation of a more porous structure with the generation of gas from gel burning (Scheme 4.2e, Fig. 4.10d). Therefore, the starch played an important role in element dispersion, metal valence regulation, and construction of porous structures and multi-active regions during the catalyst synthesis. However, it should be mentioned that the starches from different sources (e.g., wheat starch and corn starch) will definitely affect the performance of the catalyst due to their different physicochemical properties such as the proportion of branched chains and linear chains.

4.4 Conclusions

In summary, a series of nanoparticle-stacking MnCo_x composite oxide catalysts were successfully synthesized by a starch-assisted oxidative shearing method and used for catalytic toluene combustion at low temperature. The characterization results showed that the MnCo_x catalysts exhibit abundant mesoporous structures with larger SSAs, which efficiently optimized the active sites accessibility and mass transfer performance of gas feedstock on the MnCo_x catalyst. The metal dispersion and valence regulation functions of starch with special branched/linear mixed structure helped to construct a microscopically heterogeneous MnCoO_x catalyst successfully, which consists of multifarious active phases (i.e., low-crystallinity MnCo₂O₄, amorphous region, interface region between the phases and dislocation structure) with synergistic and

complementary effects. In addition, owing to the intensive synergistic effect between Mn and Co species, and among different active regions in MnCo_x catalysts, especially for MnCo_{6.6} catalyst, they not only exhibit affluent Mn³⁺, Co³⁺, surface active oxygen species, but also have superior reducibility at a low temperature as well as oxygen mobility, which are all important conditions to promote the performance. As a result, the optimal MnCo_{6.6} catalyst achieved the 90% and 100% toluene conversions at 224 and 226 °C under a WHSV of 60,000 cm³·g⁻¹·h⁻¹, respectively. The DFT calculation results show the lower adsorption energy (-4.0890 eV) and longer bond length (1.383 Å) of O₂ molecules adsorbed on the spinel MnCo₂O₄ phase, indicating the superiority of this active region in activating oxygen molecules. While, the time and temperature-dependent in situ DRIFTS spectra in various atmospheres demonstrated that not only the continuous supply of electrophilic adsorbed oxygen species was required during the toluene combustion on MnCo_{6.6} catalyst, but also lattice oxygen with superior mobility also needed to participate the deep oxidation process of toluene molecules. Especially, the amorphous region and low crystalline region ensured the superior mobility of bulk lattice oxygen and the high activity of surface lattice oxygen whereas the defect regions could continuously adsorb and activate oxygen molecules to become electrophilic oxygen species, which could not only directly take part in the toluene oxidation in the whole process, but also supplement the consumed lattice oxygen, thus ensuring the cycle efficiency of the catalyst.

References

- [1] C. Yang, G. Miao, Y. Pi, Q. Xia, J. Wu, Z. Li, J. Xiao, Abatement of various types of VOCs by adsorption/catalytic oxidation: A review, *Chem. Eng. J.*, 370 (2019) 1128-1153.
- [2] S. Zhao, Y. Yang, F. Bi, Y. Chen, M. Wu, X. Zhang, G. Wang, Oxygen vacancies in the catalyst: Efficient degradation of gaseous pollutants, *Chem. Eng. J.*, 454 (2023) 140376.
- [3] L. Chen, J. Jia, R. Ran, X. Song, Nickel doping MnO_2 with abundant surface pits as highly efficient catalysts for propane deep oxidation, *Chem. Eng. J.*, 369 (2019) 1129-1137.
- [4] J. Zhao, P. Wang, C. Liu, Q. Zhao, J. Wang, L. Shi, G. Xu, A. Abudula, G. Guan, Nanosheet-state cobalt-manganese oxide with multifarious active regions derived from oxidation-etching of metal organic framework precursor for catalytic combustion of toluene, *J. Colloid Interf. Sci.*, 629 (2023) 706-722.
- [5] W. Pei, Y. Liu, J. Deng, K. Zhang, Z. Hou, X. Zhao, H. Dai, Partially embedding Pt nanoparticles in the skeleton of 3DOM Mn_2O_3 : An effective strategy for enhancing catalytic stability in toluene combustion, *Appl. Catal. B: Environ.*, 256 (2019) 117814.
- [6] L. Ma, D. Wang, J. Li, B. Bai, L. Fu, Y. Li, Ag/ CeO_2 nanospheres: Efficient catalysts for formaldehyde oxidation, *Appl. Catal. B: Environ.*, 148-149 (2014) 36-43.
- [7] S. Xie, Y. Liu, J. Deng, X. Zhao, J. Yang, K. Zhang, Z. Han, H. Arandiyana, H. Dai, Effect of transition metal doping on the catalytic performance of Au-Pd/3DOM Mn_2O_3 for the oxidation of methane and o-xylene, *Appl. Catal. B: Environ.*, 206 (2017) 221-232.
- [8] D.A. Aguilera, A. Perez, R. Molina, S. Moreno, Cu-Mn and Co-Mn catalysts synthesized from hydrotalcites and their use in the oxidation of VOCs, *Appl. Catal. B: Environ.*, 104 (2011) 144-150.
- [9] G. Chen, D. Hong, H. Xia, W. Sun, S. Shao, B. Gong, S. Wang, J. Wu, X. Wang, Q. Dai, Amorphous and homogeneously Zr-doped MnO_x with enhanced acid and redox properties for catalytic oxidation of 1,2-Dichloroethane, *Chem. Eng. J.*, 428 (2022) 131067.

- [10] Z. Ren, Z. Wu, W. Song, W. Xiao, Y. Guo, J. Ding, S.L. Suib, P.-X. Gao, Low temperature propane oxidation over Co_3O_4 based nano-array catalysts: Ni dopant effect, reaction mechanism and structural stability, *Appl. Catal. B: Environ.*, 180 (2016) 150-160.
- [11] Z. Huang, M. Zhao, J. Luo, X. Zhang, W. Liu, Y. Wei, J. Zhao, Z. Song, Interaction in $\text{LaOx-Co}_3\text{O}_4$ for highly efficient purification of toluene: Insight into LaOx content and synergistic effect contribution, *Sep. Purif. Technol.*, 251 (2020) 117369.
- [12] P. Yang, S. Yang, Z. Shi, Z. Meng, R. Zhou, Deep oxidation of chlorinated VOCs over CeO_2 -based transition metal mixed oxide catalysts, *Appl. Catal. B: Environ.*, 162 (2015) 227-235.
- [13] J. Chen, X. Chen, W. Xu, Z. Xu, J. Chen, H. Jia, J. Chen, Hydrolysis driving redox reaction to synthesize Mn-Fe binary oxides as highly active catalysts for the removal of toluene, *Chem. Eng. J.*, 330 (2017) 281-293.
- [14] Z. Ye, J.M. Giraudon, N. Nuns, P. Simon, N. De Geyter, R. Morent, J.F. Lamonier, Influence of the preparation method on the activity of copper-manganese oxides for toluene total oxidation, *Appl. Catal. B: Environ.*, 223 (2018) 154-166.
- [15] D. Delimaris, T. Ioannides, VOC oxidation over $\text{MnO}_x\text{-CeO}_2$ catalysts prepared by a combustion method, *Appl. Catal. B: Environ.*, 84 (2008) 303-312.
- [16] W. Tang, Y. Deng, W. Li, J. Li, G. Liu, S. Li, X. Wu, Y. Chen, Importance of porous structure and synergistic effect on the catalytic oxidation activities over hierarchical Mn-Ni composite oxides, *Catal. Sci. Technol.*, 6 (2016) 1710-1718.
- [17] Q. Ren, S. Mo, J. Fan, Z. Feng, M. Zhang, P. Chen, J. Gao, M. Fu, L. Chen, J. Wu, D. Ye, Enhancing catalytic toluene oxidation over $\text{MnO}_2@\text{Co}_3\text{O}_4$ by constructing a coupled interface, *Chinese J. Catal.*, 41 (2020) 1873-1883.
- [18] X. Li, J. Zheng, S. Liu, T. Zhu, A novel wormhole-like mesoporous hybrid MnCoO_x catalyst for improved ethanol catalytic oxidation, *J. Colloid Interf. Sci.*, 555 (2019) 667-675.
- [19] D. Han, X. Ma, X. Yang, M. Xiao, H. Sun, L. Ma, X. Yu, M. Ge, Metal organic framework-templated fabrication of exposed surface defect-enriched Co_3O_4 catalysts for efficient toluene oxidation, *J. Colloid Interf. Sci.*, 603 (2021) 695-705.

- [20] P. Liu, Y. Liao, J. Li, L. Chen, M. Fu, P. Wu, R. Zhu, X. Liang, T. Wu, D. Ye, Insight into the effect of manganese substitution on mesoporous hollow spinel cobalt oxides for catalytic oxidation of toluene, *J. Colloid Interf. Sci.*, 594 (2021) 713-726.
- [21] P. Zhang, H. Lu, Y. Zhou, L. Zhang, Z. Wu, S. Yang, H. Shi, Q. Zhu, Y. Chen, S. Dai, Mesoporous MnCeO_x solid solutions for low temperature and selective oxidation of hydrocarbons, *Nat. Commun.*, 6 (2015) 8446.
- [22] S. Wu, H. Liu, Z. Huang, H. Xu, W. Shen, O-vacancy-rich porous MnO_2 nanosheets as highly efficient catalysts for propane catalytic oxidation, *Appl. Catal. B: Environ.*, 312 (2022) 121387.
- [23] G. Long, M. Chen, Y. Li, J. Ding, R. Sun, Y. Zhou, X. Huang, G. Han, W. Zhao, One-pot synthesis of monolithic Mn-Ce-Zr ternary mixed oxides catalyst for the catalytic combustion of chlorobenzene, *Chem. Eng. J.*, 360 (2019) 964-973.
- [24] Z. Sibaib, F. Puleo, J.M. Garcia-Vargas, L. Retailleau, C. Descorme, L.F. Liotta, J.L. Valverde, S. Gil, A. Giroir-Fendler, Manganese oxide-based catalysts for toluene oxidation, *Appl. Catal. B: Environ.*, 209 (2017) 689-700.
- [25] P. Yang, S. Fan, Z. Chen, G. Bao, S. Zuo, C. Qi, Synthesis of Nb_2O_5 based solid superacid materials for catalytic combustion of chlorinated VOCs, *Appl. Catal. B: Environ.*, 239 (2018) 114-124.
- [26] Z. Li, Q. Yan, Q. Jiang, Y. Gao, T. Xue, R. Li, Y. Liu, Q. Wang, Oxygen vacancy mediated $\text{Cu}_y\text{Co}_{3-y}\text{Fe}_1\text{O}_x$ mixed oxide as highly active and stable toluene oxidation catalyst by multiple phase interfaces formation and metal doping effect, *Appl. Catal. B: Environ.*, 269 (2020) 118827.
- [27] D. Yu, Y. Ren, X. Yu, X. Fan, L. Wang, R. Wang, Z. Zhao, K. Cheng, Y. Chen, Z. Sojka, A. Kotarba, Y. Wei, J. Liu, Facile synthesis of birnessite-type $\text{K}_2\text{Mn}_4\text{O}_8$ and cryptomelane-type $\text{K}_{2-x}\text{Mn}_8\text{O}_{16}$ catalysts and their excellent catalytic performance for soot combustion with high resistance to H_2O and SO_2 , *Appl. Catal. B: Environ.*, 285 (2021) 119779.
- [28] W. Gu, C. Li, J. Qiu, J. Yao, Facile preparation of porous hollow $\text{Co}_x\text{Mn}_{3-x}\text{O}_4$ normal-inverse coexisted spinel for toluene oxidation, *J. Alloy. Comp.*, 892 (2022) 162185.

- [29] G. Zhou, X. He, S. Liu, H. Xie, M. Fu, Phenyl VOCs catalytic combustion on supported CoMn/AC oxide catalyst, *J. Ind. Eng. Chem.*, 21 (2015) 932-941.
- [30] G. Li, N. Li, Y. Sun, Y. Qu, Z. Jiang, Z. Zhao, Z. Zhang, J. Cheng, Z. Hao, Efficient defect engineering in Co-Mn binary oxides for low-temperature propane oxidation, *Appl. Catal. B: Environ.*, 282 (2021) 119512.
- [31] Y. Zheng, Y. Liu, H. Zhou, W. Huang, Z. Pu, Complete combustion of methane over Co_3O_4 catalysts: influence of pH values, *J. Alloy. Comp.*, 734 (2018) 112-120.
- [32] J. Lei, P. Wang, S. Wang, J. Li, Y. Xu, S. Li, Enhancement effect of Mn doping on Co_3O_4 derived from Co-MOF for toluene catalytic oxidation, *Chin. J. Chem. Eng.*, 52 (2022) 1-9.
- [33] C. Dong, Z. Qu, X. Jiang, Y. Ren, Tuning oxygen vacancy concentration of MnO_2 through metal doping for improved toluene oxidation, *J. Hazard. Mater.*, 391 (2020) 122181.
- [34] Y. Peng, L. Zhang, L. Chen, D. Yuan, G. Wang, X. Meng, F.-S. Xiao, Catalytic performance for toluene abatement over Al-rich Beta zeolite supported manganese oxides, *Catal. Today*, 297 (2017) 182-187.
- [35] Y. Zheng, Q. Liu, C. Shan, Y. Su, K. Fu, S. Lu, R. Han, C. Song, N. Ji, D. Ma, Defective ultrafine MnO_x nanoparticles confined within a carbon matrix for low-temperature oxidation of volatile organic compounds, *Environ. Sci. Technol.*, 55 (2021) 5403-5411.
- [36] X. Jiang, W. Xu, S. Lai, X. Chen, Integral structured Co-Mn composite oxides grown on interconnected Ni foam for catalytic toluene oxidation, *RSC Adv.*, 9 (2019) 6533-6541.
- [37] X. Zhang, J. Zhao, Z. Song, W. Liu, H. Zhao, M. Zhao, Y. Xing, Z. Ma, H. Du, The catalytic oxidation performance of toluene over the Ce-Mn- O_x catalysts: Effect of synthetic routes, *J. Colloid Interf. Sci.*, 562 (2020) 170-181.
- [38] Y. Wang, L. Guo, M. Chen, C. Shi, CoMn_xO_y nanosheets with molecular-scale homogeneity: an excellent catalyst for toluene combustion, *Catal. Sci. Technol.*, 8 (2018) 459-471.
- [39] Z. Cheng, Z. Chen, J. Li, S. Zuo, P. Yang, Mesoporous silica-pillared clays

supported nanosized $\text{Co}_3\text{O}_4\text{-CeO}_2$ for catalytic combustion of toluene, *Appl. Sur. Sci.*, 459 (2018) 32-39.

[40] H. Zhao, H. Wang, Z. Qu, Synergistic effects in Mn-Co mixed oxide supported on cordierite honeycomb for catalytic deep oxidation of VOCs, *J. Environ. Sci.*, 112 (2022) 231-243.

[41] S. Mo, Q. Zhang, Y. Sun, M. Zhang, J. Li, Q. Ren, M. Fu, J. Wu, L. Chen, D. Ye, Gaseous CO and toluene co-oxidation over monolithic core-shell Co_3O_4 -based hetero-structured catalysts, *J. Mater. Chem. A*, 7 (2019) 16197-16210.

[42] F. Hu, J. Chen, S. Zhao, K. Li, W. Si, H. Song, J. Li, Toluene catalytic combustion over copper modified $\text{Mn}_{0.5}\text{Ce}_{0.5}\text{O}_x$ solid solution sponge-like structures, *Appl. Catal. A: Gen.*, 540 (2017) 57-67.

[43] S. Mo, Q. Zhang, J. Li, Y. Sun, Q. Ren, S. Zou, Q. Zhang, J. Lu, M. Fu, D. Mo, J. Wu, H. Huang, D. Ye, Highly efficient mesoporous MnO_2 catalysts for the total toluene oxidation: Oxygen-Vacancy defect engineering and involved intermediates using in situ DRIFTS, *Appl. Catal. B: Environ.*, 264 (2020) 118464.

[44] P. Wang, J. Wang, J. Zhao, X. Ma, X. Du, S. Peng, X. Hao, B. Tang, A. Abudula, G. Guan, Trace holmium assisting delaminated OMS-2 catalysts for total toluene oxidation at low temperature, *J. Colloid Interf. Sci.*, 608 (2022) 1662-1675.

[45] Y. Luo, Y. Zheng, J. Zuo, X. Feng, X. Wang, T. Zhang, K. Zhang, L. Jiang, Insights into the high performance of Mn-Co oxides derived from metal-organic frameworks for total toluene oxidation, *J. Hazard. Mater.*, 349 (2018) 119-127.

[46] C. Fan, X. Wu, M. Li, X. Wang, Y. Zhu, G. Fu, T. Ma, Y. Tang, Surface chemical reconstruction of hierarchical hollow inverse-spinel manganese cobalt oxide boosting oxygen evolution reaction, *Chem. Eng. J.*, 431 (2022) 133829.

[47] Z. Zhang, F. Lin, L. Xiang, H. Yu, Z. Wang, B. Yan, G. Chen, Synergistic effect for simultaneously catalytic ozonation of chlorobenzene and NO over MnCoO_x catalysts: Byproducts formation under practical conditions, *Chem. Eng. J.*, 427 (2022) 130929.

[48] Z. Han, Y. Liu, J. Deng, S. Xie, X. Zhao, J. Yang, K. Zhang, H. Dai, Preparation and high catalytic performance of $\text{Co}_3\text{O}_4\text{-MnO}_2$ for the combustion of o-xylene, *Catal.*

Today, 327 (2019) 246-253.

[49] S. Xie, J. Deng, Y. Liu, Z. Zhang, H. Yang, Y. Jiang, H. Arandiyani, H. Dai, C.T. Au, Excellent catalytic performance, thermal stability, and water resistance of 3DOM Mn_2O_3 -supported Au-Pd alloy nanoparticles for the complete oxidation of toluene, *Appl. Catal. A: Gen.*, 507 (2015) 82-90.

[50] P. Wang, J. Wang, X. An, J. Shi, W. Shangguan, X. Hao, G. Xu, B. Tang, A. Abudula, G. Guan, Generation of abundant defects in Mn-Co mixed oxides by a facile agar-gel method for highly efficient catalysis of total toluene oxidation, *Appl. Catal. B: Environ.*, 282 (2021) 119560.

[51] W. Zhao, Y. Zhang, X. Wu, Y. Zhan, X. Wang, C.-T. Au, L. Jiang, Synthesis of Co-Mn oxides with double-shelled nanocages for low-temperature toluene combustion, *Catal. Sci. Technol.*, 8 (2018) 4494-4502.

[52] Y. Guan, Y. Zhou, S. Wang, R. Zou, J. Zhang, X. Fan, Y. Jiao, Structured cobalt-manganese oxides on SiC nano-whisker modified SiC foams for catalytic combustion of toluene, *Chem. Eng. Res. Des.*, 177 (2022) 659-669.

[53] X. Yang, X. Ma, X. Yu, M. Ge, Exploration of strong metal-support interaction in zirconia supported catalysts for toluene oxidation, *Appl. Catal. B: Environ.*, 263 (2020) 118355.

[54] P. Wang, J. Zhao, Q. Zhao, X. Ma, X. Du, X. Hao, B. Tang, A. Abudula, G. Guan, Microwave-assisted synthesis of manganese oxide catalysts for total toluene oxidation, *J. Colloid Interf. Sci.*, 607 (2021) 100-110.

[55] C. Zhang, C. Wang, H. Huang, K. Zeng, Z. Wang, H.-p. Jia, X. Li, Insights into the size and structural effects of zeolitic supports on gaseous toluene oxidation over $\text{MnO}_x/\text{HZSM-5}$ catalysts, *Appl. Sur. Sci.*, 486 (2019) 108-120.

[56] H. Yi, X. Xie, L. Song, S. Zhao, C. Du, L. Miao, X. Tang, Promotion of rapid microwave-assisted synthesized porous manganese-cobalt catalyst on low-temperature toluene oxidation, *J. Environ. Chem. Eng.*, 10 (2022) 107086.

[57] Z. Rui, M. Tang, W. Ji, J. Ding, H. Ji, Insight into the enhanced performance of TiO_2 nanotube supported Pt catalyst for toluene oxidation, *Catal. Today*, 297 (2017) 159-166.

- [58] F. Yang, Q. Du, T. Miao, X. Zhang, W. Xu, D. Jia, Interaction between potato starch and Tremella fuciformis polysaccharide, *Food Hydrocolloid.*, 127 (2022) 107509.
- [59] J. Wang, L. Su, S. Wang, Physicochemical properties of octenyl succinic anhydride-modified potato starch with different degrees of substitution, *J. Sci. Food Agric.*, 90 (2010) 424-429.
- [60] R. Kizil, J. Irudayaraj, K. Seetharaman, Characterization of Irradiated Starches by Using FT-Raman and FTIR Spectroscopy, *J. Agric. Food Chem.*, 50 (2002) 3912-3918.
- [61] N. He, Y. Ni, J. Teng, H. Li, L. Yao, P. Zhao, Identification of inorganic oxidizing salts in homemade explosives using Fourier transform infrared spectroscopy, *Spectrochim. Acta A*, 221 (2019) 117164.
- [62] I. Govindaraju, M. Sunder, I. Chakraborty, K.D. Mumbrekar, S. Sankar Mal, N. Mazumder, Investigation of physico-chemical properties of native and gamma irradiated starches, *Mater. Today Proc.*, 55 (2022) 12-16.
- [63] X. Zhao, P. Hofvander, M. Andersson, R. Andersson, Internal structure and thermal properties of potato starches varying widely in amylose content, *Food Hydrocolloid.*, 135 (2023) 108148.
- [64] Y. Hu, C. Li, Y. Tan, D.J. McClements, L. Wang, Insight of rheology, water distribution and in vitro digestive behavior of starch based-emulsion gel: Impact of potato starch concentration, *Food Hydrocolloid.*, 132 (2022) 107859.
- [65] M. Tako, Y. Tamaki, T. Teruya, Y. Takeda, The principles of starch gelatinization and retrogradation, *Food Nutr., Sci.*, 5 (2014) 280-291.
- [66] H. Zhang, F. He, T. Wang, G. Chen, Insights into the interaction of CaCl₂ and potato starch: Rheological, structural and gel properties, *Int. J. Biol. Macromol.*, 220 (2022) 934-941.

CHAPTER 5 Conclusions and prospects

5.1 Conclusions

Catalytic combustion is recognized as the most attractive strategy for VOCs pollutant removal thanks to its low energy consumption, easy operation, and non-secondary pollution. This research provides a detailed overview firstly for the construction strategies and performance optimization effects of micro-heterostructures used in VOCs oxidation catalysts in recent years. In addition, considering the singleness of the traditional catalyst synthesis routes and the mediocrity of the reported catalyst performance, three novel microscopically heterogeneous manganese-based oxidation catalysts were reported in this work for the catalytic combustion evaluation of toluene based on the concepts of green, efficient and innovative. Combining various characterization methods, in situ DRIFTS technology and corresponding theoretical calculations, the physicochemical properties of the synthesized catalytic materials and the oxidation mechanism of toluene were parsed. The specific research conclusions are summarized as follows:

(I) In order to improve the poor oxidation-reduction performance of catalysts synthesized by the traditional sol-gel method and the problems of irritating odors in the synthesis process, we developed an eco-friendly pectin-driven sol-gel route to prepare a manganese oxide ($\text{MnO}_x\text{-P}$) catalyst for catalytic toluene combustion. Compared with the manganese oxides synthesized by the traditional citric acid sol-gel method ($\text{MnO}_x\text{-C}$) and glycine sol-gel method ($\text{MnO}_x\text{-G}$), $\text{MnO}_x\text{-P}$ catalyst synthesized by the pectin sol-gel method exhibits unique hierarchical mesoporous characteristics. The inhibition effect to long-range ordered crystals from the pectin chelation and combustion processes led to a lowest crystallinity (28.5%) and smaller grain size (8.8 nm) in $\text{MnO}_x\text{-P}$ catalyst. This phenomenon contributed to the excellent low-temperature reducibility, satisfactory oxygen mobility and active species in $\text{MnO}_x\text{-P}$ catalyst, and thus led to an improvement in catalytic performance of toluene combustion. In addition, the $\text{MnO}_x\text{-P}$ catalyst exhibited excellent long-time stability and water tolerance. Thus, the pectin-

driven sol-gel method developed in this work presents the facile, novel, green and efficient characteristics in catalytic material synthesis.

(II) Calcination of MOF precursors is a relatively novel strategy for the synthesis of catalysts in recent years. However, on the one hand, the catalyst synthesized by this method has a single active component and ordinary catalytic performance. On the other hand, the high-crystallinity materials resulting from high-temperature calcination of MOF materials are always accompanied by poor oxygen mobility, while the residual organic ligands caused by low-temperature calcination conditions always hinder the intermetallic interaction. Thus, a nanosheet-state CoMnx mixed oxide catalyst was synthesized by using the oxidation-etching MOF self-assembly strategy and used it for the low-temperature catalytic combustion of toluene, which overcame the shortcomings of the direct calcination of MOFs method for synthesizing catalysts. The specific conclusions are as follows: Enough mesoporous structures in the CoMnx catalysts with the increased SSA from 30 m²/g (CoO_x) to 163 m²/g (CoMn6) were assembled by using this suitable oxidation-etching process, which not only reduced the mass transfer resistance of toluene molecules and increased the exposure of more active sites on the catalyst. This oxidation-etching route constructed multifarious abundant active regions, i.e., amorphous structure, low crystallinity phase, dislocation region, phase interface region in the optimal CoMn6 catalyst, which greatly enriched the active species (e.g., Mn³⁺, Co³⁺, and active adsorbed oxygen species) and improved the low-temperature reducibility as well as oxygen mobility in the CoMn6 catalysts due to the strong interaction between different active regions. The DFT calculation results showed that the existence of MnCo₂O_{4.5} (311) plane in the catalyst can better adsorb and activate O₂ molecules and generate more reactive oxygen species. The in-situ DRIFTS experiments under different atmospheres for toluene combustion on CoMn6 catalyst demonstrated the significance of sufficient adsorbed oxygen species and active lattice oxygen, which could be guaranteed by the continuous supply of active oxygen from crystal defect regions and abundant amorphous crystal as well as low crystallinity structure in the CoMn6 catalyst. The synergistic complementary effects of different active regions in CoMn6 catalyst contributed to a lower T₉₀ (219 °C) during toluene oxidation with 1,000

ppm of toluene concentration under a $60,000\text{ cm}^3\cdot\text{g}^{-1}\cdot\text{h}^{-1}$ of WHSV.

(III) Furthermore, a nanoparticles-stacking MnCo_x oxide with multifarious active phases for the low-temperature oxidation of toluene was synthesized by utilizing the special branched/linear polysaccharide structure in starch and its hydrolysis during gelatinization. The characterization results showed that the abundant mesoporous structures with larger SSAs in MnCo_x catalysts optimized their active sites accessibility and mass transfer performance of gas feedstock during oxidation reaction. The metal ion dispersing effect of the branched/linear structure in the starch, the ion-regulating function of the gelatinization process, and the reducibility of potato starch contributed to the abundant active regions (i.e., low-crystallinity MnCo₂O₄, amorphous region, interface region between the phases and dislocation structure) and active species in the synthesized MnCo_x catalysts. In addition, the intensive synergistic effect between Mn and Co species, and among different active regions in MnCo_{6.6} catalyst, made its superior reducibility at a low temperature as well as oxygen mobility, and thus showed the lower T₉₀ (224 °C) and T₁₀₀ (226 °C) during toluene oxidation. The DFT calculations and in situ DRIFTS spectra in various atmospheres demonstrated the synergistic complementary effect of different active regions. It is found that not only the continuous supply of electrophilic adsorbed oxygen species was required during the toluene combustion on MnCo_{6.6} catalyst, but also lattice oxygen with superior mobility also needed to participate the deep oxidation process of toluene molecules. The amorphous region and low crystalline region ensured the superior mobility of bulk lattice oxygen and the high activity of surface lattice oxygen whereas the defect regions could continuously adsorb and activate oxygen molecules to become electrophilic oxygen species, which could not only directly take part in the toluene oxidation in the whole process, but also supplement the consumed lattice oxygen, thus ensuring the cycle efficiency of the catalyst. This study provides a new viewpoint and idea for creating of novel catalysts with multiple active regions.

5.2 Prospects

In this work, the construction strategies of micro-heterostructures in non-noble metal-based catalysts for VOC oxidation and their effects as well as advantages in

catalytic combustion reactions were reviewed. Then, three kinds of manganese-based oxide catalysts with low crystallinity or micro-heterostructures owning synergistic and complementary effects were successfully constructed and used to catalyze the toluene reaction efficiently through our own developed catalyst synthesis strategies. However, although we found that the construction of micro-heterostructures in catalysts can greatly optimize the catalytic performance for VOC combustion, there are still several issues related to the heterostructures in catalysts that need to be further explored and analyzed in order to better guide efficient catalyst synthesis.

- ◆ The impacts of the type and content of heterostructures and their distribution positions in the catalyst (e.g., surface, subsurface, bulk) on the physicochemical properties and catalytic performance of the catalyst need to be demonstrated by designing more appropriate experiments.
- ◆ The direct synthesis of specific heterostructures and their specific facilitation in combination with different oxidation mechanisms need to be further explored.
- ◆ Whether the heterostructure evolves during the oxidation of VOCs, and the evolution or recovery mechanism needs to be further explored.
- ◆ The correspondence of different types of heterostructures to the oxidation effects of different VOCs is a question worth exploring.
- ◆ The water resistance, sulfur resistance and persistence of catalysts with different heterostructures in the actual catalytic VOCs combustion process need to be explored one by one.

We believe that by continuously exploring the mechanism of action of heterostructure catalysts in the oxidation of VOCs, researchers' understanding to the synthesis of efficient catalysts will be broadened, which will guide researchers to synthesize more efficient catalytic materials.

List of publications and presentations

Publications

- (1) **Jinggang Zhao**, Peifen Wang, Jing Wang, Changlin Liu, Junli Wang, Lei Shi, Guangwen Xu, Abuliti Abudula, Guoqing Guan, “Biostarch-assisted synthesis of microscopic heterogeneous manganese-cobalt oxides for efficient catalytic combustion of toluene” *Chemical Engineering Journal*, 464 (2023) 142739.
- (2) **Jinggang Zhao**, Peifen Wang, Changlin Liu, Qiang Zhao, Junli Wang, Lei Shi, Guangwen Xu, Abuliti Abudula, Guoqing Guan, “Nanosheet-state cobalt-manganese oxide with multifarious active regions derived from oxidation-etching of metal organic framework precursor for catalytic combustion of toluene” *Journal of Colloid and Interface Science*, 629 (2023) 706-722.
- (3) **Jinggang Zhao**, Peifen Wang, Jing Wang, Xiaoxun Ma, Lei Shi, Guangwen Xu, Abuliti Abudula, Guoqing Guan, “Synthesis of MnO_x from pectin-driven sol-gel route for catalytic oxidation of toluene” *JCIS Open*, 9 (2023) 100076.
- (4) Peifen Wang, **Jinggang Zhao**, Qiang Zhao, Xuli Ma, Xiao Du, Xiaogang Hao, Bing Tang, Abuliti Abudula, Guoqing Guan, “Microwave-assisted synthesis of manganese oxide catalysts for total toluene oxidation” *Journal of Colloid and Interface Science*, 607 (2022) 100-110.
- (5) Peifen Wang, Jing Wang, **Jinggang Zhao**, Xuli Ma, Xiao Du, Shang Peng, Xiaogang Hao, Bing Tang, Abuliti Abudula, Guoqing Guan, “Trace holmium assisting delaminated OMS-2 catalysts for total toluene oxidation at low temperature” *Journal of Colloid and Interface Science*, 608 (2022) 1662-1675.
- (6) Tan Khanh Trinh Le, Suwadee Kongparakul, Haibo Zhang, **Jinggang Zhao**, Guoqing Guan, Narong Chanlek, Thi Tuong Vi Tran, Chantip Samart, “Highly efficient liquid-phase oxidation of 5-hydroxymethylfurfural over Co-Cu/activated carbon catalysts” *Molecular Catalysis*, 539 (2023) 113017.

Presentations

- (1) **Jinggang Zhao**, Peifen Wang, Abuliti Abudula, and Guoqing Guan, “Multifunctional starch paste assisted synthesis of manganese-cobalt oxide catalyst with multifarious active regions for toluene catalytic combustion”, 12th International Conference on Environmental Catalysis (ICEC2022), Osaka, Japan (on-line), July 30 - August 2, 2022.
- (2) **Jinggang Zhao**, Abuliti Abudula, and Guoqing Guan, “MnCoO_x Catalysts assembled based on oxidative etching MOF precursor strategy for VOC Catalytic Combustion”, The 14th Global Chinese Chemical Engineers Symposium (GCCES-14), Guangzhou, China (on-line), August 12-14, 2022.
- (3) **Jinggang Zhao**, Abuliti Abudula, and Guoqing Guan, “Homogeneous cobalt-manganese composite oxide catalyst derived from oxidation-etching MOF for catalytic toluene combustion”, 化学工学会第 87 年会 (SCEJ), 神戸, Japan (on-line), March 16-18, 2022.
- (4) **Jinggang Zhao**, Abuliti Abudula, and Guoqing Guan, “Nanosheet-state cobalt-manganese oxide with multifarious active regions derived from oxidation-etching of MOF precursor for catalytic combustion of toluene”, 令和4年度化学系学協会東北大会, Iwate, Japan, September 17-18, 2022.

List of patents

(1) 趙井崗、官国清、王佩芬、関和治、阿布里提、“VOC 除去触媒及びその製造方法並びに VOC の除去方法”、日本特許、出願番号：特願 2021-183610、出願日：2021 年 11 月 10 日.

(2) 趙井崗、官国清、王佩芬、関和治、阿布里提、“揮発性有機化合物(VOC) 除去触媒とその調製方法”、日本特許、出願番号：特願 2021-167022、出願日：2021 年 10 月 11 日.

(3) 趙井崗、官国清、関和治、阿布里提、“V O C 除去触媒及びその製造方法、並びに V O C の除去方法”、特願 2023-011327、出願日：2023 年 1 月 27 日.

(4) 王佩芬、官国清、趙井崗、関和治、阿布里提、“V O C 除去触媒及びその製造方法並びに V O C の除去方法、” 出願番号：特願 2021-104147、出願日：2021 年 6 月 23 日.

List of awards

- (1) **Excellent Student Award**, Hirosaki University, Japan, March 7, 2023.
- (2) **Excellent Doctoral Scholar Forum Speaker**, The 14th Global Chinese Chemical Engineers Symposium (GCCES-14), Guangzhou, China, August 11, 2022.

Curriculum vitae

PERSONAL DETAILS

Name: Zhao Jinggang

Sex: Male

Date of birth: Feb. 05, 1992

Nationality: CHINA

Address: Graduate School of Science and Technology, Hirosaki University, 1-Bunkyocho, Hirosaki, 036-8560, Japan

Tel: 080-7812-3026

Email: h20ds251@hirosaki-u.ac.jp

EDUCATION

10/2020 **Hirosaki University**, Hirosaki, Japan, Ph.D

9/2017 **Shenyang University of Chemical Technology**, Shenyang, China, Master

9/2013 **Shenyang Institute of Science and Technology**, Shenyang, China, Bachelor

HONORS

2023.03 **Excellent Student Award**, Hirosaki University, Japan

2022.08 **Excellent Doctoral Scholar Forum Speaker**, 14th Global Chinese Chemical Engineers Symposium (GCCES-14), Guangzhou, China